Transmission X-ray Absorption Spectroscopy of the Solid Electrolyte Interphase on Silicon Anodes for Li-ion Batteries

Dissertation zur Erlangung des akademischen Grades

doctor rerum naturalium (Dr. rer. nat.)

im Fach: Chemie

Spezialisierung: Physikalische Chemie

eingereicht an der

Mathematisch-Naturwissenschaftlichen Fakultät der Humboldt-Universität zu Berlin

von

Martin Schellenberger

Präsident (komm.) der Humboldt-Universität zu Berlin

Prof. Dr. Peter Frensch

Dekan der Mathematisch-Naturwissenschaftlichen Fakultät

Prof. Dr. Elmar Kulke

Gutachter/innen: 1. Prof. Dr. Philipp Adelhelm

2. Dr. Robert Seidel

3. Prof. Dr. John C. Hemminger

Tag der mündlichen Prüfung: 07.09.2022

This thesis was written under supervision of

Dr. Robert Seidel

at the

Helmholtz-Zentrum Berlin für Materialien und Energie (HZB)

Young-Investigator Group Operando Interface Photochemistry

10/2018 - 02/2022

Abstract

Silicon offers a nine times higher theoretical storage capacity than graphite anodes, which dominate the current commercial lithium-ion battery (LIB) landscape. Being comparably cheap and earth-abundant makes silicon a promising candidate to leverage LIB technology and meet ever increasing demands. To compete with graphite, silicon anodes need to be operated in a potential range outside the thermodynamic stability window of currently available organic electrolytes. Thus, cyclability requires the electrolyte to be kinetically stabilized by the so-called Solid Electrolyte Interphase (SEI), a layer that ideally forms once from in-/organic decomposition products of the electrolyte during the first charging cycles. While it works for graphite, the SEI on silicon fails to stabilize the electrolyte sufficiently, mainly due to silicon's large volume swings upon de-/lithiation. Due to its physical and chemical volatile nature as well as its inaccessibility being burrowed in the cell assembly, the picture of the SEI on silicon remains elusive. To gain a deeper understanding of the SEI and ultimately improve its efficiency, *in-situ* and *operando* approaches are necessary.

X-ray Absorption Spectroscopy (XAS) is an element-specific technique, which allows to probe the electronic and chemical structure of the SEI. In this work, I introduce a novel approach for transmission XAS on liquids and thin-film battery electrode materials under *in-situ* conditions in the soft X-ray regime. Thematically, this work is divided into two parts: 1) the introduction of this novel method and 2) its application to investigate the SEI on silicon thin film anodes.

The presented technique is based on an electrochemical half-cell equipped with a sandwich of two soft X-ray transparent silicon nitride membrane windows to encapsulate the electrolyte. One of the membranes acts as substrate for the silicon thin-film anode, which is cycled with a metallic lithium counter-electrode. After the SEI has formed, a gas bubble is intentionally introduced through radiolysis by a high intensity X-ray to push out excessive electrolyte and stabilize a thin electrolyte layer on top of the SEI, keeping it *in-situ*. The obtained stack comprised of bubble, electrolyte thin-layer, SEI and anode, is sufficiently thin to be probed with transmission XAS in the soft X-ray regime. To illuminate the process of bubble formation, I present a Finite Element Method simulation of the temperature and concentration fields which evolve within the electrolyte under the high intensity X-ray beam. Additionally, I simulate the bubble growth through Computational Fluid Dynamics and demonstrate that the bubble ends up sitting steadily between the membranes.

The second part of this work utilizes the presented method to investigate the SEI on 50 nm thick amorphous silicon thin-film anodes in 1M $LiPF_6$ ethylene carbonate:dimethyl carbonate (50:50 v/v) electrolyte at the BESSY II synchrotron facility in Berlin. The anodes' electrochemical characterization shows all significant features of silicon's de-/lithiation. Complementarily, the cell is extended to allow *operando* Optical Microscopy (OM) and *operando* UV/Vis Spectroscopy (UV/Vis), where the degree of lithiation can be monitored through visible absorption. The OM reveals a reversible wrinkling of the membrane/silicon bilayer upon de-/lithiation, indicating a swing between tensile and compressive stress within each cycle. Both UV/Vis and OM verify that the anodes remain crack-free for the cycle count of the *in-situ* XAS investigation.

The transmission *in-situ* XAS investigation at the silicon L-edge as well as the oxygen and fluorine K-edge unveils every component in the beam's path. Carbon monoxide and carbon dioxide are identified as the main radiolysis products and bubble constituents. Additionally, it is shown that the degree of lithiation can be monitored at the silicon L-edge. Finally, the SEI's main components are determined as Li acetate, Li ethylene di-carbonate or Li ethylene mono-carbonate, Li acetylacetonate, LiOH, and LiF. Additionally, the evidence for aldehyde species indicates possible liquid inclusions within a presumably porous SEI morphology.

I consider the novel method presented in this work an appropriate tool to successfully engineer a stable, efficient SEI on a future silicon-anode based LIB.

Zusammenfassung

Silizium bietet eine 9-fach höhere theoretische Kapazität gegenüber Graphit-Anoden, welche momentan die Lithium-Ionen-Batterie (LIB) Landschaft beherrschen. Da Silizium reichhaltig vorhanden und kostengünstig ist, kann es die LIB Technologie vorantreiben und den stetig wachsenden Energiespeicher-Bedarf gerecht werden. Um mit Graphit mithalten zu können, müssen Silizium-Anoden mit einer Spannung betrieben werden, die außerhalb des thermodynamischen Stabilitätsbereichs von derzeitig verfügbaren organischen Elektrolyten liegt. Damit stabile Lade- und Entladezyklen gewährleistet sind, muss der Elektrolyt durch die *Solid Electrolyte Interphase* (SEI) kinetisch stabilisiert werden. Die SEI ist eine Schicht, die sich aus den an-/organischen Zersetzungsprodukten des Elektrolyten bildet. Die Bildung der Schicht geschieht idealerweise in den ersten Ladungszyklen. Diese kinetische Stabilisierung ist bei Graphit wirkungsvoll, bei Silizium ist sie jedoch wegen der ausgeprägten Volumenschwankung während der De-/Lithiierung unzureichend. Aufgrund ihrer physikalischen und chemischen Flüchtigkeit, aber auch aufgrund ihrer im Inneren der Batterie erschwerten Zugänglichkeit, ist unser Wissen über die SEI noch immer begrenzt. Für ein besseres Verständnis bedarf es in Zukunft ausgeklügelter *in-situ* und *operando* Charakterisierungsmethoden.

Die Röntgenabsorptionsspektroskopie (XAS) ist eine element-spezifische Charakterisierungsmethode, welche es erlaubt die elektronische und chemische Struktur der SEI zu untersuchen. In dieser Arbeit stelle ich ein neues Verfahren vor, das die Transmissions-XAS von Flüssigkeiten und Dünnschicht-Batterieelektroden unter *in-situ* Bedingungen mit weicher Röntgenstrahlung ermöglicht. Thematisch ist die Arbeit in zwei Teile gegliedert. Das neuartige Verfahren wird zunächst umfangreich vorgestellt und dann zur Untersuchung der SEI auf Silizium angewendet.

Das Verfahren basiert auf einer elektrochemischen Halbzelle, die mit einem Stapel aus zwei, für weiche Röntgenstrahlung durchlässige, Siliziumnitrid-Membranfenster ausgestattet ist, um den Elektrolyten einzuschließen. Eines der Membranfenster ist gleichzeitig der Träger für die Dünnschicht-Siliziumanode, die Ladezyklen mit einer Kathode aus metallischem Lithium durchläuft. Nachdem sich die SEI gebildet hat, wird mittels eines Röntgenstrahls von hoher Intensität vorsätzlich eine Blase erzeugt, um überschüssigen Elektrolyten abzudrängen und einen dünnen Elektrolytfilm über der SEI zu stabilisieren. Durch den Elektrolytfilm bleibt die SEI *in-situ*. Das erzeugte System aus Blase, Elektrolytfilm, SEI und Siliziumanode ist dann ausreichend dünn, um mittels Transmissions-XAS im weichen Röntgenbereich untersucht zu werden. Um den Prozess der Blasenbildung zu beleuchten, präsentiere ich eine Finite-Elemente-Analyse der Temperatur- und Konzentrationsverhältnisse, die im Elektrolyten unter dem Einfluss des Röntgenstrahls entstehen. Darüber hinaus simuliere ich mittels numerischer Strömungsmechanik das Blasenwachstum und zeige, wie es zu einer stabilen Lage der Blase zwischen den beiden Membranen kommt.

Im zweiten Teil meiner Arbeit werden dann 50 nm dünne, amorphe Silizium Dünnschicht-Anoden mit dem vorgestellten Verfahren am Elektronenspeicherring BESSY II in Berlin untersucht. Der verwendete Elektrolyt ist 1M $LiPF_6$ in Ethylencarbonat-Dimethylcarbonat (50:50 V/V). Bei der elektrochemischen Charakterisierung zeigen die Dünnschichtanoden alle für die De-/Lithiierung von Silizium üblichen Merkmale. Komplementär hierzu ermöglicht die Zelle *operando* Mikroskopie (optisch - OM) und *operando* UV/Vis Spektroskopie (UV/Vis), wobei der Grad der Lithiierung anhand der optischen Absorption nachverfolgt werden kann. Die OM Untersuchungen zeigen eine reversible Faltenbildung der Dünnschichten aufgrund der De-/Lithiierung, was auf einen Zug/Druck-Spannungsumschwung innerhalb eines Zyklus schließen lässt. UV/Vis und OM belegen weiterhin, dass die Anoden bei der Zyklenzahl der XAS-Untersuchung rissfrei bleiben.

Die Transmissions-XAS wurde an der Silizium L-Kante, der Sauerstoff K-Kante sowie an der Fluor K-Kante für jede Komponente im Strahlengang unter *in-situ* Bedingungen vorgenommen. Kohlenstoffmonoxid und Kohlenstoffdioxid wurden als Radiolyseprodukte und Hauptbestandteile der Blase identifiziert. An der Silizium L-Kante kann der Grad der Lithiierung beobachtet werden. Als Hauptbestandteile der SEI wurden Lithiumacetat, Li Ethylendicarbonat oder -monocarbonat, Li Acetylacetonat, LiOH und LiF ermittelt. Darüber hinaus deuten Anzeichen von Aldehyden auf flüssige Einschlüsse in einer möglicherweise porösen SEI Struktur hin.

Damit halte ich das vorgestellte Verfahren für ein vielversprechendes Werkzeug, welches in Zukunft die Entwicklung einer effizienten SEI auf Siliziumanoden ermöglichen kann.

List of Abbreviations

AES	Auger Electron Spectroscopy
CE	Counter Electrode
CFD	Computational Fluid Dynamics
CNT	Classical Nucleation Theory
CVD	Chemical Vapor Deposition
DAQ	Data acquisition
DEC	Diethyl carbonate
DEMS	Differential Electrochemical Mass Spectroscopy
DFT	Density Functional Theory
DMC	Dimethyl carbonate
EC	Ethylene carbonate
EDX	Energy-dispersive X-ray Spectroscopy
EELS	Electron Energy Loss Spectroscopy
EIS	Electrochemical Impedance Spectroscopy
EMC	Ethyl methyl carbonate
EPICS	Experimental Physics and Industrial Control System
EQCM	Electrochemical Crystal microbalance
ESA	Electrochemically-driven solid-state amorphization
ETFE	Ethylene tetrafluoroethylene
EUV	Extreme Ulta Violet
EXAFS	Extended X-ray Absorption Fine Structure
EY	Electron Yield
FEC	Fluoroethylene carbonate
FEM	Finite Element Method
FTIR	Fourier Transform Infrared Spectroscopy
FY	Fluoresecent Yield
GIC	Graphitic intercalation compound
GPIB	General Purpose Interface Bus
GUI	Graphical User Interface
HF	Hydrofluoric acid
HOMO	Highest unoccupied molecular orbital
IP	Ionization potential
IR	Infrared Spectroscopy
LEC	Lithium ethyl carbonate
LEDC	Lithium ethylene di-carbonate
LEMC	Lithium ethylene mono-carbonate

LIB	Lithium-ion Battery
LMC	Lithium methyl carbonate
LSV	Linear Sweep Voltammetry
LUMO	Lowest occupied molecular orbital
NEXAFS	Near Edge X-ray Absorption Fine Structure
NMR	Nuclear Magnetic Resonance Spectroscopy
NRR	Neutron Reflectometry
OEMS	On-line Electrochemical Mass Spectroscopy
OM	Optical Microscopy
PC	Propylene carbonate
PEEK	Polyether ether ketone
PEG	Polyethylene glycol
PES	Poly(ethylene succinate)
PET	Poly(ethylene terephthalate)
PEY	Partial Electron Yield
PI	Peak Intensity
PMMA	Poly(methyl methacrylate)
PVD	Physical Vapor Deposition
PVMK	Poly(vinyl methyl ketone)
SCPI	Standard Commands for Programmable Instruments
SEI	Solid Electrolyte Interphase
SEM	Scanning Electron Microscopy
SH	Step Height
SIMS	Secondary Ion Mass Spectroscopy
TEM	Transmission Electron Microscopy
TEY	Total Electron Yield
TFAA	Trifluoroacetic acid
TGA	Thermogravimetric Analysis
TPFPB	Tris(pentafluorophenyl) borane
VC	Vinyl carbonate
VEC	Vinyl ethylene carbonate
XAFS	X-ray Absorption Fine Structure
XANES	X-ray Absorption Near Edge Structure
XAS	X-ray Absorption Spectroscopy
XPS	X-ray Photoelectron Spectroscopy
XRD	X-ray Diffraction
XRR	X-ray Reflectometry

Table of Contents

I Lithium-ion Battery Technology

I.A The Development and Working Principle of the Modern Lithium-ion Battery

The periodic table is at the time of writing considered to be complete and expected to not change throughout time and space. In this periodic table, lithium has the atomic number 3 with an atomic radius of 152 pm, a standard atomic weight of 6.94 and a density of 0.534 g cm^{-3} [1]. Its electron configuration is $1s^2\ 2s^1$ to form the Li^+ cation with a Li/Li^+ standard potential of -3.04 V. When it comes to battery technology, with the advantageous ratio between charge and atomic weight or, even more so, the small atomic radius paired with the extraordinary high standard potential, the relevance of the Li^+ cation is set in stone, or more precisely, in the periodic table.

For lithium's application in batteries, one distinguishes between primary not rechargeable, secondary rechargeable lithium batteries, and rechargeable lithium-ion batteries. The former two utilize lithium metal as the battery anode and rely on lithium's unmatched theoretical gravimetric capacity of 3862 mAh g^{-1} [2]. For the discussion in the following chapter, one should keep this value in mind, as it is the benchmark value, once again set by the periodic table, all electrode materials must compare them against. Despite the high energy density, up until now, lithium metal batteries have not gained widespread adoption due to safety concerns connected to the highly reactive lithium metal anode itself. In secondary batteries, the biggest safety concern arises during recharging when lithium deposits as whiskers on the lithium metal anode, penetrating the separator and shorting the battery when reaching the cathode side, as illustrated in Figure 1. In 1980, painfully early on in the history of the lithium metal battery, this safety concern manifested itself in the minds of battery manufacturers with the total recall of the Li/MoS_2 (MOLICEL) battery [3], [4] by Moli Energy Ltd, when batteries in mobile phones were catching fire [5]. This recall already damped any further research interests in lithium metal batteries within the emerging market and new ideas were explored.

The Lithium-ion battery (LIB) was the much sought-after answer to this safety concern and an ingenious way to get rid of the Li-metal while still profiting from the intrinsically advantageous attributes of the lithium cation. Up until now, LIBs utilize so called intercalation compounds with layered crystal structures on both the anode and the cathode side, where lithium cations are inserted in between the crystal lattice layers. This is where lithium's small atomic radius shines. In a suitable host material, this intercalation can take place without substantial distortion of the host's lattice or change in crystal structure, granting the whole process an intrinsic reversibility and hence cycle stability. Consequently, the battery operation of charging

and discharging, can be considered as shuffling of the lithium ions back and forth, from one electrode to the other. This process is often termed as the “Rocking Chair”-mechanism of LIBs. Figure 2 illustrates the “Rocking Chair” working principle of a LIB with its first commercialized cell configuration: a soft-carbon anode with a $LiCoO_2$ cathode.

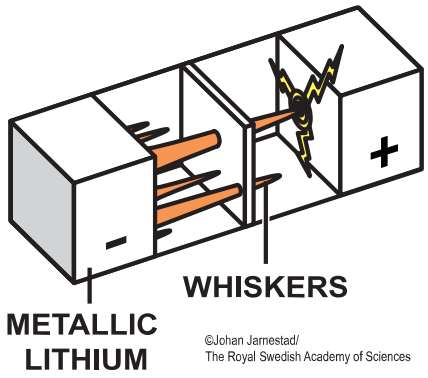

Figure 1 Fatal whisker growth of metallic lithium on the anode in secondary LIB. The whiskers penetrate the separator and short the battery when reaching the cathode side. The image is sourced from [6].

Up until now, current commercial LIBs still exclusively rely on graphite anodes, but at the end of this chapter we will discuss the tremendous benefits a transition to silicon-based anodes offers. However, to fully grasp what is there to gain, one must understand what was already achieved. For this, I first want to briefly discuss the current state of the LIB and the historic development it took to get to this point.

The successful commercialization of the LIB required a suitable anode and cathode material. Their development was carried out in parallel but independent from each other. When both sides reached sufficient performance and could be integrated into one cell system, they culminated into the successful commercialization of the LIB. The principle of intercalation can be attributed to Whittingham in 1976, who demonstrated the electrochemical intercalation of metals (Ag and Cu) into layered transition-metal disulphides, in particular into TaS_2 to form Ag_xTaS_2 and Cu_xTaS_2 [7]. Shortly after, he expanded his discovery to the electrochemical intercalation of lithium into TiS_2 [8] and transition metal dichalcogenides [9]. He demonstrated the highly reversible nature of the reaction and highlighted its potential for future secondary battery application for the first time. The MoS_2 and TiS_2 cathodes were commercialized right away in their already mentioned lithium-metal Li/MoS_2 and Li/TiS_2 [5], [10] cells, but faced restrictions in size / battery dimensions, not only due to the aforementioned safety concerns regarding the lithium metal anode, but also the instability of the cathode material itself (e.g. release of toxic H_2S gas). Besides this, in case of Li/TiS_2, while the intercalation capacity of 240 mAh g^{-1} was adequate, its application in consumer electronics was limited due to a low potential of about only 2 V.

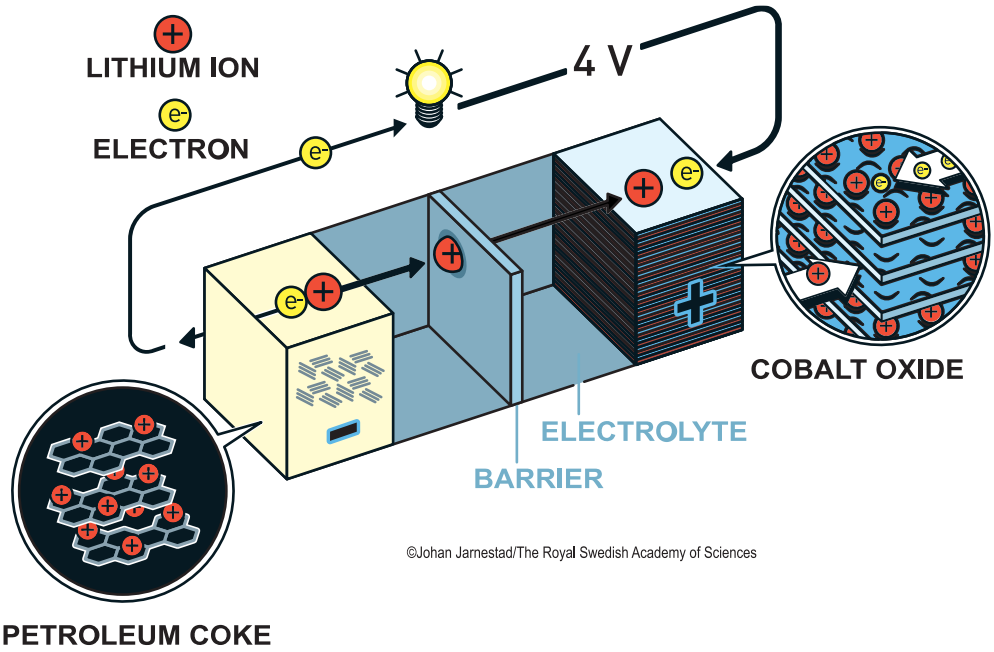

Figure 2 Cell configuration of the first commercialized LIB: a soft-carbon anode coupled with a $LiCoO_2$ anode. During dis-/charging, the lithium ions are shuffled back and forth from one electrode to the other. This process is often term as the "Rocking Chair"-mechanism of LIBs. The image is adapted from [6].

While the work of Whittingham on the principle of intercalation laid the necessary groundwork, 4 years later in 1980, Mizushima *et al.* paved the way for the modern LIB by demonstrating the lithium intercalation in the layered transition metal oxide $LiCoO_2$ [11]. Having a similar layered crystal structure as TiS_2, $LiCoO_2$ maintained the intercalation mechanism but had a much higher intercalation potential between 3.5 to 4.0 V vs. Li/Li^+. On top of that, it was stable under ambient conditions at room temperature. $LiCoO_2$ offered a theoretical capacity of 274 mAh g^{-1} but to maintain cycle stability only half of that was accessible. Still, what it lacked behind TiS_2 in intercalation capacity, it made up with the much higher, more applicable potential. However, what was most important, was the ability to produce the $LiCoO_2$ in the already lithiated state, eliminating the need of the lithium metal anode for the initial lithiation. This allowed for the possibility to merge the research on the cathode and anode side and pair $LiCoO_2$, if finally available, with a more stable, safer anode than lithium metal.

In the beginning, the search for a suitable anode pursued two approaches: conversion, as the alloying of a variety of metals with lithium, and intercalation, as it was applied on the cathode side. The principle of conversion through electrochemical alloying of lithium in an organic electrolyte 1M $LiClO_4$ in propylene carbonate (PC) was first established by Dey in 1971 [12]. At first, conversion appeared a promising concept as most metal alloys (e.g., LiAl, $Li_{4.4}Si$, $Li_{4.4}Sn$, LiZn, Li_3Cd) exhibited only a minor reduction in potential compared to lithium metal, while volumetric energy density remained acceptable for a possible application in consumer electronics [13]. Here, the binary silicon alloy system $Li_{4.4}Si$ already stood out as the most promising candidate that exhibits only 15% less volumetric energy density than the benchmark

lithium metal anode. Unfortunately, all conversion reactions are accompanied by a huge volume expansion, in case of the silicon and tin up to 400% and almost 700%, respectively [13]. These volume swings upon de/-lithiation develop stresses that lead to cracking/pulverization and the loss of active material over time. Consequently, the conversion electrodes suffer from sever capacity fading. For the material sciences in the early 1970, the volume expansion was an insurmountable obstacle, the idea of conversion anodes was discarded, and research focus was put on intercalation anodes. Nevertheless, in the end of this chapter, we will revisit the lithium-silicon alloy system and witness how emerging nanomanufacturing technologies 50 years later found ingenious ways to overcome this hurdle and put silicon back into the limelight as a promising new anode material for LIB. Back then, however, Besenhard demonstrated in 1976 the electrochemical, reversible intercalation of several alkali metals (Li, Na, K, Rb and Cs) into graphite in an organic electrolyte [14]. Graphite's capacity of 372 mAh g^{-1} [5] (theoretically value for LiC_6) was in the same ballpark as other cathode materials of that time, e.g. TiS_2 with 240 mAh g^{-1}, and thus graphite appeared to be a perfect match for possible future cell configurations. On top of that, the intercalation potential was sufficiently low and the cycle stability was adequate [5]. Nevertheless, the application of graphite was yet hold back by two detrimental processes. First, PC, as the most commonly available and used organic solvent at that time, would co-intercalate into the graphite and exfoliate the graphite layers, leading to deterioration of the anode and thus poor cyclability. Second, at the intercalation potential, PC would decompose and form a decomposition layer on the graphite [4], [15]–[17], which was originally labelled the Solid Electrolyte Interphase (SEI) by Peled in 1979 albeit for the passivation film on metallic lithium [18]. We will discuss the SEI, its formation mechanism and function in more detail later, but for now, we want to keep its picture elusive and take it as a double-edged sword. The SEI can either act in a negative manner as blocking layer, giving rise to high cell impedance, or in a positive manner by blocking the electron transfer whereby stabilizing the electrolyte kinetically and prevent further electrolyte decomposition. Although the underlying mechanisms were still unknown, it became clear, that both effects, the exfoliation and the SEI formation, were more on the positive side for carbon-based anodes with lesser graphitic content, yielding better cyclability and capacity [5], [19]. It was for this reason, that Yoshino *et al.* combined a soft carbon (coke-carbon) anode with the $LiCoO_2$ cathode of Mizushima *et al.* This cell configuration was patented by Yoshino in 1987, which is now considered the birth of the LIB [20]. Only few years later, the patented cell configuration was brought to market in 1991 by Sony Co. and in 1992 by A&T Battery Co. with 80 Wh kg^{-1} and a maximum cell voltage of 4.1 V [5], [21].

After the commercialization of the LIB, the optimization strategy in the following years was straight forward. When drawing current from a battery, the ions travel from one electrode to the other and the electrochemical potential between the electrodes drops. With this, the battery capacity C is the integral of the charge Q over the potential profile $V(q)$, as given in (1) [22]. Consequently, to increase capacity one must optimize the intercalation hosts to fit the highest possible number of cations (increasing Q), while using an electrode formulation / composition that delivers a high, stable cell potential (increasing $V(q)$).

$$C = \int_0^Q V(q)\, dq \qquad (1)$$

On the cathode side, ordered olivine phosphates $LiMPO_4$ (M = Fe, Co, Ni and Mn) with $LiFePO_4$ as the most successful representative achieved decent market share as a cheap alternative for applications with less strict requirements on energy density (market share 36% in 2016) [5], [23]. However, up until now, when it comes to energy density, layered transition metal oxides have remained undisputed since Yoshino patent in 1987. Starting from $LiCoO_2$, the most successful optimization strategy was to maintain the layered crystal structure, but substitute cobalt with other transition metals. The incentive was not only to find cathode formulations with higher intercalation capacity and cell potential, but also to get rid of cobalt. In the beginning, the endeavor to replace cobalt with cheaper, more earth abundant materials was purely economical, but with the ever-increasing market volume of LIBs, it also turned political. As the world's largest producer of cobalt (accounting for 51% in 2015 [24]), the Democratic Republic of Congo came under scrutiny, which unearthed disastrous, exploitative working conditions in mines throughout the country, including child labor. Thus, I feel the need to mention cobalt's disputed source, especially with the upcoming global shift to electric mobility, which is supposed to be powered by LIB technology. However, discussing it in its entirety lies outside of the scope of this work. Having said that, at first, the most promising candidate to replace cobalt was the layered $LiNiO_2$ system with 220 mAh g^{-1} [5], [23], [25], [26]. Unfortunately, the unary nickel system suffered from an inability to sustain deep charge cycles and had poor thermal stability, rendering it practically unusable, once again due to safety concerns [5], [23]. The remedy was to move to a binary, and later even ternary systems with cobalt, aluminum, and manganese. It was found each metal influenced certain performance parameters and the cathode's properties could easily be modified and optimized by adjusting the ratio between them [5]. Here, the ternary systems $LiNi_xCo_yMn_zO_2$ and $LiNi_xCo_yAl_zO_2$ turned out to be the most successful. Although up until now, due to the reduced thermal stability at higher nickel content, the composition of $LiNi_xCo_yMn_zO_2$ remained relatively nickel poor with 33-33-33 and 50-30-20 (% of Ni-Mn-Co) [5]. However, Tesla Inc. mitigated the reduced thermal stability through proper surface coatings and applied a nickel-rich $LiNi_{0.8}Co_{0.15}Al_{0.05}$

cathode from Panasonic [5] in their electric vehicles. In 2019, Li *et al.* (under the direction of J. R. Dahn) published a study on a series of high-nickel (> 90%) $LiNi_{1-n}M_nO_2$ (M = Al, Mn, Mg, and Co) cathodes, arguing for cobalt-free formulations, because, based on their presented study, cobalt adds little to no value regarding capacity, stability and safety [27]. Given J. R. Dahn's proximity to Tesla Inc. by forming a research partnership in 2016, one could expect cobalt-free cathodes in Tesla's future fleet.

Coming from the soft-carbon anode in Yoshino's cell, it was found that both a smaller (more graphitic) and larger (more hard carbon) d_{002} lattice constant in carbon-based anodes yields increased capacity, ranging from 150 to 300 mAh g^{-1}. Simultaneously, graphite does not only offer higher capacity, but also an intercalation voltage plateau, in comparison to the sloped dis/charging curves of soft and hard carbon. Such a charging plateau facilitates the implementation on the cell level and is a much sought-after feature. Graphite's struggle under exfoliation and unstable SEI formation, which initially limited Yoshino to the soft-carbon anode, was finally relieved by a change in the electrolyte formulation, namely the introduction of ethylene carbonate (EC) to PC in a 50:50 mixture [5], [19]. This introduced graphite back into the market and made it the anode-of-choice with a market share of 97% in 2010 [5]. It also highlights an important part of the LIB, which we have neglected so far: the electrolyte itself. In the following chapter I want to discuss the electrolyte in a more detailed manner and, even more so, the importance of the SEI it forms.

I.B The Solid Electrolyte Interphase on Graphite

I.B.1 The Electrolyte's Electrochemical Stability Window

In the previous chapter, based on (1), I outlined increasing the cell potential as a straight-forward optimization towards higher capacities. However, from a thermodynamic point of view this strategy, has its limit: the stability window of the organic electrolyte. To put it simple: if the electrochemical potential of the anode μ_A lies above the lowest unoccupied molecular orbital (LUMO) of the electrolyte, the electrolyte reduces on the anode and if the potential of the cathode μ_C is below the highest occupied molecular orbital (HOMO) of the electrolyte, the electrolyte oxidizes on the cathode [22], [28]. A diagram of a stable configuration and potentials within the stability window of the electrolyte is sketched in Figure 3. Nevertheless, with their high cell potentials above 4 V, all LIBs are operated outside the stability window of commercially available organic electrolytes. To name a prominent example: one of the most common commercial electrolytes, 1M $LiPF_6$ in a 1:1 volume to volume mixture of EC:DMC, has its reduction and oxidation potential at 1.3 V and 5.7 V vs. Li/Li^+, respectively [28]–[31]. Graphite's intercalation potential lies between 0.25 V to 0.01 V vs. Li/Li^+, and as discussed

above, one would expect the electrolyte to reduce on the anode [32]. This is where the important role of the SEI comes into play.

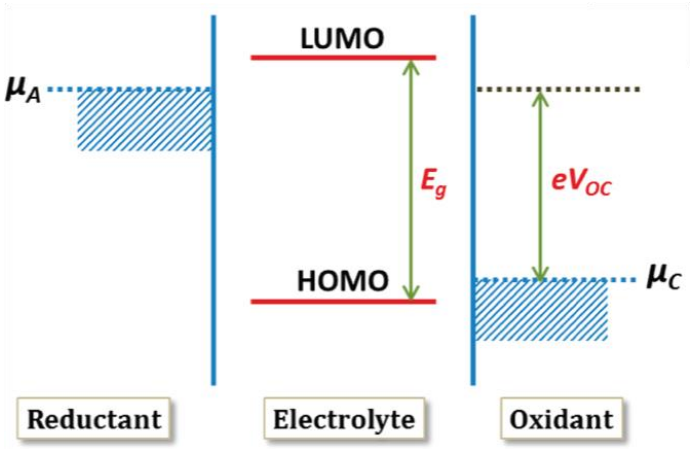

Figure 3 Energy diagram of the electrolyte's stability window (HOMO to LUMO) and a stable cell configuration with the anode potential below the LUMO and the cathode potential above the HOMO. The figure is sourced from [22].

The SEI is supposed to form during the first (few) charging cycles and is presumably comprised of an intricate mixture of organic and inorganic reduction products of the electrolyte [19], [33]. Ideally, it stabilizes the electrolyte by suppressing the electron transfer, while at the same time still allows lithium-ion diffusion/permeation and hence the ion shuffling to take place [34]. Beside this, an effective SEI supposedly influences the intercalation process as well and protects the graphitic anode from detrimental solvent co-intercalation and exfoliation [19]. To paraphrase, a certain amount of electrolyte is sacrificed to form an SEI that protects the remaining. The capacity that is lost due to the SEI formation, independent from the actual underlying mechanism, is deemed irreversible, because the lithium retained in the SEI no longer takes part in the "Rocking Chair". However, without the effective kinetic stabilization by the SEI, the electrolyte decomposes continuously until the cell dries out. In a less extreme case, with continuous electrolyte decomposition an increased overpotential prevents battery operation due to an excessive, ionically insulating SEI. Consequently, fully uncoupled from the electrodes' cyclability, the SEI's efficiency itself directly determines the cycle stability of the cell [5]. This realization naturally sparked intensive research on the formation, working mechanism, and properties of the SEI. It is commonly agreed upon, that the SEI's properties are determined by a complex interplay between its chemical species, their spatial distribution on the electrode surface and their local arrangement within the SEI itself [19]. Despite extensive research, the picture of the SEI is still very vague. Nevertheless, in 2021, the information published in literature on SEIs in general, and especially on graphite's SEI, appears to be fractal-like, with a perceived never-ending depth of detail. To put it simple: "the more we know about the SEI, the more questions remain unclear".

In the following I want to discuss the SEI on graphite and focus on its chemical composition, morphology, and formation mechanism. I will remain at the surface of said fractal and limit the description to the most accepted, prevalent information. Although this work's focus is on the investigation of the SEI on silicon conversion anodes, as we will see in the next chapter, an efficient SEI for silicon conversion anodes has yet to be found. At the same time, with its status as the anode-of-choice in the current LIB landscape, the SEI on graphite is a proof-of-concept and is without a doubt an invaluable lesson. I further intend the following chapters as a foundation to understand the fundamental differences to the SEI on conversion anodes. I consider the understanding thereof a key to find a solution for the SEI's instability on silicon. Simultaneously, for silicon anodes to gain traction in the current market, they must function as a drop-in replacement for graphite, hence stick to the current commercial electrolyte formulations and cell configurations as close as possible. If we consider the SEI simply as "reduction products of the electrolyte", the SEI on graphite is the best starting point for what to expect when investigating the SEI on silicon anodes in the same electrolyte formulations.

I.B.2 The Composition of the Solid Electrolyte Interphase

As mentioned earlier, graphite owes his reintroduction and its current market share to the addition of EC to the pure PC electrolyte. Nowadays, all major commercial electrolytes employ EC as a major component. Right after its discovery as miracle remedy, EC was obviously suspected as the origin of the stable SEI. Based on the early work of Aurbach *et al.* [35], [36] applying *ex-situ* Fourier transform infrared spectroscopy (FTIR), scanning electron microscopy (SEM) and energy-dispersive X-ray spectroscopy (EDX) on lithium metal and carbon anodes, which was later confirmed by Zhuang *et al.* in 2005 [37], [38] through X-ray photoelectron spectroscopy (XPS), nuclear magnetic resonance spectroscopy (NMR), and once again FTIR, it was commonly accepted that lithium ethylene di-carbonate (LEDC) is the main single-electron pathway reduction product of EC and consequently was assumed to be the main organic constituent of the SEI. The proposed mechanism (see Figure 4) was a nucleophilic attack between two radical anions, formed by electronation of the EC molecule, which was presumably assisted by the coordination of the carbonyl group to the Li^+ cation.

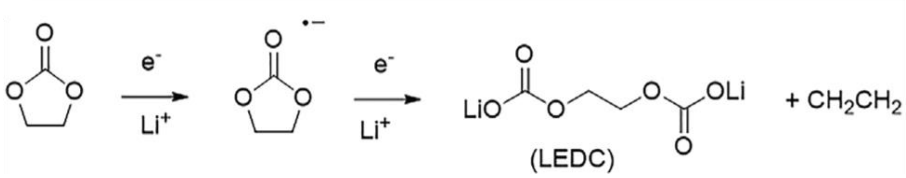

Figure 4 Single-electron reduction pathway of EC into LEDC as suggested by Aurbach et al. [35], [36]. The figure is sourced from [34].

After a thorough literature analysis and developing their own novel synthesis route accompanied by NMR, FTIR and XRD characterization, Wang *et al.* reported in 2019 that the reference standards, which were used to identify LEDC, were lithium ethylene mono-carbonate (LEMC) and LEDC has not been prepared prior to their work [39]. According to their findings, they propose LEMC as the main SEI component and argue that, if ever created at all, LEDC's instability would lead to a quick decomposition into LEMC and lithium methyl carbonate (LMC) in common LIB environments (impurities, residual moisture etc.). This put a twist to 14 years of research, but for the sake of clarity, in the following I will report the findings regarding LEDC as published to date.

Due to its high melting point of 36.4 °C [1], [40], EC is commonly mixed with linear dialkyl carbonate solvents such as dimethyl carbonate (DMC), ethyl methyl carbonate (EMC), and diethyl carbonate (DEC) in common electrolyte formulations. Through a variety of different analysis methods like electrochemical quartz crystal microbalance (EQCM), on-line electrochemical mass spectroscopy (OEMS), transmission electron microscopy (TEM), XPS, NMR and FTIR, the reduction products of these solvents were identified as: LMC, lithium methoxide, CO and methane for DMC; lithium ethyl carbonate (LEC), lithium ethoxide, CO and ethane for DEC; and LMC, LEC, lithium ethoxide and ethoxide, ethane, methane and CO for EMC [19], [34], [41]–[44]. However, based on the distinctive reduction products, it was widely found that EC is reduced preferentially, confirming the initial suspicion that EC is indeed the origin of a stable SEI [19], [34].

I.B.3 The 3D Interphase Model

As a first hint why EC might be the origin of a stable SEI, through electrochemical impedance spectroscopy (EIS) and electrospray ionization mass spectroscopy supported by density functional theory (DFT) calculations, Xu, Cresce and co-workers revealed a preferred coordination of EC in the solvation sheath of the Li^+ cation [45]–[48]. Their findings where complimentary to, and further refined the SEI formation mechanism proposed earlier by Besenhard and Winter [49], [50]. This refined model for the formation of the SEI on graphitic anodes is considered the most commonly accepted, which can explain many experimental observations to a satisfying degree [19], [47]. Initially based on dilatometry [49], but later confirmed by X-ray diffraction (XRD) [50], they proposed that the SEI formation is preceded by solvent co-intercalation between the graphene sheets. This co-intercalation was observed for PC-based electrolytes as an additional d_{002} peak in XRD at 24° with an expanded interlayer distance of 1.59 nm (increased from 0.33 nm of pristine graphite, I in Figure 5a) at around 1.5 V vs. Li/Li^+. This expanded interlayer distance is sufficiently large enough to intercalate solvated Li^+ ions (see Figure 5a,b) and the created phase is commonly referred to as ternary

graphitic intercalation compound (GIC) (see II in Figure 5a). At potentials below 1 V vs. Li/Li$^+$ the molecules in the solvation sheath can accept electrons from the p-bands of sp^2 carbons and become reduced in-between the graphene sheets. This reduction is observed through a decreasing interlayer distance back to 0.35 nm (see III in Figure 5a). This way, the reduction products form not just a 2D layer on top, but build up a partially penetrating, interwoven structure with the graphitic layers in three dimensions, hence the name “3D Interphase Model”. Although the GIC was only observed for PC, it is reasonable to assume a similar mechanism for EC, albeit a real time detection appears impossible due to its presumably reduced chemical stability and faster reaction rates [19]. With its favored place in the solvation sheath, EC is co-intercalated and thus reduced preferentially over the linear carbonates. As for the PC-vs-EC mystery, Xing *et al.* presented in 2018 a reasonable explanation based on extensive DFT calculations of the coordination sheath [51].

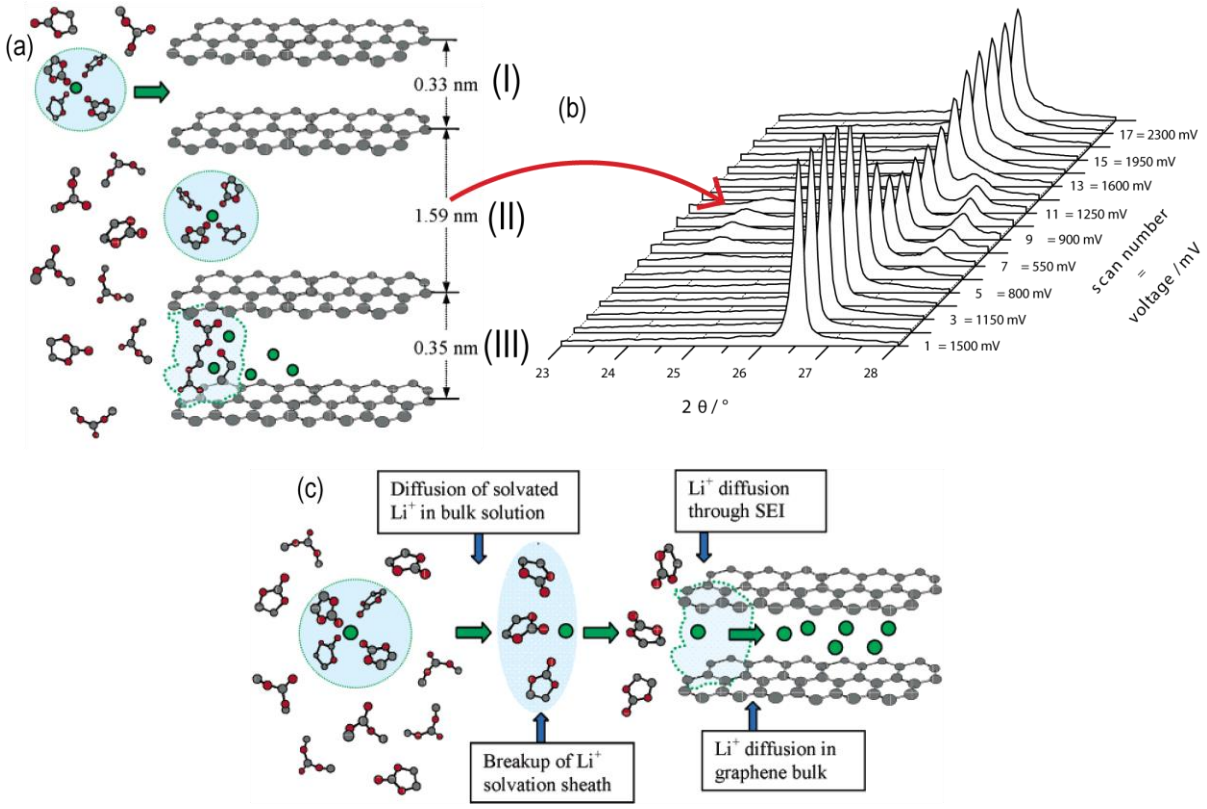

Figure 5 The "3D Interphase Model" for the SEI formation on graphite. (a) Solvent co-intercalation (I) between the graphene sheets forms the ternary graphitic intercalation compound (II). The co-intercalated solvent molecules in the solvation sheath are reduced below 1 V vs. Li/Li$^+$ in-between the graphene sheets (III). The image is adapted from [45]. (b) Waterfall diagram of the XRD data from Besenhard and Winter which reveals the structural changes from (I) to (III) discussed in (a). The image is sourced from [50]. (c) Working principle of the SEI: it requires the Li$^+$ ion to shed its solvation sheath before intercalation and prevents further solvent co-intercalation and reduction. The image is adapted from [45].

The SEI’s working principle can be directly deduced from the “3D Interphase Model”. By the reduction of co-intercalated solvent molecules, the SEI layer is not only immobilized at the surface but also acts as glue, preventing the graphene sheets from expanding and in turn preventing further solvent co-intercalation and reduction. Furthermore, it requires the Li$^+$ cation

to shed its solvation sheath (desolvate) before intercalation (see Figure 5c). Consequently, an efficient SEI must facilitate desolvation and must allow high Li^+ mobility, while it remains physically immobilized and stable on top of the anode.

When it comes to the inorganic SEI constituents, LiF was detected in almost all studies and it is considered to be the main inorganic component, stemming from the electrochemical reduction of the PF_6^- anion [19], [34]. Initially, this composed a rather simple picture of the SEI: organic lithium alkyl carbonates (semi-carbonates) and inorganic LiF [52]. However, when Wang *et al.* introduced the LEDC/LEMC controversy, they argued about LEDC's fate to quickly decompose into LEMC and LMC. They resembled the general mindset developed over the last 14 years of research: while the initial SEI composition may be simple and be traced back to one or two reduction reactions, the products are highly instable themselves and decompose into an increasingly complex SEI.

I.B.4 The Volatile Nature of the Solid Electrolyte Interphase

Figure 6 summarizes the ageing of the SEI due to its instability against certain environmental conditions. The lithium alkyl carbonates are heavily susceptible to water, and readily decompose to Li_2CO_3, CO_2, and lithium alkoxides (compare I) [34]. While nowadays water and moisture contamination can be ruled out in commercial production, the influence of the most common $LiPF_6$ salt inside the electrolyte appears to be more crucial. Parimalam *et al.* conducted an extensive XPS, NMR, infrared spectroscopy with attenuated total reflectance (IR-ATR) study coupled with mass selective gas tomography (GC-MS) and found that, in the presence of $LiPF_6$ in DMC, Li_2CO_3 decomposed into CO_2, LiF, and F_2PO_2Li (compare II), while LMC and LEDC turns into a complex mixture of CO_2, LiF, ethers, phosphates, and fluorophosphate (compare III) [53]. To investigate the thermal decomposition, Yoon *et al.* applied a thermogravimetric analysis (TGA) (compare IV) on the model system of an artificial SEI consisting of LEDC and LiF on silicon anodes and found that in the temperature range from 50 to 300 °C LEDC deteriorate into CO_2, ethylene, lithium propionate and Li_2CO_3; the lithium propionate turns yet again into Li_2CO_3 and pentanone from 300 to 600 °C; and above 600 °C Li_2CO_3 finally breaks down into Li_2O and CO_2 [54]. In this regard, it must be noted, that many of these second-generation decomposition products are either soluble or gaseous, making the SEI less densely packed over time. Further, with the inherent instability of the semi-carbonates, the SEI's nature is expected to change from more organic to more inorganic [34] (compare Figure 6).

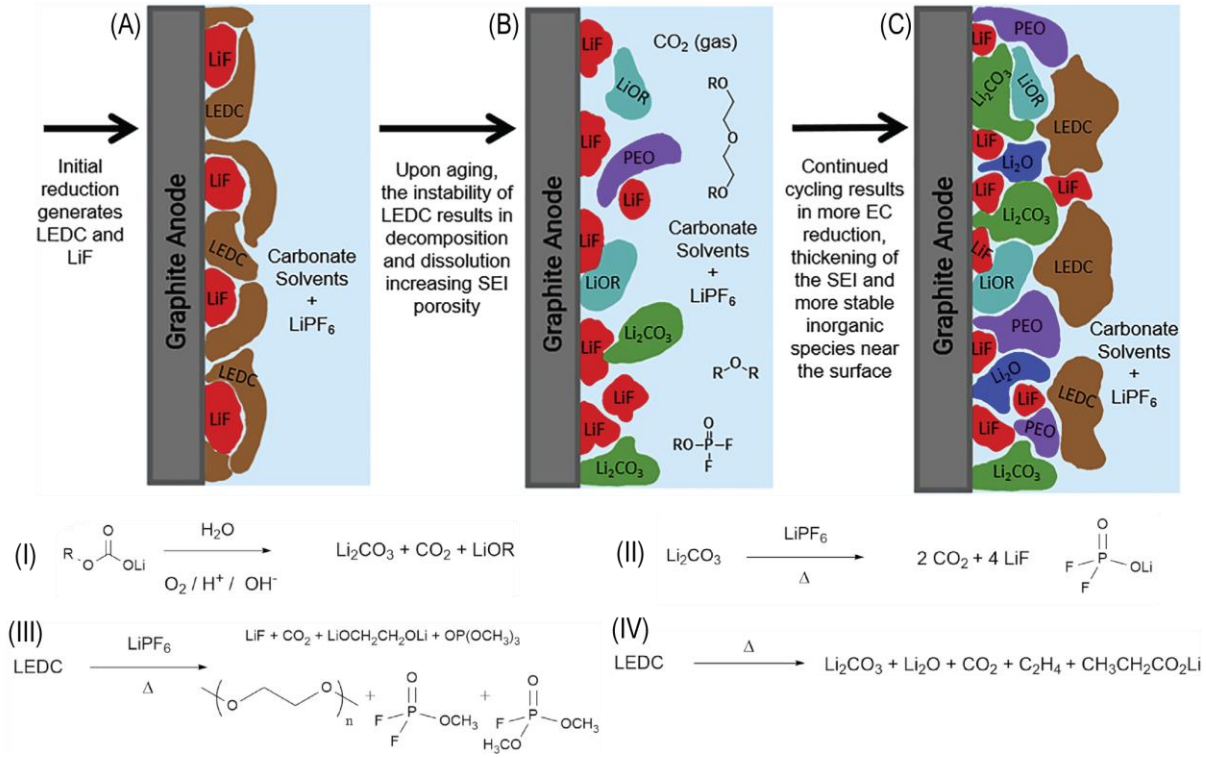

Figure 6 The volatile nature of the SEI. (A)-(C) Ageing of the SEI due to the instability against certain environmental conditions governed by the corresponding chemical reactions (I)-(IV). The image is compiled from [34].

Furthermore, the discovered instability also sparked heavy discussion about which decomposition reactions were occurring naturally (and are actual SEI constituents) and which reactions were artificially introduced by poor sample handling during characterization (exposure to atmospheric conditions, moisture contamination, etc.). A prominent and one of the most debated examples is Li_2CO_3, as it was thought to be the main constituent of the SEI [19], [33]. While Li_2CO_3 was found in most studies, there is no common agreement whether it is a real SEI component or just an artifact introduced through the mentioned moisture exposure or the reaction of Li_2O and CO_2 [55]. To settle the debates, studies compared samples exposed to the environment to samples kept meticulously in a protective atmosphere and found evident differences. In their XPS and sXAS study, Edström *et al.* found no evidence of Li_2CO_3 on graphite anodes extracted from hermetically sealed cells [56]. Cells exposed to air for 3 hours showed clear differences in the XPS spectra, which were correlated to an increased Li_2CO_3 presence. Schroder *et al.* reproduced equivalent XPS results on silicon anodes as a model system, strongly suggesting that Li_2CO_3 is indeed an artifact introduced to environmental exposure [57]. However, these experiments cannot rule out the presence of Li_2CO_3 in the SEI under certain circumstances, especially for highly aged cells as discussed earlier. Disputes like the one surrounding Li_2CO_3 and the SEI's volatility in general make *in-situ* and *operando* characterization techniques necessary. Later, I will demonstrate how the electrochemical cell I developed for this exact purpose can give new insight into the SEI composition on silicon anodes under *in-situ* conditions.

I.B.5 Electrolyte Additives for an Improved Solid Electrolyte Interphase

I consider having *in-situ* access to the SEI's composition indispensable for the effective development of electrolyte formulations which can yield optimized SEI layers. However, when it comes to optimize electrolyte formulations, with an annual global market production of 62 000 tons in 2015 [24], [58], the gears of the established electrolyte manufacturing infrastructure grind slowly and are hesitant to change. For this reason, research in the past typically focused on the development of additives which were added in minor quantities without changing the prevalent carrier solvent mixture, namely EC with linear dialkyl carbonate solvents DMC, EMC, or DEC. Because exploring the working principle of each additive turned out to be at least as difficult as the initial SEI problem itself, most endeavors of finding proper additives can be labelled as trial-and-error approaches. It does not help that the large financial advantage that is to be gained makes electrolyte additives the most kept trade secrets of electrolyte and cell manufacturers [32]. In a competitive market, industry tends to not care about how it works, if it works, and there was no incentive to publish either of them, which shows in the current state of academic literature on that topic. Modern commercial battery formulations may contain well over 20 additives (SEI forming, flame retardants, thermal stabilization, improved conductivity, temperature-stable viscosity, etc.) and for a summary of the many trial-and-error approaches reported in literature I refer to the extensive reviews in [19], [59]–[62]. Nevertheless, as a prime example, I want to highlight the mammoth task of Wang *et al.*, who screened over 55 combinations of additives in $LiCoO_2$/graphite pouch cells through a ultra-high precision charger as well as EIS and ranked them based on their Coulombic efficiency, charge endpoint capacity slippage, and charge transfer resistance [63]. Based on these criteria, the simple formulation of only 2 wt.% of vinyl carbonate (VC) emerged as the champion from all combinations. I want to conclude this chapter by highlighting a few prominent electrolyte additives, which improve the SEI on graphite, including Wang *et al.*'s champion, VC. The given examples should act as a demonstration of what is possible and draft solutions for the more intrinsically difficult, and delicate situation of the SEI on silicon anodes, which we will then discuss in the following chapter I.C.5.

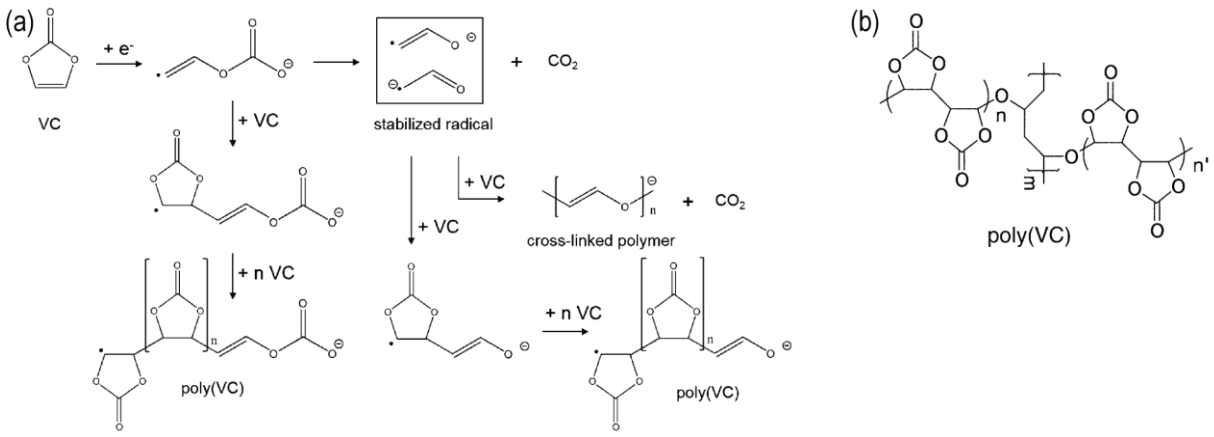

Figure 7 (a) Reduction pathway and electro-polymerization of VC. The image is sourced from [64]. (b) Cross-linking sites of VC. The image is sourced from [65].

Film-forming additives resemble the original picture of the SEI in the most straight-forward manner. These compounds must have higher reduction potentials than the electrolyte itself. This way, during the first charge, they are reduced sacrificially first and form an SEI themselves. When the electrolyte's reduction potential is reached, the electrolyte is already kinetically stabilized through the preexisting SEI [19]. It must be noted that this principle is only made possible through the fact that the cathode is manufactured in its lithiated state, while the graphite is not. It creates this potential window during the first charge, where film-forming additives can be reduced sacrificially, while the electrolyte itself is still stable. Inspired by the obvious picture of a protective polymeric film on the anode, unsaturated components with double and triple bonds or cyclic structures, which can by polymerized under reductive conditions, were sought-after candidates. Here, VC, fluoroethylene carbonate (FEC) and vinyl ethylene carbonate (VEC) showed excellent results regarding improved cycle stability and gained widespread adoption. VC is now used in almost all commercial electrolyte formulations [19], [34]. Based on a XPS study on cycled anodes and VC reference compounds, which was also supported by *ab initio* calculations, Ouatani *et al.* revealed that VC was indeed preferentially polymerized to a polymeric film of poly(VC) through a radical anion as shown in Figure 7a [66]. The structure of the polymeric poly(VC) film with possible cross-linking sites is shown in Figure 7b. Zhang *et al.* [64] (FTIR, XPS, OEMS) and Michan *et al.* [65] (NMR, XPS) confirmed the generation of poly(VC) and found it to be accompanied by CO_2 evolution. The CO_2 is further reduced to Li_2CO_3 and its content in the SEI layer is increased over the SEI from a neat electrolyte formulation. Further, the presence of a polymeric poly(VC) film appears to inhibit the decomposition of EC and $LiPF_6$, and consequently, the SEI's LEDC and LiF content is reduced while less ethylene is generated. Nie *et al.* confirmed this through a TEM investigation when they found that the presence of VC results in a much thinner SEI (10 - 20 nm) compared to the neat electrolyte formulation (20 - 40 nm) [67]. Furthermore, FEC-containing electrolytes exhibit similar results, but the SEI shows higher LiF over the one

formed through VC and is comparable to the SEI from neat electrolytes. It is suspected, that FEC forms LiF and VC first, and VC then follows the ordinary decomposition route discussed before. However, in some studies increased inversible capacity was observed for VC- and FEC-containing electrolytes, which was attributed to the poor thermal stability of both compounds [32], [68]–[70]. For this, VEC was proposed as a more stable alternative, given its electron rich double bond [32]. However, it remains unclear how the presence of the polymeric poly(VC) film, the reduced thickness and the altered SEI composition regarding its LEDC and Li_2CO_3 content leads to the improved cycle performance [34]. Nevertheless, I consider the implementation of the simple, initial concept of a polymeric film on the anode through a suitable molecule like VC a great example of how the SEI can be engineered through additives.

Another interesting way how additives influence the SEI is by high jacking its formation mechanism. In comparison to the film-forming additives, these reaction-type additives are not reduced themselves electrochemically but chemically react with intermediate species (e.g., radical intermediates, compare Figure 4 and Figure 7a). Here, molecules with well conjugated structures, e.g. carboxyl phenol or aromatic esters, are possible candidates to stabilize intermediate radical anions through delocalization of the radical [60]. As an example, Wang *et al.* found that the addition of 0.5 wt.% 1,3-benzodioxol-2-one to 1M $LiPF_6$ PC:DEC decreases the initial irreversible capacity, reflecting a more stable SEI [71]. Wang *et al.* proposed that 1,3-benzodioxol-2-one scavenges the PC radical and forms a more stable SEI compared to the neat PC:DEC electrolyte. A similar mechanism was suspected for maleic anhydride, succinimide and N-benzyloxy carbonyloxy succinimide [60].

I want to conclude this topic by giving two examples of additives that do not alter the SEI's formation process but modify its morphology and properties. Tris(pentafluorophenyl) borane (TPFPB) is a strong anion receptor, that forms a 1:1 complex with LiF and is able to dissolve more than 1M of LiF in most organic electrolytes [60]. TPFPB was successfully applied as additive (in minor 0.1-0.2 M quantities) and yielded improved cyclability, capacity retention, thermal stability, and high-power capability [72]–[77]. These positive effects were attributed to a lower LiF content in the SEI caused by the dissolution of LiF through the TPFPB complex. Unfortunately, TPFPB could not be specifically targeted at the LiF inside the SEI and affected the general cell chemistry as well. It presumably pushes the equilibrium between $LiPF_6$ with LiF and PF_5 to the product side. Thus, in higher concentrations, TPFPB entails the formation of highly reactive PF_5, which in turn deteriorates the electrolyte solvent and creases cell performance.

While mechanistically different, another way to modify the SEI's properties is best described as doping. To explore this idea, Komaba *et al.* used $NaClO_4$ as co-salt for an 1M $LiClO_4$ in

EC/DEC electrolyte [78]. While their electrochemical analysis showed no signs of sodium deposition or intercalation, the electrolyte with 0.22 M $NaClO_4$ still achieved higher reversible capacity and the irreversible reduction of the first cycle was suppressed compared to the sodium-free electrolyte. Further, based on EIS measurements they reported much better Li^+ mobility through the SEI. Through Time-of-Flight Secondary Ion Mass Spectrometry (TOF-SIMS) they detected the presence of sodium ions inside the SEI and suggested that the sodium ions were entrapped within the SEI during its formation, partially substituting Li^+. According to them, this substitution could lead to larger interstitial space within the SEI, enabling higher Li^+ conductivity.

I.C The Promises and Obstacles of Silicon Anodes

I.C.1 Silicon Lithiation Phase Diagram

The promises and obstacles of silicon anodes in LIBs can be directly derived from their working principle. In contrast to the intercalation into graphite, lithium is incorporated into silicon by an alloying reaction (also called conversion). As mentioned earlier, conversion anodes were explored as possible alternatives for the lithium metal anode even before the first commercialization of the LIB. But due to the vast volume swings upon conversion, they suffered from cracking, pulverization and ultimately severe capacity fading. In the following, I first want to discuss the de-/lithiation behavior of silicon with all its occurring phase transformations and sketch a rough picture of why they are the culprit of the cracking issue. I will go on and discuss how in the early 2000s advancements in nanomanufacturing turned out to be a remedy for the cracking issue and put silicon, almost 30 years after its initial consideration as an LIB anode, back into the spotlight. For this, I focus on silicon thin-films, as they are this work's model system to investigate the SEI on silicon via transmission XAS and are promising implementation for a successful commercialization in the future. However, we will see that the capacity fading issue of the silicon anodes is two-fold. Because even without cracking, the capacity still fades due to the SEI failing to stabilize the electrolyte sufficiently. As with the "3D Interphase Model" for the SEI on graphite, I will conclude this chapter by giving an overview of the research about the SEI on silicon and highlight how the electrochemical cell I developed in this work can provide new insights and help to engineer a more stable SEI in the future.

When Dey demonstrated the electrochemical alloying of lithium in an organic electrolyte in 1971 [12], the binary silicon alloy system already emerged as one of the most promising candidates [13]. In the late 1970s, the electrochemically alloying of the binary Li-Si system was then first explored at elevated temperatures (> 650 K) [79], [80]. The electrochemical de-

/lithiation showed several voltage plateaus, corresponding to the $Li_{12}Si_7$, Li_7Si_3, $Li_{13}Si_4$, and $Li_{22}Si_5$ phases, as it was expected from the phase diagram [81]. However, in 1995, when investigating anodes with nanodispersed silicon in a carbon matrix, Wilson and Dahn observed no voltage plateaus which would indicate the formation of any Si-Li equilibrium phases at room temperature [82]. A few years later in 2003, Limthongkul *et al.* confirmed their results and discovered through XRD and TEM on silicon powder samples that the equilibrium phases are indeed not obtained at room temperature, presumably due to the kinetically hindrance by the high activation energy of Si-Si bond breaking. They found the electrochemical lithiation of crystalline silicon (c-Si) to proceed via the formation of an amorphous, metastable, highly lithiated a-Li_xSi phase [83]. A process which they called electrochemically-driven solid-state amorphization (ESA). In their XRD experiments, Obrovac and Christensen went on to show that the metastable a-Li_xSi phase still crystallizes at potentials below 50 mV vs. Li/Li^+ to c-$Li_{15}Si_4$ [84]. They argued c-$Li_{15}Si_4$ is the terminal, fully lithiated phase at room temperature and not $Li_{22}Si_5$, as it would be expected from the equilibrium phase diagram. On top of that, they observed the silicon to not recrystallize upon delithiation and to remain amorphous. In 2007, Li and Dahn confirmed these results in their *in-situ* XRD study and developed an extensive phase diagram, which is commonly accepted to this date and summarized in Figure 8a [85].

As summarized in Figure 8 and described in the extensive review articles [86]–[88], the cycling behavior of silicon is as follows. In the first discharge, c-Si is lithiated through a two-phase reaction to form a-Li_ySi (I in Figure 8a,b,c). The two-phase behavior is clearly indicated by the charge plateau (I) and sharp peak (I, L(cr-Si)) in Figure 8b,d. It was postulated that the two-phase behavior stems from the high energy required to break up the silicon lattice. The Si-Si bonds may be weakened by a high concentration of Li atoms in their vicinity. Such high concentration is only possible at a sharp phase boundary, but not at a flat forefront of a concentration gradient present in a solid-solution reaction [89], [90]. Thus, a two-phase reaction is kinetically more favorable. As it was shown by Key *et al.* through their NMR experiment [91], the a-Li_ySi phase is indeed highly lithiated with $y = 3.4 \pm 0.2$, which is already close to the stoichiometry of the terminal c-$Li_{15}Si_4$ phase [87]. Once the c-Si/a-Li_ySi front traversed the complete volume, the anode exists in an amorphous a-Li_xSi phase. If the lithiation continues below 50 mV vs. Li/Li^+, the a-Li_xSi suddenly crystallizes through a two-phase reaction into the terminal c-$Li_{15}Si_4$ phase (II in Figure 8a,b,d). Many first principle calculations suggest that the formation of the metastable c-$Li_{15}Si_4$ phase is kinetically favored over the thermodynamic equilibrium phases ($Li_{13}Si_4$, $Li_{22}Si_5$), due to the very similar local atomic environments in a-Li_xSi and c-$Li_{15}Si_4$. In both phases every Si atom is evenly surrounded by 12 Li atoms and the phase transformation can take place without large-scale atomic migration or phase separation [86], [87], [91]–[94].

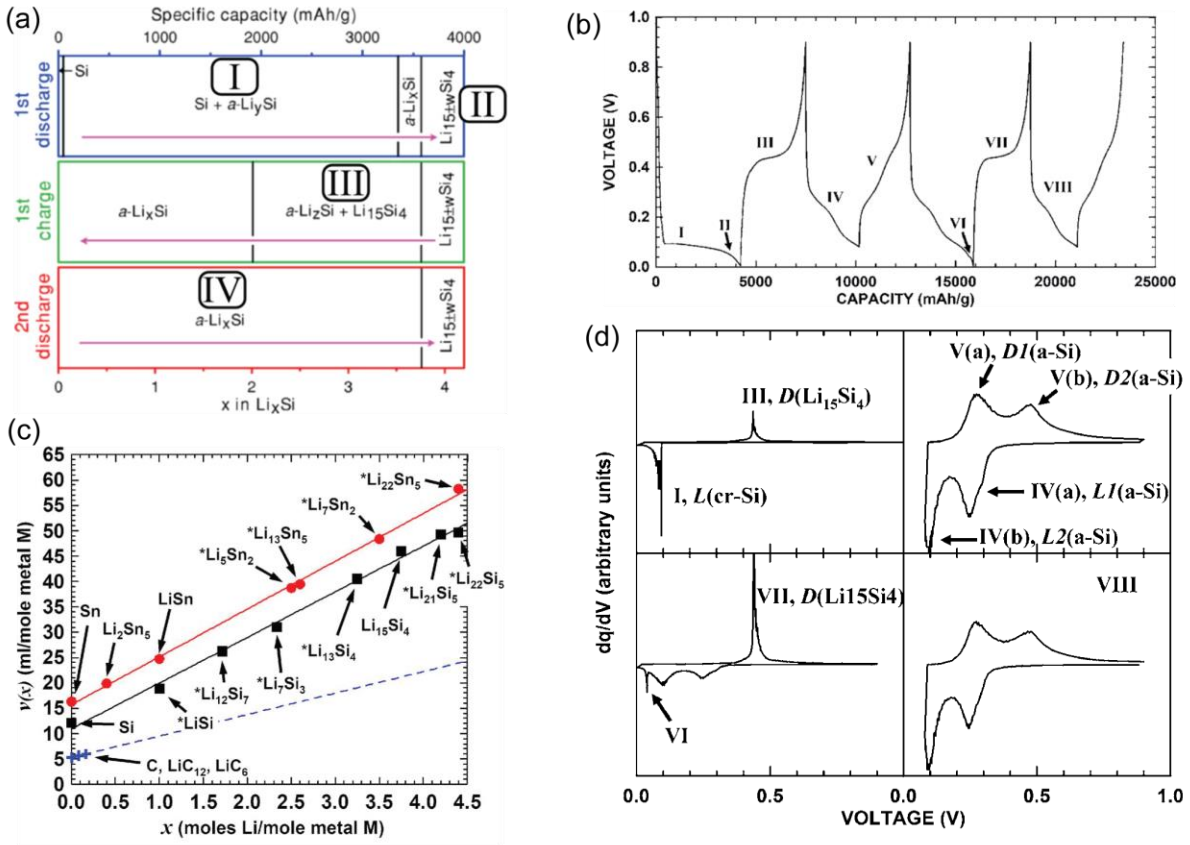

*Figure 8 (a) Phase diagram for the electrochemical de-/lithiation of a crystalline silicon anode between 5 mV and 0.9 V vs. Li/Li⁺ at room temperature. The image is sourced from [85] and annotated as in [88]. (b) Galvanostatic dis-/charge curves of a crystalline silicon electrode from Obrovac et al. [95]. The crystallization to the c-$Li_{15}Si_4$ phase is avoided in the second and fourth cycle by a cutoff potential to illustrate the two different dis-/charging behaviors. The plot is annotated as in [88]. (c) Volume per mole of host atoms for silicon, tin and carbon as function of lithium content for the corresponding binary phases. Phases marked with * are not obtained during electrochemical lithiation at room temperature. The image is sourced from [96]. (d) Differential capacity vs. potential plots from the galvanostatic dis-/charging curves from (b). The vertical scale is adjusted to make the shapes of the curves clearer. The image is sourced from [95].*

For the delithiation, the reaction path depends on the final phase achieved during lithiation. If the c-$Li_{15}Si_4$ phase was obtained, delithiation starts with a two-phase reaction to amorphous a-Li_zSi ($z \approx 2$), as it can be seen by the charge plateau (III) and sharp peak (III, D($Li_{15}Si_4$)) in Figure 8b,d. Afterwards, a-Li_zSi proceeds to delithiated via a solid-solution over the a-Li_xSi phase back to a-Si* [85] (where * denotes a-Si after the first delithiation to distinguish it from as-prepared a-Si, as discussed later in more detail). On the other hand, if a cutoff potential limited the lithiation to the a-Li_xSi phase in the first place, a-Li_xSi is delithiated through a solid-solution reaction back to a-Si* right away, as indicated by the absence of a plateau and the sloped voltage curve V in Figure 8b.

The solid-solution a-Si/a-Li_xSi transformation is of particular importance, as it becomes the prevalent phase transformation in consecutive cycles and carries the biggest part of the capacity (about 3600 mAh g^{-1}), as shown in Figure 8a. It takes place in two stages, as reflected

by the two distinguishable slopes V in Figure 8b or the peaks V(a, b), and IV(a, b) in Figure 8d. The two stages are presumably correlated to different local environments with higher and lower Li/Si coordination numbers at different Li content (later referred to as high- and low-potential stages) [87], [95], [97], [98]. After the first delithiation, the a-Si* is lithiated via the solid-solution reaction to a-Li_xSi right from the beginning (IV slopes in Figure 8) and may finally crystallize to c-$Li_{15}Si_4$ (VI in Figure 8b,d). All following delithiations are then analogues to the first one.

While the de-/lithiation behavior of as-prepared a-Si is analogous to a-Si* (as obtained from cycling c-Si), one still must distinguish its first cycle behavior. In their *in-situ* TEM studies, Wang *et al.* and McDowell *et al.* discovered a sharp phase boundary between a-Si/a-Li_xSi in the initial lithiation, indicating a two-phase transformation not a solid-solution reaction [99], [100]. However, for the following delithiation as well as further lithiations, the phase boundary was not visible anymore. It was proposed that the lithiation mechanism of a-Si is similar to the two-phase c-Si/a-Li_ySi reaction in the first cycle, where a sharp phase boundary with high Li content is necessary to weaken the Si-Si bonds of the a-Si as well. After the first delithiation, the structure of a-Si* is altered to allow the lithiation in consecutive cycles through a pure solid-solution reaction right away. McDowell *et al.* [100] proposed possible differences between a-Si and a-Si* could be trapped residual Li content in the a-Si matrix as well as a less dense a-Si structure with more dangling bonds. The latter is indicated by a 25 % volume increase after the first cycle. Both changes may potentially facilitate recurring Li incorporation in consecutive cycles. Thus, for the lithiation of a-Si, the transformation from a-Si to a-Si* is commonly observed as a unique dis-/charging behavior in the first cycle [86]–[89], [99]–[101]. Based on this, it is speculated that the first cycle behavior depends on the density of the a-Si itself as well as the used synthesis method [87]. On top of that, both c-Si and a-Si end up as a-Si* after the first charging cycle. Furthermore, within their two-phase reaction model for the first lithiation, Wang *et al.* [99] correlated the two-stage lithiation mentioned earlier to the a-Li_xSi phase with $x \approx 2.5$ and $x = 3.75$. However, no explanation was given for the occurrence of the two-stage profile in consecutive cycles when no phase boundary was observed.

I.C.2 Silicon as Next Generation LIB Anode

With c-$Li_{15}Si_4$ as the terminal lithiation phase at room temperature, silicon's promise becomes obvious when calculating the theoretical gravimetric capacity of c-$Li_{15}Si_4$ to be 3579 mAh g^{-1}. This is 93% of lithium metal anodes' 3862 mAh g^{-1}, which is the benchmark value set by the periodic table every anode must live up to. Furthermore, with an low average delithiation potential of 0.4 V vs. Li/Li^+ [102]–[104], silicon is adequate as a drop-in replacement in current cell technologies, as it finds a suitable balance between sufficient open circuit potential while

avoiding the risk of lithium plating at lower potentials. Thus, the clear advantage of replacing graphite with silicon is an almost ten-fold increase in theoretical gravimetric capacity over graphite's 372 mAh g^{-1}. And, while other elements found in LIBs like cobalt are plagued with political, economic, and environmental issues, silicon is equally cheap and earth-abundant to graphite. This made silicon one of the most promising candidates for the next generation of LIB technology and sparked tremendous research interest in finding a solution to its biggest obstacle: pulverization due to the intrinsic volume expansion upon de-/lithiation [103], [104].

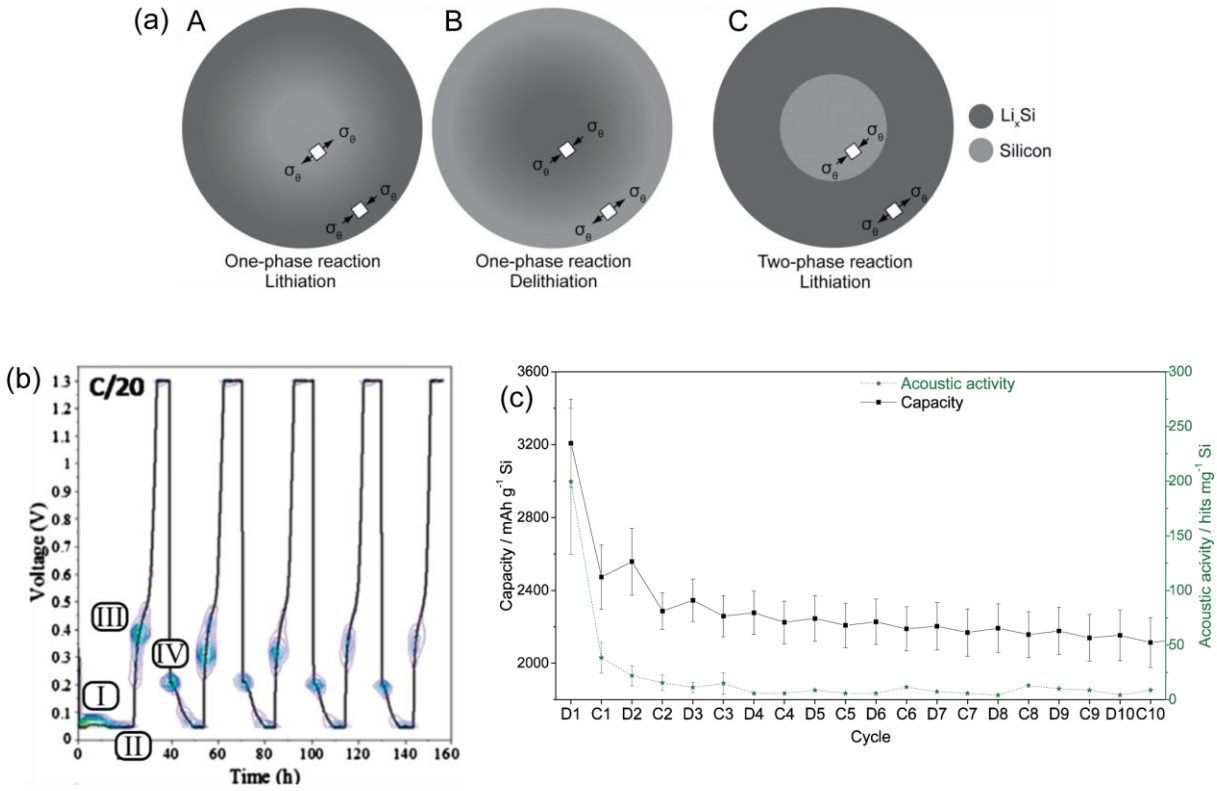

Figure 9 (a) Illustration of the predicted hoop stresses of a spherical silicon particle near the center and surface during lithiation via a one-phase solid solution reaction (A) and via a two-phase reaction (C) as well as during delithiation via a one-phase solid solution reaction (B). The images is sourced from [87]. (b) Potential vs. time curves from the acoustic emission experiment of Rhodes et al. with density contour plots indicating the high acoustic emission activity during dis-/charging. The image is sourced from [105] and shown as in [88]. (c) Correlation between the acoustic activity and the capacity fading during cycling over 10 cycles from Tranchot et al.'s in-situ acoustic emission study. The image is sourced from [106].

So far we have only discussed the phase evolution during de-/lithiation, but as it was shown by Obrovac *et al.* in Figure 8c [96], all phases adhere to a linear relationship between volume expansion and lithium content. It is apparent that for achieving high capacities extreme volume changes are inevitable. Understanding and controlling the mechanical stresses that develop under these volume changes is essential, as they cause fracture, and the mechanical degradation will lead to a loss of capacity over charging cycles. With the volume swings being detrimental for cyclability, there appears to be a trade-off between capacity and cycle life. Usually, making this deal means avoiding the c-$Li_{15}Si_4$ phase by applying a proper cutoff potential at the end of the lithiation. This strategy was demonstrated by Obrovac and Krause

in 2007 through reversibly cycling crystalline silicon powder and achieving an efficiency of 99.85% over 100 cycles with a cell capacity of 960 mAh g^{-1} by applying a 170 mV cutoff potential [95]. Here, the tradeoff is clear: while still 2.5 times the capacity of graphite, the achieved 960 mAh g^{-1} is only 27% of the theoretical value of 3579 mAh g^{-1} for c-$Li_{15}Si_4$. However, the successful increase of cyclability by avoiding the terminal c-$Li_{15}Si_4$ is not only a question of the actual volume expansion itself, but also of avoiding the detrimental two-phase transformation, as explained in the following.

I.C.3 Phase Transformations, Volume Expansion, and Cracking

As we have seen earlier in Figure 8, the de-/lithiation takes place either by a solid-solution or a two-phase reaction. The induced stresses in each of these reactions are fundamentally different [86], [87]. In a solid-solution reaction, the stresses are gradually and stem from a gradient in lithiation degree and volume expansion (see Figure 9a:A,B). For the simple case of spherical particles, where the lithiation starts from the surface, this leads to gradual compressive hoop stresses during lithiation and tensile stresses during delithiation at the surface, while the stresses at the core are the opposite, as shown in Figure 9a:A,B [87], [107]. For this reason, silicon anodes tend to be more prone to cracking during delithiation when the tensile stresses at the surface facilitate crack formation and its propagation [86]. On the other hand, in a two-phase reaction, the lithiation and volume expansion is localized to a very sharp phase boundary. Chon *et al.* revealed the c-Si/a-Li_ySi phase boundary through high-resolution TEM to be only about 1 nm wide [108]. Thus, the deformation is highly concentrated at the phase boundary and is determined by the propagation of the reaction front and not by the overall diffusion. This can lead to different stress states compared to a solid-solution reaction [109]–[111]. As shown in Figure 9a:C, during the lithiation of a crystalline spherical particle, the hoop stress on the outer shell is then tensile, because the advancing phase boundary pushes out the surrounding lithiated phase. The inner core, however, is under compressive stress. As for the solid-solution reaction, tensile hoop stress tends to facilitate cracking.

Due to the highly concentrated volume jumps, it is commonly believed that two-phase transformations are more mechanically detrimental than solid-solution reactions. Thus, avoiding them became a promising strategy to reduce mechanical degradation and to increase the cyclability of silicon anodes [86]–[88], [112]. The detrimental effects of two-phase reactions was compellingly demonstrated by the acoustic emission experiments of Rhodes *et al.* [105] and Tranchot *et al.* [106]. In their experiments, they monitored the cracking behavior/frequency via the cracks' acoustic emission with a piezoelectric sensor coupled to c-Si anodes and they were able to correlate the acoustic emission to the capacity fade. As shown in Figure 9b,c, the acoustic emission, and the associated capacity fade, was more pronounced during the first

delithiation, presumably due to the detrimental c-Si/a-Li_ySi two-phase transformation. A similar correlation is noticeable in the data of Rhodes *et al.* [105] shown in Figure 9b for the two-phase a-Li_xSi/c-$Li_{15}Si_4$ transformation in each cycle below 50 mV vs. Li/Li^+. Based on this, a-Si appeared to be the more promising system over c-Si, as it does not undergo several detrimental two-phase reactions within the first lithiation [103], [112]–[117].

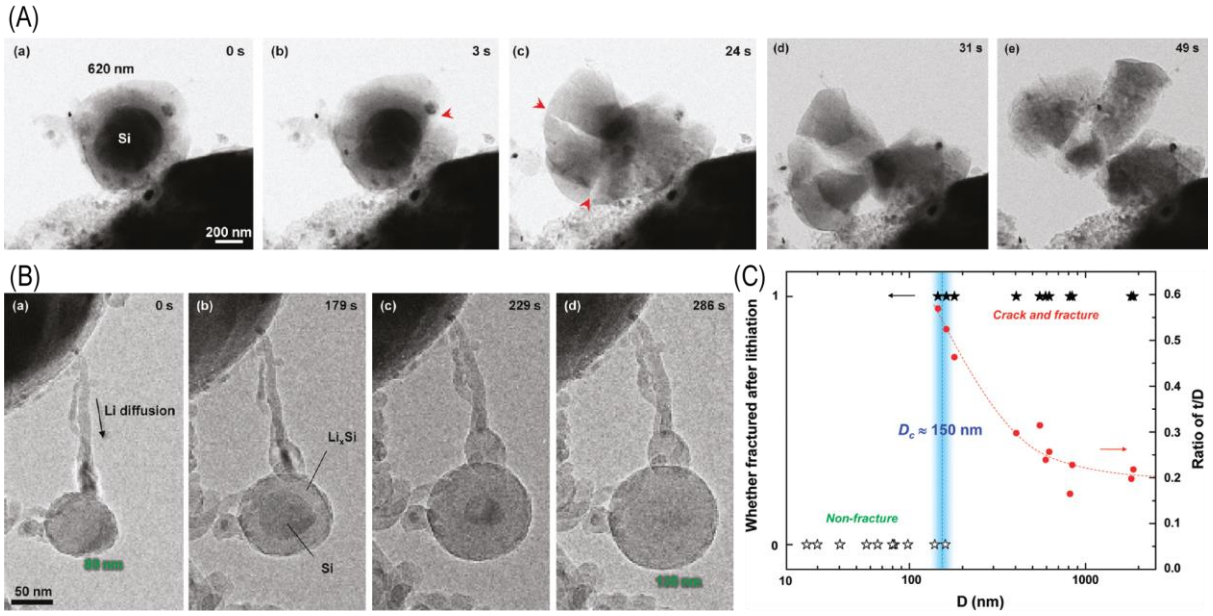

Figure 10 (A) Series of TEM images during the chemical lithiation of a c-Si nanoparticle with a diameter of 620 nm. The red arrows mark the appearance of cracks during the lithiation. The nanoparticle is not stable against fracture and pulverizes. (B) Series of TEM images during the chemical lithiation of c-Si nanoparticle with a diameter of 80 nm. Due to the size-dependent fracture behavior, the silicon particle is small enough to be stable against fracture even when fully lithiated. The fully lithiated particle has a diameter of 130 nm, which corresponds to a volume expansion upon lithiation of 300%. (C) Fracture behavior of c-Si nanoparticles during chemical lithiation as a function of diameter D. The red dots mark the first appearance of cracks with the corresponding a-Li_xSi shell thickness t. All images are sourced from [109].

Besides this, plenty of analytical und numerical models have been developed to understand the stress and cracking behavior during de-/lithiation for both types of transformations in many different anode morphologies and geometries. However, the topic in its entirety is outside of the scope of this work and I want to leave it with this short introduction. For a more deeper understanding I refer to the excellent review articles of Kim *et al.* and McDowell *et al.* [86], [87]. Without diving deeper into these models, I want to highlight one strategy to tackle cracking, which can be derived from the most general view of fracture mechanics. Simply put, the driving force for cracking is the release of volume strain energy to overcome the crack formation energy, namely the formation of new surface. Thus, decreasing the size directly limits the possible volume strain energy that is available. For nanostructures, the possible strain energy lies below the crack formation energy and the whole structure is stable against fracture. This principle was demonstrated by Liu *et al.* in their *in-situ* TEM experiment, where they studied the chemical lithiation of silicon nano-particles in real time [109]. They found a critical particle diameter of about 150 nm under which the particles remain intact, even when

fully lithiated (see Figure 10C). Figure 10A shows the pulverization of a silicon nanoparticle with a diameter of 620 nm from the work of Liu *et al*. The pulverization takes place when the c-Si/Li_xSi phase boundary proceeds to a certain point towards the center of the particle. The ratio between the diameter D and the Li_xSi shell thickness t when the first crack appears is given in Figure 10C. Figure 10C clearly marks the critical particle diameter around 150 nm below which no fracture takes place. For this case Figure 10B shows a particle with 80 nm diameter which can be fully lithiated without cracking. The fully lithiated particle has a diameter of 130 nm, which corresponds to a volume expansion of about 300%. Further, it must be noted, that for solid-solution reactions, the expected concentration gradients and thus the evolving stresses (as we have seen in Figure 9a) are much smaller in nanostructures due to the much shorter diffusion length scale within [117]. Thus, the nanostructure not only becomes tougher against fracture, but the stresses itself are also smaller.

This stabilizing size effect gained the manufacturing of silicon nanostructures tremendous attention in the last two decades [104]. Here, a vast variety of different approaches were explored to reduce the silicon to 2D (thin-films), 1D (nanowires and -tubes) and 0D (nanoparticles) nanostructures. In the following, I want to focus briefly on silicon thin-films. First, because they emerged as a promising approach, given their relative ease of fabrication and with this their potential for commercial upscaling. Second, silicon thin-films are the chosen model system in this work, because, as we will see, they remain crack-free and allow the investigation of the SEI's formation in isolation from the cracking phenomenon. For a comprehensive summary of the research efforts from the last two decades on implementing silicon as LIB anode, I want to mention the review articles of Zuo *et al.* [104], Szczech *et al.* [118], and Su *et al.* [119]. For a more narrow focus on silicon thin-film anodes in particular, I refer to the reviews of Mukanova *et al.* [103] and Salah *et al.* for pure [112] and doped silicon thin-films [120].

I.C.4 Silicon Thin-films as Lithium-ion Battery Anodes

Silicon thin-films are commonly produced via chemical (CVD) and physical vapor deposition (PVD) techniques as well as electrodeposition. PVD techniques include thermal evaporation, electron-beam evaporation, pulsed laser deposition and direct current or radio frequency magnetron sputtering. The most common CVD precursors are trichlorosilane ($SiHCl_3$), disilane (Si_2H_6), and silane (SiH_4) [112]. As basic principle, most studies revealed an increased cyclability for thinner films [103], [104], [112], [118]. Takamura, Ohara and co-workers pioneered silicon thin-films as anodes for the LIB as early as 2004 [121]–[123]. They demonstrated the prospect of this approach by depositing amorphous thin-films ranging from 50 to 300 nm in thickness by thermal evaporation onto a 30 µm thick nickel foil. The thin-films

with 50 nm thickness performed best and maintained a specific capacity of 3100 mAh g^{-1} over 1000 cycles and a Coulombic efficiency of 100% with a charging rate of 12C [103], as shown in Figure 11a. This value already accounts for 87% of the theoretical capacity of 3579 mAh g^{-1} from c-$Li_{15}Si_4$ and is by itself a tremendous result. The 50 nm thin-films remained crack free for at least 1000 cylces, even for demanding charging rates of 30C, as it can be seen in Figure 11b. Unfortunately, the much thicker films with 300 nm thickness exhibited a capacity fade down to around 1800 mAh g^{-1} over 180 cycles already. This trend was clearly confirmed by the studies of Li *et al.* on amorphous silicon thin-films sputtered on stainless steel [124]. They investigated 500, 200, and 100 nm thick films and discovered a clear correlation between thickness and cycle stability. The capacity retention curves of the different thicknesses are given in Figure 11c. Li *et al.* estimated the critical thin-film thickness under which the film remains crack-free based on the Griffith-Irwin relation. The Griffith-Irwin relation as formulated by Li *et al.* is given in (2), with the critical crack-free film thickness h_c, the fracture toughness K_{Ic}, the Poisson's ratio γ and the stress inside the thin-film σ. With a fracture toughness of 1 MPa $m^{1/2}$ and a Poisson's ratio of 0.2, as assumed for a-Si, the Griffith-Irwin relation in (2) yields a critical film thickness within the order of several hundred nanometer for a stress of 2 GPa [124]. In their study, Li *et al.* proposed the critical thickness of amorphous silicon thin-films on steel substrates to be between 100 and 200 nm under which the film remains crack free. To demonstrate the thickness dependent cracking behavior, Figure 11d,e shows a cracked 500 nm a-Si thin-film after only 5 cycles and a crack-free 100 nm a-Si thin-film after 10 cycles, respectively. While Li *et al.* noted these values for the critical thickness are specific to the substrate and preparation technique, it is commonly observed that silicon thin-films below 100 nm remain crack-free [103], [112]. The correlation between film thickness and cyclability was summarized by Szczech and Jin [118] as follows: for films up to 250 nm thickness, reversible capacities commonly reported in literature are near 3000 mAh g^{-1}, while the ones for thicker films usually range from 1000 to 2500 mAh g^{-1}.

$$h_c \approx 4\sqrt{2}\frac{K_{Ic}}{\sigma^2(1-\gamma^2)} \qquad (2)$$

Although the specific capacities are promising, the simple concept of a silicon thin-film on metal foil provides far too little mass loading and thus is not yet suitable for practical application due to the small total capacities [112]. For a commercial applications the minimum silicon film thickness is considered to be at least 500 nm to compete with current commercial anodes [119]. For a-Si with a density of 2.285 g cm^3, this correlates to a mass loading of 0.11 mg cm^{-2}. Thus, the initial research interest was to increase the thin-film thickness (mass loading) while maintaining the acceptable cycling performance. For this, surface roughing by mechanical abrasion through sandpaper, chemical etching and electrochemical deposition of additional

rougher layers turned out to be promising [112]. To give an example, Takamura *et al.* continued their earlier work and manufactured high-capacity silicon thin-films on copper foil. The foils' surface was modified by the electrodeposition of tiny pyramid-like copper bumps from an aqueous $CuSO_4$ solution [125]. With this, they were able to obtain a 3.6 µm thick silicon thin-film with a steady capacity of 2000 mAh g^{-1} over 50 cycles, an over 10-fold increase in thickness over the 300 nm thin-films discussed earlier. Furthermore, with the development of more advanced sputtering techniques in more recent years, Demirkan *et al.* and Wang *et al.* fabricated multilayered amorphous silicon thin-films with alternating high and low density [126], [127]. The low-density layers act as buffer zones for the increased volume expansion of the high-density layers, enabling an increased film thickness while maintaining good cyclability. With this, on ordinary copper foils, they were able to achieve 1700 mAh g^{-1} over 50 cycles for 380 nm thick layers [127] and 1900 mAh g^{-1} over 100 cycles for about 700 nm thick layers [126].

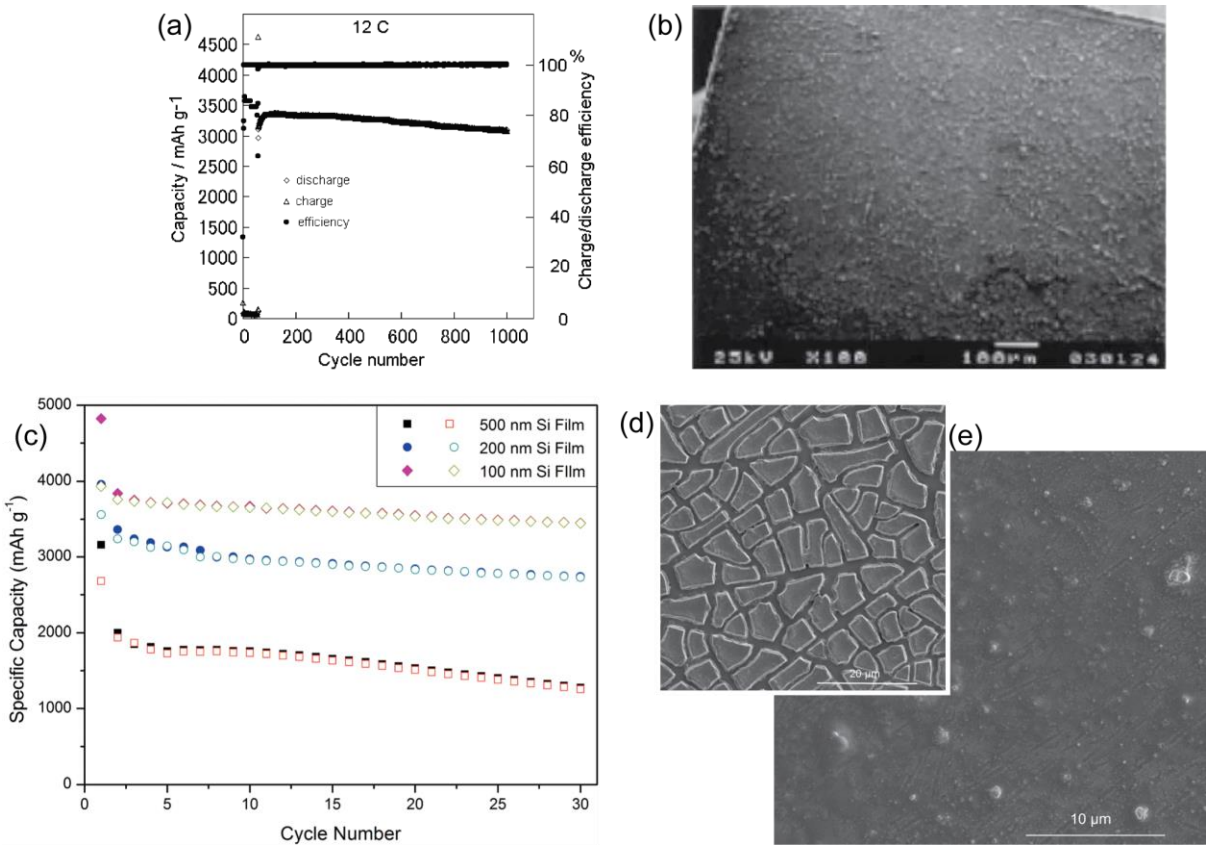

Figure 11 (a) Capacity retention and efficiency of 50 nm thick a-Si thin-film from Takamura et al. over 1000 cycles with a charge rate of 12C [121]. (b) SEM image of a crack-free, 50 nm thick a-Si thin-film from Takamura et al. after 1000 cycles with a charge rate of 30C [121]. (c) Capacity retention of a-Si thin-films on steel substrates with different thickness over 30 cycles from Li et al. [124]. (d) SEM image of a crack pattern from a 500 nm thick a-Si film after 5 cycles from Li et al. [124]. (d) SEM image of crack-free, 100 nm thick a-Si film from Li et al. after 10 cycles [124].

Another ingenious way to increase the mass loading while maintaining the cyclability of thin-films was the application of three-dimensional substrates, creating an electrode type often referred to as "composite films". Zhao *et al.* demonstrated this approach in 2012 through the

electrodeposition of silicon thin-films on a nickel foam [128]. The prepared Si/Ni foam composite films showed remarkably stable capacity of 2800 mAh g^{-1} over 80 cycles. The same concept was applied by Dogan *et al.* with a copper foam [129]. Lin et al. replaced the foam with a dense network made from copper nanowires as substrate for the RF magnetron sputtering of silicon [130]. The composites remained well above 2000 mAh g^{-1} over 60 cycles. In 2016, Huang *et al.* followed a similar approach when they utilized cobalt nanosheet arrays as a substrate for the magnetron sputtering of silicon thin-films [131]. With a high mass loading of 0.2 mg cm^{-2}, the silicon thin-films on the cobalt nanosheets had a first discharge capacity of 2950 mAh g^{-1} with a charge capacity retention rate of 82% after 100 cycles. With this result, the obtained mass loading was well above the value of 0.11 mg cm^{-2}, which was deemed necessary for any commercial competitiveness, as mentioned above.

From the examples above it appears that thin-films alleviate the cracking issue and ingenious composite films are an answer to the low mass loading of the thin-films itself. Nevertheless, the low reported cycle numbers of only 1000 or sometimes even well below, are still unacceptable for any application. For commercial use, a capacity retention of 80% over 2000 cycles and a capacity fade per cycle below 0.01% is considered the bare minimum [112], [119], [132]. No reported silicon thin-films could fulfill this benchmark so far. For high cycle numbers, in the review of Salah *et al.* from 2019 [112], only four [133]–[136] out of 165 cited articles report results which are remotely comparable to state-of-the-art graphite anodes. However, I still want to note that 2 out of these 4 are based on thin-films prepared via electrodeposition [135], [136], a fabrication method better suited for upscaling than more demanding vacuum-based PLD or CVD processes. Here, the electrodeposited thin-films of Gattu *et al.* exhibited only about 0.056% capacity loss per cycle and ended up with a capacity of about 805 mAh g^{-1} after 500 cycles [136]. With their electrodeposition method, Epur *et al.* achieved a-Si thin-films with a capacity loss per cycle of only 0.02% and reached a capacity of about 1260 mAh g^{-1} after 100 cycles [135]. Albeit both values being far lower than the theoretical value of 3579 mAh g^{-1} for c-$Li_{15}Si_4$, they still exceed the maximum theoretical capacity of graphite with 372 mAh g^{-1} by 2.2 and 3.4 times, respectively. Given their ease and low cost of manufacturing, electrodeposited thin-films like these are likely to gain commercial viability in the future.

So far, when discussing cycle stability, we only considered the silicon anodes itself. However, the cyclability is not only determined by the ageing of the electrodes, but also by the electrolyte itself. As we have seen in I.B, the electrolyte needs to be kinetically stabilized by the SEI. When it comes to the SEI on silicon anodes, it is a common perception that its inability to stabilize the electrolyte is directly and only connected to the cracking of the anode. It is argued that the cracking creates new surface and the SEI formation on the yet unprotected surface

continuously consumes the electrolyte. While this might be true, as we have seen in Figure 11b,e, silicon thin-films remain crack-free below a certain film thickness. But crack-free thin-films still suffer from continuous capacity fading, as indicated by the descending slope in their capacity retention curves commonly reported in literature (e.g., Figure 11a,c). This clearly implies that the cracking/pulverization is not the sole reason at play and the SEI itself fails to stabilize the electrolyte sufficiently. Reasons for why this might be the case will be discussed in detail in the following chapter.

To overcome silicon's biggest obstacle of severe capacity fading, both issues, the cracking and the inefficient SEI, must be addressed individually. In my opinion, the inefficient SEI appears to be the more fundamental and more urgent one. If any silicon anode implementation circumvents cracking, the inefficient SEI still remains the bottleneck for the capacity retention. If cracking is not completely avoided but mitigated by other means, e.g., through substrates or binders that maintain the electrical contact even after fracture/pulverization, an efficient, fast forming SEI to cover the unprotected crack surface is even more important. The former is also particularly crucial for silicon nanoparticle/graphite blends, which are the type of silicon anodes most likely to reach commercialization in the near future [32], [137]. Although these blends have only low loading of silicon, due to the large surface area of the nanoparticles, a stable SEI on them is of high importance.

In this work I want to present a novel approach for the *in-situ* analysis of the SEI on silicon through transmission sXAS in isolation from the cracking phenomenon. Thus, the avoidance of cracking is key. With this, I have evaluated 50 nm thick amorphous silicon thin-films as a perfect model system for this purpose. As I mentioned earlier, a-Si suffers from less cracking than c-Si, due to the lack of detrimental two-phase transformations within the first cycle. Further, with a thickness of 50 nm, I expect the thin-films to remain crack-free, even for a high number of cycles. In this regard, I chose the potential ranges during cycle accordingly to avoid the detrimental c-$Si_{15}Li_4$ phase and remain in the a-Si/a-Li_xSi system. Besides this, I found 50 nm to be a very widespread thickness applied in the reported literature, making the comparison of any findings easier. Although thin-film implementations appear far from commercialization and won't be the first kind to reach the market, I am certain that the results obtained from this model system are of general nature and are essential for all other silicon anodes as well. In the following I want to give a short overview of the current research on the SEI on silicon.

I.C.5 The Solid Electrolyte Interphase on Silicon

I want to approach silicon's SEI from our comprehensive picture of the SEI on graphite. With our current understanding, the inability of silicon's SEI to stabilize the electrolyte sufficiently is

not yet apparent from the direct comparison to graphite. As stated before, I consider graphite's SEI a proof-of-concept, that highlights first deficiencies and inspires possible solutions for a successful engineering of a fully efficient SEI on silicon.

To enter the commercial LIB landscape, silicon must act as a drop-in replacement for graphite and work with current commercial cell chemistry, particularly electrolytes. Consequently, most research is conducted with the known electrolyte formulations, 1M $LiPF_6$ in EC mixed with linear dialkyl carbonates like DMC, EMC, or DEC. With approximately 0.4 V vs. Li/Li^+, silicon operates in a comparable potential window as graphite at 0.05 V vs. Li/Li^+ [137]. Additionally, both graphite and silicon start out in their delithiated state and the SEI is expected to form only during the first few lithiation cycles. Thus, for the same electrolyte formulations at similar anode potentials one would expect the same or at least similar reduction products and thus SEI composition [138]. However, as we have learned from the "3D Interphase Model" of Besenhard and Winter [49], [50], in the case of graphite, the electrolyte reduction and SEI formation is proceeded by solvent co-intercalation and the decomposition reaction could be considered as "surface catalyzed". At a conversion electrode like silicon, co-intercalation does not take place, which already suggests the electrolyte reduction and SEI formation mechanism might be indeed different. Besides the lithiation mechanism itself, silicon's surface with its native SiO_2 layer and terminal hydroxyl functional groups (-OH) differs greatly from graphite's as well.

If and how far these differences change the SEI composition on silicon has been investigated by a variety of characterization methods: XPS [43], [139]–[146], secondary ion mass spectroscopy (SIMS) [147], [148], Auger electron spectroscopy (AES) [142], Infrared spectroscopy (IR) [43], [143]–[146], [149]–[151], X-ray (XRR) as well as neutron reflectometry (NRR) [152]–[156], and NMR [157], [158]. These studies found the SEI on silicon to be comprised of semi-carbonates (LEDC or LEMC), LiF, Li_2CO_3, lithium alkyl carboxylate, LiOH, $ROCO_2Li$, and ROLi as well as Li_XSiO_y, SiO_xF_y, $Li_xSiO_yF_z$, $Li_xPF_yO_z$, Li_2O, and siloxanes. From this we can already deduce that the solvent is still reduced to familiar, and from the research on graphite's SEI somewhat expected, organic products (LEDC/LEMC, $ROCO_2Li$, ROLi etc.) and the $LiPF_6$ decomposes mainly into LiF as well. It is also apparent that the SEI on silicon appears to be more complex with additional species like SiO_xF_y, $Li_xSiO_yF_z$, $Li_xPF_yO_z$, presumably due to the presence of the native SiO_2 layer.

For graphite's SEI we have seen that the initial SEI composition is simple and comprised of mainly LEDC/LEMC and LiF. Due to its volatile nature, the SEI's composition then evolves into a more and more complex structure with many different second-generation SEI constituents, as discussed earlier based on Figure 6A,B,C. In their recent perspective article

from 2021, Kim *et al.* pick up this notion and present a rather straightforward take on silicon's SEI [159]. They proposed that LEDC and LiF are still the main reduction products of EC. In case of silicon, however, the conditions and environment lead to a quicker transition to the second-generation SEI components, which in turn fail to stabilize the electrolyte sufficiently. They argue the formed LEDC cracks like a rigid solid under the large de-/lithiation volume swings of silicon. The cracking increases the surface area and makes the LEDC more susceptible to the attack of the acidic $LiPF_6$ decomposition products (PF_5, POF_3, and HF), what in turn decomposes LEDC into LiF, CO_2, fluorophosphates, lithium alkoxides, and poly(ethers). This process can be considered analogous to what is happening with graphite's SEI [53]. They go on and propose that on top of that, the silica and lithium silicate $Li_xSi_yO_z$ could catalyze the thermal decomposition of LEDC into Li_2CO_3, Li_2O, CO_2, ethylene and lithium carboxylates, as they claim was shown by Yoon *et al.* [54]. While I consider Kim *et al.*'s general notion here to be true, in the temperature range from 50 to 300 °C, Yoon *et al.* observed LEDC to deteriorate into CO_2, ethylene, lithium propionate and Li_2CO_3 only. Thus, given the temperature range, these are the more likely decomposition products to me. However, the general idea of the LEDC not being stable in the vicinity of the Li_xSi was backed up by the theoretical work from Leung *et al.* [160]. In their DFT calculation they show that LEDC as well as Li_2CO_3 are not stable in the vicinity of Li_xSi with high lithium content and are expected to decompose into Li_2O.

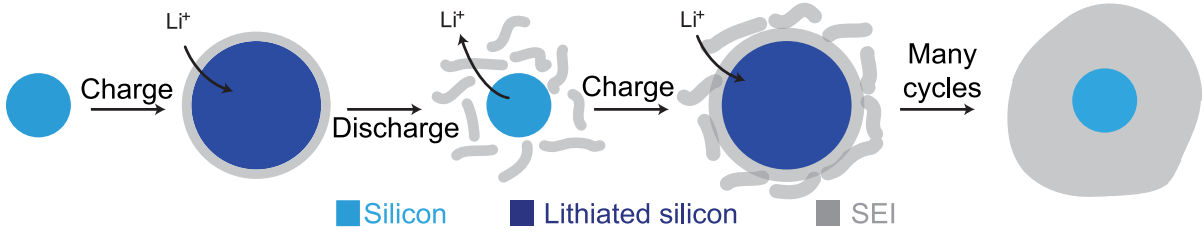

Figure 12 Sketch of the failure mechanism of silicon's SEI. The image is adapted from [161].

Kim *et al.*'s explanation is in good agreement with the following picture of silicon's SEI as it was compiled by Shin *et al.* in their review article from 2020 [137]. They wrote that, the SEI on silicon has a complex heterogeneous layered structure. The innermost layer is a reduced form of the native SiO_2 layer as $Li_xSi_yO_z$, SiO_xF_y, $Li_xSiO_yF_z$, or $Li_xPF_yO_z$. It is covered by a dense, inorganic layer of LiF, Li_2CO_3 and Li_2O. The outermost layer is highly porous and made up of organic species like LEDC/LEMC, $ROCO_2Li$, or ROLi. For its failure mechanism itself, the most commonly accepted idea is illustrated in Figure 12. In the case of graphite, due to co-intercalation of the solvent molecules, the SEI forms a 3D interphase, which is strongly interwoven with the surface and immobilized to it. This is not the case for silicon's SEI, which is assumed to be a loosely bound layer only. Consequently, when the volume decreases during delithiation, the SEI detaches, (presumably breaks), and exposes unprotected surface.

During the next lithiation, a fresh SEI layer forms once again on the uncovered surface. With this, the detrimental impact on cyclability is two-fold. First, the continued SEI formation deteriorates the capacity by consuming the limited Li-ion reservoir of the cell, taking it away from the actual "Rocking Chair" battery operation. To put the severity of this issues into ballpark numbers: if the continuous SEI growth consumes only 0.01% of the charge (meaning 99.9% charge efficiency) it will deteriorate the capacity over only 250 cycles to 78% as $0.999^{250} = 0.78$ [137]. Second, over many cycles a thick SEI layer builds up. While this thick layer may finally stabilize the electrolyte by being electrically insulating, at the same time, it crushes the cell's performance with an unacceptable overpotential by preventing all Li^+ diffusion.

In this regard, as it was postulated before, an efficient SEI is electrically insulating while still facilitating Li^+ permeation. With what we have learnt from graphite's SEI, LEDC/LEMC is assumed to satisfy this requirement. Thus, the supposed intrinsic instability of LEDC on highly lithiated Li_xSi might be another reason for the inefficiency of silicon's SEI. Furthermore, as we have seen for graphite before, many of the second-generation decomposition products are either gaseous or soluble in the electrolyte, changing the SEI's morphology and making it less effective over time. This suggests that one aspect of the failing mechanism of silicon's SEI is not fundamentally different but only accelerated and amplified by the detachment and or cracking of the SEI itself under the volume swings. The accelerated deteriorating behavior of silicon's SEI has been observed in many studies and is commonly referred to as the "Breathing Effect" [149], [152], [154], [155], [162]–[164], as the SEI appears to build up and shrink with every de-/lithiation ("breathing") cycle. However, the extent and actual effect of the "Breathing Effect", e.g., direction of the change in thickness, composition changes etc., appear to vary between reports in literature. Nevertheless, it is agreed upon that silicon's SEI behaves highly dynamic.

The "Breathing Effect" was impressively demonstrated by the work of Veith *et al.* with their *in-situ* neutron reflectometry measurements on a-Si thin-film anodes, which were supported by extensive *ex-situ* XPS and FTIR studies [154]–[156]. They were able to show that in the initial lithiation a low-density LiF-rich SEI layer forms of about 20 nm thickness, which then turns into a mixture of inorganic LiF and C-O-C polymeric type species over consecutive cycles. More importantly, as summarized in Figure 13a, they observed the SEI to grow from 18 nm to 26 nm during delithiation and shrink back to 18 nm thickness during lithiation, repeatedly. On top of that, during delithiation the polymeric content deceased from 30-40% down to only 10%. Upon lithiation, the SEI becomes more polymeric again, presumably due to the recurring decomposition of the solvent at lower potentials. This observation is in good agreement with

the idea discussed earlier, that the organic / polymeric SEI species appear to deteriorate quickly.

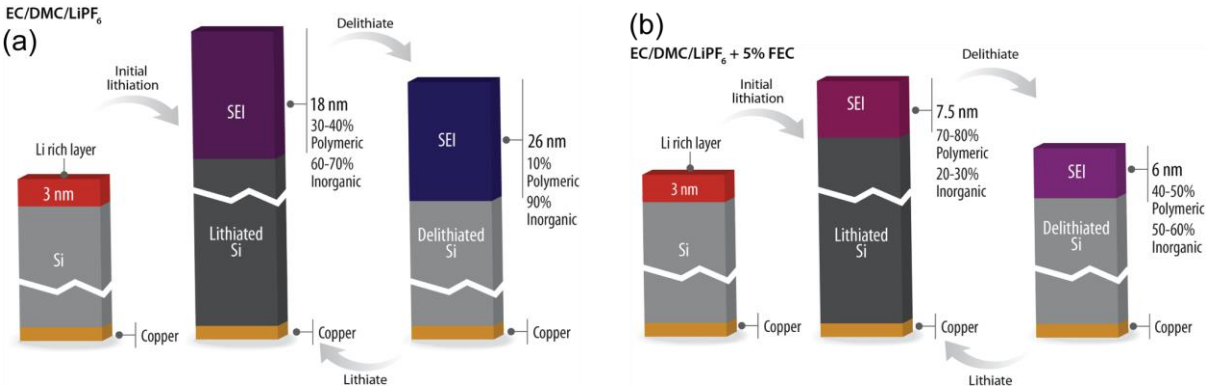

Figure 13 Graphical summary of the in-situ neutron reflectometry measurements on a-Si thin-film anodes from Veith et al. [154] using 1M $LiPF_6$ EC:DMC electrolyte with (a) and without the addition of 5% FEC (b). The images are sourced from [154].

A similar behavior was reported recently by Hasa *et al.* in their *ex-situ* FTIR study on once again 50 nm thick a-Si thin-film anodes [149]. In their FTIR analysis, they observed the spectral contribution attributed to LEDC and polyethylene glycol (PEG), as well as P-O-F and P-F containing SEI species, to vanish during delithiation. However, they note that LiF does not exhibit a “Breathing Effect” and its spectral contribution remains constant throughout cycling. What is of particular interest here is, that in their electrochemical data they did not observe any additional peaks during delithiation which would reveal any electrochemical oxidation of the organic species. This strongly suggest that the decomposition of the organic species is either of chemical or physical nature, e.g., the dissolution of the organic species back into the electrolyte. However, this would decouple the SEI’s composition from the state-of-charge and one could argue that the chemical and/or physical decay just happens simultaneously with the delithiation.

Besides this, Huang *et al.* also witnessed the decomposition of LEDC in their *ex-situ* cryo-TEM study of silicon nanowires [164]. As shown in Figure 14a,d, after lithiation down to 10 mV vs. Li/Li^+, they reported the silicon nanowires to be fully lithiated to $Li_{15}Si_4$. The lithiated nanowires were covered by Li_xSiO_y (stemming from the native SiO_2 layer) and a thin layer of LEDC with small contents of Li_2O. The LEDC was identified through electron energy loss spectroscopy (EELS) which showed a distinctive peak at the carbon K-edge in Figure 14c. However, upon delithiation back to 1 V vs. Li/Li^+, Li_xSiO_y was oxidized to SiO_x and the LEDC peak disappeared as shown in Figure 14b,c,d. Huang *et al.* labelled the new compound “oxidized LEDC” without any further specification. Nevertheless, it is evident that LEDC decomposes during delithiation. I also want to note, that the presence of Li_2O within the LEDC layer may back up the claims of Leung *et al.* [160], who showed based on their DFT calculation that LEDC is not stable in the vicinity of highly lithiated Li_xSi and might decompose to Li_2O.

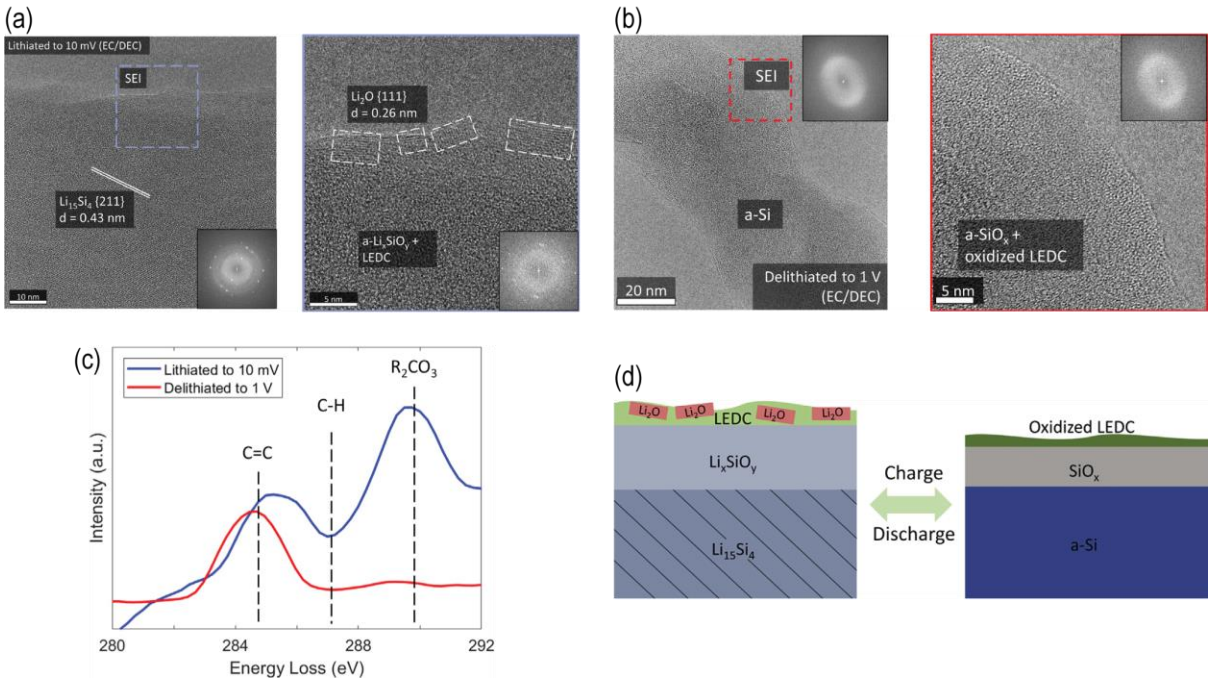

Figure 14 (a) High resolution TEM images from a silicon nanowire fully lithiated to $Li_{15}Si_4$ (left) and closeup from the SEI (right) showing a-Li_xSiO_x, LEDC and Li_2O domains. (b) High resolution TEM images from a silicon nanowire fully delithiated back to 1 V vs. Li/Li^+ (left) and closeup from the SEI (right) showing a-Si_x and oxidized LEDC. (c) EELS spectra of the SEI from the silicon nanowire at 10 mV and 1 V vs. Li/Li^+. (d) Sketch of the evolution of the SEI on the silicon nanowires upon cycling. All images were compiled from [164].

In the beginning of this chapter, I claimed that the inefficiency of silicon's SEI must be considered in isolation from silicon's cracking issue. For this, I argued that we witness severe capacity fading even for silicon thin-films which remain crack-free. In the following, I want to discuss the recent findings of He *et al.* from 2021 in more detail [165]. To me, they propose a very interesting picture, in which the volume swings of silicon, all cracking aside, are accompanied by pore formation, which appears to be deeply intertwined with the SEI development.

For their *ex-situ* cryo-TEM-EDX tomography study, they grew crystalline silicon nanowires with about 60 - 90 nm diameter on a stainless-steel substrate and cycled them inside coin cells between 20 mV and 1.5 V vs. Li/Li^+ for up to 100 cycles. In the tomography reconstructions, they observed that the nanowires show no sign of cracking and for the first cycle the SEI forms on the surface as a core/shell heterostructure. With continued cycling, however, vacancy generation and condensation during delithiation forms pores, which build up increasingly interconnected percolation channels throughout the whole nanowire volume. These channels allow the electrolyte to penetrate the nanowire and an SEI to form at the inner walls of the channels and pores. With increasing cycle number, the channels and the SEI proceed towards the core. Through this, the SEI and the silicon become more and more intertwined, and the nanowires turn into a "plum-pudding"-like structure, where silicon domains ("plums") are surrounded by the SEI ("pudding"), as illustrated in Figure 15. The "plum-pudding"-like

structure leads to capacity loss by disrupting the electron and ion conduction and thus by increasing impedance. Additionally, with increasing interconnection of the channels, silicon domains can become fully isolated and lose electrical contact, making them inaccessible for further de-/lithiation. If the loss of contact happens in the lithiated state, this results in Li trapping, which cannot further participate in the ion shuffling.

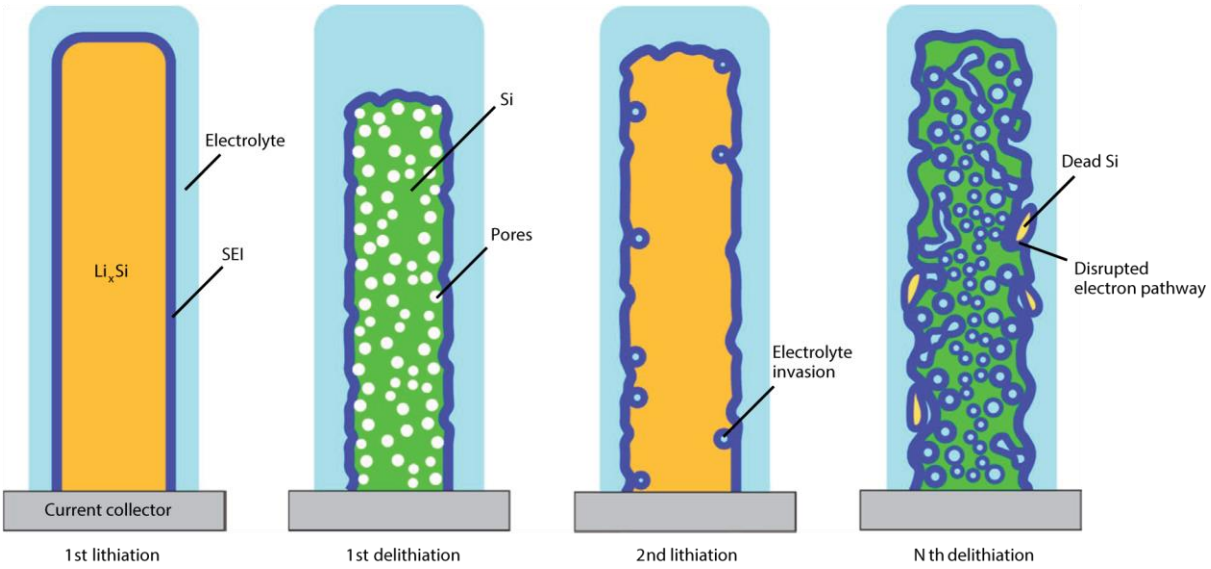

Figure 15 Illustration of the spatially coupled evolution of the SEI and the active material as proposed by He et al. [165]. Pore formation due to vacancy condensation during delithiation creates percolation channel, which can be penetrated by the electrolyte. This mechanism allows the SEI to grow towards the nanowire core. With continued cycling the silicon nanowire turns into a "plum-pudding"-like structure, with silicon domains as the "plums" in the SEI "pudding". The image is sourced from [165].

While the findings of He *et al.* do not contradict the basic idea of silicon's SEI continuously delaminating and growing as it was depicted in Figure 12, they uncover another layer of intrinsic complexity when it comes to silicon's capacity fading mechanism. I want to mention that the discovered "plum-pudding" bears a certain resemblance to the interwoven structure of the 3D interphase we have seen from graphite's SEI before. Thus, to me it appears that the pore and channel formation as discussed above might offer a mechanistic way to form a more resilient connection between SEI and silicon. When formed once inside the pores and channels close to the surface, a stable SEI that is anchored this way might prevent further electrolyte penetration and prevent the "plum-pudding" transformation from proceeding any further. Such an immobilized SEI might also be less likely to delaminate during delithiation and thus less unprotected silicon would be revealed with every cycle. This could extenuate the continuous SEI growth. A possible way to engineer such SEI is the use of suitable electrolyte additives which change the composition and morphology of the SEI. I will conclude this chapter with few examples of how electrolyte additives are applied to improve the stability of silicon's SEI and increase the cyclability.

I.C.6 Electrolyte Additives for an Improved Solid Electrolyte Interface on Silicon

The failure mechanism of silicon's SEI from Figure 12, namely the delamination and breaking upon delithiation, imposes the idea to stabilize the SEI with a mechanically stable, elastic polymeric film, which can accommodate the volume swings. Coming from this basic idea, based on the success for graphitic anodes, VC and in particular FEC quickly became the most popular electrolyte additive to increase the cycle stability of most silicon anode implementations (particles, thin-films, nanowires etc.) [137], [138], [159], [166].

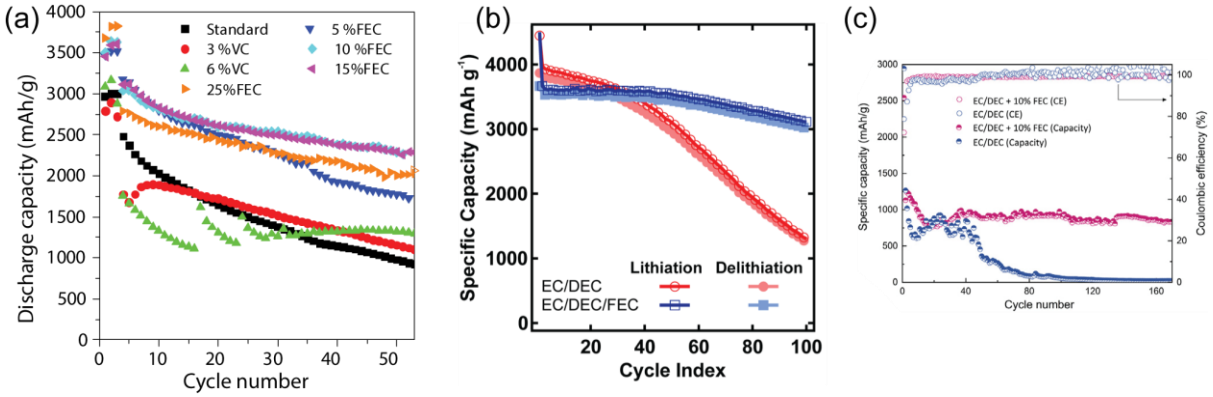

Figure 16 (a) Discharge capacity-retention curves from the comparative study of Nguyen and Lucht [145] showing different cyclability of silicon nanoparticle anodes with 1M $LiPF_6$ in EC/DEC and varying amounts of VC and FEC added, as given in the legend. (b) Capacity-retention curves from Schroder et al.'s study [147] on 50 nm thick a-Si thin-film anodes with 1M $LiPF_6$ in EC/DEC with and without 10% of FEC. (c) Capacity-retention curves from the study of Huang et al. [164] on silicon nanowires with about 50 nm diameter with 1M $LiPF_6$ in EC/DEC with and without 10% FEC.

Like for graphitic anodes, VC and FEC act as sacrificial film-forming additives which are preferentially reduced during the first lithiation, due to their higher reduction potential over the remaining solvent molecules (EC, DMC, EMC, DEC, etc.). The reduction mechanism of VC and FEC was discussed in detail in I.B.5. VC has been shown to form a polymeric film of poly(VC) (see Figure 7b), which in turn suppresses the decomposition of EC and $LiPF_6$, ultimately reducing the content of LEDC and LiF inside the SEI. Further, as shown in the extensive NMR study of Jin *et al.*, FEC is initially defluorinated to VC, releasing LiF and CO_2 [158]. Alternatively, FEC was proposed to reduce electrochemically via a ring opening mechanism to produce LiF, Li_2CO_3 and ethylene [167]. Thus, the use of FEC usually leads to an increased LiF content in the SEI over VC-containing formulations. However, the influence of the LiF content inside the SEI remains unclear, as many publications in literature report both positive and negative correlation to cyclability and battery performance [137]. While this controversy remains outside of the scope of this work, I still want to refer to the extensive recent review of Tan *et al.* [168].

In any case, for silicon, the positive effect of VC and FEC is attributed to the increased mechanical integrity of the SEI through the polymeric nature of the poly(VC) with a high degree of crosslinking. Thus, since the first demonstration of Choi *et al.* in 2007 [169], the positive effect from the addition of FEC on the cyclability has been reported in many publications [145]–[147], [158], [164], [167], [169]–[172]. Based on the protective effect of the polymeric poly(VC) layer, the SEI formed from FEC-containing electrolytes has been reported to be thinner, denser and more uniform than from FEC-free formulations [137], [138].

To come back to the *in-situ* neutron reflectometry experiment of Veith *et al.* [154]–[156] (see Figure 13b), the FEC-derived (5% FEC) SEI turned out to be much thinner with only 7.5 nm compared to the FEC-free SEI with 26 nm. On top of that, Veith *et al.* reported that the polymeric content after delithiation remained at around 40 - 50%, which was significantly higher than that of the FEC-free one with only 10%. These findings are in good agreement with the *ex-situ* cryo-STEM study of Huang *et al.* [164] we have discussed earlier based on Figure 14. They found upon the addition of 10% FEC (see Figure 16c for the corresponding capacity-retention curves), the SEI on the nanowires consists of a poly(VC) layer which remains stable upon cycling. Further, in the FEC-derived SEI they did not observe any LEDC or Li_2O, which suggest two things. First, in comparison to LEDC and Li_2CO_3, poly(VC) appears to be stable in the vicinity of highly lithiated Li_xSi and shows no “Breathing Effect”. Second, FEC is preferentially reduced and the FEC-derived SEI layer prevents the formation of LEDC in the first place.

Furthermore, the increased mechanical stability of the poly(VC)-containing SEIs, derived either from FEC or VC, appears to be of a general nature, applicable to any kind of electrode. On the other hand, based on their comparative XPS and TOF-SIMS study on 50 nm thick amorphous silicon thin-films using 1M $LiPF_6$ in EC:DEC with and without 10% FEC, Schroder *et al.* [147] proposed another positive effect of FEC which is more specific to the surface of silicon (see Figure 16b for the corresponding capacity-retention curves). In their TOF-SIMS measurement, they observed a smaller Li_xSiO_y content in the inner layer of the FEC-derived SEI. They proposed that the electrochemical reduction of FEC yields radical organic ions and fluoride ions, which in turn etch the native SiO_x suboxide layer, preventing the formation of the inner Li_xSiO_y SEI layer. They back up this claim based on their previous findings on reactive ion etched silicon, which produced a similar SEI to the FEC-derived one [148]. They go on and argue that while Li_xSiO_y has been reported as compact and stable coating, it is electronically and ionically insulating. Thus, decreasing the content of Li_xSiO_y improves the electrochemical performance of the anode by increasing the a-Si conductivity and activity. Furthermore, because it is unclear if the formation of Li_xSiO_y is electrochemically reversible,

less Li^+ would be trapped in Li_xSiO_y if the native SiO_x is etched away a priori by the sacrificial FEC additive, directly leading to a higher charge efficiency.

For the sake of truth, however, it must be noted that Schroder *et al.* report a thicker SEI for the FEC-containing electrolyte (72.3 nm) over the FEC-free formulation (20.6 nm) and argue against the presence of any poly(VC) or poly (FEC), which both contradicts the studies discussed before. Nevertheless, in their scanning-TEM and EELS experiment, Sina *et al.* [167] confirm the findings of Schroder *et al.* by reporting the missing Li_xSiO_y layer in FEC-derived SEIs and attributing it to the chemical etching of the native SiO_2 layer through the fluoride ion from FEC as well. As stated before, albeit many publications, the picture of the SEI remains elusive and reports based on different characterization and SEI preparation methods are hard to compare. However, it appears that the etching of the native SiO_x suboxides by the fluoride anion is a common denominator. In summary, for silicon anodes, FEC could be considered a combination of reactive (etching of SiO_x) and film-forming additive (formation of poly(VC)). Which of the two effects is more pronounced could depend on the experimental conditions and thus explains the discrepancies between reports in literature. Nevertheless, the reactive effect of FEC might be the reason why FEC turned out to be much more suitable for silicon (see Figure 16a for a comparison between FEC and VC), while VC was sufficient for an application for graphitic anodes.

Another type of additives which are specifically targeted at silicon's surface are silane-type additives [118], [138], [166]. From sol-gel synthesis it is well known that alkoxy-silane functional groups react readily with the hydroxyl functional group on silicon's surface to form stable Si-O-Si bonds. Thus, alkoxysilanes appear to be promising candidates to form a stable SEI which is directly anchored to the silicon's surface. Based on this, with quartz crystal microbalance measurements, monomethoxy trimethyl silane ($CH_3OSi(CH_3)_3$), dimethoxy dimethyl silane ($(CH_3O)_2Si(CH_3)_2$), and trimethoxy methyl silane ($(CH_3O)_3SiCH_3$) have been shown to reduce the consumption/deposition of activate material and improving the cyclability, implying a more stable SEI formation [118], [134], [173], [174]. Recently in 2019, Aupperle *et al.* investigated *tetraethoxysilane* and (2-cyanoethyl)triethoxysilane as cheaper alternatives to VC as well as FEC and achieved comparable results by direct comparison [175]. Through differential scanning calorimetry, they also demonstrated (2-cyanoethyl)triethoxysilane by itself and in combination with VC and FEC to yield a SEI with much higher thermal stability.

The last type of additive I want to mention gets back to Kim *et al.*'s take on silicon's SEI. According to their explanation, in case of silicon, upon cracking during delithiation, LEDC becomes more susceptible to the attack of the acidic $LiPF_6$ hydrolysis products (PF_5, POF_3, and HF), accelerating the chemical decay into second-generation SEI constituents. As it was

first proposed by Zhang [176], and picked up by Eshetu and Figgemeier in their review from 2019 [138], aromatic isocyanate-based additives could scavenge both HF directly and also residual H_2O to prevent any hydrolysis of $LiPF_6$ in the first place. Decreasing the overall concentration of PF_5, POF_3 as well as HF and stabilizing the electrolyte's chemistry this way could slow down the decay of the first-generation SEI species.

I.D Silicon Anodes for Lithium-ion Batteries and the Need for Novel *In-Situ* and *Operando* Characterization Methods

In this first chapter of my work, I've described the historic development of the modern LIB. With its intercalation electrodes, namely graphite on the anode side and predominantly layered transition metal oxides at the cathode side, it was the much sought-after answer to the big safety problem of secondary lithium metal batteries. The high energy densities of today's LIB stem not only from the high reversible intercalation capacities of the electrodes itself but are also based on the high achievable cell potentials. These high cell potentials exceed the thermodynamic stability windows of modern organic electrolytes and are only possible thanks to the Solid Electrolyte Interphase. The SEI is a sacrificial layer made of reduction products of the electrolyte which forms on the anode during the first few charging cycles and acts as an electronically insulating layer, stabilizing the electrolyte kinetically against further reduction. The formation of an efficient SEI works flawlessly on graphitic anodes and allows them to obtain unmatched cyclability. This made graphite the anode-of-choice of the last two decades.

Nevertheless, to meet the world's ever-increasing demand for mobile electricity, especially for the long-overdue electrification of transportation, new electrode materials for the next generation of high energy density LIBs are necessary. Here, on the anode side, silicon turned out to be one of the most promising candidates, as it offers a 9 times higher theoretical capacity than graphite by incorporating the lithium ions via a conversion reaction (alloying to $Li_{15}Si_4$). Unfortunately, up until now, two main issues make silicon anodes suffer from severe capacity. First, the huge volume expansion of up to 300% upon conversion develops stresses, which lead to cracking and ultimately the loss of active material with ongoing cycling. Second, while ingenious anode implementations (nanoparticles, thin-films, nanowires etc.) have been found to mitigate the cracking issues, the SEI that forms on the silicon appears to be not stable by itself and fails to protect the electrolyte sufficiently. Thus, without an efficient SEI the electrolyte is consumed continuously and the cyclability plummets. Consequently, for a successful application of silicon anodes a holistic approach is required, that combines a mechanically stable silicon anode with a suitable electrolyte/additive formulation which can form a stable SEI. However, as we have seen in the discussion above, our understanding of the SEI in general and especially in case of silicon is still very elusive. While there is indeed extensive

literature, there is still no coherent picture, and many reports are founded on vague mechanistic assumptions that lack validation. The intrinsic difficulty to investigate the SEI stems from its volatile nature and inaccessibility. As decomposition products, the SEI species are not expected to adhere strongly to the electrode surface. Disassembling cells and washing the electrodes already risks losing the SEI all together or at least alter its morphology. Further, with its nanometer thickness, extracting enough of the SEI for subsequent mass spectroscopy is difficult. In the same manner, isolating the small SEI signal from the background, e.g., the rest of the electrode material like binder, substrate, etc., is very hard for most spectroscopic methods. On top to that, the lithium, fluorine, and organic compounds in the SEI are expected to be highly reactive and chemically volatile. Hence, even minor exposure to the environment can alter the chemistry substantially. The risk of changing the SEI during sample preparation makes it very difficult for ex-situ / post mortem methods to analyze the SEI in its true, unaltered state. Thus, to gain a clearer picture of the SEI and the working principle of additives, new *in-situ* and *operando* characterization techniques are necessary.

By highlighting this issue, I now come the next part of my work. With this first chapter I've explained thoroughly *why* I want to investigate silicon's SEI and now I will continue with *how* I went on with this undertaking. For this, in chapter III, I will introduce my novel approach for the investigation of silicon's SEI under *in-situ* conditions via transmission soft X-ray Absorption Spectroscopy using a gas bubble-stabilized liquid thin-layer. Beforehand however, in the upcoming chapter II, I will first explain the fundamentals of XAS in combination with the creation of synchrotron radiation at the BESSY II synchrotron facility in Berlin, Germany. Further, I will summarize current sXAS techniques currently used to investigate electrode materials and electrolytes under *in-situ* and *operando* conditions in transmission X-ray Absorption Spectroscopy. Getting to know the achievements of these great techniques but also learn about their current drawbacks will allow us to put my novel approach into perspective and see what new prospect it brings to this field of research.

II Soft X-ray Absorption Spectroscopy with Synchrotron Radiation

The term X-ray Absorption Spectroscopy is broad, and this technique comes in many flavors and with many names. These flavors can be distinguished by what kind of information from which part of the absorption spectrum they have been extracted. Commonly used terms are X-ray Absorption Fine Structure (XAFS), Extended X-ray Absorption Fine Structure (EXAFS), X-ray Absorption Near Edge Structure (XANES), as well as Near Edge X-ray Absorption Fine Structure (NEXAFS). In this work, I investigate the SEI on silicon anodes based on its X-ray absorption fine structure (XAFS) around the ionization edges of oxygen and fluorine (K-edge) as well as of silicon (L-edge). All ionization edges of interest, oxygen, fluorine, and silicon, lie in the soft X-ray regime between 100 and 1500 eV. For simplicity, throughout this work I will refer to it as sXAS where the "s" denotes the soft X-ray regime. An EXAFS study, which examines the interference of the outgoing photoelectrons is not part of this investigation.

II.A Interaction of X-ray Radiation with Matter

There are three fundamental types of interaction between X-ray radiation and matter: elastic and inelastic scattering as well as absorption [177]. In the process of elastic scattering, coming from a classical point of view, an incoming photon with angular frequency $\omega = 2\pi f$ and wave vector $\vec{k}$ makes the sample's electrons (bound to an atom) oscillate. In turn, the oscillating electrons emit a secondary wave field with the same ω but different $\vec{k}$. In case of inelastic scattering, ω changes to lower frequency, as part of the incoming photon's energy is transferred to the sample's electrons, exciting them to higher energetic states. However, in sXAS we are interested in the third kind of interaction: absorption. Here, in contrast to inelastic scattering, the incoming photon's energy is fully transferred to an electron. The electron is excited from a lower into a higher energetic state and the photon is consumed, thus absorbed, in the process.

From a quantum dynamics point of view, the absorption process can be described by the electron's transition from an initial state $|i\rangle$ into a final state $|f\rangle$, driven by the incoming photon as a harmonic time-dependent perturbation $V(t) = \bar{V}e^{-i\omega t}$. The probability per unit time P_{if} of this transition is given by Fermi's "Golden Rule" as described in (3), where $\rho_f(E)$ is the energy density of final states and $\hbar$ the Planck's constant [178].

$$P_{if} = \frac{2\pi}{\hbar}|\langle f|\bar{V}|i\rangle|^2\rho_f(E) \quad (3)$$

While P_{if} is an abstract quantity, the X-ray absorption event is more precisely described by the so-called X-ray absorption cross section σ_x. It describes the number of electrons excited per unit time divided by the number of incident photons per unit time per unit area, and based on this, it has a unit of area. Applying the dipole approximation, σ_x is given by (4) with the unit vector $\boldsymbol{e}$, the sum of the linear momentum operators of the electrons $\boldsymbol{p}$ as well as the electron's charge and mass e and m [178].

$$\sigma_x = \frac{4\pi^2\hbar^2}{m^2}\frac{e^2}{\hbar c}\frac{1}{\hbar\omega}|\langle f|\boldsymbol{e}\cdot\boldsymbol{p}|i\rangle|^2\rho_f(E) \quad (4)$$

Albeit in quantum mechanics a state is considered observable, while an orbital is a theoretical construct [178], in the following I will use both terms interchangeably for simplicity. As it can be seen from (4), the X-ray absorption cross section is a function of the photon energy but also of the initial $|i\rangle$ and final state $|f\rangle$. The X-ray absorption cross section as a function of photon energy, which is simply an XAS spectrum, is experimentally accessible as I will discuss in more detail later. When the photon's energy matches the transition energy, it can resonantly excite an electron from an occupied into an unoccupied orbital. For this specific energy the X-ray absorption cross section rises intensively, which results in a peak in the XAS spectrum. From the position of the absorption peak, the corresponding electronic transition can then be deduced. This represents the foundation of XAS.

In the notation of XAS, the initial state at the K-edge corresponds to an electron in the 1s orbital, at the L-edge to the 2s (L_I) and 2p (L_{II}) orbitals. Further, at the K-edge the ionization potential (IP) plays an important role. The IP is the energy threshold necessary for the excitation of an electron from the 1s orbital into a continuum state. This energy threshold is element specific and is represented by a sudden step in the absorption cross section. However, the ionization step is always superimposed by bound and unbound states before and after the step itself. The bound states commonly correspond to Rydberg orbitals which are natural solutions of the Schrödinger equation and who's binding energies converge to the ionization potential (compare Figure 17) [178], [179]. More importantly, however, these bound and unbound states may also correspond to molecular antibonding orbitals [179]. Figure 17 illustrates this for a diatomic molecule with π-bonding, where unoccupied antibonding π^*- and σ^*-orbitals are found closely below and above the vacuum level, respectively. These orbitals give rise to 1s to π^* and 1s to σ^* resonances which can be found as two separate sets of peaks in the XAS spectrum before and after the ionization step, as shown in Figure 17c. In summary, based on (4), XAS probes the unoccupied electronic states. Given the sensitivity of the unoccupied valence states to their chemical surrounding, XAS has proven itself as

capable, element-specific probe of the intra- and intermolecular chemical environment of the targeted atom species.

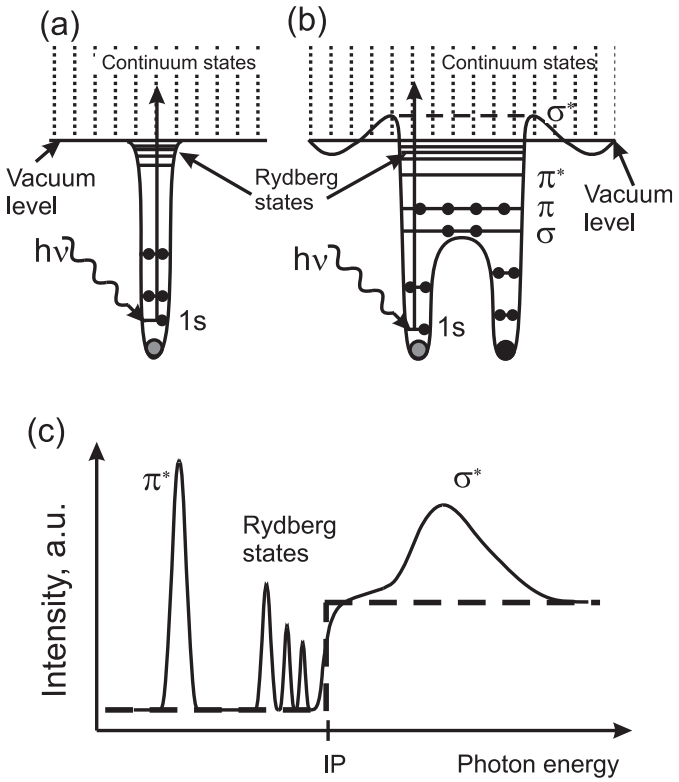

Figure 17 (a) Illustration of potential well with energy states from an isolated atom. (b) Illustration of potential well with energy states from a diatomic molecule with π-bonding. Unoccupied antibonding π- and σ*-orbitals are present slightly below and above vacuum level, which give rise to 1s to π* and 1s to σ* resonances. (c) Schematic XAS absorption spectrum (X-ray absorption cross section as function of photon energy) from a diatomic molecule as sketched in (b). The IP corresponds to a step-like increase in absorption cross section as marked by the dashed line. The ionization step is superimposed by the peaks corresponding to Rydberg states as well as 1s to π* and 1s to σ* transitions. The image is sourced from [179].*

In this regard, I want to briefly highlight an example that sets the stage for the sXAS investigation of the SEI on silicon anodes presented in this work. The SEI is a reduction product of the organic battery electrolyte. The resonances from 1s to unoccupied antibonding orbitals arise from molecular subgroups, too. This is particularly important for organic molecules, where different functional groups can be identified based on their individual resonances. On top of that, the resonances of each functional group experience a certain shift in energy based on its chemical backbone. To give an example, Urquhart and Ade investigated the 1s to π^* resonance of the carbonyl functional group in different polymers. As it is summarized in Figure 18, depending on the chemical backbone of each polymer's repeating unit, the carbonyl 1s to π^* resonance varies by about 2 eV at the oxygen K-edge and by about 4 eV at the carbon K-edge (see Figure 18c). In my work I used 1M $LiPF_6$ in EC:DMC as the model electrolyte and both EC as well as DMC contain a carbonyl group. This illustrates how resonances in XAS may be used to investigate the reduction of the organic electrolyte and SEI's formation during battery operation. It also demonstrates that every molecule, and even

every functional group on its own, has its specific X-ray absorption fine structure fingerprint. The goal of this work is to investigate the SEI on silicon anodes via sXAS. I will derive the SEI's chemical composition by comparing its own spectral fingerprint to the fingerprints of various reference species. To do so, however, I first want to discuss how these fingerprints, or XAS spectra in general, can be obtained experimentally.

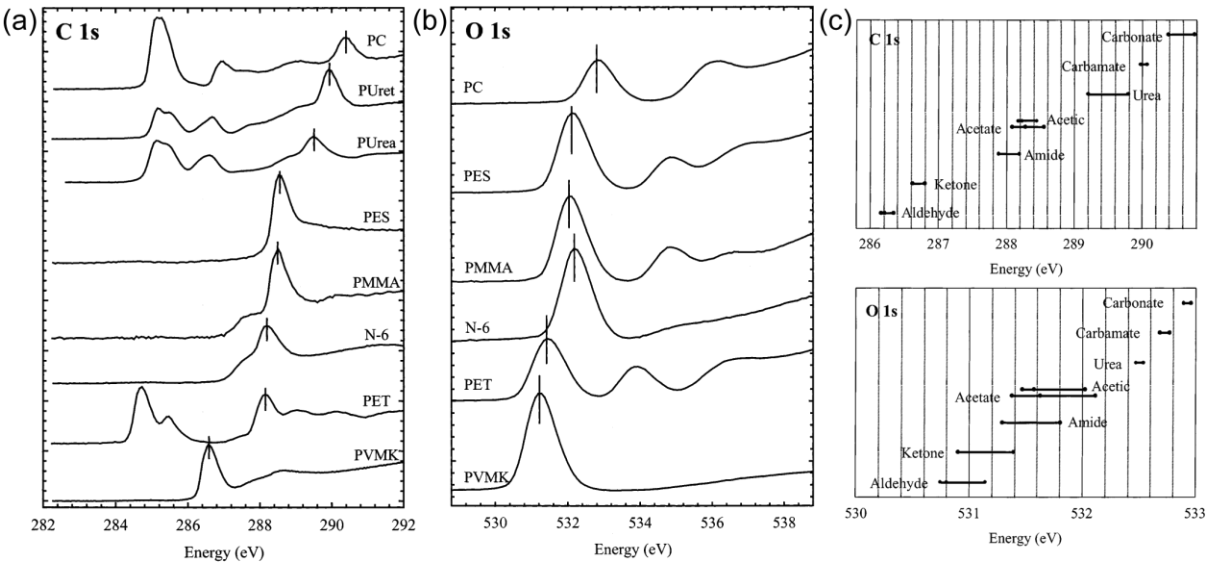

Figure 18 (a)-(b) sXAS spectra at the carbon and oxygen K-edge of polycarbonate (PC), polyurethane (PUret), polyurea (PUrea), poly(ethylene succinate) (PES), poly(methyl methacrylate) (PMMA), nylon-6 (N6), poly(ethylene terephthalate) (PET) and poly(vinyl methyl ketone) (PVMK). The 1s to π^* resonance of the carbonyl functional group is marked with a vertical line. (c) Expected energies of the 1s to π^* resonance from the carbonyl functional group for different molecular backbones at the oxygen and carbon K-edge. All images are sourced from [180].

II.B Transmission, Electron and Fluorescent Yield Measurements of X-ray Absorption: Principle, Limitations and the "Thickness Effect"

As the incoming X-ray photons are fully consumed in an absorption event, the most straight-forward way to determine the X-ray absorption cross section is to measure how strongly a sample attenuates an incoming beam of photons, i.e., to determine the ratio between incoming and outcoming intensity in a transmission geometry. One finds experimentally for a sample with density ρ that the transmitted intensity decreases incrementally by ΔI relative to the incoming intensity I_0 for incremental increases of the sample thickness by Δx. This correlation is described by (5), where $\mu(E,Z)$ is the photon energy E- and material Z-dependent mass absorption coefficient. With the differential limits $\Delta I \rightarrow dI$ and $\Delta x \rightarrow dx$, (5) integrates into the exponential form (13). While (6) is a macroscopic description of the attenuation phenomenon, it can also be written as (14) with the atomic density n_a. This relates the macroscopic attenuation back to the microscopic X-ray absorption cross section σ_x from (4). Thus, the micro- and macroscopic view of the absorption coefficient is related through $\mu = \sigma_x / A m_u$, where A is the number of atomic mass units and m_u is an atomic mass unit itself [181]. Figure

19 illustrates the micro- and macroscopic view of the absorption by comparing the absorption of a copper foil (Figure 19a-b) to the absorption of a single copper atom (Figure 19c-d) at its L-edge. Figure 19d also nicely illustrates how the absorption coefficient that is obtained experimentally by measuring I/I_0 in transmission is always a convolution of all individual transitions. Furthermore, the measured absorption coefficient also contains contributions from in-/elastic scattering. However, the X-ray absorption cross section σ_x is dominant in the energy range of sXAS and scattering is negligible [177].

$$\frac{\Delta I}{I_0} = -\rho\mu(E,Z)\Delta x \tag{5}$$

$$\frac{I}{I_0} = e^{-\rho\mu x} \tag{6}$$

$$\frac{I}{I_0} = e^{-n_a\sigma_x x} \tag{7}$$

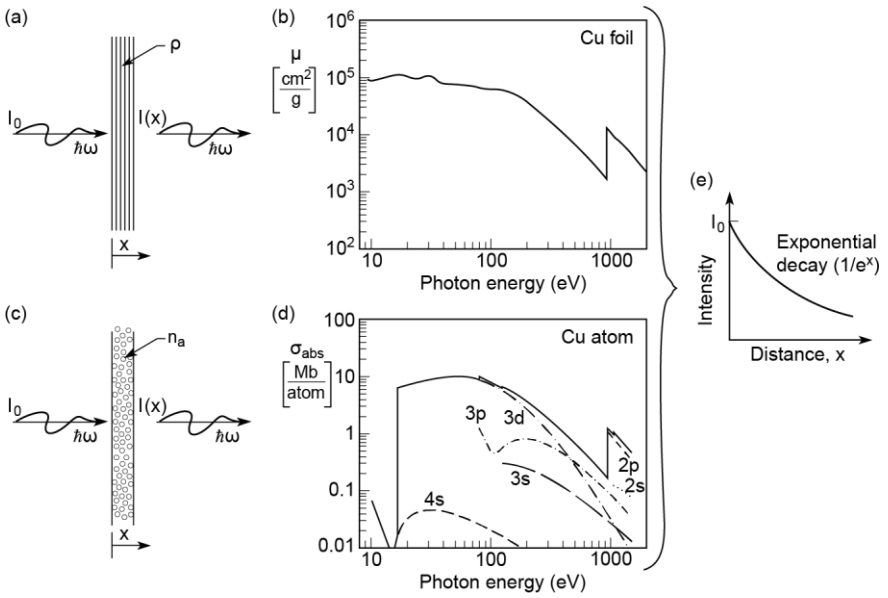

Figure 19 Illustration of the micro- and macroscopic view of the absorption by comparing the absorption of a copper foil (a-b) to the absorption of a single copper atom (c-d) at its L-edge. (e) Experimentally observed exponential decay of the incoming beam intensity in transmission. The image is sourced from [181].

While the measurement principle of transmission appears simple at first glance, the devil is in the detail. Speaking in terms of experimental feasibility, in the soft X-ray regime, the devil comes as an extremely high X-ray absorption coefficient. To give a few examples, the X-ray attenuation length, that is the thickness where I drops to $1/e$ of I_0, at 100 eV is 63 nm for silicon, 22 nm for iron and 190 nm for carbon as well as 105 µm for O_2 and 177 µm for N_2 at 1 atm [181], [182]. This makes transmission XAS in the soft X-ray regime only applicable for thin-film samples and puts strong constraints on the setup when it comes to *in-situ* and *operando* experiments. The values for O_2 and N_2 also make clear that soft X-ray absorption

experiments are commonly performed in vacuum. However, the attenuation length of helium at 500 eV is about 10 cm, which gives some leeway for some experimental techniques as we will see later.

Given the strong constraint on the sample thickness for a transmission experiment, the soft X-ray absorption is more commonly measured through secondary processes. After the absorption of an X-ray photon and the excitation of a core electron to a higher energetic state, the atom is left with a core vacancy. This excited, energetically unstable state is then relaxed through the following two competing processes [181]. First, another electron is pulled by the strong nuclear potential from a higher orbital into the core hole and emits a photon with a specific energy that matches the energy difference between its initial and final (the core hole) state, as illustrated in Figure 20a. This process is called X-ray fluorescence. Second, the core hole is filled by an electron from a higher-lying orbital, but in the process a so-called Auger electron instead of a photon is emitted, which is shown in Figure 20b. As with the fluorescent emission, the emitted Auger electron's energy is specific for its transition. The respective yield of both processes strongly depends on the atomic number Z. As it can be seen in Figure 20c for the K- and L_{III}-orbitals, the non-radiative Auger process is favored for low-Z elements, while fluorescent emission of radiation is dominant in high-Z atoms.

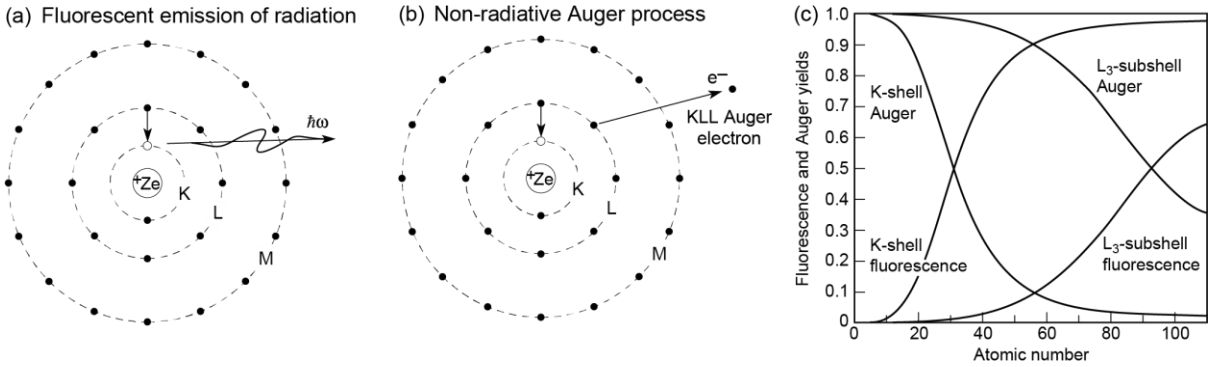

Figure 20 (a) Illustration of the relaxation through fluorescent emission of radiation. (b) Illustration of the relaxation through the non-radiative emission of an Auger electron. (c) Fluorescence and Auger yields as function of atomic number at the K- and L_3-shell. The figure is adapted from [181].

Disregarding their respective yields, both processes are still proportional to the initial absorption event and can be used as a measurement thereof. Depending on the measured quantity, one distinguishes between (photon in/electron out) electron yield (EY), and (photon in/photon out) fluorescent yield (FY) techniques. As discussed above, the fluorescent photons and Auger electrons have characteristic energies given their specific transitions. If the photons and electrons are measured by energy-dispersive means the technique is labelled as a partial (PFY and PEY), when the energy is not resolved as total measurement (TFY and TEY). Albeit this work focuses on transmission sXAS, I still want to briefly summarize the experimental implementations and characteristics of FY and EY measurements in the soft X-ray regime.

Without focusing too much on their shortcomings, I want to motivate the application of my novel transmission sXAS approach, which I will introduce in chapter III.

In the emergence of XAS, fluorescent detection was carried out by liquid nitrogen-cooled solid-state detectors, but most experiments moved on to the much easier to handle semiconductor photodiodes later. In comparison to the solid-state detectors, photodiodes do not offer energy resolution and only allow TFY measurements. However, for low-Z elements, the Achilles' heel of every FY technique is the low signal-to-noise ratio given the extremely low signal strength due to the low fluorescent yield, as seen in Figure 20c. To put this into perspective, the quantum yield of carbon at its K-edge was found to be only $2.8 \cdot 10^{-3}$ [183], [184]. In practice, this often demands high beam intensities and long counting times, making beam damage to the sample a considerable concern. On top of that, the evaluation of FY spectra is intricate as they are very often distorted by several effects. The most intrinsic one is the transition-dependence of the quantum yield itself. This might distort the obtained spectra in favor of spectral features correlating to a transition with a higher fluorescent yield. In general, the measured fluorescence signal does not directly correlate to the absorption cross section and the spectral shape needs to be corrected through the individual fluorescence yield of each transition [185]. From a more practical point of view, FY spectra may suffer from saturation and self-absorption effects, especially for highly concentrated samples. The fluorescent photons are of lower energy than the incoming beam. Thus, at the absorption edge, being off-resonant, the attenuation length of the fluorescent photons is much larger (they are less absorbed) compared to the incoming photons. If there is only little background absorption, that is the absorption through other elements, as it is the case for highly concentrated samples, scanning through the absorption edge would yield a significantly distorted spectrum. This effect is called saturation. Thus, to avoid saturation, the effect of the edge absorption needs to be much smaller than the background absorption, which is only the case for dilute samples. [185]–[187]. For highly concentrated samples, similar distortions can occur when the fluorescent photons are reabsorbed by the sample itself and cannot escape to the detector. This effect is commonly referred to as self-absorption.

EY measurements are commonly performed with an electron analyzer which allows for energy resolution (PEY), or simply by putting an electrode (under positive bias to collect the electrons) close to the sample (TEY). Another simple implementation of TEY is the measurement of the drain current. Here, the sample is grounded and the drain current through the photoionization is measured with a pico-amperemeter [183], [186]. In all cases, however, the Auger electrons need to escape the sample to reach the detector or induce a drain current. This has two important implications. First, given the very shallow electron escape depth of only a few nanometers, EY methods are commonly considered to be surface-sensitive, and the obtained

spectra differ from their bulk (e.g. obtained from transmission) counterparts [186]. It must be noted that the escape depth is different from the electron mean free path [183], which is only tens of angstroms. The initial Auger electron can induce a cascade of scattering events and secondary electrons still can reach and escape the surface over a much larger distance, albeit with lower energy. This effect can be exploited in PEY measurements. In electrode-based TEY measurements applying a certain bias rejects electrons with too little energy after too many scattering events and narrows the TEY signal to the surface. Besides all this, when it comes to *in-situ* and *operando* investigations, the sample is required to be surrounded by matter, e.g. the battery electrode inside the electrolyte or a catalyst inside a solution. Thus, the shallow escape depth of electrons makes EY measurements in most cases infeasible for this type of experiment. However, it must be mentioned that it was demonstrated by Schön *et al.* that the surface in contact with a solution can be probed by detecting the ions which are created by the escaping electrons [188]. However, this method cannot be combined with electrochemical processes as the EY currents (in the range of pA) tend to be overshadowed by the much larger galvanic currents (µA to mA).

While free of self-absorption and saturation effects, the spectral shape obtained from transmission XAS measurements still depends on the sample thickness. This was first described by Parratt *et al.* in 1957, and it was named the “Thickness Effect” [189]–[193]. This effect was initially attributed to the spectral window of the detector, which leaks flux with higher and lower energy compared to the set photon energy [189]. Parratt *et al.* explained this effect for a two-crystal X-ray spectrometer paired with a continuous X-ray source. The sXAS measurements in the experimental part of this work were conducted using a non-energy-dispersive photodiode paired with monochromatized synchrotron radiation. Albeit the monochromatizating happens before the transmission event instead of after, I consider both cases analogous when the spectral window of the detector, as described for Parratt *et al.*’s case, is replaced by the energy distribution (e.g., Gaussian or Lorentzian) of the monochromatized incoming beam [194]. With the non-energy dispersive photodiode, the leaking flux is indistinguishable from photons of only the set photon energy. Thus, as illustrated in Figure 21a, the signal $D(\nu_S)$, which is measured by the photodiode at a set photon energy ν_S, is always a convolution of the true transmission function of the sample T and the energy distribution of the incoming beam B, as described through (28) in analogy to Parratt *et al.*’s first formulation [189]. Besides this, the following other sources of leaking flux, that is flux not as strongly attenuated in the sample as expected, can be identified [193]. For undulator radiation (described in more detail in II.C) the energy spectrum of the incoming beam B may also contain contributions of higher harmonics at energies ν_H with lower absorption $\mu(\nu_H) < \mu(\nu_S)$. Besides this, although not created through a photon flux, the dark current of the diode

D_{Dark} is measured as such and contributes a baseline leakage to $D(\nu_{\mathrm{s}})$. On top of that, an inhomogeneous sample thickness and pinholes can cause leakage of unattenuated photon flux. Thus, in the recorded absorption spectrum, the convolution with the leaking flux leads to a “washing out” of the maxima and minima and is notably dominant in the vicinity of absorption peaks and valleys. The ratio between the leaking flux and the actual true sample attenuation depends on the sample thickness. Consequently, the “Thickness Effect” is more pronounced for thicker samples as shown in Figure 21. As proposed by Parratt *et al.*, the degree of “washing out” can be quantified based on the ratio between spectral features, e.g., the ratio between peaks and valleys, like A, B, α or γ in Figure 21a,b. As shown in Figure 21c, for thinner samples these ratios converge towards a value that resembles the true spectral shape of an infinite thin sample. However, I want to note that using a non-energy dispersive diode is no shortcoming of the experiment as there are no detectors and monochromators with infinite resolution, making the “Thickness Effect” experimentally unavoidable. With synchrotron radiation, relying on the resolving power of the beamline monochromator appears adequate.

$$D(\nu_{\mathrm{s}}) = D_{\mathrm{Dark}} + \int_0^{\infty} T(\nu) \cdot B(\nu_{\mathrm{s}} - \nu)\, d\nu \tag{8}$$

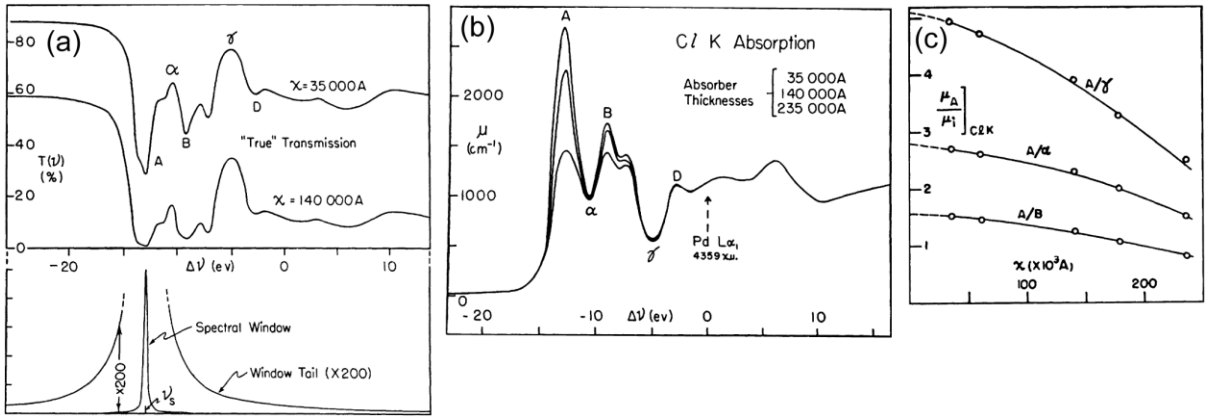

Figure 21 Summary of the “Thickness Effect” as described by Parratt et al. [189]. (a) Upper-half: absorption spectra of potassium chloride at the chlorine K-edge for sample thickness of 14 µm and 3.5 µm. Lower-half: schematic of the spectral window of the monochromator. The window’s tail is partly enlarged by 200 times to show how leaked flux convolutes with adjacent peaks and valleys. (b) Demonstration of the influence of sample thickness on the spectral shape: absorption spectra of potassium chloride at the chlorine K-edge for a sample thickness of 23.5 µm, 14 µm and 3.5 µm. (c) Ratio between spectral features marked in (a) and (b) as a function of absorber thickness. All images are sourced from [189].

To summarize, the attenuation of an incoming X-ray beam when transmitting the sample is the most straight-forward measurement of the X-ray absorption. The measurement performed in transmission can be considered a true transmission spectrum. However, in the soft X-ray regime, the small attenuation length puts strong constraints on the experiment and limits transmission measurements to thin-film samples. EY and FY techniques avoid this limitation by inferring the absorption event from its subsequent relaxation processes, namely fluorescent

emission of radiation or non-radiation ejection of Auger electrons. However, FY techniques may suffer from spectral distortions from saturation and self-absorption effects. Moreover, the low fluorescent yields at the K-edge of low-Z elements often require high beam intensities and long counting times, making beam damage a considerable concern. Furthermore, as photon in/electron out technique, EY measurements tend to be infeasible for *in-situ* and *operando* experiments, due to the low escape depths of electrons. Given the drawbacks of FY and EY, in the last two decades there has been extensive efforts towards ingenious *in-situ* and *operando* transmission techniques. In II.D, I will first introduce some notable examples and then finally present my own novel technique for *in-situ* transmission sXAS in III. Beforehand, however, I want to discuss what all these techniques have in common: the X-ray source, namely the synchrotron radiation.

II.C Synchrotron Radiation for X-ray Absorption Spectroscopy

Charged particles emit electromagnetic radiation when accelerated. When oscillating with non-relativistic speeds, the radiation pattern has a toroidal shape. But, when moving at relativistic velocities, relativistic length contraction and time dilation change the emission pattern to a narrow radiation cone tangent to the particle's path, which is referred to as the searchlight effect. Simply put, synchrotron radiation refers to the radiation emitted by relativistic charged particles (most commonly, and treated as such in the following: electrons) when accelerated in magnetic fields [177], [181].

Given its nature, synchrotron radiation was first observed in 1949 as a side effect in large-scale particle accelerators for high energy physics [195]. Bending dipole magnets were used to control the beam's trajectory where the relativistic charged particles produced the first synchrotron radiation. Thus, the early-stage synchrotron light sources of the first generation where simply parasitic ports in existing storage rings, which "recycled" the otherwise lost radiation. Due to the scientific success of these early experiments, storage rings exclusively dedicated to synchrotron radiation were constructed. These facilities, in hindsight referred to as second generation synchrotrons, were simple circular rings with bending magnets as radiation sources. The third, and most recent generation of synchrotrons' storage rings are shaped like a polygon with rounded corners (fitted with bending magnets). On top of that, so called insertion devices, namely wigglers and undulators, are inserted into the straight sections of the polygonal storage ring to explicitly create the synchrotron radiation [177], [181]. The experimental part of this work was conducted at the undulator beamlines U49-2_PGM-1 [194] and UE56-2_PGM-2 beamlines at the third-generation synchrotron facility BESSY II in Berlin. In the following, I will briefly describe BESSY II, the basic principle of undulator radiation and the setup of both used beamlines.

Like most third-generation synchrotrons, BESSY II consists of a linear accelerator, a booster synchrotron, and the storage ring itself, as illustrated in Figure 22a. Electron bunches are created by a hot-cathode electron gun and are pre-accelerated up to 50 MeV by the linear accelerator. The bunches are then transferred into the booster synchrotron (96 m circumference) to be brought up to their relativistic speeds with a target energy of 1.7 GeV by multiple synchronized dipoles. Finally, the relativistic electron bunches are injected into the storage ring (240 m circumference), where they pass through the insertion devices to emit synchrotron radiation into the, at the time of this writing, 38 beamlines. The energy emitted through synchrotron radiation is replenished by radio frequency cavities spread around the storage ring.

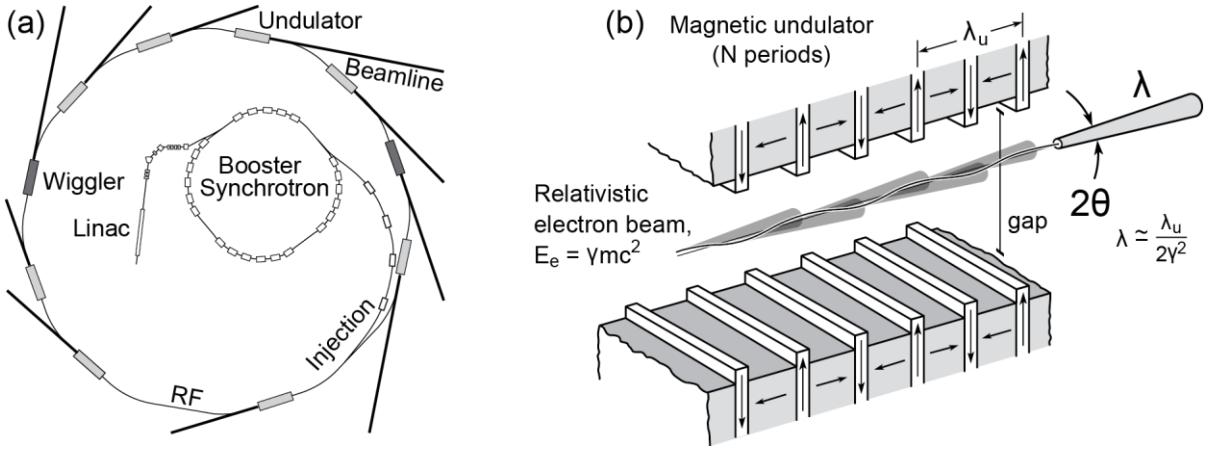

Figure 22 (a) Overview of a third-generation synchrotron facility. (b) Schematic working principle of an undulator. The figures are adapted from [181].

The insertion device of choice for soft X-ray radiation are undulators. An undulator is an array of magnet pairs with alternating orientation separated by a gap, which the electrons pass through. The alternating magnetic field induces a force that sends the electrons on an oscillating, sinusoidal trajectory, perpendicular to the magnetic field and the beams direction. At each bend, the relativistic electrons emit synchrotron radiation in tangential direction in a narrow cone. The half angle of this radiation cone is given by $\theta_{\mathrm{Cone}} = \frac{1}{2\gamma}$ with the Lorentz factor $\gamma = \frac{1}{\sqrt{1-\beta^2}}$ and $\beta = \frac{v}{c}$ as the ratio of the electron velocity v to the speed of light c [181]. When the angular excursion of the electrons inside the undulator's alternating magnetic field is smaller than the cone's half angle, the radiation cones of each bend interfere constructively. The amplified wavelength λ is given by the so called undulator equation (9) with the magnet period λ_u, the order/harmonic of the constructive interference n, the dimensionless undulator parameter K and the angle off-axis θ. The undulator parameter K is calculated through (9), with the elemental charge e, the magnetic field strength B_0, the mass of an electron m and the speed of light c. From (9) it is apparent that the amplified wavelength λ emerges through a

reduction of the magnet period λ_u by a factor of $2\gamma^2$ through Lorentz contraction and the relativistic Doppler shift [177], [181]. The basic principle of an undulator is illustrated in Figure 22b.

$$\lambda = \frac{\lambda_u}{2\gamma^2 n}\left(1 + \frac{K^2}{2} + \gamma^2\theta^2\right) \quad (9)$$

$$\mathrm{K} = \frac{eB_0\lambda_u}{2\pi mc} \quad (10)$$

Equation (15) and (16) make it obvious why synchrotron radiation from an undulator is so desirable for sXAS experiments. With $\lambda(\gamma, \lambda_u, B_0)$, the wavelength can be chosen freely through three experimental parameters, γ (given by the energy of electrons inside the storage ring $E_e = \gamma mc^2$), λ_u and B_0. The first two, γ and λ_u, can be considered design parameters for the construction of the storage ring and the undulator itself. For this reason, over the last decades, spread around the world, many synchrotron facilities came into operation with different energies to cover all experimental needs. To give two examples: BESSY II in Germany with 1.7 GeV and a focus on soft X-ray radiation or Spring-8 in Japan with 8 GeV for hard X-rays. Further, for a given γ at a particular facility, undulators with different magnetic periods λ_u can be inserted to offer beamlines with radiation from the extreme ultraviolet (EUV) regime over soft X-rays to hard X-rays. Most importantly, however, is the magnetic field strength B_0. While variable field strength undulators are possible, most undulators are built with permanent magnets. Albeit only to a certain degree, the magnetic field strength B_0, can still be changed “on the fly” by changing the vertical gap between the two magnetic arrays. With this, the energy of the emitted undulator radiation can be changed continuously. This makes it ideal for XAS as the radiation can be used to scan over an absorption edge. Furthermore, without going into details about the undulator beam’s optics, what sets synchrotron radiation apart and makes it even more desirable for XAS, is its extraordinarily high brilliance. Brilliance describes the number of photons per second per source area in mm^2 per source angular divergence in $mrad^2$. To put it simple, an undulator emits a large number of photons from a small source size under a small angular divergence. This makes collecting, forming, and focusing the beam through slits, mirrors, and monochromators easier and allows high energy and spatial resolution without severely diminishing the photon flux. The series of slits, mirrors, and monochromators between the undulator and the actual experiment / sample is commonly referred to as a beamline. The properties and characteristics of the undulators and beamlines used in the experimental part of this work are summarized in the following. For a detailed description of the beam optics, particularly in the soft X-ray regime, I refer to the work of Attwood [181].

The U49-2_PGM-1 [194] beamline uses the U49/2 undulator of BESSY II, which has a magnetic periodicity of 49.4 mm over 84 magnetic periods and a minimal gap of 16 mm. With this, U49/2 offers linear horizontally polarized light with photon energies down to 84.4 eV at 1.7 GeV ring energy [196]. The beamline utilizes a plain grating monochromator for the available energy range 85 to 1600 eV with 0.4 and 0.2 mrad horizontal and vertical divergence, respectively. The focal size can be controlled via the slit size setting and ranges between 25 to 105 µm in vertical and 85 to 110 µm in horizontal direction [197]. The micro spot size was essential for the *in-situ* investigation of the SEI on silicon anodes presented later in IV, as it allowed to pick fresh probing spots from the sample (square with side length 500 µm) for every XAS measurement to avoid beam damage artifacts. The optical layout and the photon flux of the U49-2_PGM-1 beamline is shown in Figure 23.

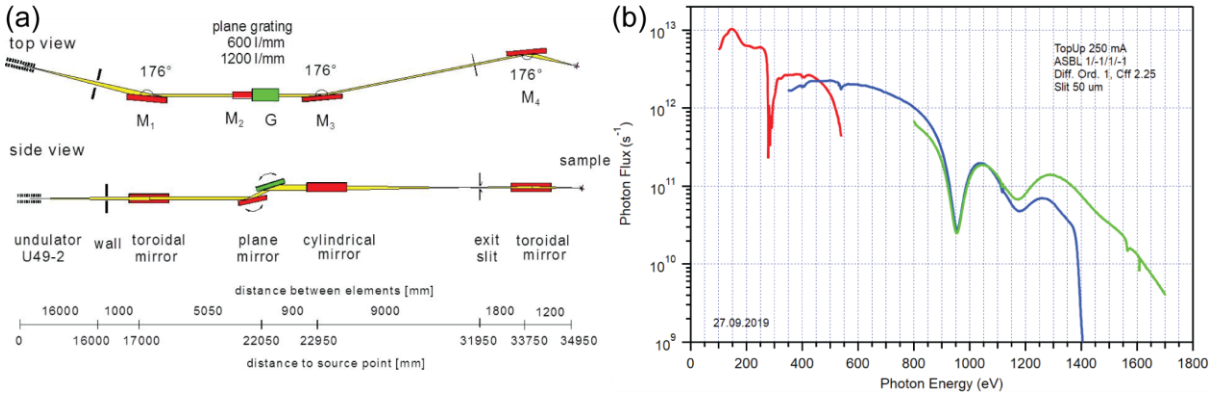

Figure 23 (a) Optical layout of the U49-2_PGM-1 beamline at the BESSY II synchrotron facility in Berlin. The schematic is sourced from [194]. (b) Available photon fluxes at the U49-2_PGM-1 beamline. The plot is sourced from [197].

The UE56-2_PGM-2 beamline uses the UE56/2 undulator of BESSY II, which has a magnetic periodicity of 56 mm over 30 magnetic periods and a minimal gap of 16.5 mm. The UE56/2 offers linear horizontally, vertically, elliptical and circular polarized light with photon energies down to 60.5 eV at 1.7 GeV ring energy [198]. The beamline utilizes a plain grating monochromator for the available energy range 60 to 1300 eV with 1 mrad horizontal and vertical divergence [199]. The horizontal focus size is 900 µm. Give the windows' side length of only 500 µm, this spot size is too large for the *in-situ* investigation of the SEI on silicon anodes presented later in IV. Thus, the UE56-2_PGM-2 beamline was only used for reference measurements of powder compounds.

II.D Current *In-situ* and *Operando* Transmission Soft X-ray Absorption Spectroscopy Approaches and Silicon Nitride Window Technology

Given the drawbacks of FY and EY measurements discussed in II.B, in the last decade ingenious techniques for *in-situ* and *operando* investigation of materials through transmission

XAS in the soft X-ray regime have been developed. For many applications, e.g., batteries or catalysts, both *in-situ* as well as *operando* techniques require the material under investigation to be in contact with a liquid or electrolyte. Thus, the development of these techniques started out solely with transmission XAS of liquids. Later, they were adapted to include thin-film materials for *in-situ* and *operando* experiments. As discussed earlier, sXAS requires vacuum conditions as the X-ray attenuation length of air is only a few hundreds of micrometers. Thus, ionic liquids aside, most conventional liquids must be isolated from the vacuum given their high vapor pressure. For the soft X-ray regime, this became possible with the development of soft X-ray-transparent, ultra-thin, freestanding silicon nitride SiN_x membranes. Consequently, to my knowledge, cell-based sXAS techniques for liquids rely almost exclusively on some form of SiN_x windows. Although liquid flatjet systems are another ingenious approach towards transmission sXAS on liquids [200]–[202], given the lack of any solid/liquid interface, I consider them not adaptable to *in-situ* or *operando* experiments on thin-film and they are not discussed any further.

SiN_x membrane windows are manufactured from standard silicon wafers through low-pressure chemical vapor deposition and standard lithography micromanufacturing (see Figure 24a). For most applications, the freestanding membrane remains attached to the silicon frame after the final patterning etching step as shown in Figure 24c. All involved manufacturing steps are standard in the industry, by now SiN_x membrane windows are commercially available from many different vendors. The windows commonly used for sXAS are amorphous, non-stoichiometric (hence SiN_x, not Si_3N_4) and silicon-rich. The amorphous structure determines the residual stress, which gives SiN_x its outstanding mechanical properties. The SiN_x membranes can be manufactured with thicknesses commonly ranging from 10 to 200 nm. The freestanding membrane windows are rectangular or square-shaped, with side lengths from 100 µm up to even 2 mm. Albeit depending on window dimensions, membranes thinner than 100 nm can already withstand cross-membrane pressure differences larger than 1 atm. This makes SiN_x membranes an ideal window material for sXAS. The transmission of SiN_x windows from 0 to 2 KeV photon energy with 10, 100 and 1000 nm thickness is shown in Figure 24b. For a more in-depth summary of SiN_x membrane window technology I refer to the work of Dwyer and Harb [203].

With soft X-ray transparent SiN_x windows at hand, Nagasaka *et al.* introduced their ingenious implementation in 2010 [204]. Their cell for transmission sXAS of liquids features a layer stack of two SiN_x membranes separated by a 20 µm thick Teflon spacer sheet. The membranes and the Teflon spacer form a channel where the liquid is pushed through by a tubing pump system. The membranes are sealed by two rubber O-rings on top of each silicon frame and their initial distance can be adjusted by squeezing the Teflon spacer through a certain clamping pressure

(1 µm in the presented study). Additionally, the cell is placed in a helium atmosphere. As mentioned earlier, the helium's X-ray absorption length in the soft X-ray regime is about 10 cm, which gives leeway to the vacuum requirement. Then, by adjusting the helium pressure, the membrane windows (square, 2 mm side length) bulge towards each other, reducing the thickness of the liquid layer in-between. Nagasaka *et al.* found the degree of bulging to be about 10 nm/Pa at the membrane's center, allowing them to achieve liquid layers of variable thickness between 100 and 800 nm. The liquid film between the membranes was sufficiently X-ray transparent to obtain high resolution transmission sXAS. The transmitted X-ray was measured by placing a photodiode inside the helium chamber.

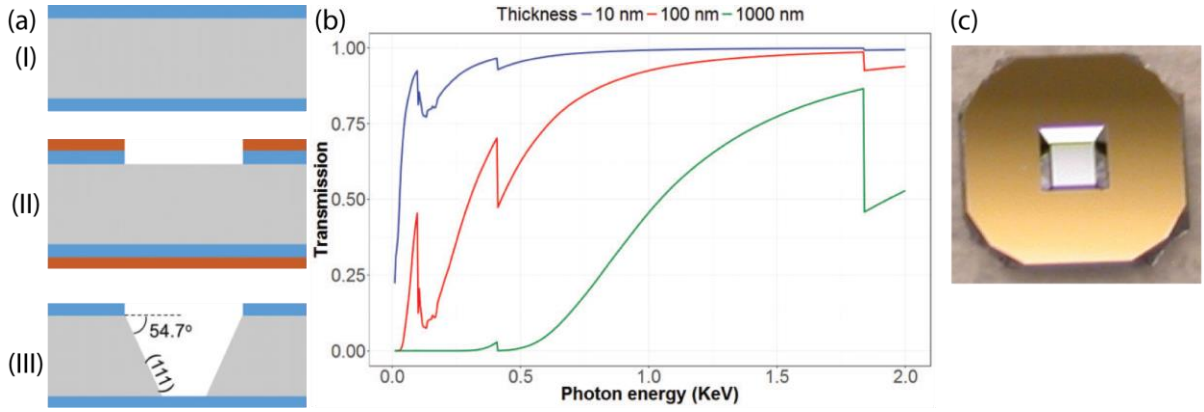

Figure 24 (a) Lithography micromanufacturing process of SiN_x membrane windows. (I) Non-stoichiometric (silicon-rich) SiN_x (blue) is deposited onto a silicon wafer (grey) via low-pressure chemical vapor deposition. (II) The window geometry is patterned via standard photoresist (orange) through reactive iron etching. (III) The freestanding SiN_x membrane is created by etching the silicon wafer with potassium hydroxide. For most applications the freestanding membrane remains attached to the silicon wafer as shown in the picture in (c). The schematic is adapted from [203] (b) Transmission of SiN_x membrane windows from up to 2 KeV photon energy for 10, 100, and 1000 nm thickness. The plot is sourced from [203] (c) Picture of a SiN_x membrane window. The silicon frame has a diameter of 3 mm and the square freestanding membrane window with 500 µm side length sits in the middle. The 54.7° chamfer from the potassium hydroxide etching process is clearly visible as marked in (a). The image is taken from [205].

Schreck *et al.* introduced a similar implementation shortly after in 2011, utilizing in-house custom made silicon nitride windows together with rigid gold spacer of 500 nm thickness [206]. Their sample holder is placed inside the vacuum of the experimental beamline station, where the membranes bulge outwards given the pressure difference between vacuum outside and the atmospheric pressure inside the sample holder. Thus, the differential pressure, and with this the bulging and the thickness of the liquid layer, is fine-tuned by refilling the chamber with helium by some tens of mbar. With their sample holder, Schreck *et al.* demonstrated liquid films with variable thickness starting at the spacer's thickness of 500 nm up to several micrometer.

Finally, in 2016, Schwanke *et al.* extended Nagasaka *et al.*'s method to allow electrochemical *operando* studies by adding counter- and reference electrodes to the liquid cell [207]. Additionally, one SiN_x membrane is used as substrate for a thin-film sample, commonly

prepared by means of sputtering, CVD, or electrodeposition. By electrically contacting the sample via an underlying gold layer, the sample thin-film then acts as the working-electrode in a three-electrode setup. In their proof-of-concept study, at the manganese L-edge (635 to 660 eV photon energy), they showed the change in oxidation state of an MnO_x thin-film under varying potentials.

In summary, cell-based methods for transmission sXAS exclusively rely on a sandwich of two soft X-ray transparent SiN_x membrane windows, which encapsulate a thin liquid layer. The thickness of liquid layer is controlled by the thickness of spacer separating both layers and through the differential pressure between the inside of the cell and its surrounding environment. By using one window as a sample substrate, electrochemical *in-situ* and *operando* transmission sXAS experiments are possible. In the following chapter I will introduce my method that puts a novel twist to this concept. Here, a liquid thin-layer is created by the controlled formation of a gas bubble between the two SiN_x membranes.

III Novel Approach for *In-Situ* Transmission Soft X-ray Absorption Spectroscopy of Electrode Materials with Gas Bubble-Stabilized Liquid Thin-Layers

In this chapter I want to introduce my novel approach for the transmission sXAS of thin-film electrode materials under *in-situ* conditions through a gas bubble-stabilized liquid thin-layer. I will first anticipate the basic principle of the approach and then briefly come back to my main inspiration: the bubble formation through the electron beam in liquid cells for *in-situ* TEM, as it was described by Zhu *et al.* in 2013 [208] and Grogan *et al.* in 2014 [209]. While bubbles must be strictly avoided in TEM, by bringing up this inspiration, I want to show how I took the intrinsic drawback of bubble formation under high intensity electron radiation, adapted it to X-rays and used it to my advantage for this new technique.

To better understand the radiolysis of the electrolyte, which ultimately leads to the formation of the bubble, as well as the subsequent expansion of the bubble within the reaction cell, I have modelled both processes in a Finite Element Method (FEM) simulation. Because the simulation and the actual experimental procedure were developed in tandem, it is hard to explain one without the other. Thus, for a coherent description, I will describe the simulation first and add the necessary experimental observations when it fits. Still, a complete description of the actual experimental implementation of the cell, as it was used in this work for the investigation of the SEI on silicon thin-film anodes in chapter IV, will be given in the end.

While the final experimental procedure turned out to be straight forward, the prototyping required a highly flexible and adaptive experimental setup. Thus, I felt the need to develop my own data acquisition and instrument control software (including all instruments of the experimental stations as well as the beamlines at BESSY II). This allowed me to adapt the software on my own quickly to the needs of the rapidly changing experimental procedure during prototyping. In the end, it turned out to be a complete, highly adaptable, and extendable software suit for XAS experiments at a soft X-ray beamline with a fully-fledged graphical user interface (GUI). The software is written in the Python programming language and is made available as open source by me for everyone to pick up and adapt to one’s needs. At the end of this chapter, I will briefly describe its implementation and features.

I want to define a few terms which I will use throughout the following chapters. As I have done so far, with thin-films I refer to solid thin-films of electrode material, like the silicon investigated in this work. With thin-layers, however, I will refer to the thin liquid layers which are formed and used in the transmission sXAS approach I will describe in the following chapters. When

speaking of liquids, the terms liquid and electrolyte will be used interchangeably. Although all liquids investigated in this work are electrolytes, the presented technique in III and IV is in principle also applicable to all kind of liquids, not just electrolytes. Furthermore, when it comes to the SiN_x membrane windows, I will refer to them interchangeably as windows or membranes as well.

III.A Gas Bubble-Stabilized Liquid Thin-Layers for *In-situ* Transmission Soft X-ray Absorption Spectroscopy

As I have described in chapter II, XAS appears to be a suitable characterization method to gain useful insight into the composition and structure of the SEI. For the *in-situ* investigation of silicon's SEI via transmission sXAS I had to overcome the following challenge. Fundamentally, the small attenuation length of the soft X-ray radiation imposes the biggest constraint on the experiment. While the SEI's thickness in the nanometer range (typically 10 to 50 nm) is ideal for soft X-ray transmission, the simultaneous *in-situ* preparation and characterization are intricate. The SEI is comprised of decomposition products of the electrolyte, hence for the *in-situ* preparation an excess of electrolyte must be present for a sufficient SEI to form. However, this excess of electrolyte inevitably overshadows the SEI signal in a transmission measurement and must therefore be removed somehow. The novel approach I present in this work is a way to overcome this challenge.

In the following I will describe the approach as it was developed for the investigation of silicon's SEI and used in the investigation presented in chapter IV. Like the cells we have discussed in chapter II.D, the experimental procedure is based on a microfluidic electrochemical half-cell with two soft X-ray transparent silicon nitride (SiN_x) membrane windows. The formation of bubbles in electrolytes under high intensity X-ray radiation has been a known problem inside this type of cells and ultimately led to the wide adoption of flow cells, where the electrolyte is replenished continuously. In this work, however, I use this to my advantage by removing the excessive electrolyte through the controlled formation of a gas bubble. The individual steps of my approach are illustrated in Figure 25. The two silicon nitride membranes are arranged as a sandwich assembly separated by a spacer to form an electrolyte channel in-between them. The silicon thin-film anode has been deposited onto the back-facing silicon nitride window (omitted in Figure 25A) beforehand. Then, while the excess electrolyte is still present, the silicon thin-film is cycled (de-/lithiated to Li_xSi_y) and the SEI forms *in-situ* on top of the anode (B). After the SEI has been formed, a gas bubble is created through radiolysis of the electrolyte with a high intensity X-ray. The bubble forms in the vicinity of the entrance window and pushes out excessive electrolyte from the probing volume (C). As shown in Figure 25, the SiN_x windows bulge to the outside, due to the pressure difference between the atmospheric

pressure inside the cell and the surrounding vacuum. Thus, stabilized by their resulting concave shape, the bubble remains steadily in the center between the membranes. What is left in the beam path is a thin-layer of electrolyte that covers the SEI and the anode, keeping both under *in-situ* conditions. This arrangement allows the investigation of the SEI on silicon thin-film anodes *in-situ* through transmission sXAS, without the need to disassemble the cell and risk any environmental exposure (D). Due to the small thickness of the electrolyte thin-film, a very low X-ray intensity is sufficient for the sXAS measurements and avoids any detectable beam damage to the anode and SEI. In this regard, it must be noted that during the bubble formation, the electrolyte shields the SEI and the anode from beam damage through the high intensity X-ray. Nevertheless, the radiolysis of the electrolyte leaves trace products in the remaining thin-layer, which must be considered when interpreting the data.

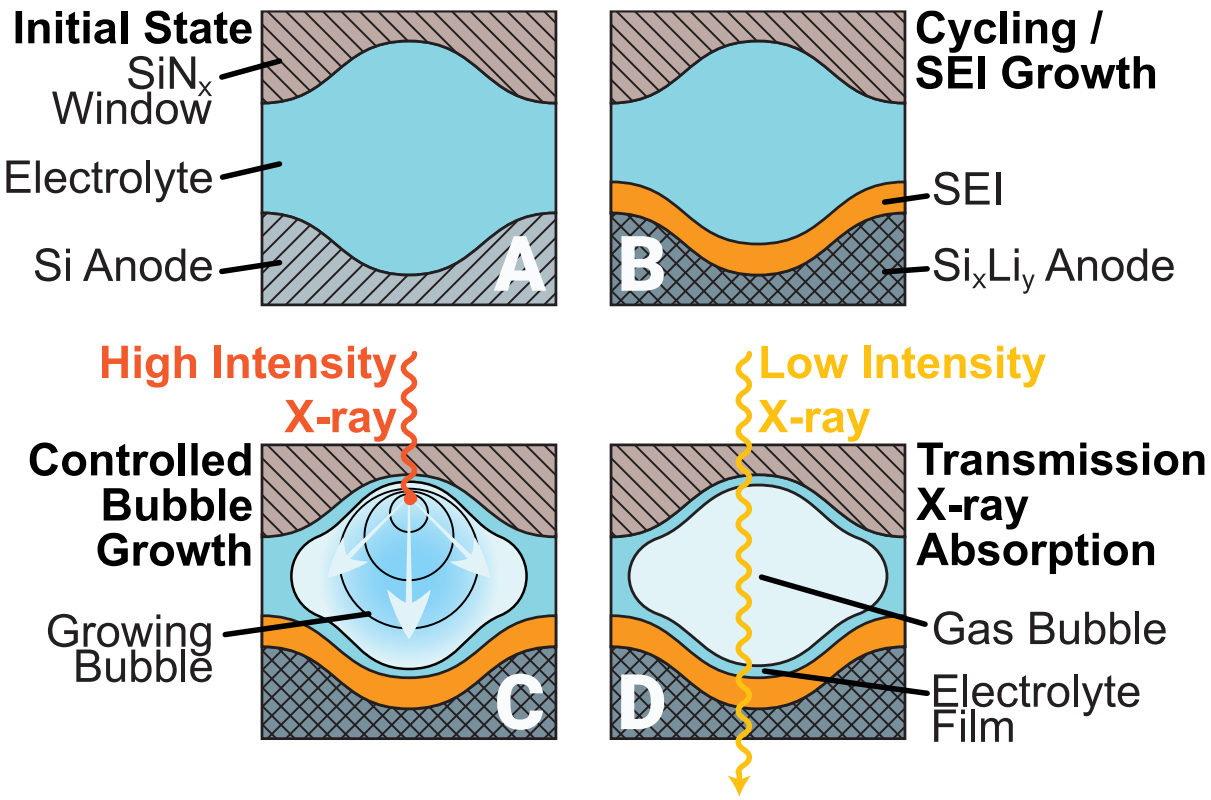

Figure 25 Illustration of my novel approach to investigate the SEI on silicon thin-film anodes in Li-ion batteries in-situ through transmission sXAS. A: The electrochemical cell for transmission sXAS consists of two silicon nitride membranes with an electrolyte channel in-between. The silicon thin-film anodes are deposited via plasma enhanced chemical vapor deposition onto the back-facing silicon nitride window (omitted in this illustration). B: The anodes are electrochemically cycled in a two-electrode setup, where the SEI forms on top of the then lithiated Li_xSi_y anodes. C: A bubble is formed by a high intensity X-ray beam in a controlled manner to push away the excessive electrolyte. D: The SEI is investigated in-situ through transmission XAS with a low intensity X-ray to avoid any beam damage.

At this point I, want to highlight a few key aspects. What is most important is the huge difference in thickness between the liquid thin-layer for sXAS and the excess electrolyte for any *in-situ* preparation. The thickness of the liquid thin-layer is either determined by the size of the bubble or in most cases by the surface tension of the liquid. As we will see later in

chapter IV.B.3, the thin-layer thickness of my model system 1M $LiPF_6$ in EC:DMC ranges from 100 nm up to 2 µm, depending on the sample/beam position. The thickness of the excess electrolyte before bubble creation, however, is given by a spacer which is placed between the two membranes when assembling the cell. Thus, the thickness can be chosen freely, albeit, depending on the surface tension of the liquid, some constraints may still apply due to the stability of the bubble for a too small or too large spacer thickness. For my model system, a thickness between 12.5 and 25 µm has been proven successful.

Even if no excess electrolyte for any electrochemistry is desired, the thickness of the liquid thin-layer still appears to be ideal for transmission sXAS of liquids. Thus, the described approach can easily be simplified by using two uncoated windows without any electrochemical procedures. Using this, later in chapter IV.B.3, I extensively characterized 1M $LiPF_6$ in EC:DMC on its own as my model electrolyte without any electrochemical procedure. I demonstrate the viability of this approach by achieving results comparable to EY liquid microjet approaches published in literature. Here, in comparison to liquid microjets or other fluorescent flow cell implementations, I argue that the required sample volume below 0.23 mL is much smaller. This makes my approach suitable for expensive or rare samples which are not readily available. Additionally, the obtain transmission spectra can be considered a true absorption measurement, free of any self-absorption or saturation effects as discussed earlier in II.B.

III.B Inspiration: Electron Beam-Induced Bubble Formation in Water

After I have explained the general principle behind the transmission sXAS based on a gas bubble-stabilized liquid thin-layer, I now want to take a step back and put forward my main inspiration for this approach: the bubble formation induced in water by an electron beam in TEM as it was observed and described by Grogan *et al.* in 2014 [209]. This will illustrate how I came up with the idea to utilize a phenomenon, which was initially perceived as an intrinsic drawback, to my advantage. Many considerations presented by Grogan *et al.* are vital to the understanding of my FEM simulation to model the X-ray beam interaction with the electrolyte, which I will describe in more detail in the next chapter.

Grogan *et al.* applied traditional micro-fabrication methods to construct a transmission liquid cell for TEM, which they called the “nanoaquarium” [210], [211]. Analogous to my novel approach described before, their “nanoaquarium” is made up of a sandwich of two 50 nm thick SiN_x membrane windows on both sides and a 100 nm thick water layer in-between. The side length of the square windows was 100 µm. A sketch of the “nanoaquarium” with all important dimensions is shown in Figure 26a.

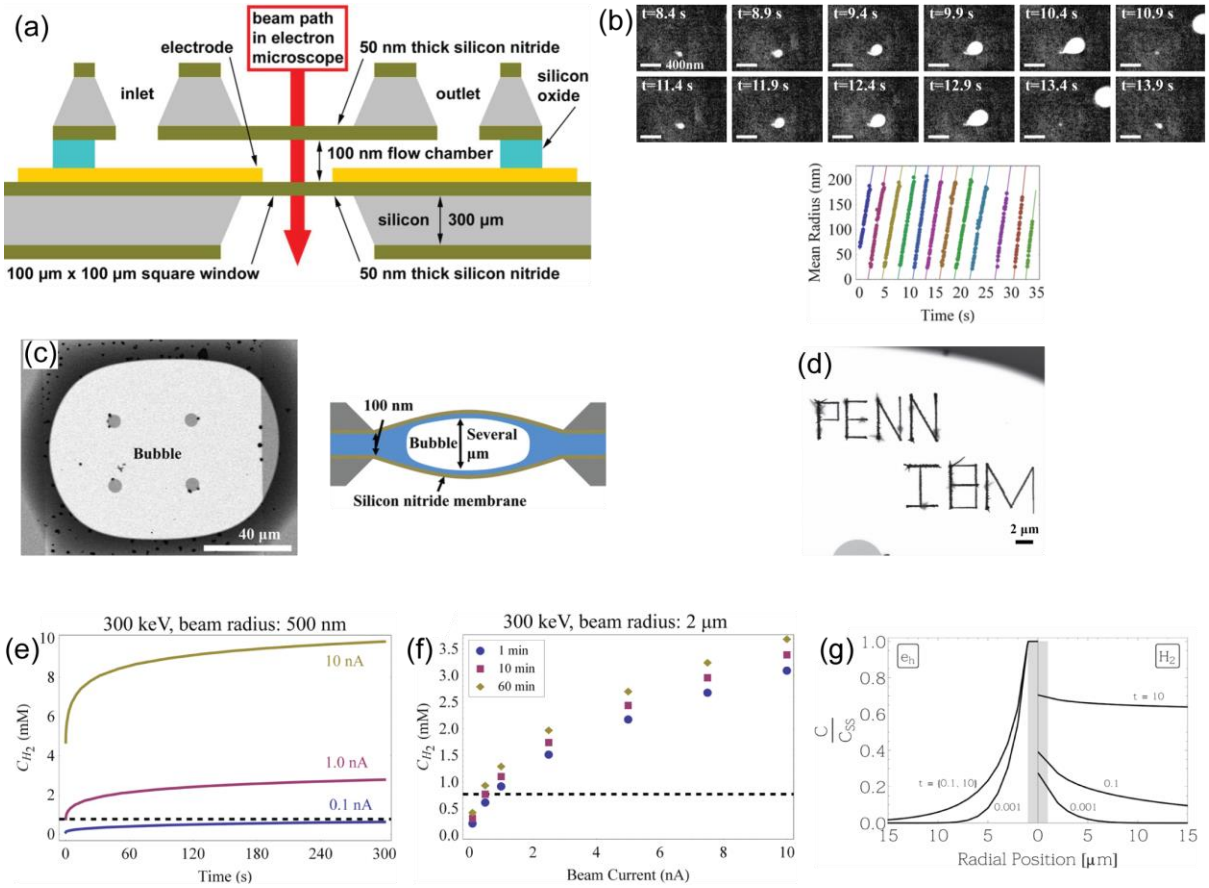

Figure 26 Summary of the work from Grogan et al. on the bubble and pattern formation in an aqueous electrolyte induced by an electron beam in TEM [209]. (a) Sketch of the liquid-cell for TEM used by Grogan et al. called the "nanoaquarium". The schematic is sourced from [211]. (b) Top: TEM image sequence from periodically formed small bubbles at an imperfection of the SiN_x membrane window. The small bubbles grow continuously until they detach from the imperfection and leave the imaging window. Bottom: Mean radius of the small bubbles as a function of time during their growth until detachment. (c) Left: TEM image of a large gas bubble sitting steadily in the center of the SiN_x sandwich stack. Right: Illustration of the cell and bubble geometry. (d) TEM image of gold nanowires deposited from an $HAuCl_4$ aqueous solution in an arbitrary pattern by scanning the electron beam over the liquid thin-layer which was stabilized by a large bubble like the one shown in (c). The nanowires depict the letters of the author's institutions. (e) Simulated H_2 concentration at the beam's center (300 keV, 500 nm radius) as a function of time for 3 different beam currents: 0.1, 1.0 and 10 nA. Horizontal dashed line correlates to the equilibrium concentration of H_2. (f) Simulated H_2 concentration at the beam's center (300 keV, 2 µm radius) as a function of beam current after 1, 10 and 60 min irradiation time. Horizontal dashed line correlates to the equilibrium concentration of H_2. (g) Simulated normalized spatial distribution of H_2 and e_h as a function of the distance to the beam's center at three different points in time. All images in (b)-(g) are summarized from [209].

When Grogan *et al.* were investigating an aqueous solution of gold nanorods with a trace amount of cetrimonium bromide inside their TEM using the "nanoaquarium", they witnessed two types of bubble formation depending on the applied electron beam properties [209]. First, in TEM mode with a high intensity beam with 300 keV acceleration potential, 1 to 10 nA beam current and a beam radius of about 2 µm, they observed the periodical formation of smaller bubbles at imperfections on the silicon nitride membrane. The periodic formation of two consecutive bubbles is shown in the TEM pictures of Figure 26b. The plot in Figure 26b demonstrates the bubbles to grow with a constant rate until they detach from the membrane imperfection with a final mean radius between 150 to 200 nm. During STEM operation of a 1 µm^2 raster area, however, with a lower beam intensity of only 30 keV acceleration potential,

0.05 to 1.2 nA beam current and a beam radius of 0.5 to 1.5 nm, they witnessed the explosive formation of a single large bubble after prolonged irradiation times from several minutes up to hours. The large bubbles formed this way spanned almost the complete SiN_x window and sat steadily in the center of the sandwich assembly, as it is shown in Figure 26c.

Based on the estimated beam-induced temperature increase in the range of only a few degrees, Grogan *et al.* ruled out bubble formation by boiling and attributed its origin solely to the formation of gaseous products through radiolysis, namely O_2 and H_2 for the aqueous electrolyte. By taking the back-reaction of the radiolysis products into account, through a FEM calculation they found that the radiolysis products reach a constant steady-state concentration which is determined by the beam current. Figure 26e shows the simulated H_2 concentration at the center of the beam (300 keV, 500 nm radius) for 0.1, 1.0 and 10 nA beam current as a function of time and Figure 26f gives the concentration at the center of the beam (300 keV, 2 µm radius) after 1, 10 and 60 min irradiation time as a function of beam current. Additionally, Figure 26g shows the normalized spatial distribution of H_2 and hydrated electrons e_{h} at three different points in time.

The horizontal dashed line in Figure 26e,f correlates to the saturation concentration of H_2 at atmospheric pressures. Based on its solubility, Grogan *et al.* propose that H_2 remains supersaturated for an extended period of time and at some point leads to the bubble nucleation. Further, given its higher solubility, they suggest that O_2 does not form a bubble on its own, but as soon as a bubble is nucleated by H_2, O_2 will add to the bubble growth as well. They further conclude that for bubble-free imaging in TEM, the beam current must be chosen accordingly for the steady-state concentration of H_2 to remain close or below its equilibrium concentration. Furthermore, they argue that if the steady-state concentration exceeds the equilibrium concentration, the electrolyte is enriched over time with supersaturated H_2 (as shown in the spatial concentration profile in Figure 26d). This supposedly increases the probably of heterogeneous nucleation and provides more gaseous radiolysis products to form a bigger bubble. Unfortunately, Grogan *et al.* give no detailed explanation why different beam parameters in TEM and STEM mode yield two different bubble growth modes as we have discussed before, namely periodically formed small bubbles or a single large bubble. In my opinion, the mode of bubble growth is given by the interplay between the local maximum concentration at the beam center, which ultimately triggers the bubble nucleation, and how far and how much the electrolyte was enriched with supersaturated radiolysis gases. I propose that this interplay is strongly determined by the beam intensity as I will explain later in greater detail based on my own FEM simulations.

Grogan *et al.* observed in their FEM simulation that the highly reactive hydrated electrons are localized to the beam center due to their much shorter lifetimes, as shown in Figure 26g. Inspired by this, they came up with the following interesting application. Gold ions are readily reduced to metallic gold by hydrated electrons. Thus, they first formed a large, stable bubble within a $HAuCl_4$ aqueous solution, that sits steadily in the center of the SiN_x membranes. Afterwards, they were able to precipitate gold nanowires from the liquid thin-layer which was stabilized by the bubble on the SiN_x membranes by scanning the electron beam in an arbitrary pattern. Figure 26d shows the nanowires to depict the letters of the authors' institutions. Additionally, the created gold nanowire patterns were detached and moved around by the bubble and liquid thin-layer motion, indicating that the liquid thin-layer is indeed of a certain thickness.

While the beam-induced nanowire patterning is without a doubt a fascinating technique, I was more intrigued by the presence of the liquid thin-layer itself. I imagined the liquid thin-layer might be of the ideal thickness for transmission measurements in the soft X-ray regime. With the SiN_x membrane windows in Grogan *et al.*'s approach being only 50 nm thick, their cell approach appeared to be directly adaptable to transmission sXAS as well. On top of that, the formation of bubbles in electrolytes under high intensity X-ray radiation has been a known problem inside this type of cells and ultimately led to the wide adoption of flow cells, where bubble formation is circumvented by replenishing the electrolyte continuously. With this, my idea of transmission sXAS of a gas bubble-stabilized liquid thin-layer was born. To bring it to life, I had to figure out how to form the bubble in a controlled manner. The work of Grogan *et al.* already revealed two bubble growth modes, of which apparently only one is suitable for this approach. The goal here is to create a single large bubble that sits steadily in the center of the SiN_x membrane sandwich and stabilizes a sufficiently thin liquid layer on top of the windows. To conceptually explore this approach, I have developed an FEM and CFD simulation of the beam interaction with the electrolyte and the bubble growth dynamics. In the following chapter, I will explain both simulations in more detail.

Before I conclude this interlude, I want to mention that my approach is not the first to utilize the gas bubble-stabilized liquid thin-layer. In the field of liquid cell TEM, Zhu *et al.* [208] intentionally created a gas bubble inside a liquid cell to reduce the thickness of the liquid phase as illustrated in Figure 27 and to increase the spatial resolution this way. They were able to achieve atomic resolution for Pd nanoparticles with 5 nm diameter within the gas bubble-stabilized thin-layer. Figure 27b,c demonstrates the increased achievable resolutions from the thick (Figure 27b) to the liquid thin-layer (Figure 27c). Further, from the electron transmission Zhu *et al.* estimated the thin-layer thickness to be about 40 nm. In a similar manner, Wang *et al.* were able to image Escherichia coli cells within a gas bubble-stabilized liquid thin-layer of

water through TEM [212] as illustrated in Figure 27d-f. In their study, however, the gas bubble was not induced by the electron beam itself but was present a-priori and introduced presumably due to insufficient filling of the cell.

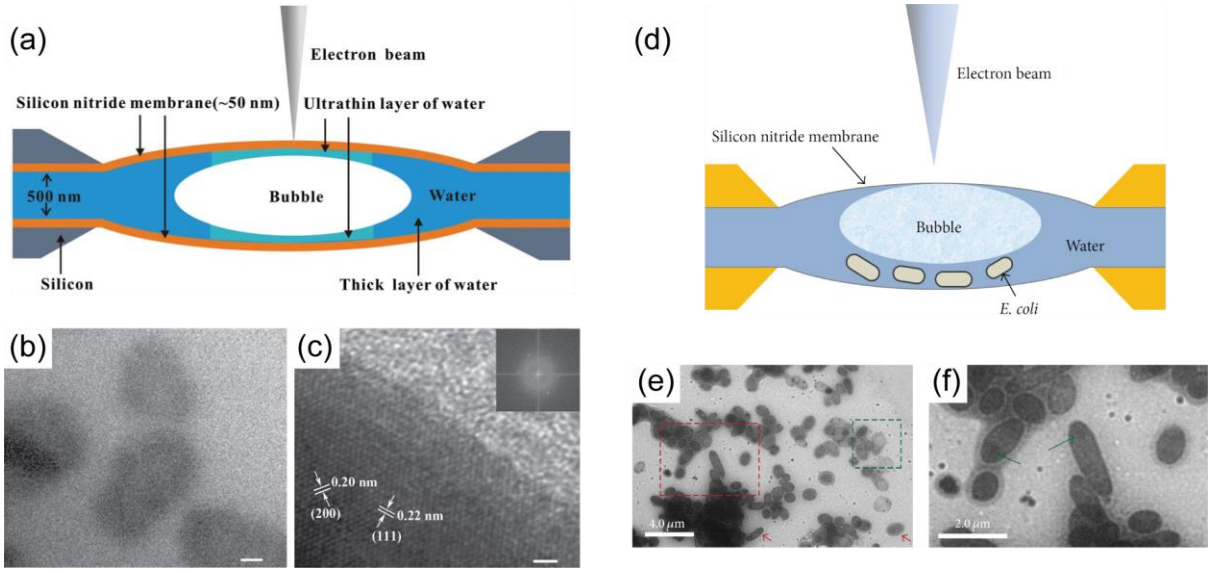

Figure 27 (a) Schematic of the liquid TEM cell used by Zhu et al. to investigate Pd nanoparticles in aqueous solution utilizing a gas bubble-stabilized liquid thin-layer. (b) Low resolution TEM image of Pd nanoparticles in thick liquid layer. Scale bar is 20 nm. (c) High resolution TEM image of a Pd nanoparticle in thin liquid layer as stabilized by the bubble. Scale bar is 2 nm. All images in (a)-(c) are summarized from [208]. (d) Schematic of the liquid TEM cell used by Wang et al. to investigate Escherichia coli cells in aqueous solution utilizing a gas bubble-stabilized liquid thin-layer. (e)-(f) TEM images of Escherichia coli cells. All images in (d)-(f) are sourced from [212].

III.C Heating, Radiolysis and Bubble Formation in an Organic Electrolyte under Soft X-ray Radiation: A Finite Element Analysis

I propose that the bubble formation is governed by the heating of the electrolyte under the high intensity X-ray beam and the increasing concentration of gaseous dissolved radiolysis products inside the electrolyte. Because the solubility limits of such gaseous species are usually temperature dependent, both processes are strongly coupled. To better understand the dynamics of both effects and to guide the development of the experimental procedure, I developed an FEM simulation of the beam interaction with the electrolyte using the commercial COMSOL Multiphysics® software [213]. In the first step of the simulation, I model the heating together with the creation and diffusion of radiolysis products inside the electrolyte. Then, in a second step, I apply Computational Fluid Dynamics (CFD) to simulate the growth of a bubble between the two SiN_x membranes within the concentration distribution obtained in the first step.

The first simulation step will answer an important question regarding a key experimental parameter: what is the ideal beam intensity to create the bubble in the most reliable manner? I expect the beam intensity to be crucial for several reasons. The bubble creation will leave

traces of radiolysis products in the liquid thin-layer. These must be minimized, and I want to induce just enough radiolysis for a bubble of sufficient size, but not more. On top of that, the highly focused beam develops a diffusion gradient of hydrolysis products originating from its center. If the beam intensity is too low, the gas species might have enough time to spread throughout the whole electrolyte volume. They might never reach the solubility limit and no bubble is formed at all, or at least not in an acceptable time frame. On the opposite side, if the beam intensity is too high, the solubility limit might be exceeded locally too quickly, leading to the prematurely formation of many small bubbles, like the bubble formation observed by Grogan *et al.* [209] in Figure 26b. In an even more extreme case, a high beam intensity might boil the liquid right away. A bubble formed of gaseous electrolyte is not stable and will condense when the electrolyte is cooling down after switching to a low intensity X-ray for the sXAS measurements.

The second part of the simulation will yield insight into how the bubble grows between the SiN_x windows. The most important question this will answer is where to expect the bubble or more important the liquid thin-layer for the subsequent sXAS investigation. As I have claimed earlier, due to the concave shape of the bulging membranes, the bubble sits steadily in the center. The CFD simulation will show, whether the bubble will always end up in the center and whether this arrangement is indeed predefined by the geometry of the bulging membranes. If this is not the case, I want to explore if I can manipulate the bubble position through the beam position by nucleating the bubble at different locations.

Although in my experimental study I investigate 1M $LiPF_6$ in a 50/50 (v/v) EC:DMC solvent as the most common electrolyte for LIBs, in the simulation presented here, I take neat propylene carbonate (PC) as a simplified model solvent. I will discuss in more detail later why I consider this simplification to be reasonable. The simulation parameters for PC were taken from values reported in literature.

III.C.1 Finite Element Method and Computational Fluid Dynamics Implementation

III.C.1.a Computational Domain and Boundary Conditions

My simulation can be divided into two steps: In the first step (I), the beam interaction with the electrolyte is simulated, which leads to a local rise in temperature and a continuous increase of the dissolved gas species concentration throughout the computational domain. The governing equations for the heat transfer and the diffusion are solved, but the equations for the fluid flow are not solved. For the second step (II), I transform the concentrations from (I) into *saturation* concentrations, hence the concentrations above the individual temperature-

dependent solubility limits. In the second part (II), the growth of the bubble is simulated by solving the governing equations for the *saturation* concentrations and the fluid flow. The heat equations are not considered in (II), assuming the electrolyte cools down quickly back to room temperature. Further, the bubble growth in (II) starts from a stable bubble, i.e., no nucleation processes between (I) and (II) are considered. The computational domain and the boundary conditions vary slightly between each part of the simulation.

An overview of the computational domain with the corresponding mesh and the highlighted boundary conditions are shown in Figure 28. For (I), the computational domain is comprised of the electrolyte, which is encapsulated by two SiN_x windows 25 µm apart and a surrounding electrolyte reservoir. The SiN_x windows itself are modelled as the 200 µm thick silicon frames with a 3 mm diameter and the freestanding SiN_x membranes in the center. The membranes are described as boundary with a length of 707.1 µm, which correlates to the diagonal direction of the square-shaped membranes with 500 µm side length. The electrolyte reservoirs are square-shaped with a side length of 500 µm. The membranes bulge outwards under the pressure difference between the atmospheric pressure inside the cell and the surrounding vacuum. The maximum membrane deflection d can be calculated through (11) with the membrane thickness t, the Young's modulus E, the residual stress σ_0, the pressure difference p and the side length of the square membrane as $2a$ [203], [214]. In this work, I assumed a residual tensile stress of 200 MPa and a Young's modulus of 300 GPa [203], [215], [216], yielding a maximum membrane deflection of 23.5 µm for a pressure difference of 1 atm. The shape of the membranes is modelled based on the load-deflection in diagonal direction $w(x = y)$ as given by an analytical solution in (12), where d is the maximum membrane deflection and x the distance from the centre with $s = \sqrt{2}a$ and the window side length a [217]. In the following, the volume encapsulated by the membranes is referred to as the probing chamber and the volume between the silicon frames as the electrolyte channels. Furthermore, for (II), only the probing chamber and the electrolyte channels are included in the computational domain. On top of that, (II) starts with a stable bubble with a radius of 5 µm (highlighted as Nucleus in Figure 28).

$$\left(\frac{Et}{a^4}\right)d^3 + \left(\frac{1.66t\sigma_0}{a^2}\right)d = 0.547p \tag{11}$$

$$w(x = y) = d\left(1 + 0.401\frac{2x^2}{a^2} + 1.1611\frac{x^4}{a^4}\right)\cos^2\frac{\pi x}{2a} \tag{12}$$

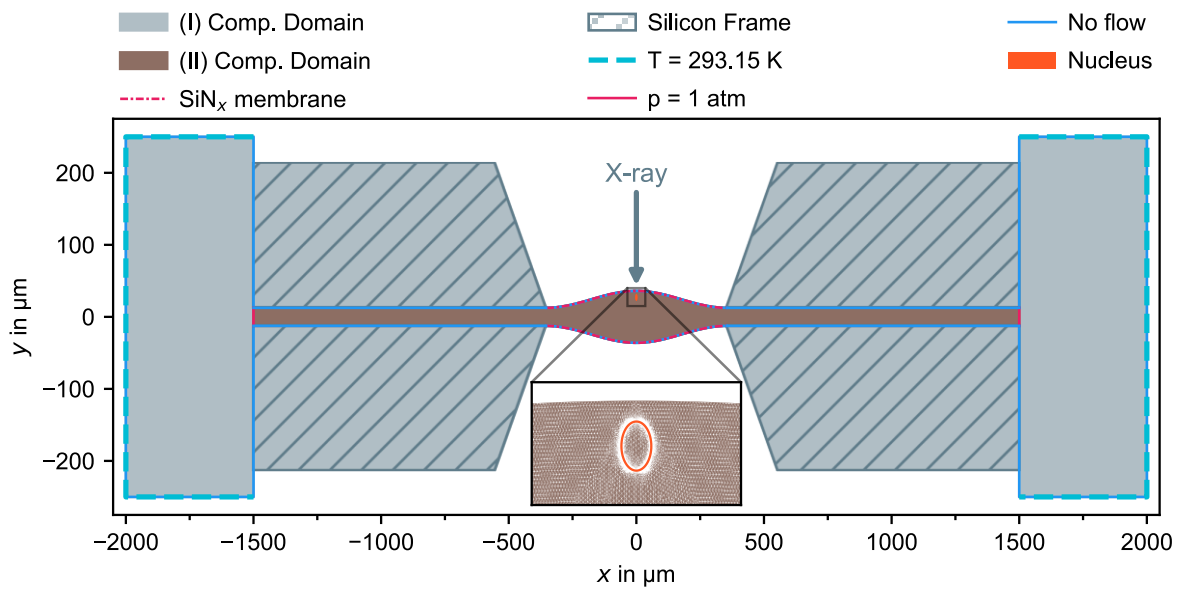

Figure 28 Geometry of the computational domain and the computational mesh with highlighted boundary conditions. The computational domain for the first part of the simulation (I, grey area) is comprised of the electrolyte, which is encapsulated by two SiN_x windows 25 µm apart and a surrounding electrolyte reservoir. The SiNx windows are modelled as the 200 µm thick silicon frames (hatched area) with a 3 mm diameter and the freestanding SiN_x membranes in the center with a length of 707.1 µm. The electrolyte reservoirs are square-shaped with a side length of 500 µm. The computational domain for the second part of the simulation (II, brown area) is comprised of the electrolyte between the SiN_x windows without the electrolyte reservoirs. No nucleation processes between (I) and (II) are considered and a stable bubble is introduced at the beginning of (II), marked as orange Nucleus and shown in the inset.

The applied boundary conditions are described in the following and the corresponding equations are given in III.C.1.b. In (I), the electrolyte is encapsulated by a no flow boundary condition for the solved gas concentration. Consequently, the gas species accumulates over time within the electrolyte. For the temperature, the whole surrounding boundary is described by an isolation, no heat flow boundary condition, except for the borders of the electrolyte reservoir. Here, I assume the cell to have an infinite thermal mass to keep the electrolyte at 293.15 K. In (II), the ends of the electrolyte channels at $x = \pm 1500$ are modelled as outlets with average constant atmospheric pressure. Furthermore, the concentration at the ends of the electrolyte channels is assumed to be zero as any concentration is quickly diluted infinitely when reaching the electrolyte reservoirs. Based on the findings of Grogan *et al.* [209] discussed in the previous chapter, I assume the bubble stabilizes a liquid thin-layer at the membrane windows. Thus, I consider the bubble growth inside the cell to resemble a “plug/slug flow” (termed by Kawaji *et al.* [218]) similar to a gas-liquid flow in microchannels. With this, I assume full electrolyte wetting at the membranes and the channel walls in (II).

III.C.1.b Governing Equations

In the following, the simulation is described using the terminology of the COMSOL Multiphysics® software [213]. I refer to the documentation of COMSOL Multiphysics® for the terminology and the numerical implementation itself.

The heat transfer is modelled within the “Heat Transfer in Fluids Interface” and is governed by equation (13) [213], [219]. The diffusion of the beam radiolysis products is simulated through the “Chemical Species Transport Interface” and governed by equation (14).

$$\rho C_p \left(\frac{\partial T}{\partial t} + u \cdot \nabla T\right) + \nabla \cdot \mathrm{q} = \sum_j Q_j \qquad (13)$$

$$q = -d_z k \nabla T$$

T: Temperature

t: Time

ρ: Density

C_p: Specific heat capacity, at constant pressure

u: Velocity vector

q: Heat flux by conduction

d_z: Numerical correction for out of plane fluxes

k: Thermal conductivity

p: Pressure

Q: Heat sources

$$\frac{\partial c_i}{\partial t} + \nabla \cdot (J_i + u c_i) = \sum_j R_i^j \qquad (14)$$

$$J_i = -D_i \nabla c_i$$

J_i: Diffusive flux

i: Species

c_i: Concentration

t: Time

D_i: Diffusion coefficient

u: Velocity vector (mass average)

R_i: Reaction term

In analogy to the simulation of Grogan *et al.* [209], the beam interaction is included as a heat source term Q_j in (13) and reaction term R_i^j in (14). With the photon flux density I_{Beam}, the heat source term Q_{Beam} and the reaction rate R_{Beam} were calculated through (15) and (16), respectively.

$$Q_{\mathrm{Beam}} = I_{\mathrm{Beam}} * E_{\mathrm{Photon}} * C_{\mathrm{Heat}}^{\mathrm{Conversion}} \tag{15}$$

E_{Photon}: Photon energy

$C_{\mathrm{Heat}}^{\mathrm{Conversion}}$: Photon-heat conversion coefficient

$$R_{\mathrm{Beam}} = \frac{I_{\mathrm{Beam}} * C_{\mathrm{Radiolysis}}^{\mathrm{Conversion}}}{N_{\mathrm{A}}} \tag{16}$$

$C_{\mathrm{Radiolysis}}^{\mathrm{Conversion}}$: Photon-radiolysis conversion coefficient

N_{A}: Avogadro's constant

I_{Beam} in (15) and (16) is described by (17), assuming a Gaussian intensity distribution and a linear attenuation based on the Beer-Lambert law in (6).

$$I_{\mathrm{Beam}}(x,\mathrm{y}) = I_{\mathrm{Total}}^{\mathrm{1D}} * T_{\mathrm{SiN_x}} * \underbrace{\mu_{\mathrm{abs}} e^{-(y-y_{\mathrm{Beam}})\mu_{\mathrm{abs}}}}_{\text{attenuation in } \vec{y}} * \underbrace{\frac{1}{\sigma\sqrt{2\pi}} e^{\frac{-(x-x_{\mathrm{Beam}})^2}{2\sigma^2}}}_{\text{distribution in } \vec{x}}$$

$$I_{\mathrm{Total}}^{\mathrm{1D}} = I_{\mathrm{Total}} * \underbrace{\frac{D_{\mathrm{Beam}}^{\mathrm{FWHM}}}{A_{\mathrm{Ref}}^{\mathrm{BL}}}}_{\text{2D to 1D}} \tag{17}$$

$$D_{\mathrm{Beam}}^{\mathrm{FWHM}} = 2\sqrt{2\ln 2}\,\sigma$$

I_{Total}: Total photon flux

$D_{\mathrm{Beam}}^{\mathrm{FWHM}}$: Beam diameter

$A_{\mathrm{Ref}}^{\mathrm{BL}}$: Spot size

$T_{\mathrm{SiN_x}}$: Membrane transmission

μ_{abs}: Linear absorption coefficient

$y_{\mathrm{Beam}}, x_{\mathrm{Beam}}$: Beam/membrane intersection

The "no flux" / "thermal insulation" boundary condition for the heat and the concentration is modelled based on the boundary normal n through (18) and (19), respectively.

$$-n \cdot J_i = 0 \tag{18}$$

$$-n \cdot q = 0 \tag{19}$$

For the growth of the bubble inside the electrolyte, the electrolyte itself is described by the Navier-Stokes equation for incompressible flow within the "Laminar Flow Interface" in COMSOL Multiphysics®. The governing equation for the incompressible flow is (20). Furthermore, the interface between the gas bubble and the electrolyte is tracked through a phase field approach, which's evolution in time is governed by the Cahn-Hillard equation, as

it is described by (21). In the phase field approach, the phase field variable ϕ evolves continuously from -1 to 1 at the phase boundary. The center of the phase boundary is defined at $\phi = 0$. Hence, the spatial position of each phase is then described by the corresponding phase field variable value at each side of the boundary. Consequently, the material properties ϱ^i within the computational domain evolve continuously with the phase field variable based on a volume average $\varrho^i = \varrho_1^i + (\varrho_2^i - \varrho_1^i)\phi$. Equation (22) maps the ϕ phase field variable to values between 1 and 0, with 1 correlating to the gas phase. In the simulation, the phase field is coupled to the Navier-Stokes flow through the velocity field u in (20) and (21).

$$\rho \frac{\partial u}{\partial t} + \rho(\mathrm{u} \cdot \nabla)\mathrm{u} = \nabla \cdot [-pI + K] + \mathrm{F} \qquad (20)$$

$$\text{Continuity equation: } \rho \nabla \cdot \mathrm{u} = 0$$

u: Velocity vector

t: Time

ρ: Density

p: Pressure

K: Viscous stress tensor

F: Volume forces

For (II), I transform the dissolved gas concentrations c_i into saturation concentrations $\widehat{c_i}(c,T)$ based on their temperature dependent solubility $c_i^{\mathrm{eq}}(T)$ using (23). Expecting the electrolyte to cool down rapidly back to room temperature, $\widehat{c_i}(c,T)$ is calculated for 293 K and 1 atm pressure. The corresponding saturation concentration diffusion fluxes are noted as $\widehat{J_i}$. The saturation concentrations are coupled to the electrolyte flow through the velocity u in (14) and (20). With this, $\widehat{c_i}$ can be considered the concentration above the solubility limit for $\widehat{c_i} > 0$ and below for $\widehat{c_i} < 0$.

To simulate the actual dynamics of the bubble growth, I adapted the approach of Jafari *et al.* [220] and modified the continuity equation from (20) through (24) with the divergence profile Φ described by (25). As given in (24) and (25), the divergence is proportional to the diffusion flux $\widehat{J_i}$ within the phase boundary $\nabla\phi$ (transformed into the divergence profile Φ) and the molar volume V_m^i of each species. Thus, the phase boundary $\nabla\phi$ acts as a source in the Navier-Stokes equation which is coupled to the diffusion via $\widehat{J_i}$. This can be considered a quasi-empirical approach, where a bubble grows based on a concentration flux from a supersaturated electrolyte. However, the simulation does not consider a physically exact description of the migration from the gas molecules through the phase boundary. The divergence profile Φ derived from the corresponding phase field variable ϕ is illustrated in

Figure 29. In (25), ϱ is introduced to resemble the asymmetric nature of the phase boundary transition. Gas species traversing the phase boundary from liquid to solid create a positive divergence (source) inside the gaseous phase $\phi > 0$. At the same time, for a lower dissolved gas concentration, the density of the liquid increases marginally, leading to a negative divergence at $\phi < 0$ (sink). The ratio of 0.01 is chosen arbitrarily as I found the introduction of ϱ to influence the solution only negligible. However, it increases the numerical convergence and reduces computation time.

$$\frac{\partial \phi}{\partial t} + \nabla \cdot (u\phi) = \nabla \cdot \frac{\gamma \lambda}{\varepsilon_{\mathrm{pf}}^2} \nabla \psi$$

$$\psi = -\nabla \cdot \varepsilon_{\mathrm{pf}}^2 \nabla \phi + (\phi^2 - 1)\phi + \frac{\varepsilon_{\mathrm{pf}}^2}{\lambda} \frac{\partial f}{\partial \phi} \qquad (21)$$

$$\lambda = \frac{3\varepsilon_{\mathrm{pf}}\sigma}{\sqrt{8}}$$

$$\gamma = \chi \varepsilon_{\mathrm{pf}}^2$$

ϕ: Phase field variable

t: Time

u: Advection velocity field

γ: Interface mobility parameter

λ: Mixing energy density

$\varepsilon_{\mathrm{pf}}$: Interface thickness

f: Free energy density

σ: Surface tension

χ: Numerical mobility tuning parameter

$$\Theta = \min_{<1} \left[\max_{>0} \left\{ \frac{1+\phi}{2} \right\} \right] \qquad (22)$$

$$\widehat{c_i}(c_i, T) = c_i - c_i^{\mathrm{eq}}(T, p) \qquad (23)$$

$$\nabla \cdot \mathrm{u} = \Phi \sum_i \widehat{J_i} V_m^i \qquad (24)$$

$$\Phi = |\nabla(1-\phi^2)|\, \phi\, \varrho \text{ with } \varrho = \begin{cases} 0.01 \text{ for } \phi < 0 \\ 1 \text{ for } \phi > 0 \end{cases} \qquad (25)$$

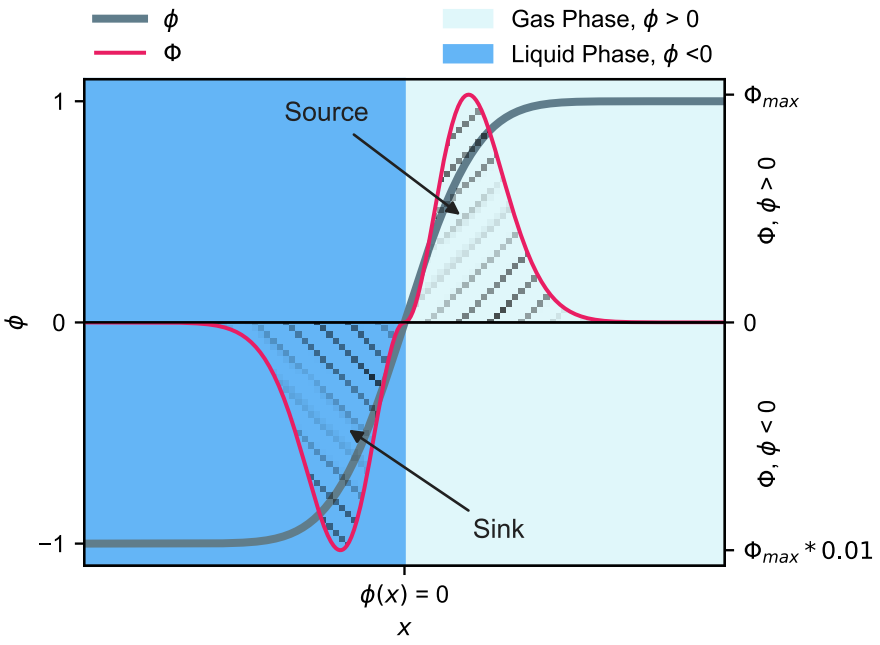

Figure 29 Illustration of the divergence profile Φ as a function of the phase field variable ϕ to introduce the growth of the gas bubble in the CFD simulation.

To create a driving force for the bubble growth, I include a reaction rate R_i^{Bubble} in (14) which is described by (26). With the simulation time step dt, (26) pins the oversaturation concentration $\hat{c_i}$ to zero within the gas phase for $\Theta > 0.9$.

$$R_i^{\text{Bubble}} = -\frac{\hat{c_i}}{dt} \text{ for } \Theta > 0.9 \tag{26}$$

Furthermore, in (II) the outlet boundary condition at $x = \pm 1500$ is described by (27) with $p_0 = 0$ at atmospheric pressure.

$$[-\rho I + K]n = p_0 n \tag{27}$$

In (II), for the concentration at the end of the electrolyte channels, the infinite dilution (via the electrolyte reservoirs) is modelled through (28) at $x = \pm 1500$.

$$c_i = 0 \tag{28}$$

Further, I assumed full electrolyte wetting at the membranes and channel walls with (29).

$$\phi = -1 \tag{29}$$

III.C.2 Heating and Radiolysis Simulation

In my simulation the beam parameters for (17) are modelled according the soft X-ray microfocus beamline U49-2_PGM-1 [194] at BESSY II, where I carried out all of my experimental work for the study on silicon's SEI, which I will present later in chapter IV. The

parameters used in this work are summarized in Table 1 and the corresponding I_{Beam} is shown in Figure 30.

Table 1 Summary of the beam model parameter for the heating and radiolysis simulation.

Property	Value	Comment	Source
I_{Total}, s^{-1}	$1{\cdot}10^{12}$		[194]
$A_{\mathrm{Ref}}^{\mathrm{BL}}$, µm	95 * 42		[194]
$T_{\mathrm{SiN_x}}$, %	90	50 nm thick SiN_x membrane	[182]
$D_{\mathrm{Beam}}^{\mathrm{FWHM}}$, µm	42		[194], [197]
μ_{abs}, cm^{-1}	7092	EC:DMC at 521.36 eV	[221], [222]

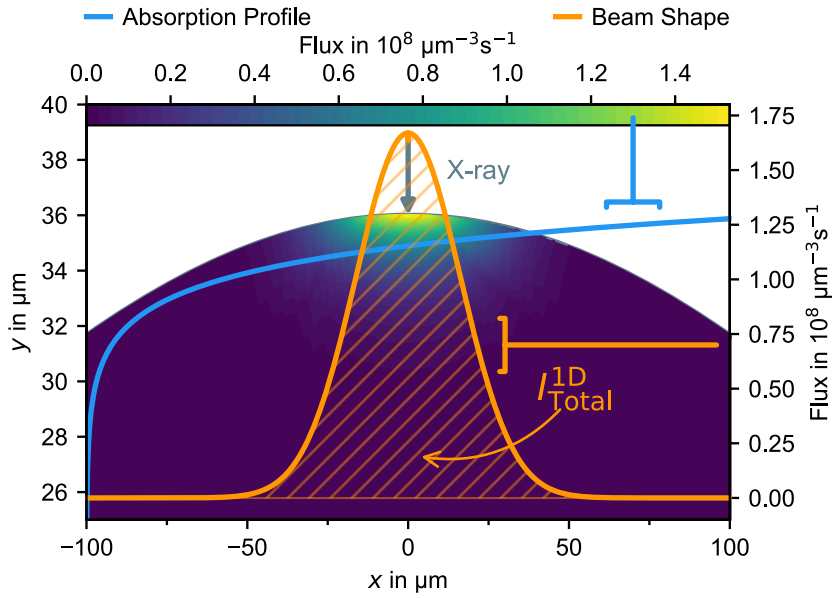

Figure 30 Beam model for the spatial distribution of the photon flux inside the computational domain. Modelled based on (17) with the parameter from Table 1 for the soft X-ray microfocus beamline U49-2_PGM-1 [194] at BESSY II.

From (15) and (16) it becomes clear, that the solution for the temperature and for the radiolysis product concentration are mainly determined by $C_{\mathrm{Heat}}^{\mathrm{Conversion}}$ and $C_{\mathrm{Radiolysis}}^{\mathrm{Conversion}}$. However, guessing $C_{\mathrm{Radiolysis}}^{\mathrm{Conversion}}$ is delicate and appears to be specific for the soft X-ray excitation energy [223] and the type of organic solvent. Unfortunately, there is only little information about radiolysis in organic solvents under soft X-ray radiation available in literature. Thus, for my simulation I rely on the study of Coffey *et al.* on various different organic polymer films [224]. They quantified the observed beam damage by the so-called G-value, which correlates to radiolysis events per 100 eV dose. This value can easily be transformed in $C_{\mathrm{Radiolysis}}^{\mathrm{Conversion}}$ through $C_{\mathrm{Radiolysis}}^{\mathrm{Conversion}} = G * 0.52$. According to Wallander *et al.* [225], for $C_{\mathrm{Heat}}^{\mathrm{Conversion}}$ it is reasonable to assume that the photon energy of 520 eV is fully converted into heat after a variety of relaxation processes.

However, for my simulation I took a more conservative approach and I assumed that 1.6 radiolysis events correlate to fission of carbonyl C=O bonds with a formation enthalpy of 7.7 eV [226] and hence 12.4 eV in total per photon. With the remaining photon energy of 507.6 eV, this assumption yields $C_{\mathrm{Heat}}^{\mathrm{Conversion}} = 0.976$. In the following the temperature is simulated assuming a photon energy of 520 eV.

While the conversion parameters $C_{\mathrm{Heat}}^{\mathrm{Conversion}}$ and $C_{\mathrm{Radiolysis}}^{\mathrm{Conversion}}$ control the amount of substance and heat, the spatial distribution and in turn the maximum, minimum, and mean values of the temperature and the concentration are determined by the diffusion coefficient and the thermal conductivity as well as the heat capacity and density. Table 2 summarizes the used material parameters in (I) for the liquid and the silicon frame. Values at the temperature limits are given when temperature-dependent parameters are used. For the complete dataset I refer to the individual literature.

Table 2 Summary of the material parameters for the liquid and the silicon frames used in (I).

Property	Value	Comment	Source
Liquid			
D_{CO_2}·10^9, m^2 s^{-1}	4.9 at 298 K, 8.8 at 348 K	CO_2 in toluene	[227]
C_p, J K^{-1} mol^{-1}	164 at 287 K, 169 at 323 K	Values for DMC	[228]
k, W m^{-1} K^{-1}	0.22 at 280 K, 0.14 at 520 K	Values for PC	[229], [230]
ρ, g cm^{-3}	1.3	1M $LiPF_6$ EC:DMC at RT	[231], [232]
Silicon Frame			
C_p, J K^{-1} mol^{-1}	703 at 290 K, 829 at 480 K		[233]
k, W m^{-1} K^{-1}	155 at 290 K, 80 at 480 K		[234]
ρ, g cm^{-3}	2.330 at 290 K, 2.326 at 290 K		[235]

As stated in the beginning, solubility limits of gaseous species are temperature dependent. For bubble formation the temperature and concentration must be considered. I will first look at the general evolution of the temperature and concentration as a function of time independently of each other. Then I will discuss the bubble formation based on the temperature dependent gas solubility.

The amount of substance and the heat are preserved quantities and thus share the same mathematical formulation, namely a first order partial differential equation in (13) and (14). As expected from their equal mathematical description, the concentration and the temperature show the same spatial distribution shape in Figure 31. In Figure 31, both quantities clearly originate from the beam at $x = 0\ \mu\mathrm{m}$. Further, they gradually spread throughout the cell with time. Due to the different nature of the transport mechanism (thermal conduction vs. diffusion), they clearly evolve on different time scales as it can be seen in Figure 31 at 0.3 and 60.0 s. From Figure 31b it becomes clear, that the large thermal mass of the silicon frames together with the high interfacial area keep the liquid inside the channel almost at room temperature and the temperature raises only noticeably within the probing chamber.

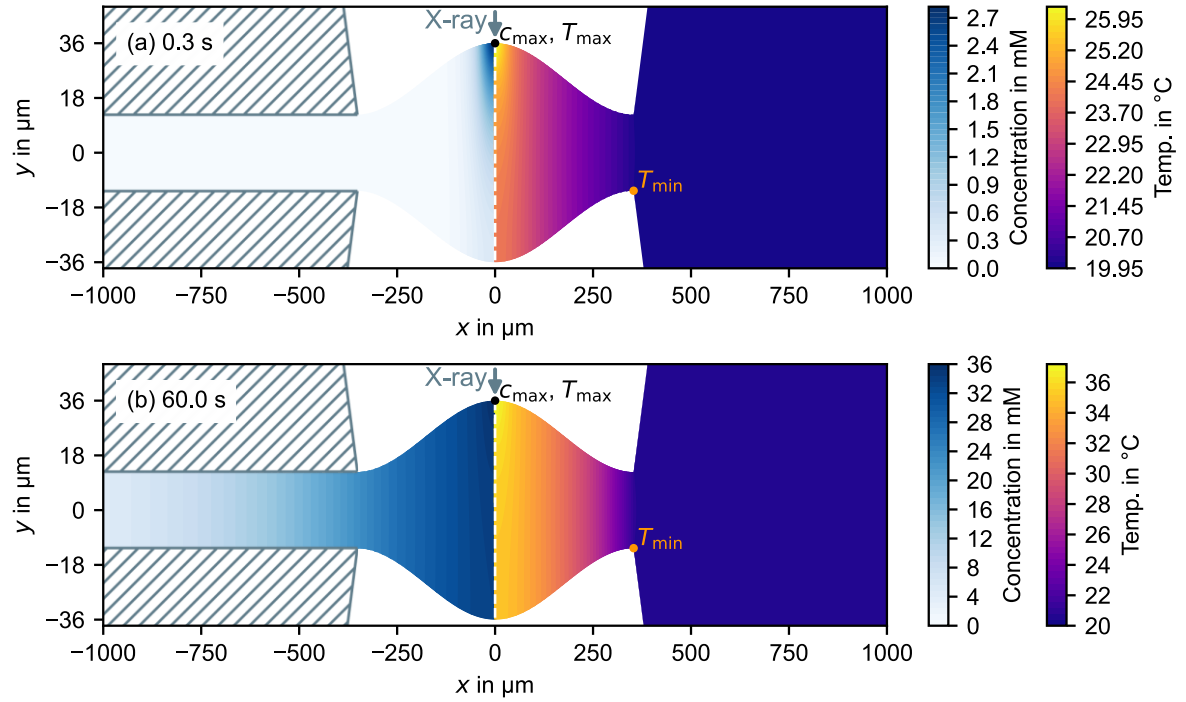

Figure 31 Spatial distribution of the concentration (on the left in shades of blue) and temperature (on the right in shades from purple to yellow) after 0.3 and 60.0 s. Simulated for a total photon flux of $1{\cdot}10^{12}$ s^{-1} at 520 eV photon energy with $C_{Radiolysis}^{Conversion} = 1.6$. The beam is placed at the center at $x = 0\ \mu m$ and the spatial distributions of both quantities are axially symmetric to the beam. The silicon frames (hatched areas) are excluded from the concentration computational domain.

Figure 32 shows the maximum, minimum and average temperature within the probing chamber as function of time. Because of the boundary condition at the reservoir walls with a constant temperature at 293.15 K (compare Figure 28a), the temperature within the probing chamber reaches a plateau within about 12 s. For a total photon flux of $1{\cdot}10^{12}$ s^{-1} at 520 eV photon energy, the plateau values are 36.5 °C, 31 °C and 21 °C for the maximum, average and minimum temperature, respectively. The maximum value is reached at the center at $x = 0\ \mu\mathrm{m}$ on the upper membrane where the beam enters the probing chamber, and the minimum

value lies at the edge of the lower membrane bordering on the silicon frame at $x = \pm 353.6\ \mu\mathrm{m}$ and $y = -12.5\ \mu\mathrm{m}$, as marked in Figure 31.

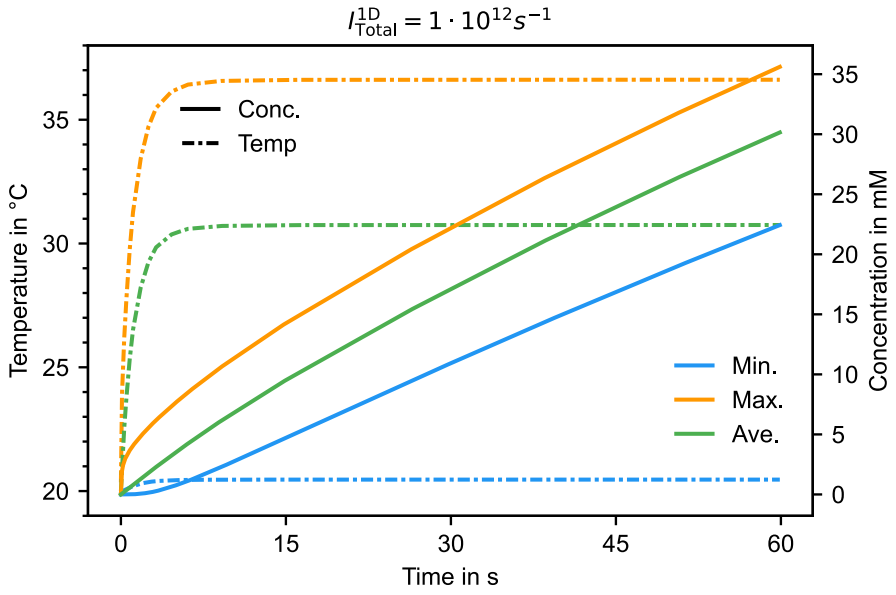

Figure 32 Maximum, average and minimum values of the concentration and temperature within the probing chamber as function of time. Simulated for a total photon flux of 1·10[12] s[-1] at 520 eV photon energy with $C_{Radiolysis}^{Conversion} = 1.6$ *and the beam placed at the center at* $x = 0\ \mu m$*. The location of the maximum and minimum values for the concentration and temperature are marked in Figure 31.*

Furthermore, the total photon flux and the beam position are the main experimental control variables. Thus, to gain better control over my experimental procedure, for the temperature I present a parameter study regarding both parameters in Figure 33. From Figure 32 we can derive that the temperatures reach their steady-state plateaus after a couple of seconds. In the following discussion, I only consider the steady-state values after 12 s. As it can be seen in Figure 33c-e, with the beam closer to the silicon frame (beam positions marked as vertical black lines), the heat is dissipated more easily and the heat distribution within the probing chamber changes drastically. Figure 33b shows the correlation between the beam position and the minimum, maximum, and average temperature values within the probing chamber as a fraction of the respective value at $x = 0\ \mu\mathrm{m}$. It is apparent that the influence of the beam position on the temperature is more crucial for higher beam intensities. For a total photon flux of 1·10[12] s[-1], by moving the beam to the corner of the membrane window at $x = 315\ \mu\mathrm{m}$, the maximum temperature can be decreased by about 30%. For a higher total photon flux of 5·10[12] s[-1], however, the maximum temperature is decreased by about 54%. This correlates to a reduction in maximum temperature from 111.3 °C down to 51.0 °C when moving the beam from the center next to the silicon frame at $x = 315\ \mu\mathrm{m}$.

Furthermore, Figure 33a summarizes the expected maximum temperatures after 12 s for beam positions from 0 to 315 µm and total photon fluxes between 1·10[11] s[-1] and 1·10[13] s[-1].

The presented values give a range of feasible beam intensities and answer a few of the initial questions. First, even for high photon flux intensities of $1 \cdot 10^{13}$ s^{-1}, the boiling points of EC and PC at 242 °C and 248 °C will not be reached [1], [40], [236]. Thus, bubble creation due to boiling of the electrolyte appears to be of no concern in my experiment. Furthermore, 1M $LiPF_6$ in EC:DMC was shown to be stable up to 180 °C under argon atmosphere [237]–[240]. Thus, by not exceeding a total photon flux of about $7 \cdot 10^{12}$ s^{-1}, the temperature of the electrolyte remains below 160 °C and I expect no thermal decomposition. This confines the decomposition of the electrolyte to radiolysis, which in turn may narrow the possible number of different decomposition products. As described earlier, the bubble formation / radiolysis leaves traces in the electrolyte thin-layer, which must be considered when interpreting the sXAS data. The smaller the number of decomposition products is, the more reliable and easier will be the evaluation of the data. Given the gas solubility being strongly temperature dependent, which in turn is heavily influenced by the beam position, I conclude that the beam position is crucial for a good reproducibility of the bubble creation procedure.

When it comes to the concentration of the gaseous decomposition products, the amount of substance, which is injected into the computational domain through R_{Beam} in (16) accumulates with time due to the no flux boundary condition encapsulating the whole liquid. In comparison to the temperature, no plateau value is reached, and the concentration increases steadily. Consequently, as it can be seen in Figure 31, a concentration gradient originates from the center of the beam at the upper membrane at $x = 0\ \mu\mathrm{m}$ and extends throughout the probing chamber into the channels and reservoirs. Figure 32 shows the maximum, minimum and average concentration within the probing chamber as function of time. The maximum, minimum, and average concentration after 60 s is 36.8 mM, 22.6 mM and 30.3 mM, respectively. Figure 34 summarizes how the concentration gradient evolves with different beam positions after 60 s of irradiation. From Figure 34a, it is apparent that the maximum concentration is less dependent on the beam position than what we have seen for the temperature before. Here, the maximum concentration is increased only by about 20% percent when moving the beam position from the center of the membrane window ($x = 0\ \mu\mathrm{m}$) to its corner at $x = 315\ \mu\mathrm{m}$. The influence of the beam position on the average and the minimum concentration turned out to be negligible (<3%) and is not shown here. Further, the influence of the beam intensity appears to be less pronounced compared to the temperature behavior. For all beam intensities between $1 \cdot 10^{12}$ s^{-1} and $1 \cdot 10^{13}$ s^{-1} the curves in Figure 34a are comparable. I conclude that the small deviation stems from the temperature dependence of the diffusion coefficient (see Table 2) and the position dependence of the maximum temperature discussed above.

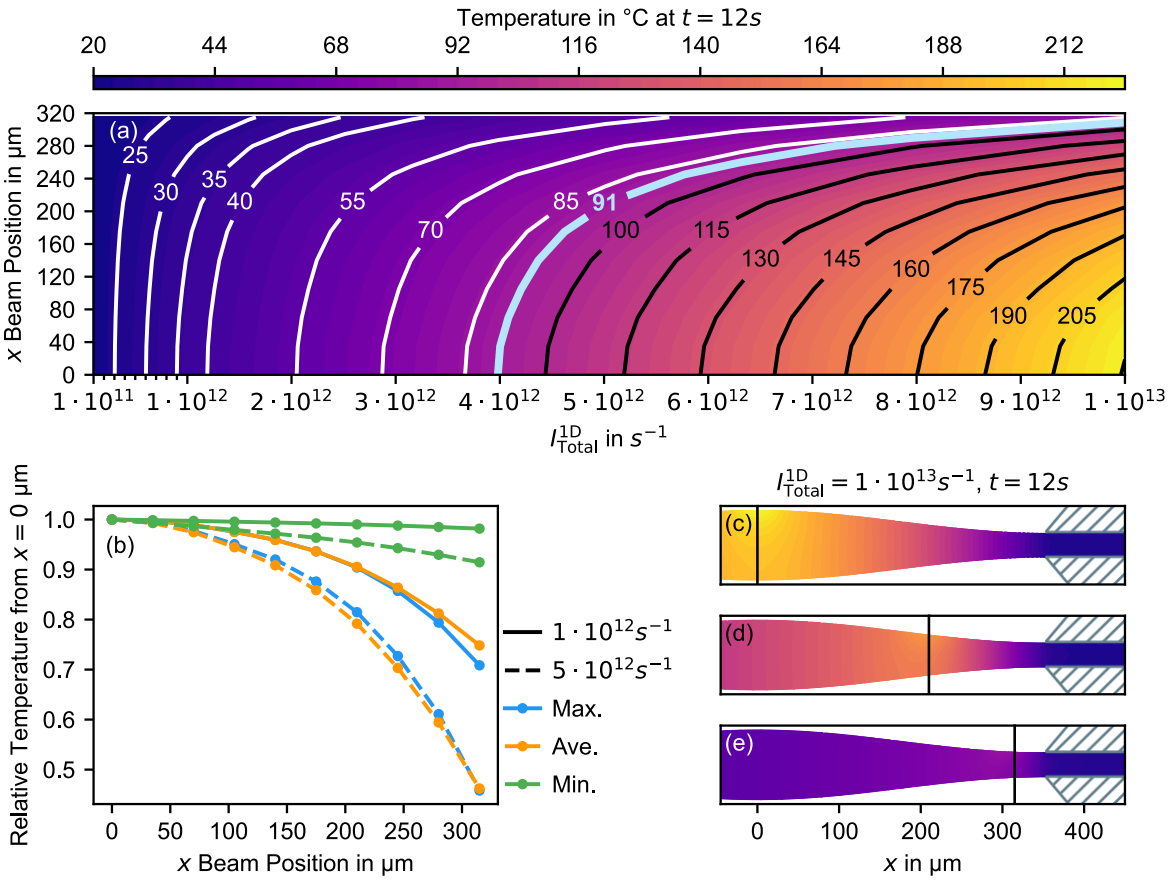

Figure 33 (a) Maximum temperature within the probing volume after 12 s as a function of the total photon intensity I^{1D}_{Total} and the beam's off-center position from the center of the membrane window at $x = 0\ \mu m$ in the direction of the silicon frames as shown in (c)-(e). Simulated for a photon energy of 520 eV. The location of the maximum temperature correlates to the beam's x position along the upper membrane window. (b) Influence of the beam position on the temperature for total photon intensities of $1 \cdot 10^{12}$ s^{-1} and $5 \cdot 10^{12}$ s^{-1}. The values relate to the value of each quantity with the beam at the center $x = 0\ \mu m$. (c)-(e) Spatial distribution of the temperature after 12 s with a total photon intensity of $1 \cdot 10^{13}$ s^{-1} with the beam at $x = 0\ \mu m$ (a), $x = 210\ \mu m$ (d) and $x = 315\ \mu m$ (e). Beam position is marked as a vertical black line. Colors correspond to the color bar shown at the top.

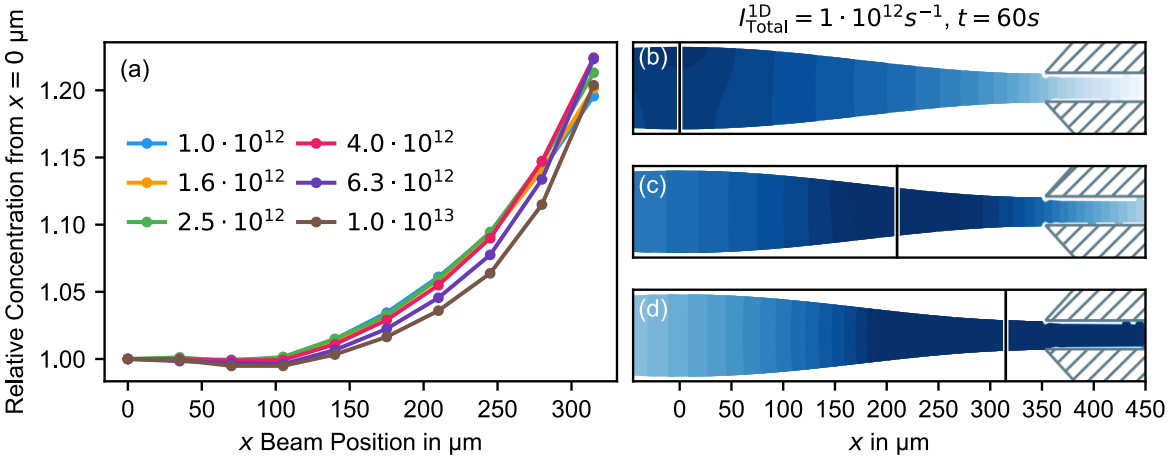

Figure 34 (a) Influence of the beam position on the maximum concentration for total photon intensities between $1.0 \cdot 10^{12}$ s^{-1} and $1.0 \cdot 10^{13}$ s^{-1} with $C^{Conversion}_{Radiolysis} = 1.6$. The values relate to the value with the beam at the center $x = 0\ \mu m$. (b)-(d) Spatial distribution of the concentration after 60 s with a total photon intensity of $1 \cdot 10^{12}$ s^{-1} with the beam at $x = 0\ \mu m$ (b), $x = 210\ \mu m$ (c) and $x = 315\ \mu m$ (d). Beam position is marked as a vertical black line. Color coding ranges from 200 to 307 mM in all plots.

I want to mention that Grogan *et al.* [209], who modelled the bubble formation in Transmission Electron Microscopy (TEM) in aqueous solution, took concentration dependent back reactions of radiolysis products into account (e.g. $2\mathrm{H}^{+}+\mathrm{O}^{2-}\leftrightarrow\mathrm{H_2O}$). This dampens the evolution of product concentration and allows the system to reach a time-independent concentration plateau, similar to what we have seen for the temperature in my simulation. When the beam intensity is adjusted in a way that this plateau lies below the nucleation supersaturation, then continuous TEM operation without bubble formation appears to be possible. While such back reactions are reasonable in the case of water, I take them as negligible for the decarboxylation and decarbonylation of an organic electrolyte. However, I still suggest a concentration dependent $C_{\mathrm{Radiolysis}}^{\mathrm{Conversion}}(c)$, because the effective cross section of radiolysis might decrease for higher concentrations. To limit the complexity of my simulation and the number of necessary parameters, I did not include such consideration.

Furthermore, the total amount of substance within the whole liquid domain including the reservoirs is given as a function of time in Figure 35a, with the slope being proportional to the total beam flux $I_{\mathrm{Total}}^{\mathrm{1D}}$ and $C_{\mathrm{Radiolysis}}^{\mathrm{Conversion}}$. To put the amount of substance from Figure 35a into perspective, I calculated the corresponding ideal gas volume assuming 22.4 $\mathrm{dm^3\,mol^{-1}}$ and plotted different ellipses with equivalent area in Figure 35b. With this I want to present a ballpark figure of how much gas is required to fully fill the probing chamber with a bubble.

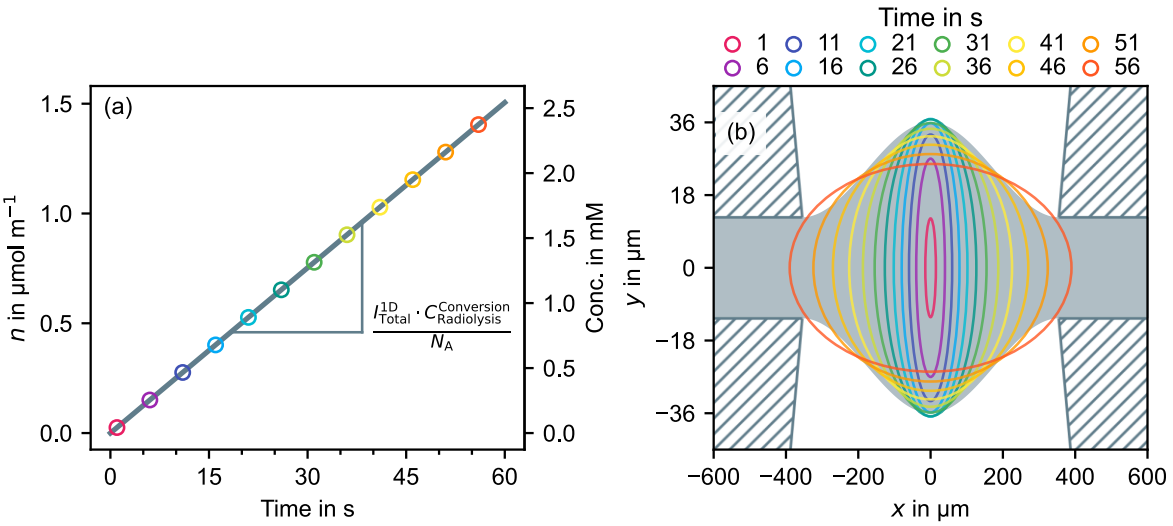

Figure 35 (a) Total amount of substance n (left vertical axis) injected into the computational domain through R_{Beam} in (16) as a function of the irradiation time. Simulated for a total photon intensity of $1{\cdot}10^{12}$ s^{-1} with $C_{Radiolysis}^{Conversion} = 1.6$. Secondary vertical axis on the right gives the corresponding equilibrium concentration when the total amount of substance is spread evenly across the whole computational domain. (b) Ellipses that illustrate the equivalent area when the total amount of substance from (a) is considered an ideal gas with 22.41 dm^3 mol^{-1}. Ellipses are color coded to match the points in time and n from (a). Ellipses are plotted on top of the computational domain's geometry shown in Figure 28 to illustrate how much n is necessary to fill the probing chamber.

I want to distinguish two types of concentration quantities which are of particular importance for the following discussion. First, the local concentration during X-ray irradiation, which follows

a concentration gradient that originates from the center of the beam, as it is shown in Figure 31. The concentration gradient of the local concentration field is determined by the interplay between the total photon intensity (creation of the radiolysis species) and diffusion (dissipation of the radiolysis species). Second, the equilibrium concentration, which refers to the constant concentration in an infinite future after the irradiation stopped and the total amount of radiolysis products has spread evenly within the whole liquid volume. The equilibrium concentration is solely proportional to the total radiation dose. We have witnessed in Figure 32 the maximum, minimum and average concentration to be 36.8 mM, 22.6 mM and 30.3 mM after 60s. In contrast, the secondary axis in Figure 35a gives the theoretical equilibrium concentration, which ends up at about 2.5 mM after 60 s. This already highlights the huge discrepancy between these two quantities.

When it comes to the intentional formation of a bubble, each quantity determines a distinctive aspect of the problem. For the bubble nucleation, the maximum of the local concentration field in relation to the solubility limit is crucial. Thus, the bubble forms and grows within the oversaturation of the local concentration field. Due to the convection caused by the bubble growth itself and by diffusion, this oversaturation disperses over time and converges to the equilibrium concentration. Thermodynamically, the bubble is only stable over time inside a saturated electrolyte, because otherwise the bubble gas species redissolve, making the bubble shrink and disappear again [241]. Thus, for a stable bubble, the respective equilibrium concentration must lie above the solubility limit of the bubble gas species. Based on this, I want to stipulate a hard requirement for a successful experimental procedure: before the maximum of the local concentration field triggers the bubble nucleation due to local oversaturation, the electrolyte must have been sufficiently enriched with gaseous radiolysis products to remain fully saturated at the equilibrium. The total amount of radiolysis products above its solubility limit determines the ultimate size of the bubble.

The local concentration field is determined by the beam intensity. Moreover, the solubility limits are temperature dependent, which in turn changes with the beam position as seen in Figure 33. This makes the beam intensity and position the main experimental control variables. I will come back to the above stipulation, but for a more elaborate understanding, I want to briefly discuss the topic of nucleation first.

A bubble emerges via the formation of a stable nucleus. Nucleation is described in its most fundamental form by the Classical Nucleation Theory (CNT) [242]. From a thermodynamic point of view as grounded in the CNT, the formation of a nucleus requires the surface energy of the boundary between the solvent and emerging gas phase. This energy in turn is gained from relieving the high chemical potential of the dissolved gas species inside the solvent [243].

For sufficient chemical potential and thus driving force, the concentration c_i of the solute i must exceed its equilibrium concentration $c_i^{\mathrm{eq}}(T,p)$. With this, I quantify the degree of oversaturation ζ through (30). In the following, $c_i^{\mathrm{eq}}(T,p)$ is also referred to as c_{Sol}^{i}.

$$\zeta_i = \frac{c_i}{c_i^{\mathrm{eq}}(T,p)} \tag{30}$$

One can distinguish between hetero- and homogeneous nucleation [244]. Heterogenous nucleation takes place at an already existing surface like the container wall or on the surface of particles dispersed in the liquid. In that case, less total surface energy is required. Heterogenous nucleation is favored kinetically and takes place more readily. Homogeneous nucleation, on the other hand, happens on its own without additional pre-existing surfaces. Homogeneous nucleation was found experimentally to require large oversaturation ζ^{homo} with $c_i^{\mathrm{homo}} \gg c_i^{\mathrm{eq}}(T,p)$. Based on this, the solution can exist in two concentration regimes: undersaturation $c_i < c_i^{\mathrm{eq}}(T,p)$ where no nucleation, and oversaturation $c_i^{\mathrm{eq}}(T,p) < c_i < c_i^{\mathrm{homo}}$ where only heterogeneous nucleation can take place. Homogeneous nucleation takes place when $c_i = c_i^{\mathrm{homo}}$ and consequently determines the upper concentration limit of the oversaturation regime. In general, nucleation is considered a statistical event which becomes more likely for a high degree of oversaturation [243]. While the probability of a single nucleation event is hard to formulate, the kinetics of nucleation are commonly described by the rate of nucleation J_{Nuc} as given in (31) [244] with a kinetic constant B, the specific interfacial free energy γ, the volume growth unit Ω, the degree of supersaturation ζ and the factor f, which describes heterogenous nucleation for $0 < f \ll 1$ and homogeneous nucleation for $f = 1$.

$$J_{\mathrm{Nuc}} = Be^{-f\frac{16\pi}{3}\frac{\Omega^2\gamma^3}{(kT)^3\,[\ln 1+\zeta]^2}} \tag{31}$$

In my experimental work, through XAS at the oxygen K-edge, I have identified CO_2 and CO as the main bubble gas species. The identification of the gas species based on their sXAS spectra are presented in more detail later under IV.B.2.b and Figure 62. Based on Figure 62b, for my simulation I assume CO and CO_2 to be produced by radiolysis in a 2:1 ratio according to (32). $\mathrm{M_{Trace}}$ corresponds to the non-gaseous radiolysis products that remain dissolved as trace products within the electrolyte thin-layer. These compounds must be considered when interpreting the obtained transmission sXAS spectra and their contribution therefore needs to be minimized. This already makes clear, that the radiolysis is supposed to create just the right amount necessary for a sufficient bubble, but not more.

$$\text{Electrolyte} \xrightarrow{C_{\text{Radiolysis}}^{\text{Conversion}}} 2\text{CO} + \text{CO}_2 + x\text{M}_{\text{Trace}} \quad (32)$$

For the solubility limits of CO_2, I rely on the data from Anouti *et al.* for the pure solvents PC, EC and DMC [245]. However, Dougassa *et al.* reported that the CO_2 solubility at room temperature in EC:DMC decreases from 143 mM to 124 mM upon addition of 1M $LiPF_6$ [246]. On top of that, their data shows that the CO_2 solubility at room temperature in 1M $LiPF_6$ EC:DMC is comparable to the solubility of 120 mM in the 1M $LiPF_6$ in PC electrolyte. Thus, for the solubility considerations in this work, I see the solubility of CO_2 in neat PC as an appropriate simplified model system and consider this approximation at the same time to be on the conservative side. In contrast to CO_2, CO exhibits a much smaller solubility in PC of only 18 mM at room temperature and appears to remain almost constant in the range between 25 °C and 70 °C [247].

Unfortunately, there are only few literature entries on the saturation for bubble nucleation in organic electrolytes, even fewer on CO or CO_2 in PC. Thus, I rely on the available values for aqueous solutions. It can be argued that the oversaturation phenomenon is mostly determined by the gas species itself, given the same type of solvent. I will focus on heterogeneous nucleation for the estimation of ζ^{bb}, as it is kinetically favored, and I consider it the more probable type of nucleation for the present conditions. As Lubetkin summarized in [248] for aqueous solutions, experimentally observed values of the supersaturation for heterogenous nucleation range from 1.3 to 20 for CO_2 and was reported to be around 80 for CO. To put these number into perspective: $\zeta_{\text{CO}_2}^{bb} = 5$ is commonly bottled in carbonated soda drinks, which have a high, thus sparkling, bubble nucleation rate on purpose. Therefore, in the following discussion I take $\zeta_{\text{CO}_2}^{bb} = 3.0$ as a guideline and consider it an estimate on the conservative side.

With this information, I want to pause and assign distinctive roles to CO and CO_2. This is in analogy to the consideration of Grogan *et al.* [209], who proposed this model for O_2 and H_2 in the bubble formation in aqueous solution in TEM. In comparison to each other, CO_2 has a much higher solubility but requires a much lower degree of oversaturation for heterogeneous nucleation. Additionally, it's solubility is strongly dependent on the temperature as shown in Figure 36a, which gives me additional control over the nucleation timing as I will demonstrate at the end of this chapter. With this, I consider CO_2 to be the decisive species for the bubble nucleation via heterogeneous nucleation. Due to its high solubility however, I assume CO_2 to mostly remain dissolved in the electrolyte and only have a minor contribution to the final bubble gas. On the other hand, CO's nucleation oversaturation is much higher compared to CO_2 and I assume it does not precipitate on its own. Based on its overall much smaller solubility however, if a bubble is already present, I propose CO to provide the main contribution to the

bubble growth and volume. Considering all this, CO_2 acts as the nucleation and CO as the bubble formation agent.

The roles of CO and CO_2 are demonstrated by the simulation presented in Figure 36b,c assuming $C_{\mathrm{Radiolysis}}^{\mathrm{Conversion}}$ of 5.7 and a total beam intensity $I_{\mathrm{Total}}^{\mathrm{1D}}$ of $1 \cdot 10^{12}$ s^{-1} for a critical bubble formation oversaturation $\zeta_{\mathrm{CO_2}}^{\mathrm{bb}} = 3.0$. The solubility limits are calculated based on the maximum value of the temperature, which was 36.1 °C in the simulation for Figure 36. The degrees of supersaturation are derived from the minimum value of the solubility and the maximum value of the concentration at the center of the beam at $x = 0\ \mu\mathrm{m}$ (see Figure 31). As it can be seen in Figure 36b,c, the maximum concentration of both CO as well as CO_2 (Figure 36c) and the corresponding degrees of oversaturation (Figure 36b) increase steadily with irradiation time. The degree of oversaturation for CO_2 is simultaneously amplified by the reduction in solubility due to the heating of the electrolyte. After 54.8 min, with CO_2's oversaturation at the value of 3.0, I assert bubble nucleation and the irradiation is stopped. Note that at this point CO's oversaturation itself is only at about 33.6 and, compared to its critical heterogeneous oversaturation of 80, unlikely to nucleate a bubble on its own, yet. The electrolyte cools down rapidly and the CO_2's solubility increases again. At the same time, the local concentration gradient starts to dissipate. In this simulation I neglect the bubble formation and I approximate the dissipation solely based on diffusion without any convection caused by the bubble growth. Both concentrations (CO and CO_2) disperse with time via diffusion to ultimately converge the equilibrium concentration over a time frame of about 30 min. The equilibrium concentrations of both CO and CO_2 end up above their solubility limits ($c_{\mathrm{eq}}^{\mathrm{CO}} \gg c_{\mathrm{Sol}}^{\mathrm{CO}},\ n_{\mathrm{Bubble}}^{\mathrm{CO}} > 0$ as well as $c_{\mathrm{eq}}^{\mathrm{CO_2}} \gg c_{\mathrm{Sol}}^{\mathrm{CO_2}},\ n_{\mathrm{Bubble}}^{\mathrm{CO_2}} > 0$) and one would expect a bubble containing both gas species. However, CO's contribution is much larger with $n_{\mathrm{Bubble}}^{\mathrm{CO_2}} \ll n_{\mathrm{Bubble}}^{\mathrm{CO}}$, making CO the bubble formation agent. Note that $n_{\mathrm{Bubble}}^{i} = n_{\mathrm{Total}}^{i} - n_{\mathrm{Sol}}^{i}$ with n^i being the integral of the equilibrium concentrations c_{eq}^{i} over the whole electrolyte computational volume. If not stated otherwise, for the solubility limits I assume 293 K and 1 atm pressure.

Being aware of the distinct rules of CO_2 and CO, with the help of my simulation, I want to find the ideal total photon intensity for my experimental procedure. For this, based on Figure 37, I want to judge the influence of the total photon intensity based on 3 different quantities, which I consider to be very critical for a successful experiment.

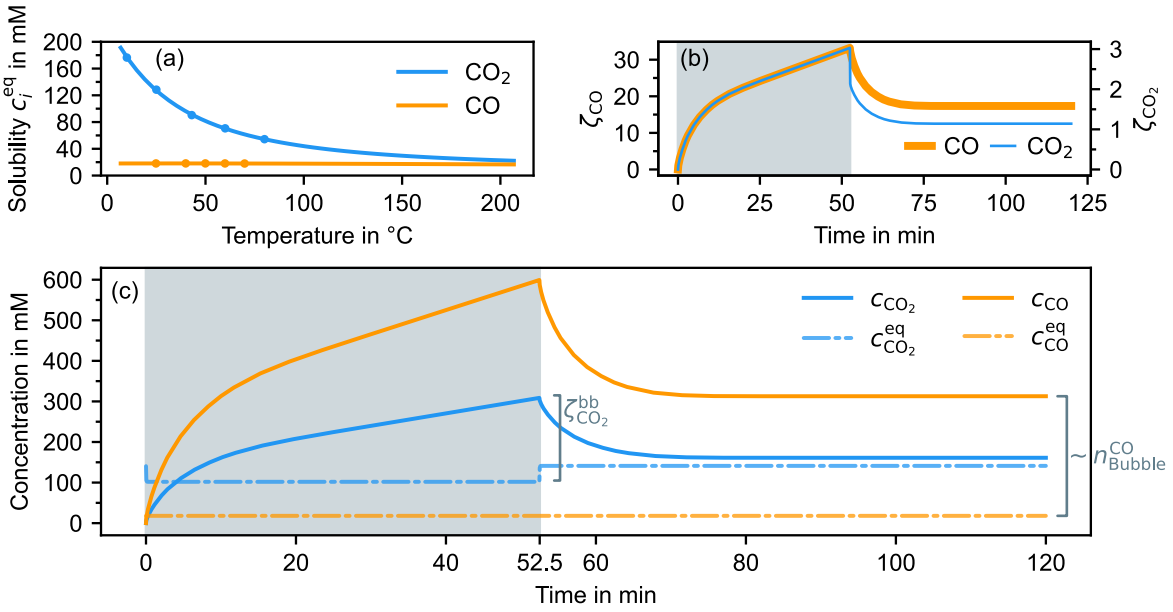

Figure 36 (a) Temperature dependence of the solubility of CO_2 from [245] and CO from [247]. Experimental values are marked as points, interpolation curves are calculated based on the equations and parameters given in the corresponding references. (b) Degree of oversaturation ζ for CO and CO_2 as function of time, corresponding to the data in (c). (c) Maximum concentration of CO and CO_2 as function of time together with their solubility limits $c_i^{eq}(T,p)$. Data simulated for a total photon intensity I_{Total}^{1D} of $1{\cdot}10^{12}$ s^{-1} and $C_{Radiolysis}^{Conversion}$ of 5.7. The solubility limits are calculated with the data from (a) at the point of maximum temperature at the center of the beam with the beam at $x = 0$ μm. When CO_2 has reached its asserted critical bubble formation oversaturation $\zeta_{CO_2}^{bb}$ of 3.0, bubble formation is assumed and the beam is then turned off. The maximum concentrations dissipate to converge the equilibrium concentration. n_{Bubble} and the bubble size is proportional to the difference between equilibrium concentration and solubility limit.

The first one considers the final, equilibrium bubble size. As I stated in the beginning, the simulation and the experimental procedure were developed in tandem. In my experimental work, I struggled creating a bubble that was large enough to stabilize a sufficiently thin liquid thin-layer. The probing chamber in my model has an area of $3.45{\cdot}10^{-6}$ dm^2. I assume an ideal gas with 22.41 dm^3 mol^{-1} and n_{Bubble}, which is required to fill the whole probing chamber, is 1.53 µmol m^{-1}. In Figure 37 the orange line with diamond-shaped markers gives the degree of supersaturation of CO_2 for the point in time when n_{Bubble} (calculated for CO as the bubble formation agent) reached the threshold value of 1.53 µmol m^{-1}. The way to interpret this correlation is as follows. The rate of nucleation grows exponentially with the degree of supersaturation as described in (31). Thus, the probability to find a bubble-free system in each state plummets with increasing degree of supersaturation $\zeta_{\mathrm{CO_2}}$. Consequently, Figure 37 indicates that the likeliness of a premature bubble formation of an insufficiently large bubble grows exponentially with the total photon intensity $I_{\mathrm{Total}}^{\mathrm{1D}}$. However, when it comes to premature bubble formation, Figure 37 yields a crucial threshold value for the total photon intensity. For intensities below $1.0{\cdot}10^{12}$ s^{-1} CO_2 remains undersaturated with $\zeta_{\mathrm{CO_2}} < 1$ until the electrolyte is enriched with the necessary n_{Bubble} of 1.53 µmol m^{-1}. Because no bubble formation is to be expected with $\zeta_{\mathrm{CO_2}} < 1$, I deduce that premature bubble formation does not take place with

beam intensities at or below $1.0 \cdot 10^{12}$ s^{-1}. This threshold value is marked as the dashed orange horizontal line in Figure 37. Choosing the total beam intensity as small as possible appears to be a straightforward remedy to avoid premature bubble formation all together.

However, the blue line with circles in Figure 37 shows the total amount of gaseous radiolysis products $n_{\mathrm{Total}} = n_{\mathrm{CO_2}} + n_{\mathrm{CO}}$ up to the point where CO_2 reaches supersaturation $\zeta_{\mathrm{CO_2}} = 3.0$ as a function of the total beam intensity $I_{\mathrm{Total}}^{\mathrm{1D}}$. The value for n_{Total} at $\zeta_{\mathrm{CO_2}} = 3.0$ increases rapidly with decreasing $I_{\mathrm{Total}}^{\mathrm{1D}}$. From (32) we know that n_{Total} is connected to non-gaseous radiolysis products $\mathrm{M_{Trace}}$, which must be avoided for easier interpretation of the transmission sXAS spectra. Thus, albeit choosing small $I_{\mathrm{Total}}^{\mathrm{1D}}$ avoids premature bubble formation, it is detrimental for the transmission sXAS afterwards by contaminating the liquid thin-layer with trace species. When we judge both quantities discussed so far based on their positive contribution, we can infer that the ideal total photon intensity lies around $2.0 \cdot 10^{12}$ s^{-1} as it is illustrated at the top of Figure 37. In this range one would accept a certain failure rate through premature bubble formation to reduce the trace contamination.

The last quantity I want to discuss stems from a pure practicability point of view. The green line with squares in Figure 37 shows the time until CO_2 reaches supersaturation $\zeta_{\mathrm{CO_2}} = 3.0$ and bubble formation can be somewhat expected. Considering the time constrained nature of synchrotron experiments, one should not waste unnecessary time for bubble formation before being able to conduct any sXAS measurement. As it can be seen in Figure 37, the time to bubble formation increases rapidly for total beam intensities below $9.0 \cdot 10^{11}$ s^{-1}. Furthermore, considering how long it takes to prepare a cell and conduct the electrochemical procedures beforehand, when it comes to time management, losing a cell to premature bubble formation is way costlier than a supposedly slower bubble formation. Thus, because avoiding premature bubble formation is the key aspect, I would still consider $1.0 \cdot 10^{12}$ s^{-1} the ideal beam intensity for my experimental approach. Unfortunately, as we have seen in Figure 36b,c, with this beam intensity of $1.0 \cdot 10^{12}$ s^{-1} reaching $\zeta_{\mathrm{CO_2}} = 3.0$ takes about an hour (54.8 min), which I deem too long for any synchrotron sXAS experiment. Thus, with the insight I obtained from my simulation so far, I went on and improved my experimental bubble formation procedure as follows.

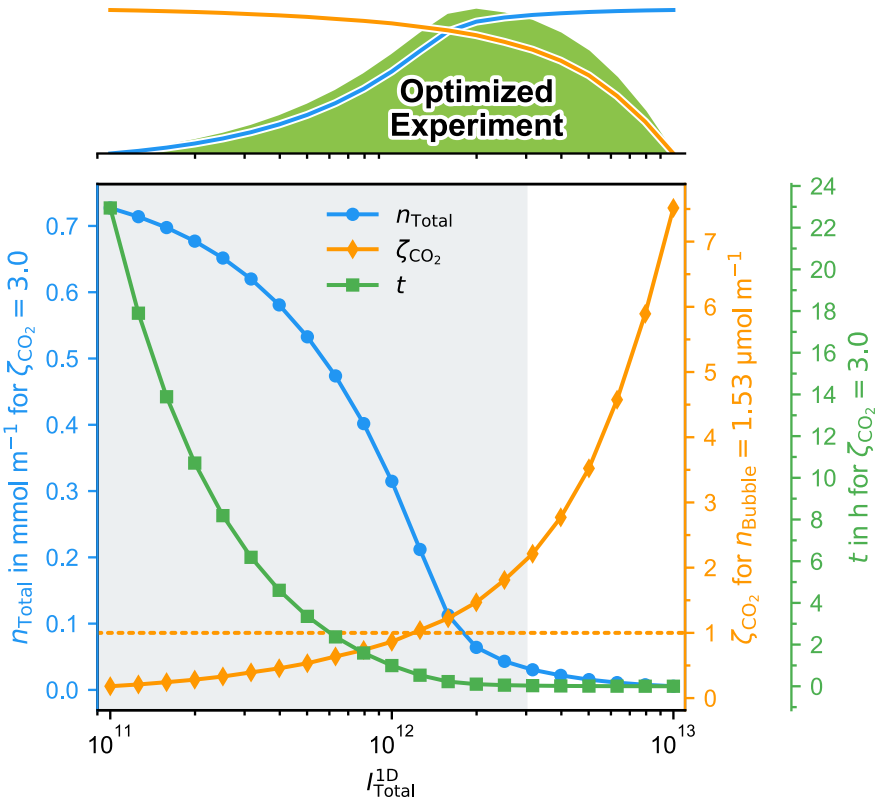

Figure 37 (Blue) Total amount of substance injected into the computational domain until CO_2 has reached its asserted critical bubble formation oversaturation $\zeta^{bb}_{CO_2}$ of 3.0 as a function of total photon intensity I^{1D}_{Total}. (Orange) CO_2's degree of oversaturation as a function of total photon intensity when the threshold value of n_{Bubble} with 1.53 µmol m^{-1} has been reached. n_{Bubble} is calculated for CO as the bubble formation agent. (Green) Time for CO_2 to reach its asserted critical bubble formation oversaturation $\zeta^{bb}_{CO_2}$ of 3.0 as a function of total photon intensity. All values have been simulated with $C^{Conversion}_{Radiolysis}$ of 5.7. The grey area in the background indicates the maximum temperature below 70 °C, which correlates to the limits of the experimental values of the solubility data from Figure 36a.

My idea was to utilize the temperature-dependent solubility of CO_2 to trigger the bubble formation intentionally after enriching the electrolyte with sufficient radiolysis gas products to form a stable bubble. This way, I can reduce the risk of premature bubble formation (and with this making the process more reliable), while at the same time minimize n_{Total} together with $\mathrm{M}_{\mathrm{Trace}}$ and save overall experimental time. The procedure for this works as follows and the data from the corresponding simulation is demonstrated in Figure 38, assuming $C^{\mathrm{Conversion}}_{\mathrm{Radiolysis}}$ of 5.7. First, I use my preferred total photon intensity of $1.0 \cdot 10^{12}$ s^{-1} to enrich the electrolyte as fast as possible, but without risking any premature bubble formation, as we have discussed before. As soon as n_{Bubble} reached its required quantity of 1.53 µmol m^{-1} after 209 s, I increase the photon intensity to $5.0 \cdot 10^{12}$ s^{-1}. In my experimental approach this is done by opening the beamline apertures. The higher photon intensity increases the temperature rapidly from 36.7 to 109.8 °C and with this the oversaturation degree of CO_2 rises from 0.92 (undersaturated) to 3.0 (oversaturated) within 5 s, from which I assert to trigger the bubble nucleation. The time

frame when CO_2's supersaturation is amplified by the step up in X-ray intensity is shaded in light blue in Figure 38b.

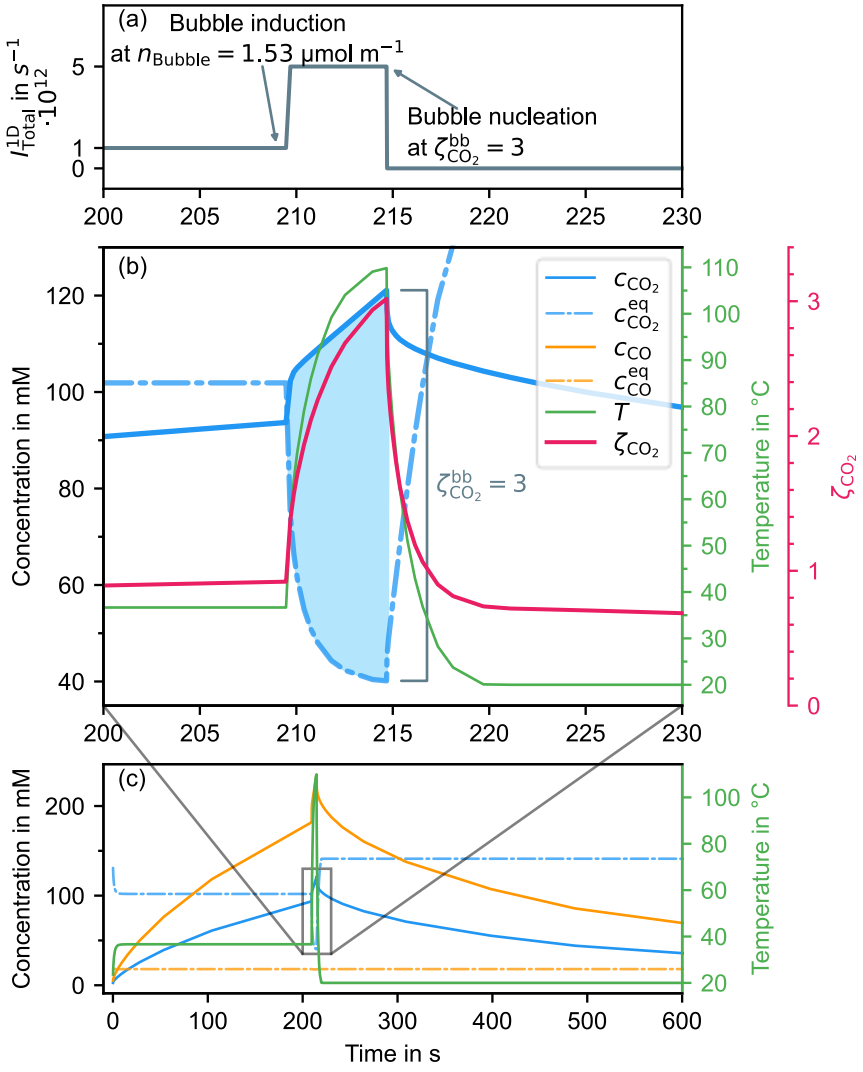

Figure 38 (a) Total photon intensity profile used to trigger the bubble on purpose. When the threshold value of n_{Bubble} with 1.53 µmol m^{-1} has been reached (calculated for CO as the bubble formation agent), the beam intensity is increased by 5 times from 1·10^{12} s^{-1} to 5.0·10^{12} s^{-1} to abruptly decrease CO_2's solubility. When CO_2 has reached its asserted critical bubble formation oversaturation $\zeta^{bb}_{CO_2}$ of 3.0, bubble formation is expected to take place and the beam is then turned off. (b)-(c) Maximum concentration as well as the solubility limits of CO and CO_2 as function of time together with the maximum temperature at the center of the beam with the beam at $x = 0\ \mu m$. The solubility limits are calculated with the data from Figure 36a at the point of maximum temperature. All values are calculated with $C^{Conversion}_{Radiolysis}$ of 5.7.

We can evaluate the achieved improvement by this approach ("bubble trigger approach") by comparing it to the simulation discussed before in Figure 36, where I simulated it with a constant total photon intensity of 1.0·10^{12} s^{-1} ("conventional approach"). The comparison is summarized in Figure 39. With the bubble trigger approach, the bubble is intentionally formed after only 3.5 min, which is about 15 times faster compared to the conventional approach with 52.5 min. The bubble has a n^{CO}_{Bubble} of 3.2 µmol m^{-1} and with this is both stable and sufficiently large $1.53\ \mu mol\ m^{-1} < n^{CO}_{Bubble}$. In general, n^{CO}_{Bubble} and the size of the bubble can be controlled

via the beam intensity and the bubble trigger time. However, the discrepancy between the targeted value of 1.53 µmol m^{-1} and the final value of 3.2 µmol m^{-1} stems from the radiolysis within the 5 s window between bubble induction and the bubble nucleation (see Figure 38a,b). If a precise control of the bubble size is necessary, this discrepancy must be accounted for in the calculation of the induction time. For now, to only explore the general idea of this approach, this exceeds the scope of this discussion. More importantly, it must be noted that the total amount of radiolysis products n_{Total} to reach $\zeta_{\mathrm{CO_2}} = 3.0$ is only 21.0 µmol m^{-1} for the bubble trigger approach compared to 280.5 µmol m^{-1} for the conventional one. Because n_{Total} is proportional to $\mathrm{M_{Trace}}$, the bubble trigger approach facilitates the sXAS measurements as less trace radiolysis products must be considered. In the same regard, with the bubble trigger approach, the bubble is expected to not contain any CO_2 because $n_{\mathrm{Bubble}}^{\mathrm{CO_2}} < 0$. Having to deal with only one gaseous species would once again simplify the interpretation of the sXAS data.

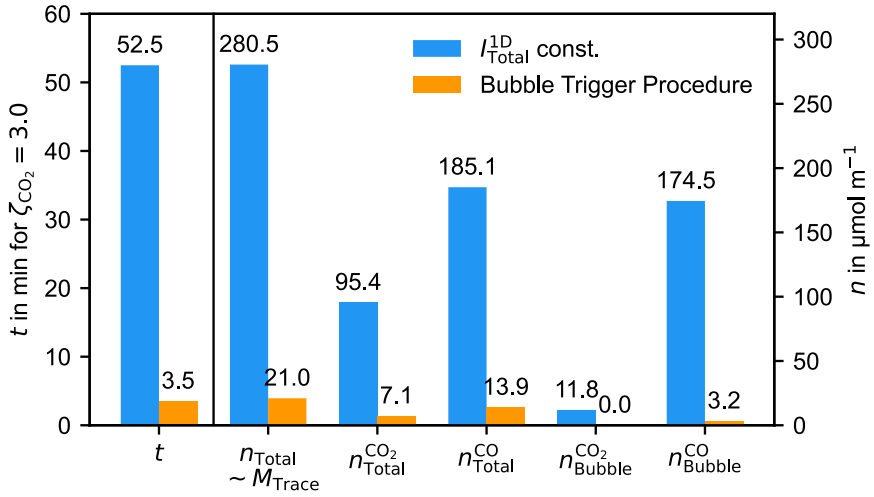

Figure 39 Comparison between the two bubble formation procedures: (blue) with a constant total photon intensity of 1·10^{12} s^{-1} as shown in Figure 36b,c, and (orange) by purposely triggering the nucleation of the bubble when the threshold value of n_{Bubble} with 1.53 µmol m^{-1} has been reached, as shown in Figure 38. The compared values are: the time t until a bubble nucleates at ζ_{CO_2} of 3.0, the total amount of substance that has been introduce into the computational domain n_{Total} and the corresponding values n^i_{Total} for CO and CO_2 assuming a 2:1 ratio according to (32) as well as the amount of substance expected as the bubble n^i_{Bubble} for CO and CO_2, calculated through $n^i_{Bubble} = n^i_{Total} - n^i_{Sol}$.

So far, I have discussed the total photon intensity as important experimental control parameter and demonstrated with the help of my simulation how a refined intensity profile can be used to control the bubble size and avoid unnecessary contamination of the liquid thin-film. This approach relies on the local heating of the electrolyte by the high intensity X-ray beam to reduce the local solubility limit of CO_2. As we have seen in Figure 33b and Figure 34b, both the electrolyte temperature as well as the maximum concentration within the local concentration field depend on the beam position. Besides the beam intensity itself, the beam position is the second crucial experimental parameter I must control in my experiment. To

conclude this chapter, I briefly want to explore the beam position's influence on the experimental bubble induction procedure discussed above. In analogy to Figure 38b, Figure 40a shows CO_2's maximum concentration and its solubility limit simulated at different beam positions with a total photon intensity of $1.0 \cdot 10^{12}$ s^{-1} and $C_{\text{Radiolysis}}^{\text{Conversion}}$ of 5.7. The total photon intensity was increased to $5.0 \cdot 10^{12}$ s^{-1} when n_{Bubble} reached its required quantity of 1.53 µmol m^{-1} after about 209 s for all beam positions. Due to the lower resulting electrolyte temperature for beam positions closer to the corner of the membrane windows, CO_2's solubility is higher and less responsive to the sudden increase in the total photon flux for off-centered beam positions. It therefore takes longer to finally reach $\zeta_{CO_2} = 3.0$ for bubble nucleation (see Figure 40a) and ultimately results in higher n_{Total} and M_{Trace} as summarized in Figure 40, where n_{Total} increases by about 60% when moving the beam 315 µm away from the center. For an ideal result with good reproducibility one must aim the beam at the center. However, from Figure 40 I deduce that the experimental procedure has a certain leeway, as n_{Total} remains within a deviation below 5% for beam positions up to 175 µm off-center.

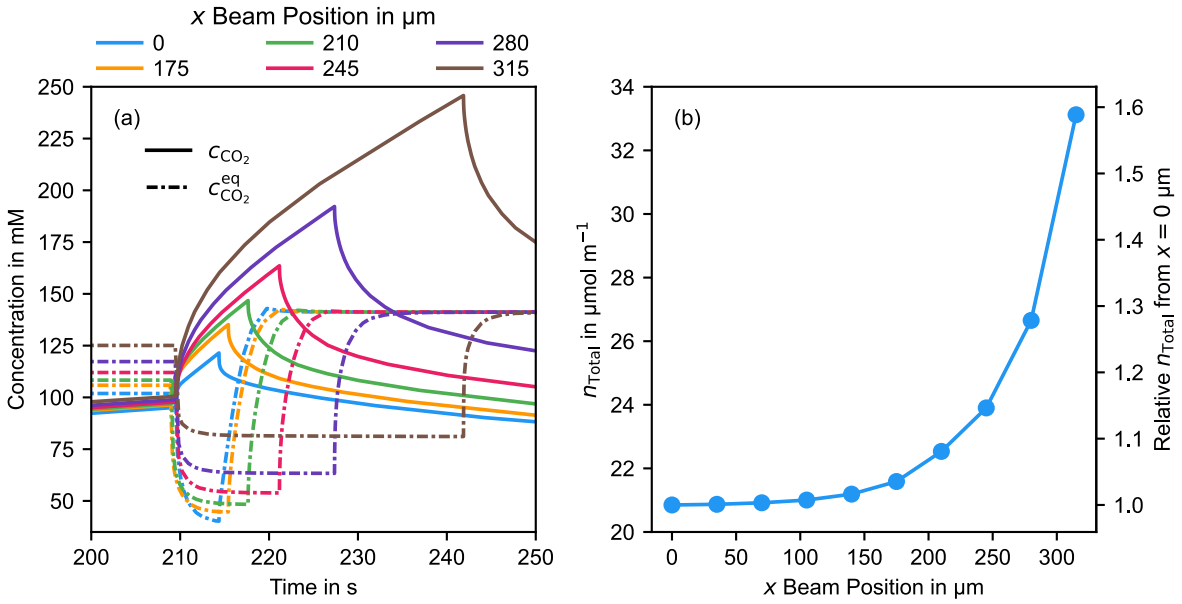

Figure 40 Influence of the beam position on the bubble trigger procedure. (a) Maximum concentration as well as the solubility limit of CO_2 as a function of time for six different beam positions in analogy to Figure 38b. The same beam intensity profile as shown in Figure 38a is used. (b) Total amount of substance that has been introduce into the computational domain n_{Total} until a bubble nucleates at ζ_{CO_2} of 3.0 as function the beam position.

At the end of the first part of the simulation, I would like to return to my initial questions. Based on Figure 33, I conclude that boiling of the electrolyte is of no concern in my experiment, as the boiling points of PC and EC:DMC are not reached inside the probing chamber, even for very high beam intensities up to $1 \cdot 10^{13}$ s^{-1}. Nevertheless, the first part of my simulation shows that it is advised to not exceed total photon intensities above $7 \cdot 10^{12}$ s^{-1} to stay below 160 °C maximum temperature and with this remain in the thermal stability window of the electrolyte.

As a side note, the simulation results indicate that beam intensities of $4 \cdot 10^{12}$ s^{-1} or higher could lead to boiling of more volatile organic electrolytes like pure DMC with a boiling temperature of only 91 °C. In this regard, my simulation demonstrates that the maximum temperature within the liquid strongly depends on the actual beam position relative to the silicon frame. As it is shown in Figure 33b, for a total photon intensity of $5 \cdot 10^{12}$ s^{-1}, the maximum temperature in the beam's center can be reduced by over 50% by moving the beam closer to the silicon frames. I consider this a vital take-home message from the first part of my simulation, which is certainly adaptable to all kind of liquid cell-based sXAS experiments. Further, with the beam position having such drastic effect on the maximum temperature, it becomes clear that beam positioning is crucial for a reliable repeatability of the experiment.

Furthermore, Figure 37 can be considered the answer to my initial question how to create the bubble in the most reliable manner. Here, the simulation shows that by keeping the total photon intensity below $1 \cdot 10^{12}$ s^{-1}, premature bubble formation is unlikely. Any bubble that forms at this beam intensity will have sufficient volume to stabilize a liquid thin-film. On top of that, the results of my simulation guided me further to develop an experimental procedure that not only optimizes the reliability of bubble formation but also reduces the amount of residual trace products in the liquid thin-layer. My simulation revealed that CO_2 can be brought from a state of undersaturation into a state of supersaturation abruptly by reducing its solubility through heating the electrolyte rapidly via an increase in beam intensity. With this, the bubble nucleation can be triggered on demand after enough gaseous radiolysis products for a sufficiently large bubble have been formed. This process, relies on the evolving electrolyte's temperature under the X-ray beam. The maximum temperature is determined by the beam position and the bubble trigger approach yields the best results if the beam is positioned right at the center of the membrane window. However, this process has a certain leeway and the deviations remain below 5% for off-centered positions smaller than 150 µm.

III.C.3 Bubble Growth Simulation

In the second part of the simulation (II), the bubble formation is simulated through CFD based on the local concentration profile obtained in the first step discussed before (I). For this, the dissolved gas concentrations are transformed into saturation concentrations $\widehat{c_i}$ based on solubilities at room temperature, as discussed earlier with (23). Here, $\widehat{c_i}$ can be considered the concentration above and below the solubility limit for $\widehat{c_i} > 0$ and $\widehat{c_i} < 0$, respectively. With this, the following CFD simulation yields insight into where and how quickly the bubble growths within the (oversaturation) concentration field between the SiN_x membrane windows.

The second part of the simulation was performed for a pure CO bubble, thus only taking $\widehat{c_{\mathrm{CO}}}$ into account. For V_m^i in (24), the gas bubble is treated as an ideal gas with a molar volume of 24.45 $dm^3\ mol^{-1}$ at 298 K and 1 atm. All other material parameters for (II) are summarized in Table 3 together with Table 2. The simulation does not consider any transition kinetics through the phase boundary and solely assumes the diffusion of the gas species to be the overall rate limiting process (compare Figure 29 and (24)).

Table 3 Summary of the material parameters for the liquid and the gas phase used in (II).

Property	Value	Comment	Source
Liquid			
Viscosity η, mPa s	4.15	1M $LiPF_6$ EC:DMC at 298.15 K	[246]
Surface tension σ, mN m^{-1}	40.13	EC:DMC at 293 K in argon atmosphere	[249]
Gas			
ρ, kg m^{-3}	1.145	CO as ideal gas with 28.01 g mol^{-1} at 298 K and 1 atm	
Viscosity η, µPa s	17.64	CO at 298 K and 1 atm	[229], [230]

Figure 41a shows the simulated bubble/liquid phase boundary at different points in time to demonstrate how the bubble grows within the supersaturated electrolyte and how it reaches its stable position in the center. At the start of the simulation, I introduce a stable bubble with a radius of 5 µm into the computational domain. Its nucleation site is chosen to coincide with the maximum temperature and concentration at $x = 0\ \mu\mathrm{m}$. The saturation concentration $\widehat{c_{\mathrm{CO}}}$ at an exemplary point in time is shown as the blueish color surface plot in the background and the corresponding bubble/electrolyte phase boundary is marked by the dotted line. Figure 42a-d shows the corresponding color surface plots of the saturation concentration and the liquid flow velocity at four different times in more detail. The bubble growth in Figure 41 and Figure 42 was simulated in a concentration field with CO's amount of substance above the solubility limit $\widehat{n_{\mathrm{CO}}}$ of 1.0 µmol m^{-1}, which was created through a total photon flux of $5 \cdot 10^{12}\ s^{-1}$ up to a supersaturation of CO_2 $\zeta_{\mathrm{CO_2}}^{bb}$ of 1.3. This concentration field is a very conservative assumption with the smallest expected $\zeta_{\mathrm{CO_2}}^{bb}$ and a relatively high total photon flux intensity as discussed in the previous chapter. Although this concentration distribution creates only a small bubble, it still serves to describe the general characteristics of the bubble growth dynamics. A simulation within a higher concentration that yields a larger bubble will be discussed afterwards.

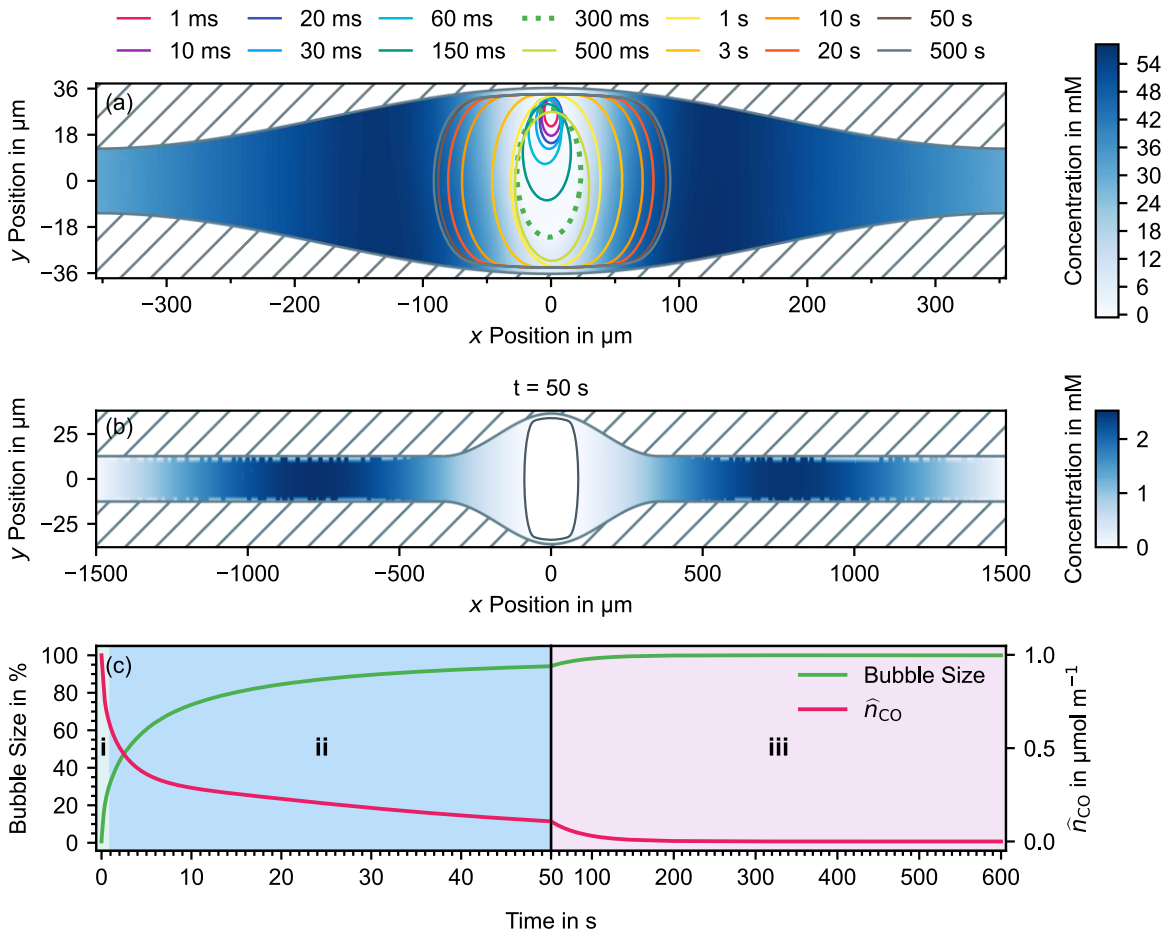

Figure 41 Summary of the three-stage bubble growth within the probing chamber in a low concentration field ($\hat{n}_{CO}$ of 1.0 µmol m^{-1}). (a) Expanding phase boundary of the bubble/electrolyte, color coded by time. Color surface plot in the background correlates with the spatial distribution of the saturation concentration $\hat{c}_{CO}$ at 300 ms and the corresponding phase boundary is highlighted by the dashed line. (b) Overview of the complete computational domain at 50 s with the phase boundary (grey line) and the corresponding color surface plot of the saturation concentration $\hat{c}_{CO}$. (c) Percentile bubble size and CO's amount of substance within the computational domain $\hat{n}_{CO}$ as function of time. The three stages of bubble growth (i), (ii), and (iii) are color-coded in the background.

The bubble growth is fueled by the diffusion flux of the gas species from the surrounding supersaturated electrolyte towards the gas bubble. Simultaneously, the expanding bubble pushes away the electrolyte, creating a depletion zone around itself and effectively reducing the growth rate. The evolving depletion zone around the phase boundary is clearly visible in Figure 41a and throughout Figure 42a-d. Based on this, the bubble growth within the probing chamber's geometry can be considered self-dampening. Thus, I classify the bubble growth into three distinct stages, as marked in Figure 41c. In the first stage (i) right after nucleation, the bubble is fully surrounded by supersaturated electrolyte and grows rapidly in horizontal and vertical direction. In this initial rapid growth stage, it obtains 33% of its final volume and reaches the upper and lower membrane window within 1 second. As it can be seen from Figure 42d, the rapid bubble growth forms an initial depletion zone. Although at a slower rate, in the second stage (ii) the bubble continues to grow in horizontal direction to reach about 94% of its final volume after 50 s. As it can be seen in Figure 41b, the bubble has consumed almost

all dissolved CO at this point and $\widehat{c_{CO}}$'s maximum has dropped from its initial value of 72 mM down to about 2.5 mM. The depletion zone grew to an extend where the growth rate effectively grinded to a halt. The remaining dissolved CO lingers inside the electrolyte channels and the bubble grows very slowly to its final size over the course of about 4 minutes in the third stage (iii).

As I will discuss in more detail in IV.B.2.a, I observe the bubble formation as a sudden jump in the transmission diode current from 10pA to 10 µA in less than one second. My simulation is in good agreement with this observation. Even within the low concentration, the bubble reaches the upper and lower membrane window within 1 s and efficiently removes the excess electrolyte in the beam's path. This explains the observed sudden rise in transmission diode current in less than one second. Further, from this observation I deduce that the bubble formation takes place in the vicinity of the beam. On the one hand, this allows me to control where the bubble is formed, but on the other hand, this might make the beam position an experimental variable that must be controlled precisely for a reliable and reproduceable bubble formation procedure. Later, I will explore if the nucleation location influences the final bubble position and shape.

For the XAS investigation of the SEI on silicon anodes with this technique, I'm interested in how the bubble growth could influence the SEI. As decomposition products of the electrolyte, the SEI is not expected to adhere strongly to the anode's surface. Given the no slip boundary condition applied in my simulation, the fluid velocity at the liquid/membrane interface is zero. Nevertheless, I still take the fluid velocity in the vicinity of the membrane as a good indication of how the bubble might interact with the SEI. As it can be seen in Figure 42a-d, the growing bubble accelerates the fluid towards the electrolyte channel. During the first half of the growth stage (i), the maximum of the velocity is found right at the gas/fluid phase boundary with fluid velocities around 0.6 mm s^{-1}. Later, the velocity maximum is at the center of the electrolyte channel, as one would expect from Stoke's law, given the reduced cross-section of the electrolyte channels. With the beginning of the growth stage (ii), the fluid velocity remains below about 0.15 mm s^{-1}. More importantly, the rapid bubble growth in stage (i) pushes the electrolyte against the membrane windows at $x = 0$, creating a stream to the left and right in the center close to the membrane windows. This drift at the center aside, the fluid velocity in the vicinity of the membranes remains remarkably small. The displacement shown in Figure 42e is the time integral of the fluid velocity over stage (i). It is apparent that the displacement remains below 50 µm near the membranes. When the bubble forms at the center, the probing chamber's geometry forms a safe place, where the SEI resides widely unchanged. From this, I deduce the strategy to focus the XAS investigation to this area in order to analyze the SEI in its most pristine state.

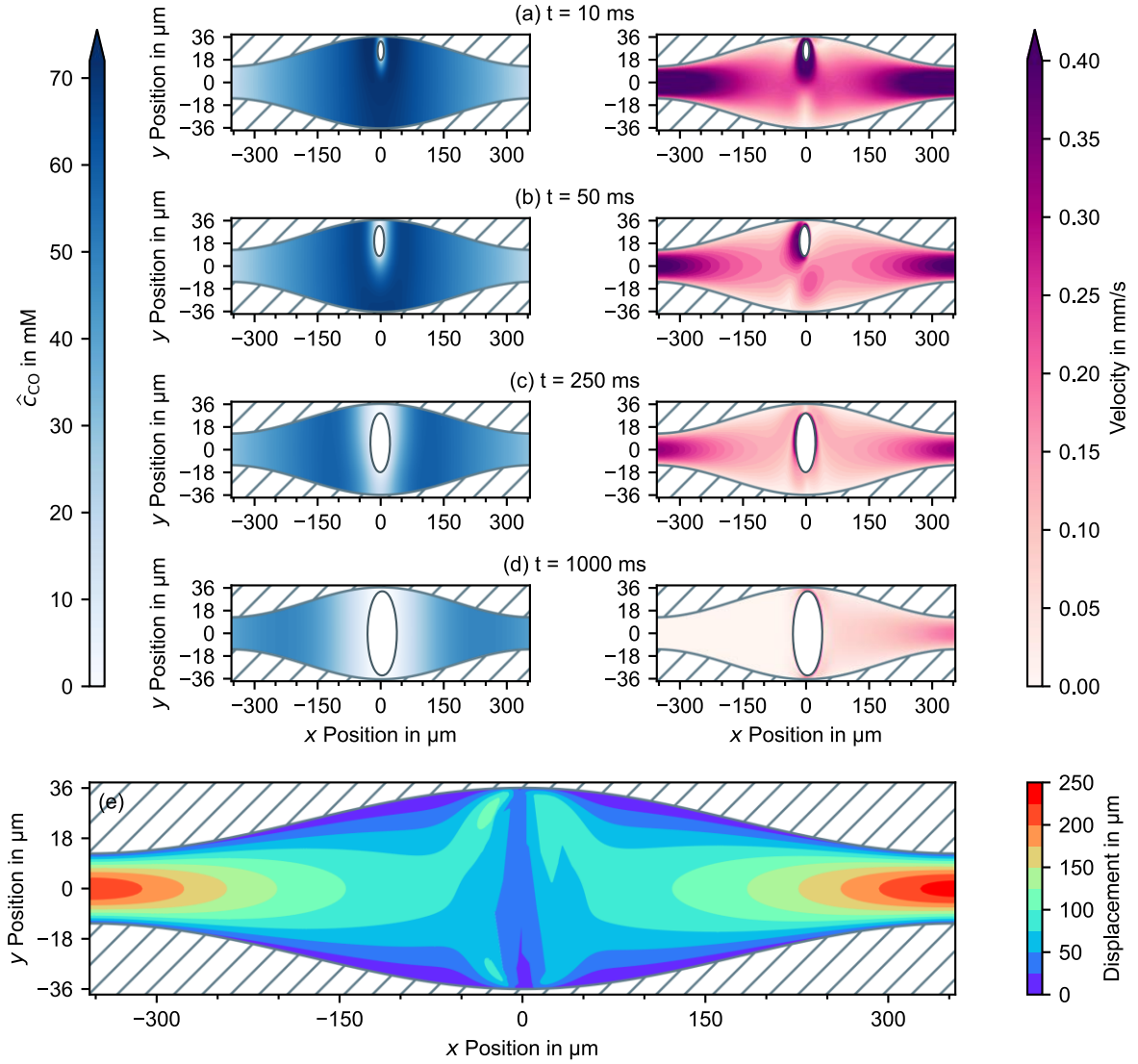

Figure 42 (a-d) Saturation concentration $\widehat{c_{CO}}$ and fluid velocity with the corresponding bubble/electrolyte phase boundary at 4 different points in time during the first growth stage (i) from the bubble growth in a low concentration field ($\widehat{n_{CO}}$ of 1.0 µmol m^{-1}) as shown in Figure 41. (e) Corresponding fluid displacement (time integral over fluid velocity) in the probing chamber during the first growth stage (i).

While the bubble growth discussed so far assumes a rather conservative oversaturation of CO, Figure 43 now summarizes the bubble growth simulation within a much higher concentration field with CO's amount of substance above the solubility limit $\widehat{n_{\mathrm{CO}}}$ of 7.5 µmol m^{-1}, which was created by a total photon flux of 5·10^{12} s^{-1} up to a CO_2 supersaturation $\zeta_{\mathrm{CO_2}}^{bb}$ of 3. Figure 43a shows that at the higher supersaturation concentration, the speed of the bubble growth is strongly increased in the first stage (i) and the bubble already reaches the upper and lower membrane window within 150 ms. In the second stage (ii), the bubble grows to 90% of its maximum volume within 73 s. With the increased amount of substance of CO, the bubble grows to a much larger extent and covers 89% of the probing chamber's volume. The bubble's volume fraction of the probing chamber as a function of time is given in Figure 43f. Furthermore, during the first half of growth stage (i), the fluid at the gas/fluid phase

boundary reaches a much higher velocity with about 3.6 mm s^{-1}. In stage (ii), the fluid velocity at the center of the electrolyte channel remains below 0.80 mm s^{-1}. Although the higher concentration field leads to an accelerated bubble growth and overall higher fluid velocity, the general flow behavior remains the same and. As it can be seen from Figure 43b-e, the fluid velocity in the vicinity of the membranes remains below about 0.6 mm s^{-1}.

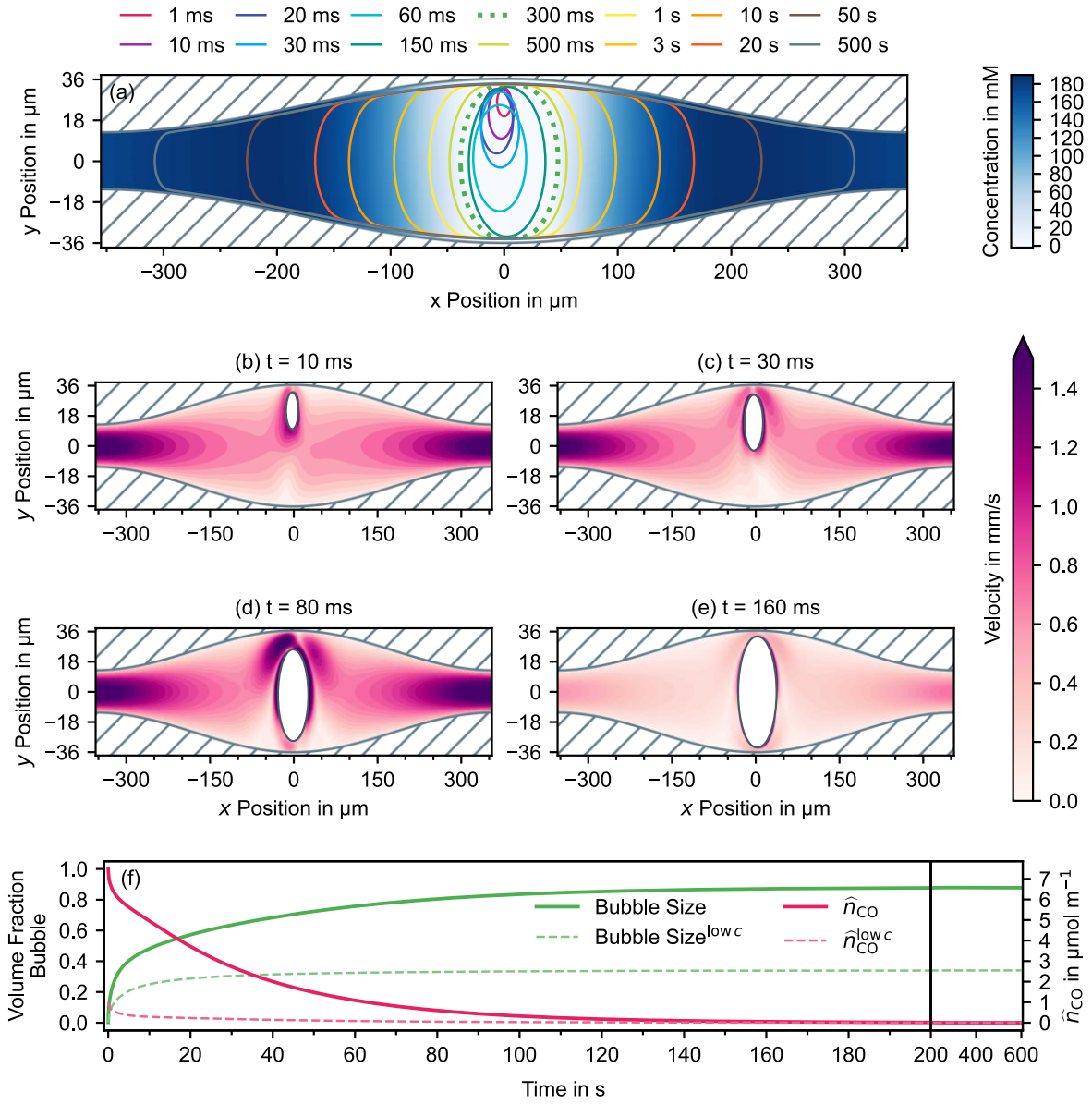

Figure 43 Summary of the bubble growth within the probing chamber in high concentration field ($\hat{n_{CO}}$ of 7.5 µmol m^{-1}). (a) Expanding phase boundary of the bubble/electrolyte, color coded by time. Color surface plot in the background correlates with the spatial distribution of the saturation concentration $\hat{c_{CO}}$ at 300 ms and the corresponding phase boundary is highlighted by the dashed line. (b-e) Fluid velocity with the corresponding bubble/electrolyte phase boundary at 4 different points in time during the first growth stage (i). The bubbles volume fraction of the probing chamber and CO's amount of substance within the computational domain $\hat{n_{CO}}$ as function of time. For comparison, the data from the simulation in a low concentration field ($\hat{n_{CO}}$ of 1.0 µmol m^{-1}) from Figure 41 is added.

Based on the sudden increase of transmission diode current upon bubble formation and the bubble growth kinetics demonstrated in Figure 41a and Figure 43a, I assume the bubble

formation takes place in the vicinity of the X-ray beam. Thus, with the help of my simulation, I want to explore if the beam position and the location of the bubble nucleation, influences the bubble growth and determines its final geometry and position. Figure 44a shows the simulated bubble/liquid phase boundary at different points in time with the beam positioned 200 µm off-center and the bubble nucleation at the center of the beam close to the upper membrane.

As it can be seen in Figure 44a, the bubble initially remains at its off-centered position for the first growth stage (i). The bubble reaches the upper and lower membrane after 60 ms. Then, the bubble preferentially grows at the left-hand side along the concentration gradient, while simultaneously slowly sliding towards the center of the probing chamber. It reaches its final symmetric center position after 3 s. From this point on, the bubble sits steadily at the center of the probing chamber and grows symmetrically in both horizontal directions like we have seen for the second growth stage (ii) in Figure 41a and Figure 43a. I observe the same growth behavior in Figure 44b when the nucleation and beam position are on opposite ends of the probing chamber at ±200 µm, respectively. Comparing Figure 44a and Figure 44b, due to the self-dampening growth behavior inside the probing chamber's geometry, the bubble grows to a larger extent when the nucleation location is closer to the beam position.

The scenarios presented in Figure 44 strongly indicate that the bubble's final symmetric center position is independent of the nucleation location and it is solely determined by the geometry of the probing chamber. Thus, the bubble geometry and position cannot be controlled through the beam position. On the contrary, in case the beam position cannot be controlled reliably in an actual experimental implementation, I consider my method fail-safe when it comes to the final bubble position itself.

In summary, the second part of my simulation demonstrates that the bubble growth can be divided into three stages: a rapid initial growth in both dimensions until touching the upper and lower membrane windows in less than a second, followed by a horizontal growth of the bubble to 90% of its size within about a minute and finally a sluggish growth to its final size over the course of several minutes. With the observed sudden increase of the transmission diode current upon bubble formation in my experimental work, the bubble growth kinetics from my simulation indicate that the bubble nucleation takes place in the vicinity of the beam. While this suggests that the nucleation location can be controlled through the beam position, my bubble growth simulation shows that the final bubble position and geometry is solely controlled by the probing chamber's geometry, independent from the nucleation location. Thus, the bubble always ends up sitting symmetrically at the center of the probing chamber, which makes the method fail-safe in case the beam position cannot be controlled precisely. Nevertheless, when the bubble forms at the center, the simulation shows that the fluid velocity

close to the sample membrane remains small, leaving the SEI supposedly unchanged. Although the bubble always ends up in the center no matter of the nucleation location, I still deduce from my simulation that the best beam position to induce the bubble formation is right at the center of the membrane windows. Thus, I assume the SEI is found in its most pristine state at positions 50 to 200 µm off-center.

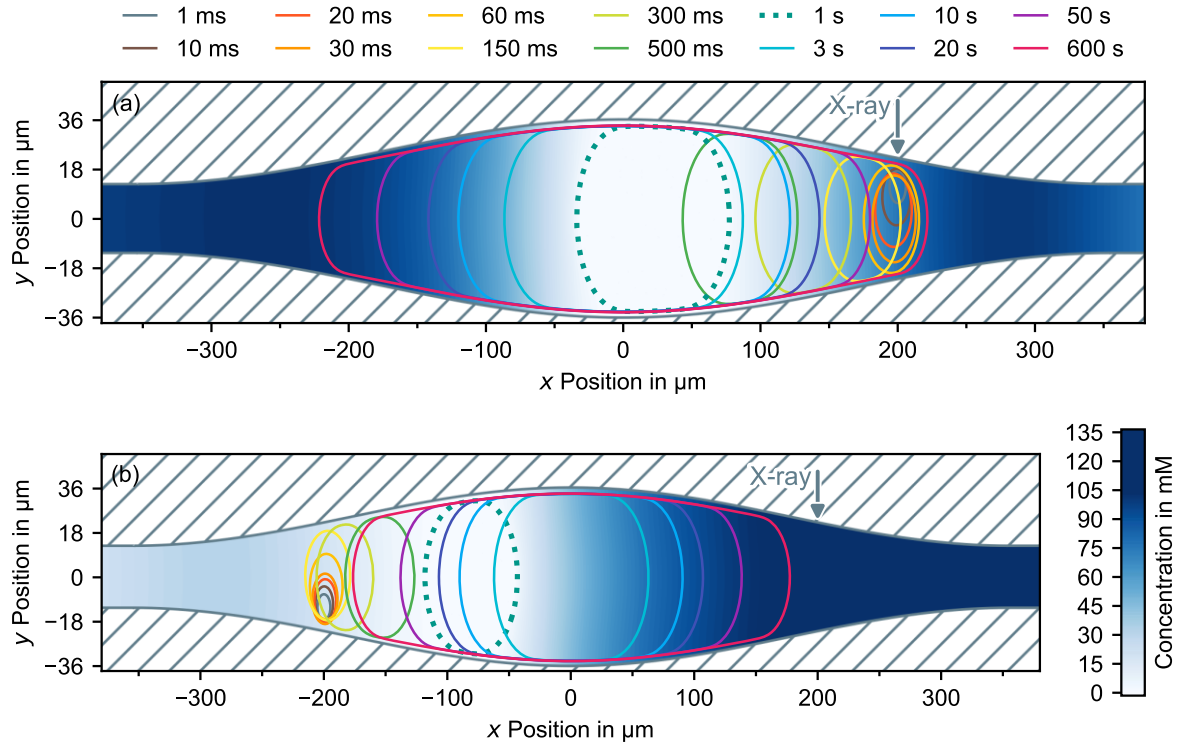

Figure 44 Summary of the bubble growth with off-center beam positions and nucleation locations. Expanding phase boundary of the bubble/electrolyte, color coded by time. Color surface plot in the background correlates with the spatial distribution of the saturation concentration $\widehat{c_{CO}}$ at 1 s and the corresponding phase boundary is highlighted by the dashed line. (a) Beam position and nucleation location are 200 µm off-center. (b) Nucleation and beam position are on opposite ends of the probing chamber at ±200 µm, respectively.

III.D Cell Design

After having explored the idea of transmission *in-situ* sXAS with a bubble-stabilized liquid thin-layer on a conceptual level through my simulation, I now want to present an actual implementation of this idea. The following cell design is not only suitable for the formation of a bubble-stabilized liquid thin-layer but it is also implemented as an electrochemical half-cell that allows the growth and investigation of the SEI on a silicon thin-film anode which is deposited on one of the SiN_x membrane windows. The basic concept is illustrated in Figure 25.

For my cell implementation, I had to adhere to the following design constraints. First, as I have discussed in chapter III.C.1.a based on (11) and (12), the SiN_x membranes bulge outwards under the pressure difference between the atmospheric pressure inside and the surrounding

vacuum [203]. Based on (11), the maximum membrane deflection increases with its side length and the membrane itself becomes more fragile. Simultaneously, the bulging determines the ultimate shape of the gas bubble. Thus, the ideal window side length for my approach turned out to be 500 µm. I found it to be a good tradeoff between three important aspects: first, sufficient mechanical stability to withstand both the vacuum pressure and the stresses induced by the de-/lithiation of the silicon anode on top; second, maximum membrane deflection/bulging (23.5 µm calculated in III.C.1.a based on (11)) and with this decent bubble stability; and third, sufficient available measurement area considering a soft X-ray microfocus beamline with a spot size of 95 µm times 42 µm like the U49-2_PGM-1 beamline [194] at BESSY II, where I conducted most of my experimental work.

Furthermore, it is quite common for this type of cells to use square silicon frames with a side length between 5 to 10 mm to facilitate handling and to reduce the risk of breaking the membrane window. However, the 500 µm square-shaped windows allow circular frames as small as 3 mm in diameter. Although the small frame size makes assembly much more difficult, it makes it possible to reduce the distance between working- and counter-electrode, which ultimately improves the electrochemistry significantly. As a bonus, with the SiN_x membranes being manufactured by standard means of lithography, their price is directly determined by their silicon die area. Thus, the membrane windows in 3 mm frames are much cheaper (at the time of writing about 1/5 of the price compared to a 10x10 mm frame) and allow easier prototyping with many more iterations. Thus, for my approach, I chose commercially available (Micro to Nano V.O.F.), 50 nm thick, square SiN_x membrane windows with a side length of 500 µm in an octagonal silicon frame with a 3 mm encircling diameter.

With the silicon nitride windows being the centerpiece of the cell and the requirement to have the counter-electrode as close to the working-electrode as possible, almost all other dimensions of the cell are constrained by this. At the same time, due to the high sensitivity of the electrolyte and lithium metal to moisture, the cell must be assembled inside an argon-filled glovebox. Thus, the main constraint can be summarized like this: everything must be as small as possible, but large enough to be handled and assembled inside a glovebox. On top of that, all materials must be chemical resistant to the harsh 1M $LiPF_6$ EC:DMC electrolyte. Figure 45 shows a sketch of my cell design, which is described in more detail in the following.

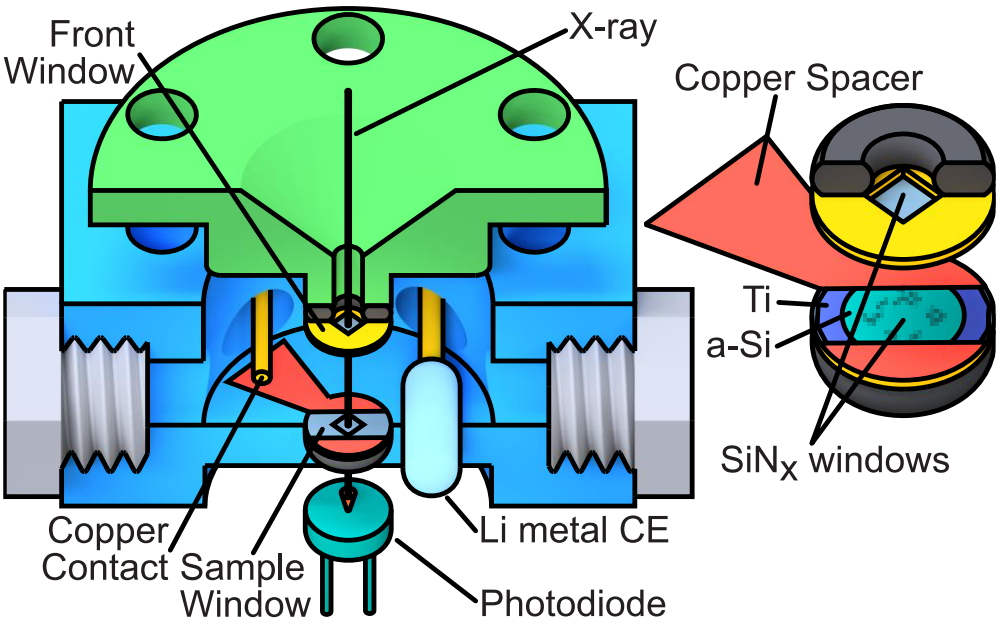

Figure 45 Sketch of the electrochemical cell for transmission sXAS. The cell consists of two PEEK parts: the lid (green) and the main body (blue). The silicon thin-film anode (teal) and an underlying titanium contacting layer (purple) are deposited onto a free-standing silicon nitride window (silver, side length 500 µm) in the center of a silicon frame (yellow, Ø 3 mm). The titanium contacting layer and in turn the anode are electrically contacted through the copper spacer (red). The copper spacer and a second silicon nitride window (yellow) form a sandwich assembly with an electrolyte channel in-between. This sandwich assembly sits in the center of the main body and is sealed by two O-rings (black) on each side. A small ribbon of lithium metal (light blue) acts as a counter-electrode (CE) and is placed 2 mm next to the sandwich assembly. Both the copper spacer and the lithium ribbon are contacted though a Kapton coated copper wire that is inserted into the cell through vacuum tight fittings on the back (not visible in the illustration). After assembly, the main body can be filled with electrolyte through two inserts (left and right) and sealed vacuum tight with two plugs (light grey). The X-ray enters the cell through the front window, penetrates the sample(-window) and its transmitted intensity is measured by a photodiode (teal).

The cell body (45 mm x 35 mm x 10 mm) and lid are machined out of polyether ether ketone (PEEK) (TECAPEEK, Ensinger GmbH). The membrane sandwich assembly sits in the center of the electrolyte reservoir, which is sealed from the surrounding vacuum by the lid with two EPDM (ethylene propylene diene monomer rubber) O-rings on each silicon frame. The electrolyte reservoir is 10 mm in diameter and 3 mm high. The total electrolyte volume of the cell is 0.23 mL, including all electrode channels. One SiN_x membrane (labelled as Sample Window in Figure 45) acts as the substrate for the 50 nm thick amorphous silicon thin-film anode. In the direction of the X-ray beam, the sample window sits on the back-facing side. This way, the formed SEI is shielded from the high intensity X-ray beam by the electrolyte during bubble creation. The silicon thin-film is contacted by a 30 nm thick titanium layer underneath. In addition, a 3 nm thick layer of chrome is used as a bonding agent between the titanium and the SiN_x. The chromium as well as the titanium was applied through evaporation and the silicon was deposited through plasma enhanced chemical vapor deposition (see IV.B.1.e). Although copper is commonly used as contact on the anode side, titanium was used in this work to avoid copper contamination of the CVD chamber available to me at this time.

While the chrome and titanium cover the whole silicon frame, the silicon is deposited only in the center as a circle with a 2 mm diameter. This way the uncovered titanium at the border is

used as an electrical contact via the copper spacer. A thin ribbon of lithium metal is used as a counter-electrode and is placed outside of the beam path, about 0.5 mm away from the silicon frames. Both the lithium ribbon and the copper spacer are each contacted by a copper wire, which is fed through from the outside vacuum. The ethylene tetrafluoroethylene (ETFE) feedthroughs are on the back side of the cell, thus not visible in Figure 45, and are sealed with silicone (room-temperature-vulcanizing, TFC4000 from TFC Troll Factory) as it demonstrated excellent chemical resistance to 1M $LiPF_6$ in EC:DMC [250]. Furthermore, the copper wires are tightly pressed onto the lithium and copper spacer by a ring of PEEK that sits between the wires and the lid (omitted in Figure 45 for visual clarity). Further, the copper wires are coated with polyimide to minimize the active copper/electrolyte interface and to localize the electrochemistry signal to the silicon thin-film. For the same reason, the copper spacer is shaped to be fully covered by the silicon frames on both sides and not to be in contact with the electrolyte. Due to the lithography manufacturing process of the membranes, SiN_x covers the whole silicon frame [203] and electrically isolates the silicon frame of the opposite window from the copper spacer.

While, in principle, a reference electrode can easily be put inside the electrolyte reservoir as well, I decided on a two-electrode setup, because no reliable reference electrode materials are available for LIBs chemistry [251]. At the same time, the comparison to ordinary coin and pouch cells is more straightforward with a two-electrode setup.

Before assembly, the whole cell and all components are thoroughly rinsed with methanol and dried with nitrogen. The cell is then assembled inside an argon glovebox (M. BRAUN, O_2 and H_2O kept <0.1 ppm) and filled with electrolyte through the two ports on both sides. Afterwards, the cell is sealed vacuum tight with two ETFE caps and is transferred into the experimental chamber at the beamline.

SiN_x membranes with only 10 nm thickness were shown to be already gas tight, with no detectible helium leaks above $3x10^{-10}$ mbar s^{-1} [252]–[254]. I am therefore confident that the transfer is safe and the electrochemical procedure can also be performed outside the vacuum or glovebox without risking contamination of the cell chemistry. However, as I will discuss in chapter IV.B.4.b.2 regarding the sXAS at the fluorine K-edge, I observe traces of hydrofluoric acid (HF) in a cell that has been aged under atmospheric conditions for 4 days. The evolution of HF is a known phenomenon in lithium-ion battery technology and is often connected to water and moisture contamination of the electrolyte or cell. Nevertheless, HF was not evident in any of my *in-situ* samples which have been investigated right away. Thus, I am convinced that the cell is sufficiently sealed, even through the 50 nm SiN_x membranes, and water and moisture contamination is not an issue for the 12-hour time frame of my *in-situ* measurements.

Furthermore, except from the sample sandwich (silicon frame, SiN_x membrane window, a-Si thin-film as well as chromium and titanium), the materials of the cell in contact with the electrolyte are PEEK, ETFE, silicone, copper, polyimide and EPDM, which all have been found to be chemical resistant to 1M $LiPF_6$ in EC:DMC for the time frame of the experiment.

III.E Custom X-ray Absorption Spectroscopy Data Acquisition Software

For the development of my novel transmission sXAS technique, I needed a highly flexible and adaptive experimental setup. Thus, I develop my own data acquisition and instrument control software to iterate efficiently and to adapt quickly to ever changing experimental procedures during prototyping. The software allows to fully control and read out a collection of electrometers (Keithley 6514) simultaneously, which are used to measure the transmission photodiode's current, TEY drain currents, and the drain current of the refocusing mirror upstream as reference for the incoming beam's intensity. Furthermore, the beamline and undulator can be controlled remotely to directly set all important parameters like the monochromator photon energy, slit size, aperture sizes, desired undulator harmonic and monochromator diffraction order, etc. Additionally, the software allows the direct control of the cell holder's manipulator for spatial scans of the sample in addition to reliable positioning of the X-ray beam for the bubble formation procedure and XAS measurements. Having access to this toolbox enables the user to quickly build measurement procedures by combining desired controls and readouts. Figure 46 shows a screenshot of the application's GUI with the main- and sub-window(s).

The software is written in an object-oriented fashion in the Python programming language with the use of the following libraries. The handling of the measurement data is based on the file structures of the "NumPy" [255] and "pandas" [256] packages. The GUI is implemented with the "PyQt5" Python-binding [257] to the C++ "Qt" framework [258] and the "PyQtGraph" graphing library [259]. The communication with all devices, in particular the data acquisition itself and the instrument control, is based on the "PySerial" [260] and "PyVISA" [261] library. The object-oriented architecture provides several interfaces to facilitate switching between and adapting to new devices, e.g., manipulators or electrometers. The communication with the electrometers is based on the Standard Commands for Programmable Instruments (SCPI) protocol and provides interoperability with many devices and manufacturers. The beamline is controlled via the local Experimental Physics and Industrial Control System (EPICS) of the BESSY II synchrotron facility using the "PyEpics" Python-bindings [262]. This makes the software useable at every BESSY II beamline.

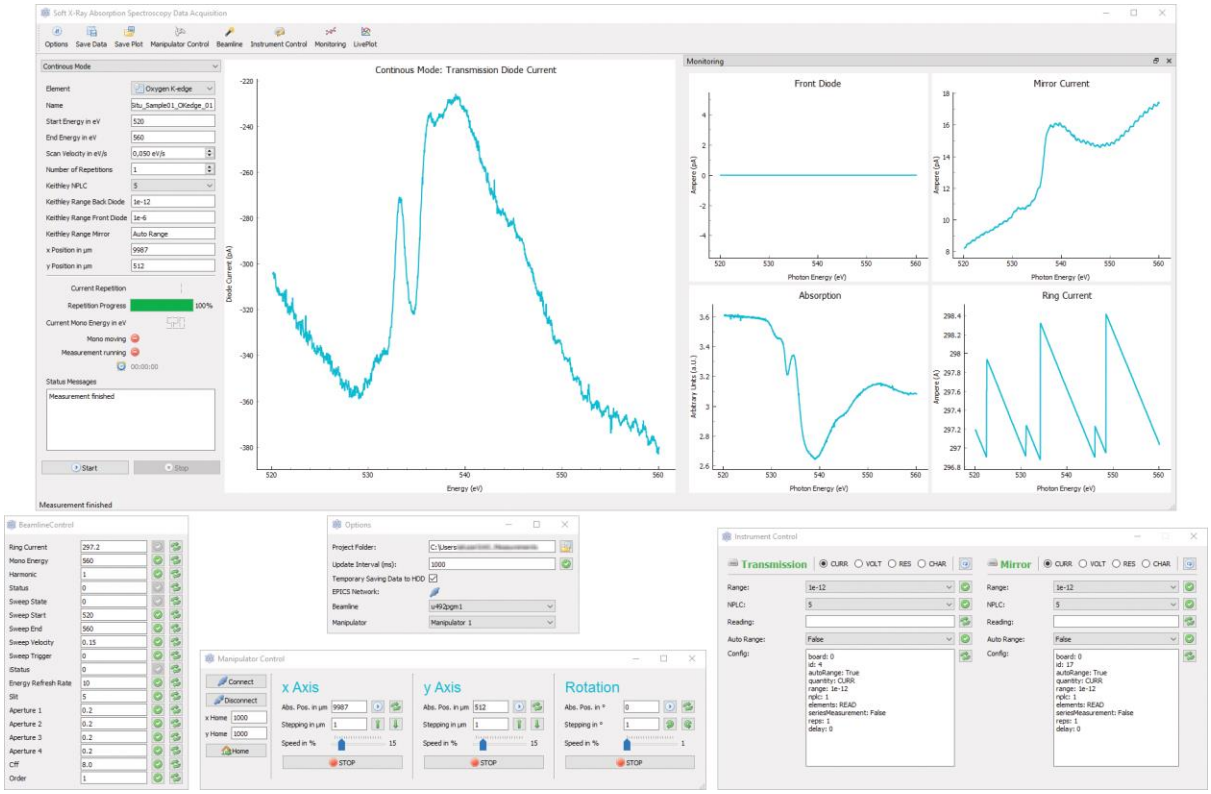

Figure 46 GUI screenshot of the custom sXAS DAQ software developed in the course of this work.

The software has a multithreaded, multicore architecture. The main process manages the GUI in Qt's multithreaded event-driven fashion and lets the user setup and schedule each measurement. For each measurement a child process is spawned with the parameters and a set of instructions (called procedure) specified by the user (further referred to as data acquisition (DAQ) process). The DAQ process is explicitly dedicated to the instrument control and DAQ workload. A procedure is commonly structured in three segments: first, the initialization and setup of all necessary devices; second, the measurement loop to acquire data continuously; and third, final data processing and controlled shutdown of instruments. The measurement loop is commonly either time-driven, e.g., continuous measurement for a given amount of time, or by a set number of data points with a given sampling rate. The data acquired in the measurement loop is fed into NumPy arrays, which are shared in memory among all processes. This allows the main process to process and visualize the obtained data simultaneously in the GUI without compromising the DAQ process' performance. The separation into two processes also provides flexibility, as the DAQ process can be spawned with different procedures. To give an example, the procedure can either be implemented to continuously increase the monochromator's set photon energy to obtain an XAS spectrum at a fixed sample position, or continuously change the manipulator's position to spatially scan over a sample with a fixed photon energy. The way the main process visualizes and processes the measurement loop's data for each procedure can easily be configurated and new experiments can be realized within minutes.

IV Accessing the Solid Electrolyte Interphase on Silicon Anodes *In-situ* through Transmission Soft X-ray Absorption Spectroscopy

In this last chapter of my work, I present my investigations of the Solid Electrolyte Interphase on silicon anodes under *in-situ* conditions through transmission XAS in the soft X-ray regime utilizing a gas bubble-stabilized liquid thin-layer. While I have approached this novel method in chapter III on a more conceptual level, chapter IV can be considered as an implementation and application thereof.

While the focus lies on the sXAS investigation, I want to start this final chapter by presenting the electrochemical procedure to create the SEI and electrochemically characterize the cell and the silicon thin-films. Additionally, the electrochemical characterization is accompanied by *operando* UV/Vis spectroscopy (UV/Vis) and *operando* optical microscopy (OM). I will briefly explain how my transmission sXAS cell can easily be adopted to both techniques. This multi-*operando* technique characterization provides a complete picture of the silicon thin-film anodes' de-/lithiation process within the sXAS cell.

IV.A Supplementary Characterization of the Cell and the Silicon Thin-films

IV.A.1 Electrochemical Procedure and Characterization

The main goal of this work is to present a novel approach for the *in-situ* analysis of the SEI on silicon anodes via transmission sXAS in isolation from the cracking phenomenon. Thus, the avoidance of cracking is key. For this, I have evaluated 50 nm thick amorphous silicon thin-films as a suitable model system. Due to the absence of detrimental two-phase transformations within the first cycle, a-Si is expected to suffer from less cracking than c-Si. With a thickness of only 50 nm, the thin-films remain crack-free, even for a large number of cycles, as I will demonstrate in the following *operando* UV/Vis and OM investigation. To achieve this, I have chosen the potential ranges accordingly to avoid the detrimental c-$Si_{15}Li_4$ phase and, as we will see, remain in the a-Si/a-Li_xSi system.

The silicon thin-film anodes were cycled via linear sweep voltammetry (LSV) in 1M $LiPF_6$ EC:DMC using a potentiostat (Interface 1010T, Gamry Instruments) inside the sXAS cell. If not explicitly stated otherwise, all potentials in the following are given vs. Li/Li^+. Sweeps with decreasing potential are referred to as lithiation sweeps while sweeps with increasing potential

as delithiation sweeps. The scan speed in all voltammetry sweeps was 0.5 mV s^{-1}. The electrochemical procedure looked as follows. The initial lithiation sweep ran from the individual OCP value (usually around 3.2 V for Si vs. Li) down to 10 mV. Afterwards, the anodes were cycled for a given number of times between 10 mV to 800 mV. Between every lithiation and delithiation sweep the anodes were potentiostatically held at 10 mV for a certain amount of time depending on my experimental goal. In the supplementary *operando* UV/Vis investigation, I put focus on the de-/lithiation behavior of the silicon thin-films and the holding time was only 100 s with 21 cycles in total. For the *in-situ* sXAS investigation of the SEI, however, the silicon thin-films were potentiostatically held at 10 mV for 1000 s instead, to give the SEI sufficient time to form over 10 cycles total, not counting the initial lithiation starting from the OCP. However, the holding time of the *in-situ* cells' initial cycle is still only 100 s to preliminarily validate their electrochemical behavior by comparison to the UV/Vis investigation. Representative electrochemical data from the *operando* UV/Vis investigation is summarized in Figure 47. The corresponding *operando* UV/Vis data is discussed in more detail in the upcoming chapter IV.A.2.a. The electrochemical characterization of a representative sXAS *in-situ* cell is shown in Figure 48.

Silicon's de-/lithiation was described extensively in I.C.1 together with Figure 8. The observed current/potential response of the silicon thin-films in my cell can be explained accordingly. I will first discuss the behavior of the UV/Vis cells in Figure 47. Here, judging the overall shape of the current/potential curves in Figure 47a,b, the electrochemical behavior of the thin-films in my cell is in good agreement with reports on amorphous silicon thin-film anodes in simple "silicon in a beaker" and coin cell assemblies [57], [116], [148], [263]–[268].

As expected, looking at Figure 47a,b, the current/potential response of the initial cycle differs drastically from the consecutive cycles, presumably due the structural changes from a-Si to a-Si*. The initial cycle also exhibits an overall higher anodic current with a pronounced plateau starting at 0.53 V vs. Li/Li^+. An increased anodic current at potentials below 1 V vs. Li/Li^+ in the initial cycle is common in literature and is correlated to the formation of the SEI [112], [265], [269]–[272]. I assume that the plateau is caused by the surface-limited electrolyte decomposition reaction on all electrode surfaces, i.e., the silicon thin-film itself as well as all copper contacting rods which are in contact with the electrolyte. In particular, Horowitz *et al.* correlated the plateau at 0.5 V to the specific reduction of EC to poly-EC and LEDC [272]. I attribute the anodic reaction at around 2.2 V in the first cycle at 0.56 h in the inset of Figure 47b and Figure 47c to a copper-catalyzed decomposition of PF_6^- at the copper contacts [273].

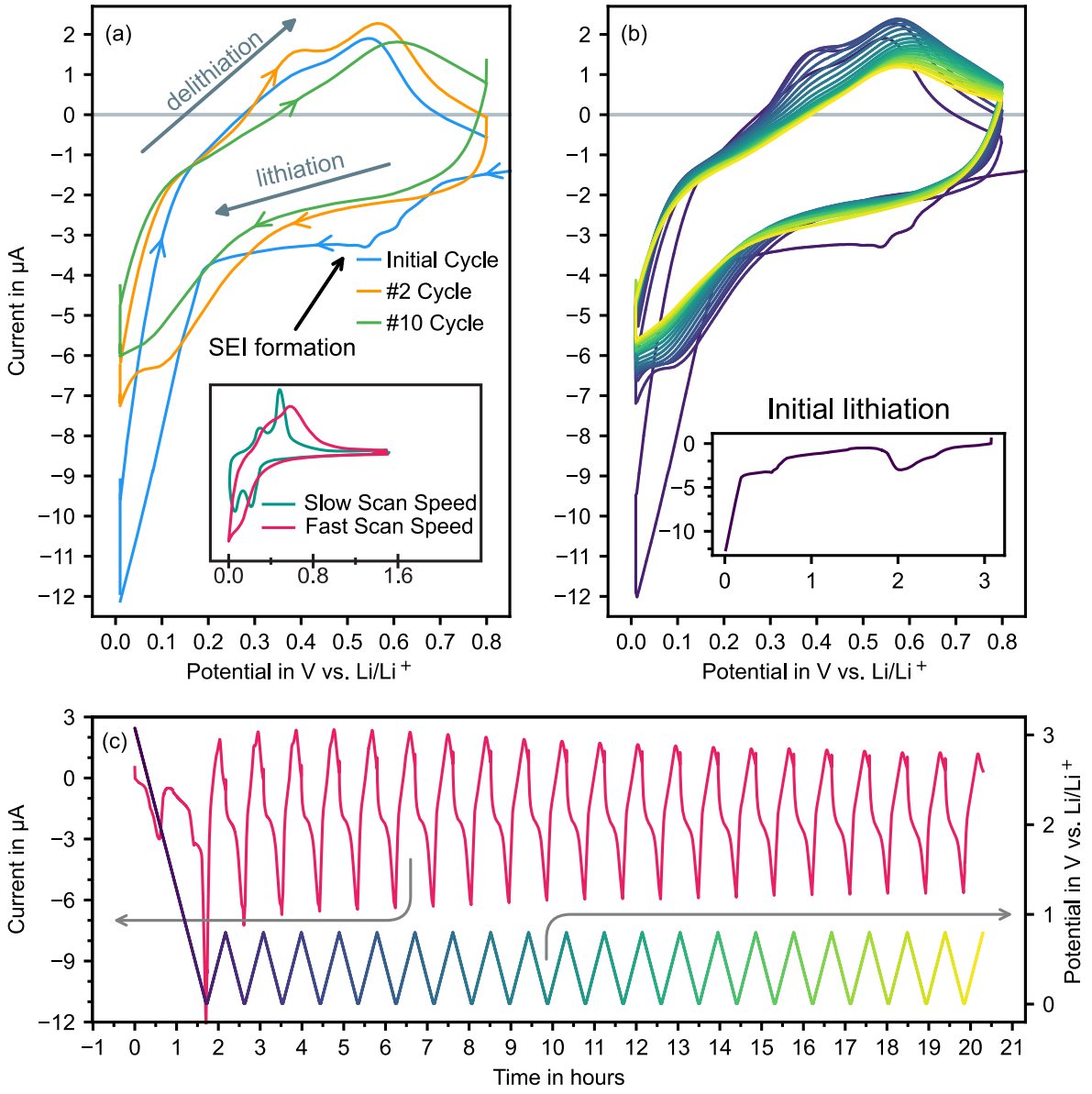

Figure 47 Summary of the electrochemical data from a representative cell of the UV/Vis investigation. (a) Current/potential curves from the initial, second and 10th cycle of the electrochemical procedure. Between every lithiation and delithiation sweep was a 100 s long potentiostatic holding at 10 mV vs. Li/Li⁺. The inset illustrates how the current/potential curves transform for different scan speeds. The data is adapted from [263]. (b) Current/potential curves from all 21 cycles color coded by time corresponding to the color-code of the potential in (c). Inset shows the current/potential curve of the initial lithiation starting from the OCP value at around 3 V vs. Li/Li⁺ down to 10 mV vs. Li/Li⁺. (c) Current and potential as function of time over the 21 cycles of the full experiment. Potential is color-coded to give the time for the current/potential curves in (b).

Furthermore, in the initial cycle, I observe a steep current increase at 190 mV, which can be correlated to the onset potential of the high-potential a-Si/a-Li_xSi lithiation stage. In literature, the onset potential in the initial cycle is reported to be around 200 to 220 mV vs. Li/Li⁺ [116], [149], [274]–[276]. Further, the low-potential stage is not visible in the initial lithiation sweep. In the initial delithiation sweep, both low- and high-potential a-Li_xSi/a-Si delithiation stages are visible, albeit as broad convoluted peaks. After the initial cycle, the current/potential response of the silicon thin-films changes drastically. In the second cycle, the high-potential lithiation stage becomes visible as a small plateau at 80 mV and the onset of the low-potential stage

can be suspected at 10 mV. I attribute the plateau character to the high contribution of the double layer capacity (compared to the rather small bulk lithiation process), which distorts the current/potential curves by an anti-clockwise rotation, turning peaks into plateaus. Nevertheless, the low- and high-potential delithiation stages are apparent in the second sweep as distinctive peaks at around 390 mV and 570 mV vs. Li/Li^+. In Figure 47, the time is color-coded in the potential in Figure 47c and the current is plotted as a function of time in Figure 47b. The lithiation plateau and the low-potential delithiation peak vanish with continuous cycling. The high-potential delithiation peak is shifted temporarily to higher potentials until the 9^{th} cycle but reaches its initial potential after 21 cycles again. In general, all peaks show reduced intensity with increasing cycle number. A possible explanation for the observed behavior could be an increased overpotential due to an increasing SEI thickness (which is responsible for the potential shift) coupled with a depletion of Li^+ inside the electrolyte (which is responsible for the decreasing current). Here, the oscillating shift of the high-potential delithiation peak may already be a hint for a changing SEI. In summary, the silicon thin-films cycled inside the sXAS cell show all distinct features of the de-/lithiation of a-Si [86]–[88]. Thus, the results from the *in-situ* transmission sXAS experiment using the presented cell appear applicable to real batterie implementations like coin or pouch cells.

However, as it can be seen in the inset of Figure 47a (slow and fast correlate to 0.1 and 2.0 mV s^{-1} based on the data of Xia *et al.* [263]), for high LSV scan speeds the de-/lithiation peaks broaden, convolute and shift to higher and lower potentials [277], respectively. Although I apply a rather slow scan speed of 0.5 mV s^{-1}, I already observe extensively broadened and convoluted peaks in Figure 47a. From this I deduce rather sluggish kinetics within my cell and attribute it to the thin electrolyte channel. Because the scan speed also shifts the peak positions, an estimation of the overpotential presumably introduced through the large distance between working and counter electrode (compare III.D) is difficult. The onset potential of the high-potential a-Si/a-Li_xSi lithiation stage in the initial cycle at 190 eV suggests an overpotential as large as 30 mV vs. Li/Li^+, when compared to literature values [116], [149], [274]–[276] between 200 to 220 mV vs. Li/Li^+. Furthermore, although the lithiation was carried out down to 10 mV, no distinct peaks for the formation of the c-$Li_{15}Si_4$ phase are visible. From this, I infer that the cycling occurs between a-Si* and a-Li_xSi. Staying in the amorphous regime by avoiding the crystallization of c-$Li_{15}Si_4$ with an appropriate cutoff potential during lithiation is a common strategy to increase the cycle stability of silicon anodes [95]. With regards to my findings from the SEI on the silicon thin-film anodes investigated in this work, these are still relevant for their application. On top of that, with the SEI formation plateau in the initial cycle appearing already at 0.53 V vs. Li/Li^+, I argue the estimated overpotential around 30 mV is not expected to change the SEI's composition drastically.

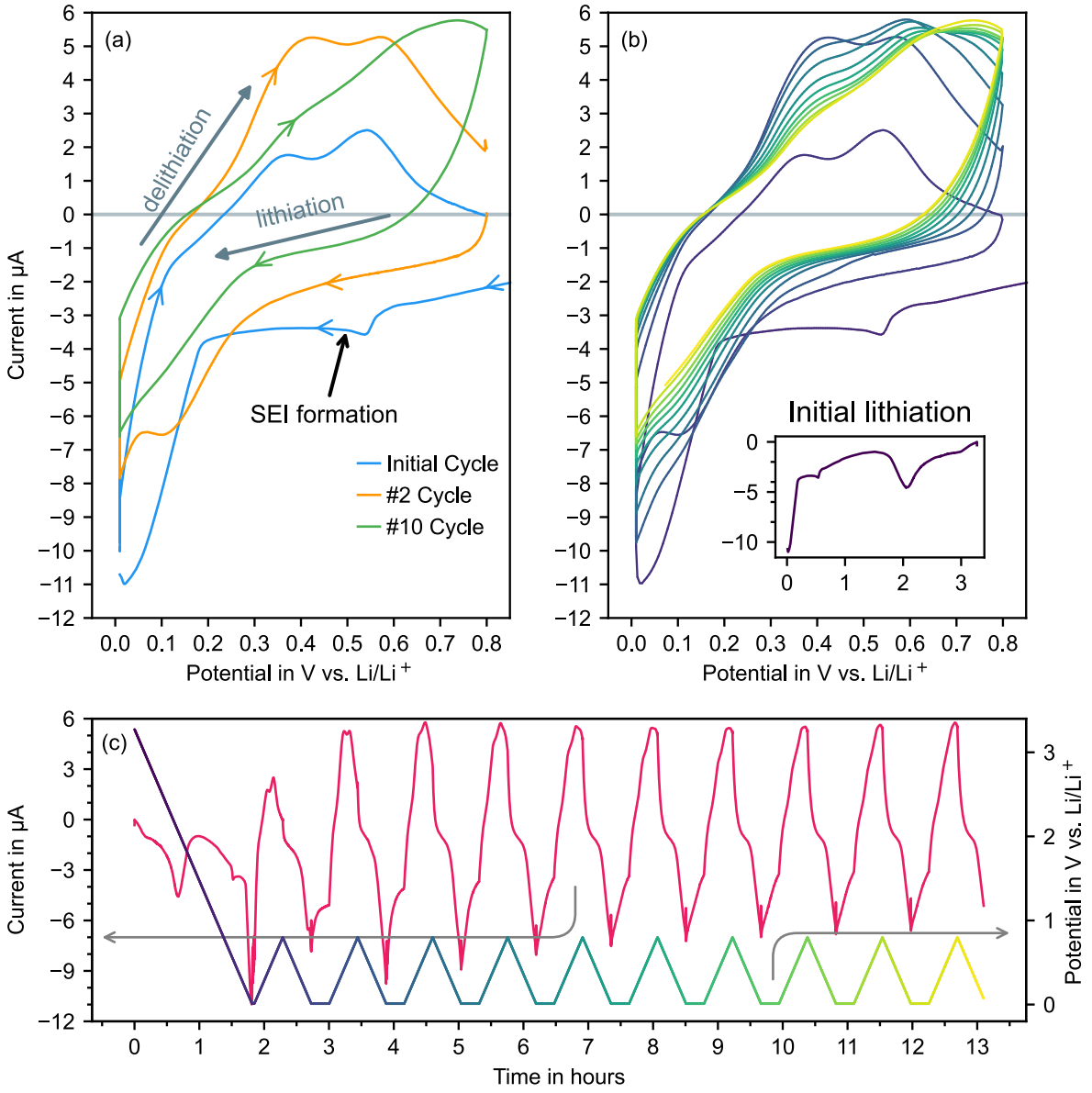

Figure 48 Summary of the electrochemical data from a representative cell of the sXAS investigation. (a) Current/potential curves from the initial, second and 10th cycle of the electrochemical procedure. Between every lithiation and delithiation sweep was a 1000 s long potentiostatic holding at 10 mV vs. Li/Li⁺. (b) Current/potential curves from all 10 cycles color coded by time corresponding to the color-code of the potential in (c). Inset shows the current/potential curve of the initial lithiation starting from the OCP value at around 3.2 V vs. Li/Li⁺ down to 10 mV vs. Li/Li⁺. (c) Current and potential as function of time over the 10 cycle of the full experiment. Potential is color-coded to give the time for the current/potential curves in (b).

In Figure 48, the current/potential response of the *in-situ* sXAS cells with a holding time of 1000 s is comparable to the behavior of the *operando* UV/Vis cells. In particular, the initial and second cycle are identical, showing the exact same distinct features: SEI formation plateau in the initial cycle together with the steep current increase for the initial lithiation of a-Si at around 0.2 V vs. Li/Li⁺, and all high- as well as low-potential de-/lithiation peaks in the second cycle. However, due to the increased holding time at 10 mV vs. Li/Li⁺, the silicon thin-films become more and more lithiated with an increasing cycle number. Thus, the delithiation is not fully completed at 0.8 V vs. Li/Li⁺ and the current response remains cathodic and the high-potential

delithiation peak shifts to higher potentials for higher cycles. As we have seen for the 100 s holding time, the low-potential delithiation peak disappears for higher cycle numbers. However, with 1000 s holding time, the high-potential delithiation peak does not decrease in intensity with continued cycling, presumably due to the longer holding time compensating the Li^+ depletion and slower reaction rates.

IV.A.2 *Operando* UV/Vis Spectroscopy and *Operando* Optical Microscopy

In addition to the electrochemical characterization, I monitored the de-/lithiation of the silicon thin-films inside my cell through *operando* UV/Vis spectroscopy and *operando* optical microscopy. Combining the electrochemical data with the UV/Vis absorption allowed me to correlate the degree of lithiation to the optical transmission. Furthermore, in optical microscopy, the lithiation-induced stresses inside the silicon thin-films also revealed themselves as wrinkling of the SiN_x window/silicon thin-film bilayer system. I want to present the results of both techniques because they produced crucial information for the development of the electrochemical procedures discussed in the previous chapter. I also consider them as valuable experiments for the future investigation of silicon thin-films, especially on flexible substrates like the SiN_x membranes. Nevertheless, I will focus on the monitoring aspect of these experiments and consider an in-depth reasoning for the changes in the UV/Vis absorption to be outside the scope of this work.

For the UV/Vis experiment I combined a “Flame UV-VIS Spectrometer” (200-850 nm) from Ocean Insight with a mercury-xenon short-arc benchtop lamp (Thorlabs, Inc.) as a light source. In analogy to the *in-situ* sXAS, the UV/Vis was conducted in transmission geometry. For this I modified the sXAS cell to accept uncollimated standard step-index multimode fiber optic patch cables (Thorlabs, Inc.), through which the spectrometer and the light source were coupled into the cell. For the optical microscopy a “Researcher Trino 40-1000x” from Bresser GmbH was heavily modified, where the necessary backlight (MWWHF2 4000 K Fiber-Coupled LED from Thorlabs, Inc.) was fed into the cell via one of the fiber optic cables. The microscope was equipped with a “MikroCam SP 5.0” and operated using the “MikroCamLabII” software, both from Bresser GmbH. Unfortunately, the optical absorption of the fully-lithiated silicon thin-films is so high that the transmitted intensity is too low to be picked up through the microscope’s beam splitter. Thus, the UV/Vis spectrometer had to be directly coupled into the cell and the *operando* UV/Vis and *operando* OM cannot be carried out simultaneously. A picture of the UV/Vis and OM setup with all labelled components is shown in Figure 49.

Furthermore, the optical absorption of the silicon thin-films changes heavily upon de-/lithiation. For this reason, I integrated the spectrometer into my custom DAQ software (as described in III.E) to dynamically adjust the spectrometer's integration time and keep a particular xenon

emission line at 823.2 nm at a fixed exposure value. This allowed me to obtain normalized UV/Vis absorption spectra for every degree of lithiation as I will present in the following.

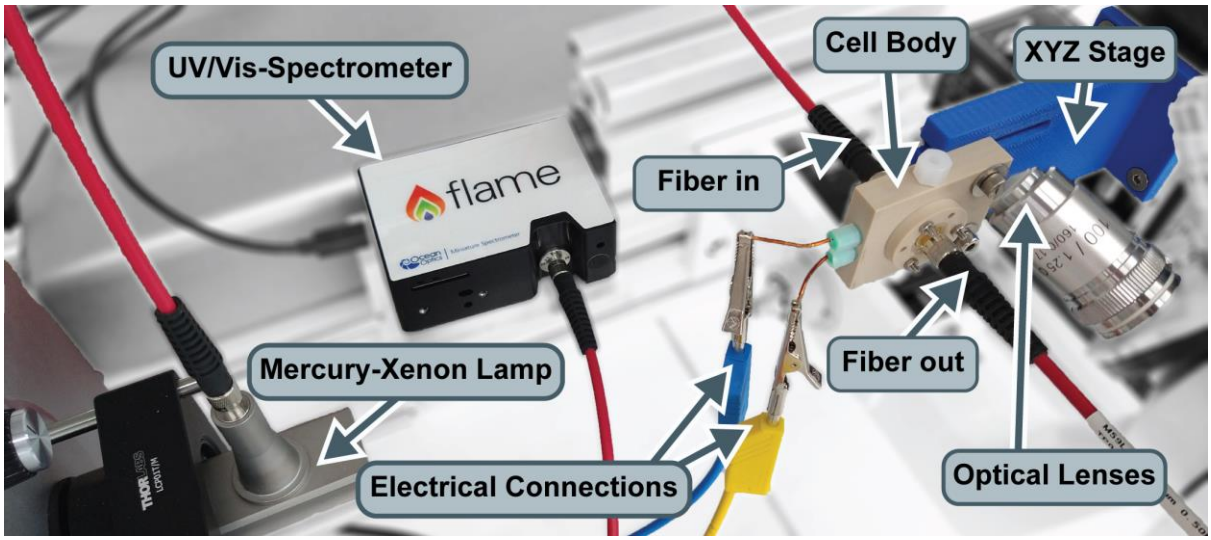

Figure 49 Picture of the operando UV/Vis spectroscopy and operando optical microscopy setup with labels for all essential components. A mercury-xenon short-arc benchtop lamp is used as a light source. Both the light source and the UV/Vis spectrometer are directly coupled into the cell through uncollimated step-index multimode fiber optic patch cables. A standard benchtop optical microscope was modified to have the optical lenses directly in front of the cell body. The necessary backlight for optical microscopy is coupled into the cell through the back-facing fiber optics cable.

IV.A.2.a *Operando* UV/Vis Spectroscopy

Figure 50a shows the current response until the third cycle from a representative cell of the UV/Vis investigation's electrochemical procedure, namely cycling between 10 mV and 0.8 V vs. Li/Li^+ and 100 s holding time at 10 mV vs. Li/Li^+. The UV/Vis data discussed in the following corresponds to the electrochemical data shown in Figure 47 and was recorded simultaneously *in operando*.

Figure 50b shows the acquisition time of the spectrometer, which was dynamically adjusted by a software algorithm to maintain a fixed count intensity at the xenon emission line at 823.2 nm, as marked in Figure 49c. The data points are color-coded by the corresponding current. It is apparent that the change in acquisition time and thus the transmission at 823.2 nm responds to the current. I take that for an anodic current (color-coded in blue) the degree of lithiation increases, the transmission decreases and the necessary acquisition time rises from around 8 ms to about 200 ms during the initial lithiation sweep and to 330 ms for the second and third cycle. As expected, this process is reversible and with a cathodic delithiation current (color-coded in red) the transmission increases again, and the acquisition time drops back down to 14 ms. While the acquisition time is a measurement for the transmission at 823.2 nm, from Figure 50c it is apparent that the transmission also changes over the whole UV/Vis wavelength range. Thus, Figure 50 shows the measured intensities over the full wavelength range at different points in time of the cycling procedure, which are

marked with their corresponding symbol in Figure 50a. For reference, the emission spectrum of the mercury-xenon short-arc benchtop lamp together with a reference optical spectrum is given in Figure 50c as well. The change in the optical transmission is also observed in the OM as a change in color, as I will discuss in the next chapter IV.A.2.b. Furthermore, with the light source emission spectrum the corresponding absorption spectra were calculated and summarized in Figure 51. Note that the obtained absorption spectra are not absolute in the sense of the Lambert-Beer law as described in (6) and (34), due to the normalization at 823.2 nm through the dynamically adjusted acquisition time. Thus, the given absorption values in Figure 51 are relative to the absorption at 823.2 nm, which was normalized to zero.

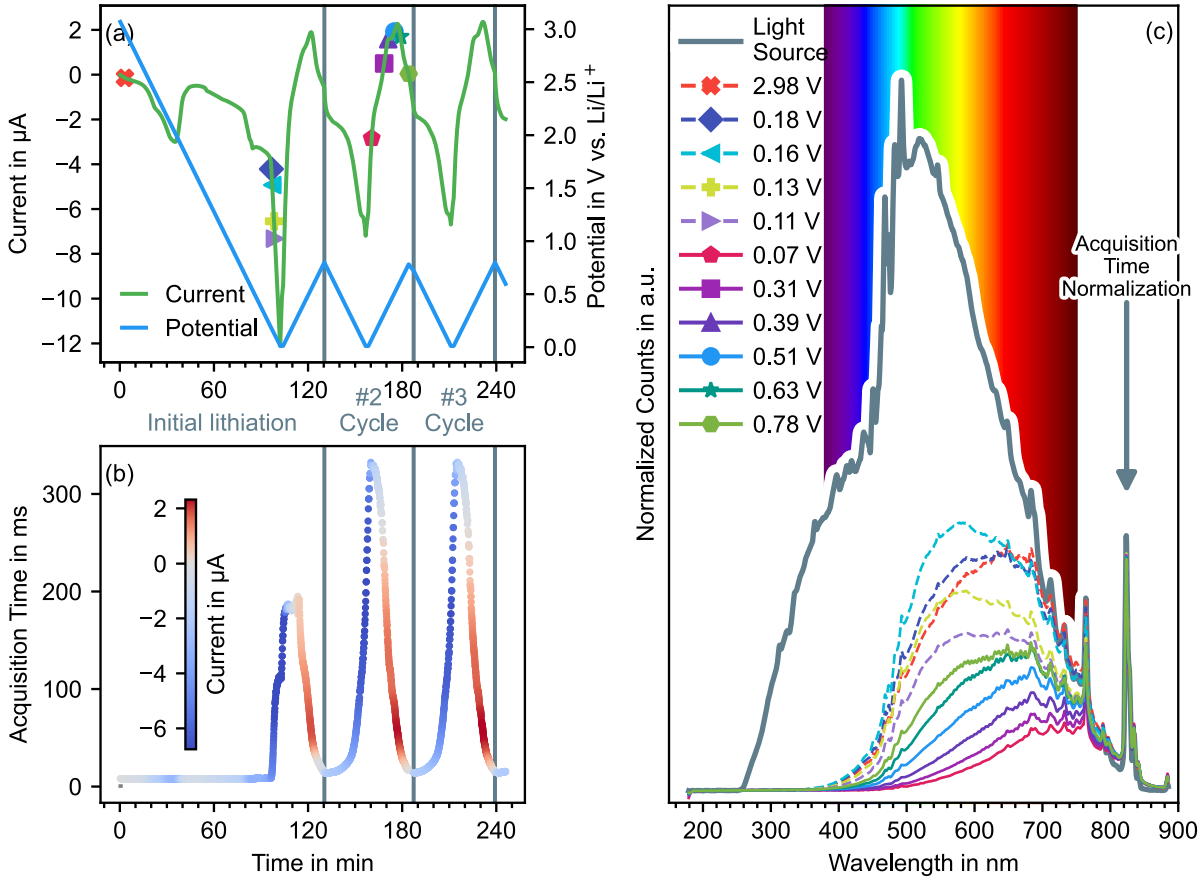

Figure 50 Summary of the UV/Vis spectroscopy raw data from a representative cell. (a) Current and potential as a function of time from the investigated UV/Vis cell for the first three cycles. The symbols mark the points in time of the UV/Vis transmission spectra in (c). (b) UV/Vis spectrometer acquisition time as a function of time for the first three cycles. Acquisition time is dynamically adjusted by a software algorithm to maintain a steady count intensity at 823.2 nm as marked in (c). (c) UV/Vis transmission spectra recorded at different points in time under operando conditions during the electrochemical procedure as marked in (a) together with the emission spectrum of the used mercury-xenon short-arc benchtop lamp light source and a reference visible spectrum in the background.

Individual UV/Vis absorption spectra during the initial lithiation as well as the delithiation of the second cycle are shown in Figure 51b and are marked correspondingly in the current/potential curves in Figure 51a. The symbol assignment was adopted from Figure 50, where the point in time can be obtained from Figure 50a.

The evolution of the UV/Vis absorption follows the current/potential response and, based on the cathodic and anodic nature of the current, changes continuously with the degree of lithiation. For a higher degree of lithiation, the absorption increases in the whole measured spectral region from 300 nm to 800 nm, and the absorption maximum moves from 350 nm to 400 nm. The biggest change in absorption is observed at around 450 nm. In the following discussion the absorption at 450 nm is determined from the average value between 445 nm and 455 nm, as indicated by the white bar in Figure 51c,d.

The absorption as a function of the degree of lithiation can be observed during the delithiation sweep of the second cycle when the absorption evolves continuously from 0.07 V (red pentagon) to 0.78 V vs. Li/Li^+ (green hexagon). The continuous and reversible nature of this process is also demonstrated in Figure 51c, which depicts the evolving absorption over the complete electrochemical procedure of 20 cycles. This continuous change in the UV/Vis absorption supports my initial claim that, after the initial cycle, the silicon thin-films remain in the amorphous regime and the cycling takes place between a-Si* and a-Li_xSi. Thus, I assign the spectra of the higher lithiated (red pentagon, 0.07 V vs. Li/Li^+) and lower lithiated state (green hexagon, 0.78 V vs. Li/Li^+) to a-Si* and a-Li_xSi, respectively.

Since the largest absorption change occurs around 450 nm, I note that this is the most reliable measurement of the degree of lithiation. As demonstrated with the absorption at 450 nm in Figure 51f, the degree of lithiation throughout each charging cycle can be tracked. The hysteresis-like curve of the absorption reveals two plateaus between lithiation and delithiation and highlights their onset potentials. During the lithiation sweep, the absorption remains at around 3 until the onset of the high-potential lithiation peak at around 0.3 V vs. Li/Li^+. The degree of lithiation then increase rapidly to reach its maximum value of 6 after the potentiostatic holding at 10 mV vs. Li/Li^+. When delithiating, the absorption value stays at its plateau value of 6 until the onset potential of the low-potential delithiation regime at 0.3 V vs. Li/Li^+ is reached. As indicated by the tangents in Figure 51f, the absorption changes with two different kinetics, which in turn appears to correspond to the low- and high-potential delithiation stages. As discussed in I.C.1, the two stages are presumably correlated to different local environments with higher and lower Li/Si coordination numbers at different Li content [87], [95], [97], [98]. This suggests that the absorption at 540 nm is not only sensitive to the degree of lithiation in the sense of a “total lithium loading”, but also might correspond to the local environments with different Li/Si coordination.

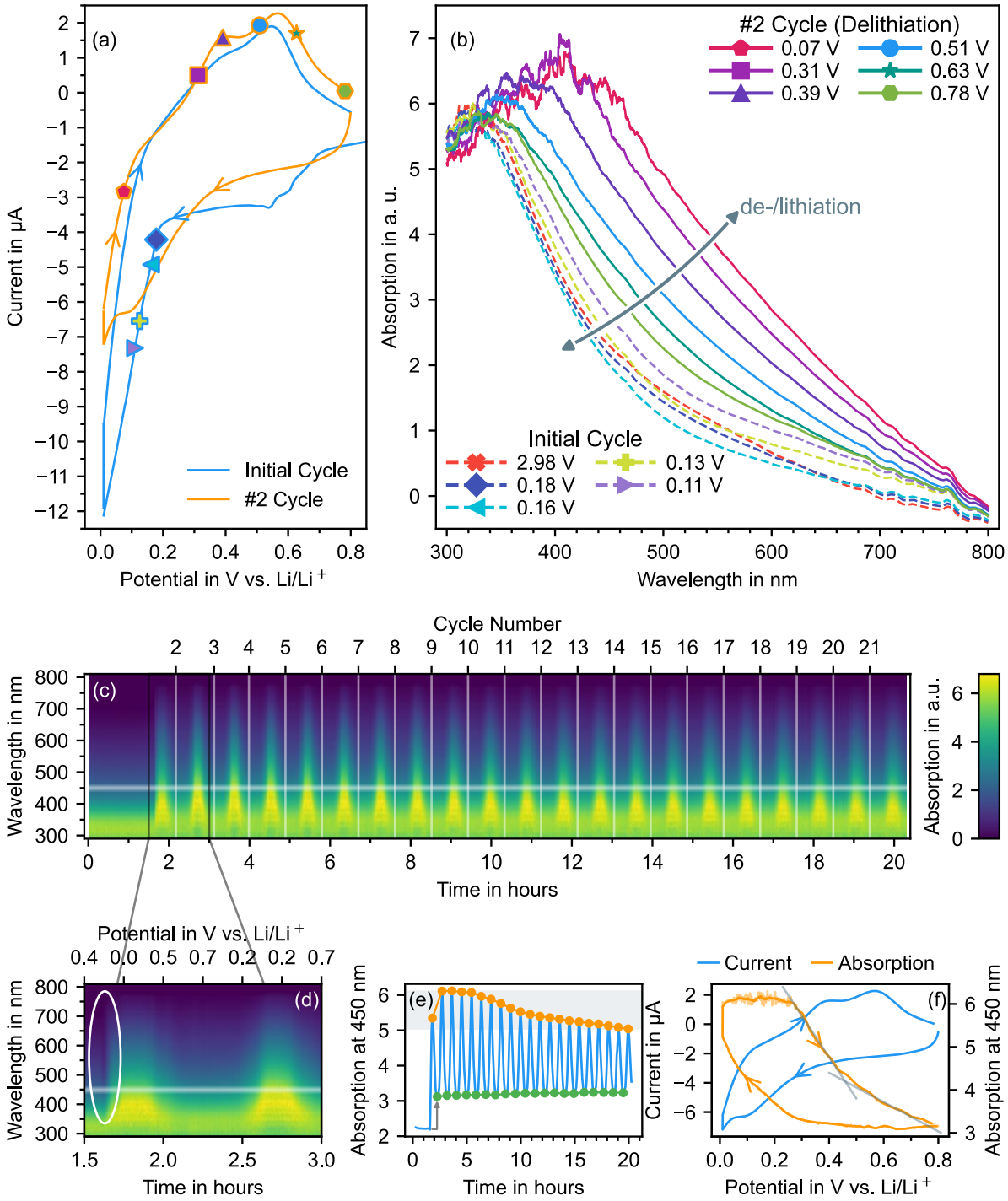

Figure 51 Summary of the UV/Vis evaluation from a representative cell. (a) Current/potential curves from the investigated UV/Vis cell for the initial and second cycle. The symbols mark the points in time of the UV/Vis absorption spectra in (b). UV/Vis absorption spectra recorded at different points in time under operando during the electrochemical procedure as marked in (a). (c) UV/Vis absorption as a function of time over the course of the complete electrochemical procedure of 21 cycles. (d) UV/Vis absorption as a function of time for the initial and second cycle. (e) Average absorption in the wavelength range from 445 to 455 nm as a function of time over the course of the complete electrochemical procedure of 21 cycles. Orange dots mark the maximum absorption and green dots mark the minimum absorption at 450 nm of each individual cycle. Grey area marks the capacity fade of 18% over 21 cycles. Grey arrow marks the small increase of absorption after the initial lithiation. (f) Current/potential curves from the investigated UV/Vis cell of the second cycle together with the corresponding average absorption in the wavelength range from 445 to 455 nm.

Furthermore, as expected from the current/potential response discussed before, the initial cycle differs from all other cycles. As it can be seen in Figure 51b as well as Figure 50c for 2.98 V, 0.18 V, 0.16 V, 0.13 V, and 0.11 V, the UV/Vis absorption changes rapidly during the initial lithiation of a-Si. I suggest that these changes correlate to the breaking open of the silicon structure with a presumably increasing degree of dangling bonds, similar to the structural changes from a-Si to a-Si*, as proposed by McDowell *et al.* [100]. For a short duration, this rearrangement is even accompanied by an increased transmission as it can be seen for the spectra at 0.18 and 0.16 V vs. Li/Li^+. This reduction in optical absorption during the first lithiation is also highlighted by the white circle in Figure 51c. The increase in transmission during lithiation between 0.2 and 0.1 V vs. Li/Li^+ is not present in any consecutive cycle.

When comparing the absorption spectrum of the pristine a-Si thin-film, represented by the spectrum close to the OCP at 2.98 V vs. Li/Li^+ in Figure 50 and Figure 51, with spectra measured after the initial cycle, it is apparent that the silicon thin-films are not fully transformed back to their pristine state. This effect can be quantified through the absorption at 450 nm. The absorption at 450 nm is shown in Figure 51e as a function of time during the cycling procedure. After the initial cycle, the absorption value for the delithiated state (marked as green points) remains with about 3.1 above the absorption value from the pristine thin-film with about 2.2 (marked with a grey arrow in Figure 51e). The overall slight increase in UV/Vis absorption may correlate to the expected a-Si/a-Si* structural changes described earlier in chapter I.C.1. I propose that this may hint at trapped residual lithium content as suggested by McDowell *et al.* [100].

Besides this, the absorption at 450 nm can also be used to monitor the capacity of the cell and its fading. In Figure 47, we observe the de-/lithiation current to decrease with an increasing cycle number and attribute this behavior to a presumable increase in overpotential due to an increasing SEI thickness coupled with a depletion of Li^+ inside the electrolyte. Looking at Figure 51e, this behavior is also reflected by the absorption at 450 nm in the lithiated state, as marked by the orange dots. Here, the maximum lithiated absorption at 450 nm drops from 6.1 down to 5.0 over the course of 20 cycles, which corresponds to a fading of 18%. However, as described in chapter I.C.3, silicon thin-films are expected to crack during delithiation. If cracking leads to a loss of contact, this leaves behind lithiated debris, which would then increase the UV/Vis absorption at 450 nm continuously with each cycle. In Figure 51e, however, the absorption after delithiation does not increase over time and remains at around 3.1. Based on this, I infer that the observed capacity fade of 18% is not caused by pulverization of the silicon thin-film but more likely stems from an increase in overpotential and depletion of Li^+ inside the electrolyte.

In the same regard, UV/Vis measurements were not possible for imperfect pristine samples with holes and cracks, because the unattenuated transmission of the mercury-xenon lamp through large cracks overshadows all sample signal in the UV/Vis spectrum (see Figure 52 and Figure 54). When looking at the emission spectrum of the mercury-xenon lamp in Figure 50c, smaller cracks and holes, which evolve over time with increasing cycle count would reveal themselves through transmission in the UV region below 400 nm. However, such leaks are not observed in the UV/Vis data presented here. With this, I am confident that thin-film anodes, which are initially flawless in their pristine state, remain free of cracks and holes throughout the experiment for a minimum of 20 cycles.

IV.A.2.b *Operando* Optical Microscopy

Figure 52 summarizes the *operando* OM investigation by showing OM images from the initial and second cycle of a representative cell. The depicted cell has been cycled according to the procedure of the UV/Vis investigation (100 s holding time at 10 mV vs. Li/Li^+), except for the first four cycles where the cycling was limited between 10 mV and 0.6 V vs. Li/Li^+. Figure 52a,b shows the current/potential response of the initial and second cycle from the investigated cell with the moments in time of the OM images (0) to (19) marked by the corresponding symbol. In analogy to the acquisition time in the UV/Vis investigations, the exposure time has been adjusted dynamically throughout the electrochemical procedure between 0.01 s and 2 s to maintain a fixed exposure value, as it is given in the title of each OM image. Like in the UV/Vis investigation, the exposure time changes synchronously with the degree of lithiation. Furthermore, the white balance was calibrated once to match the pristine state of the silicon thin-film at the OCP, which is resembled by (0) in Figure 52 (no change occurred from the OCP to this point during the electrochemical procedure). The corresponding white balance setting was 3951 K with a tint of 835, as expected from the 4000 K backlight LED.

The bright white spot visible in every OM image in Figure 52 is a hole in the silicon thin-film which lets through the unattenuated light source. It renders this particular sample unfeasible for an UV/Vis investigation, because it overshadows the sample spectrum, as I have discussed at the end of the previous chapter. Nevertheless, I found it in no way detrimental for the OM investigation. Figure 54a gives the current and potential as function of time over the complete electrochemical procedure of 25 cycles, demonstrating that such flaws are unharmful for the cyclability. Here, the bright intensity through the hole can serve as an imminent measurement for the exposure time of each image.

When looking at (1) to (4) in Figure 52, the initial lithiation of a-Si is visible as a change in color, an increase in absorption, which is reflected by a prolonged exposure time from 0.01 s to 1.5 s, and an extensive wrinkling of the SiN_x window/silicon thin-film bilayer system. The

change in color and the increased absorption itself are complementary information to the UV/Vis investigation discussed earlier. However, the OM now adds spatial information and in (1) to (3) of Figure 52 clearly shows that the lithiation of a-Si during the initial cycle is concentrated at the center of the membrane window and proceeds gradually to the sides. I propose that the wrinkling is a direct result of the stresses induced by the volume expansion upon lithiation. The wrinkling and hence the stresses are most pronounced at the sides while the center remains almost wrinkle- and stress-free. As it was summarized by Kim *et al.* [86], there is a strong coupling of the electrochemistry and the mechanical changes and with this a stress effect on the electrochemical potential. I propose that the increased mechanical stress at the sides of the membrane window lowers the lithiation potential and delays the lithiation there, as it can be observed especially in (3) of Figure 52. However, the stress appears to only delay the lithiation and not prevent it altogether, as (4) shows both a homogeneous color and absorption (perceived as brightness in OM) shortly after the 100 s long potentiostatic holding time at 100 mV.

To further focus on the wrinkling and the corresponding stresses, looking at (5) to (7) in Figure 52, during the first delithiation sweep the wrinkles disappear between 0.27 V and 0.30 V vs. Li/Li^+ over the course of only about 1.1 minutes and the membrane appears completely wrinkle-free in (8). The color and the absorption value (perceived brightness with same exposure time), however, do not change drastically from (5) to (7), indicating that the wrinkling's extent is not directly correlated to the degree of lithiation. Nevertheless, while traversing the low- and high-potential delithiation peaks, the degree of lithiation and with this the exposure time decreases between (8) and (9) from 2.0 s to 0.1 s. This is in perfect agreement with the UV/Vis investigation discussed earlier.

Note that the change in the visible absorption spectrum observed in Figure 50 and Figure 51 is not as extensively perceived in the OM color due to the narrow emission peak of the white LED at 450 nm (see Appendix 1) compared to the broader emission spectrum of the mercury-xenon lamp used in the UV/Vis investigation (see Figure 50). Nevertheless, a slight change in color between (8) and (9) is still noticeable.

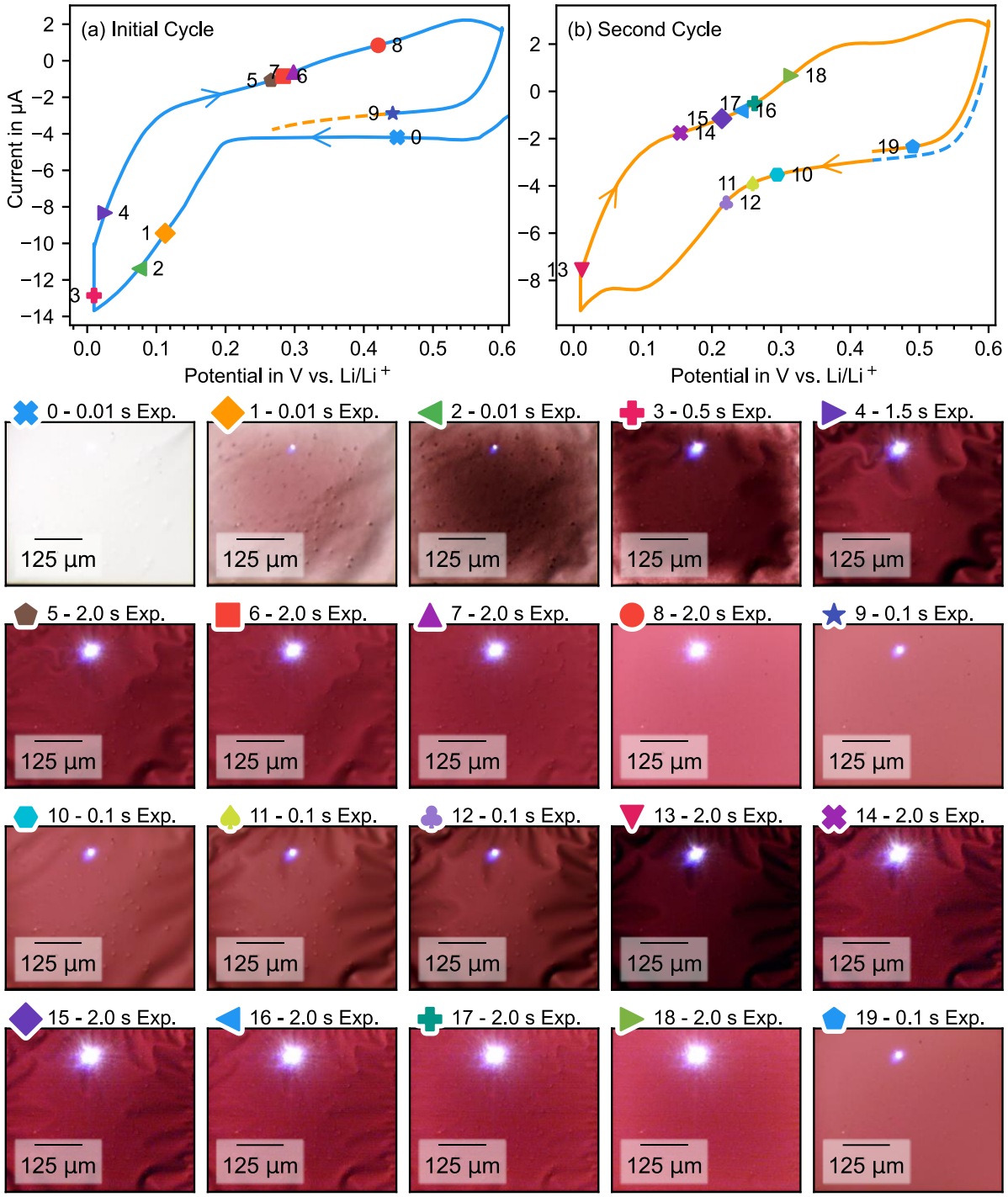

Figure 52 Summary of the operando OM investigation from a representative cell. (a)-(b) Current/potential curves from the investigated OM cell for the initial and second cycle following the electrochemical procedure of the UV/Vis investigation. The symbols mark the points in time of the OM images (1) to (19). The exposure time is given in the caption of each image.

In the second cycle, the wrinkling suddenly reappears between 0.29 V to 0.22 V vs. Li/Li$^+$ over the course of about 2.5 minutes from (10) to (12). The wrinkling pattern then remains unchanged until the end of the 100 s long holding time at 10 mV vs. Li/Li$^+$ as shown in (13). Like before, the optical absorption and hence the exposure time increased accordingly from (12) to (13) as expected for an increase in degree of lithiation. In contrast to the initial lithiation,

in (9) to (14), the second cycle's lithiation occurs homogeneously throughout the whole window area and is not focused at the center, as initially observed in (1) to (3). Further, in analogy to the initial delithiation, the disappearance of the wrinkling then again takes place between 0.15 V to 0.26 V vs. Li/Li^+ over the course of about 4.6 minutes at the onset of the low-potential delithiation peak, as it can be seen in (14) to (17). Afterwards, the thin-film / membrane stack appears wrinkle-free in (18) again. When traversing both delithiation peaks, the degree of lithiation and optical absorption decrease simultaneously from (18) to (19). Comparing (5) to (15), (8) to (18) and (9) to (19), the reversibility of both the wrinkling and the change in visible absorption (perceived brightness and color) is apparent.

Although the volume expansion is proportional to the degree of lithiation (compare Figure 8c), the stress state inside silicon thin-films is not. Through *operando* multi-(laser)beam optical sensor measurements, Sethuraman *et al.* revealed that the de-/lithiation of silicon thin-films is governed by elastic and plastic deformation and alternates between a compressive and tensile nature in each cycle [108], [278], [279]. As it can be seen in Figure 53, the initial lithiation's volume expansion leads to a linear increase in the compressive stress up to about 1.7 GPa, where the film appears to reach its elastic limit and begins to flow plastically. Any further lithiation, and hence volume expansion, is then accommodated through plastic deformation. With increasing degree of lithiation, the flow stress appears to decrease as the compressive stress slowly decays down to about 1 GPa until the cut-off capacity of about 1875 mAh g^{-1}. In the beginning of the delithiation, the stress reverses elastically to quickly reach a plateau of about 1 GPa in tension, where any further delithiation appears to be carried by the plastic flow again. Here, the flow stress appears to increase with decreasing degree of lithiation. With each cycle, the silicon thin-films undergo plastic and elastic deformation. Moreover, at the beginning of each process, there is a linear and rapid transition from compressive to tensile stress (lithiation) and the other way round (delithiation).

Coming back to Figure 52, the wrinkling dis-/appears abruptly in the potential range between 0.15 V and 0.30 V vs. Li/Li^+. The initial lithiation aside, this behavior continues throughout all cycles, as it is shown in Figure 54a, where the dots on top of the current response mark the onset and final stage of the de-/wrinkling, respectively. In Figure 51f, the hysteresis-like curve of the absorption at 450 nm correlates this potential range to the onset of the de-/lithiation process. Thus, the wrinkling appears to be only determined by the stress and not by the degree of lithiation itself. Based on the findings of Sethuraman *et al.* discussed before, I attribute the sudden de-/wrinkling to the elastic stress transition at the beginning of each de-/lithiation process as highlighted in Figure 53. Furthermore, I propose that the wrinkling's extent is determined by the interplay between the overall stiffness of the SiN_x window/silicon thin-film bilayer system and the flow stress of a-Li_xSi. On the one hand, at some point during lithiation

plastic deformation becomes energetically favorable and the wrinkling remains constant. On the other hand, straightening releases more energy imminently and the wrinkles disappear right at the beginning of the delithiation process.

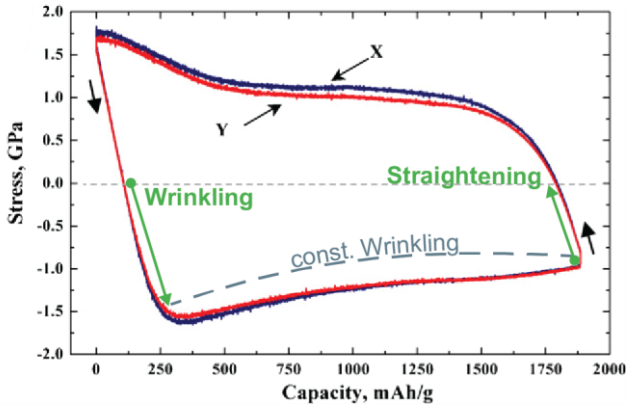

Figure 53 Stress inside silicon thin-film anodes during de-/lithiation as function of capacity. Determined through multi-(laser)beam optical sensor measurement in X and Y direction. Annotated and adapted from [278].

In summary, the wrinkling's extent of the silicon thin-films on a square SiN_x membrane window cannot be considered a suitable measurement for the degree of lithiation. Given the complexity of the bilayer system and the chaotic nature of the wrinkling itself, corresponding stresses cannot be deduced reliably. Nevertheless, the OM investigation provides useful insights into the de-/lithiation behavior of silicon thin-film anodes used as a sample system in this work to investigate the SEI through sXAS. The OM shows that after the initial cycle, the lithiation appears to be homogeneous throughout the whole SiN_x window and a homogeneous SEI is expected. Furthermore, it clearly highlights that there is a time window in which the SiN_x membrane/silicon thin-film stack is wrinkle-free. For the experimental feasibility of the *in-situ* sXAS this turned out to be an essential piece of information. After the electrochemical procedure, I found the risk of breaking the SiN_x membrane window during pumping to be highly reduced when the cycled cell is loaded into the vacuum of the experimental beamline in a low-lithiated, wrinkle-free state. Furthermore, in good agreement with the UV/Vis investigation, the OM reassures in Figure 54a,b that the silicon thin-film anodes remain crack-free over a course of at least 20 cycles, when cycled between 10 mV and 0.8 V vs. Li/Li^+. In this regard, during the development of a suitable electrochemical procedure for the silicon thin-films, the OM revealed that the silicon thin-films develop severe cracks at potentials above 0.9 V vs. Li/Li^+, as shown in Figure 54b,c. Thus, the cut-off potential of delithiation was set to 0.8 V vs. Li/Li^+ accordingly.

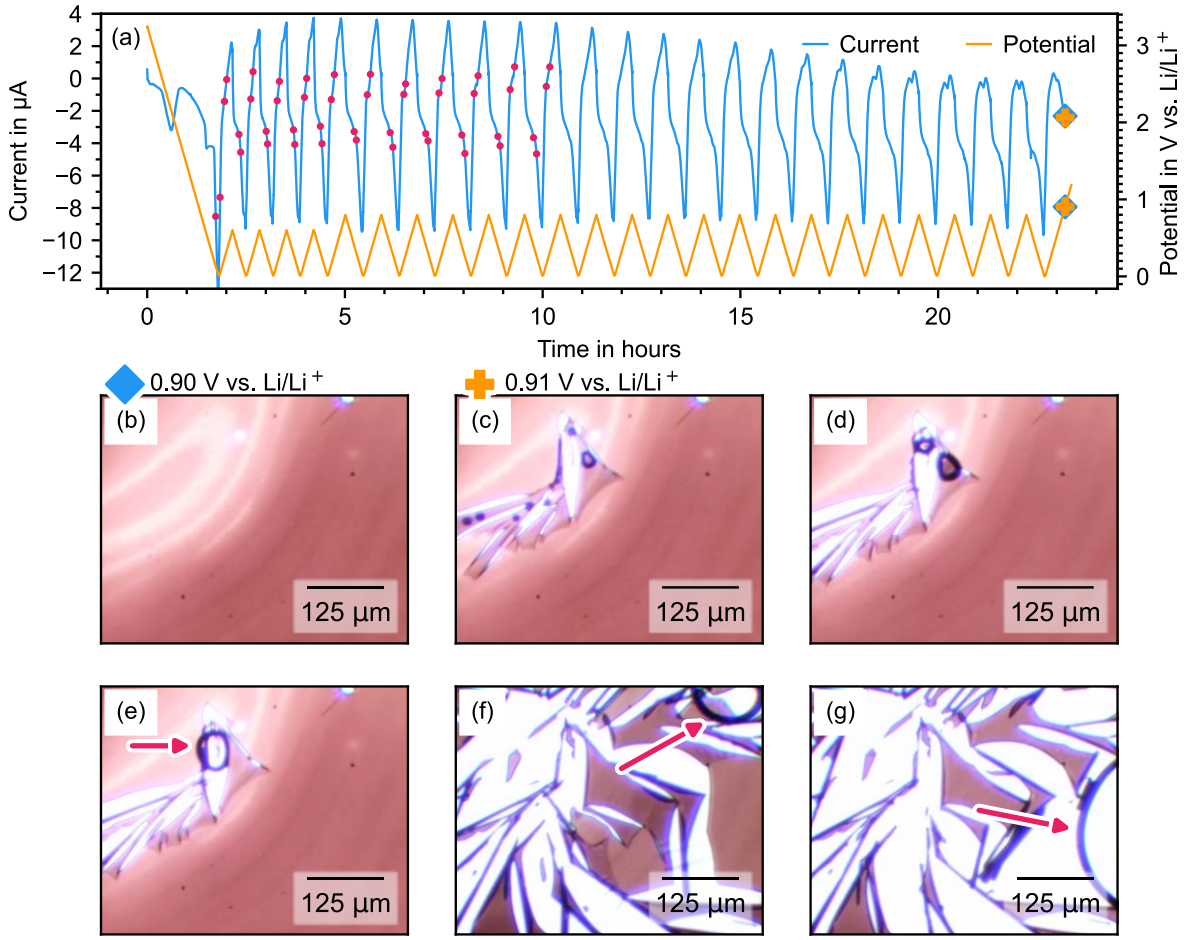

Figure 54 Continued summary of the operando OM investigation from the cell presented in Figure 52. (a) Current and potential as a function of time over the complete course of the experimental procedure of 25 cycles. The symbols mark the point in time of the OM images in (b) and (c). (b) OM image of an intact silicon thin-film after 25 cycles at 0.90 V vs. Li/Li$^+$. (c) OM image of emerging cracks in the silicon thin-film at 0.91 V vs. Li/Li$^+$. (d)-(g) OM images of emerging bubbles (indicated by red arrows) from the electrolyte at the crack sites. Over time, bubbles continuously emerge, grow and move slowly outside of the SiN_x window.

As it can be seen in Figure 54c-g, right after cracking, gas bubbles emerge from the electrolyte. This shows that gas is dissolved inside the electrolyte and exceeds its solubility limit. Before cracking, the solution is in a supersaturated state and the cracks then provide heterogeneous nucleation sites for bubbles to emerge. Based on the discussion in chapter I.B.1, it is reasonable to attribute the presence of gas to the electrochemical reduction of the electrolyte and the SEI formation itself. The a priori presence of gas inside the electrolyte also has decisive implications for the bubble formation in the sXAS experiment. In the theoretical simulation of this novel sXAS approach presented in chapter III.C.2, I assume the electrolyte to be gas-free initially. With this, the presented simulation is more general and applicable to experiments without electrochemical pre-treatments. The presence of gas inside the electrolyte, as it was revealed by the OM in Figure 54c-g, however, now anticipates that a smaller radiation dose for the bubble formation is necessary.

IV.A.2.c *Post-mortem* Optical Microscopy

When it comes to the bubble itself, from the *in-situ* sXAS investigation presented in the next chapter, I have obtained *post-mortem* OM pictures of the cells after they have been removed from the vacuum chamber. The *post-mortem* OM pictures are shown in Figure 55a,b. In both pictures the bubble's outline can be seen in each corner. Furthermore, the picture in Figure 55a was taken right after the cell was removed from the vacuum chamber. I assume that upon deflation of the membranes (through removing the vacuum on the outside), the electrolyte thin-layer gets disrupted into small isles, which can be seen through the colorful iridescence pattern they create. Thus, the observed colorful iridescence pattern puts the thin-layer thickness in the sub micrometer range. Over time, the surface tension coalesces the isles into smaller droplets, which are visible in Figure 55b. The iridescence pattern is not visible anymore in Figure 55b, clearly indicating a thicker droplet height. It must be noted that the three diagonal marks visible in Figure 55a,b correspond to the X-ray beam of sXAS measurements at the silicon L-edge with high flux and the initial bubble formation procedure. When disassembling the membrane stack, the marks are only visible at the window facing the beam, but not at the sample itself. sXAS measurements at the oxygen or fluorine K-edges with much lower flux do not leave such marks. For this reason, the L-edge investigation is performed at the end to avoid any beam damage artifacts. A more detailed consideration of beam damage at the oxygen and fluorine K-edge is described in chapter IV.B.1.d.

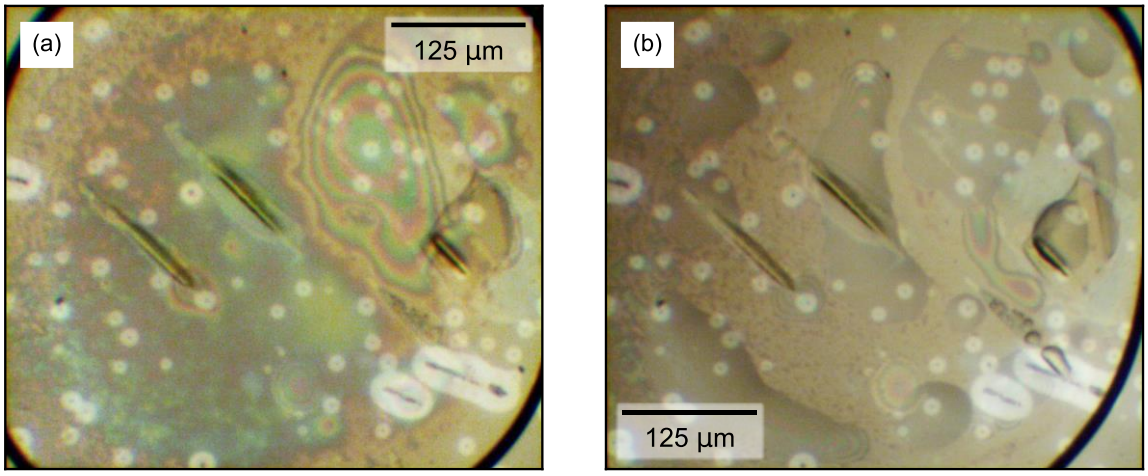

Figure 55 Post-mortem OM pictures from the cells used in the in-situ sXAS investigation. (a) OM picture of a cell right after it was removed from the vacuum chamber. (b) OM picture after the liquid thin-layer isles coalesced into small droplets.

IV.B *In-situ* X-ray Absorption Spectroscopy

When it comes to the interpretation of the transmission sXAS data, I want to anticipate one fundamental principle right at the beginning. All transmission sXAS spectra presented in this work can be considered a linear combination of the individual absorption of every component

within the beam's path. Thus, for its interpretation, a transmission sXAS spectrum must always be considered in its entirety, taking every component into account.

To double down on the picture of "the X-ray goes through everything", I have structured the following discussion in the order of the components the X-ray transmits: the gas bubble at first, then the liquid thin-layer, finally the SEI and the silicon thin-film anode itself. Thus, I will first discuss the sXAS spectrum at the oxygen K-edge of the bubble in chapter IV.B.2. Here, I will present how I identified CO and CO_2 as the main gaseous bubble components, which was essential information for my simulation presented in the previous chapter. Then, in chapter IV.B.3, I will focus on the sXAS at the oxygen K-edge of the model electrolyte system: 1M $LiPF_6$ in EC:DMC. With this, I will demonstrate my novel approach's capability for the transmission XAS in the soft X-ray regime by comparing it to a liquid microjet measurement from literature of a comparable electrolyte, namely 1M $LiBF_4$ in PC. With the knowledge about the individual absorption spectrum of the gas bubble and the electrolyte, I will then unravel the obtained *in-situ* spectra of cycled silicon thin-film anodes to extract the spectrum of the SEI in chapter IV.B.4. Based on the extracted SEI spectrum, I will go on and identify possible SEI species based on their spectral fingerprints at the oxygen and fluorine K-edge. At last, in chapter IV.B.5, I will present how the degree of lithiation of the silicon thin-films can be monitored at the silicon L-edge.

IV.B.1 X-ray Absorption Spectroscopy Technical Details

The sXAS was performed at the U49-2_PGM-1 [194] and UE56-2_PGM-2 beamlines of the BESSY II synchrotron facility in Berlin using the SOL³PES [280] and LiXEdrom [281] experimental stations. Both stations were operated under high vacuum conditions of $2x10^{-6}$ mbar.

The transmission signal was measured with a GaAsP (Hamamatsu G1127) or GaP (ifw optronics JEP5-365) photodiode and an electrometer (Keithley 6514). For the *in-situ* measurements at the U49-2_PGM-1 beamline, the slit size was set to 5 µm, which correlates to a focal size of about 85 µm x 25 µm [194] at the sample position. Hence, the focal size was sufficiently small to probe the sample at several different positions within the 500 µm x 500 µm SiN_x windows. This allowed me to pick a fresh sample spot for each measurement, as illustrated in Figure 60, and avoided noticeable beam damage effects. To decrease the data acquisition time and minimize the radiation dose, the absorption spectra were recorded in continuous mode - monochromator and undulator were accelerated once and then move synchronously through the desired spectral region [282]. This reduces scanning time and dose by a factor of 4 – 5 compared to ordinary step mode measurements [283]. The oxygen K-edge (520 – 560 eV) was recorded in 7 min with a scan speed of 0.1 eV s^{-1} and the fluorine K-edge

(670 – 760 eV) in 7 min with a scan speed of 0.2 eV s^{-1}. With a data acquisition rate of 10 Hz (Net Power Line Cycles NPLC 5) the sampling resolution is 5 meV and 20 meV for the oxygen and fluorine K-edge, respectively. For representative measurements, we estimated a total dose below 2 µJ at the oxygen K-edge and about 5 µJ at the fluorine K-edge for each recorded spectrum, respectively. This estimation is described in more detail in chapter IV.B.1.c and chapter IV.B.1.d based on Table 4 as well as Figure 58 and Figure 59.

The absorption was calculated from blank measurements of the bare photodiode each day. Both the blank and the sample measurement themselves were normalized by the individual drain current of the refocusing mirror upstream, which was again measured with an electrometer (Keithley 6514). The diode and mirror current were measured simultaneously, by triggering the electrometers synchronously through their GPIB interface. The background of the absorption spectra was removed by fitting linear slopes to the pre- and post- ionization edge regions. Because the exact ionization edge-step function is unknown, the transition between both slopes was approximated by a second-degree Bezier curve. The energy in the oxygen K-edge region was calibrated to the 1s to $2\pi_u$ transition of CO_2 at 535.5 eV photon energy from a reference gas transmission spectrum measurement at the end of each day. Alternatively, the energy values where calibrated by aligning the blank diode current signals. At the fluorine K-edge we relied on the energy calibration of the U49-2_PGM-1 [194] beamline. The full data treatment, i.e., the calculation of the absorption signal, the energy calibration, and the background subtraction procedure, is described in more detail in chapter IV.B.1.a.

Furthermore, reference compounds commercially available as powders were ground in a mortar and deposited onto a conductive carbon tape or pressed into an indium foil. The measured reference powders and liquids were: 1M $LiPF_6$ in EC:DMC (Battery Grade, Sigma-Aldrich), 1M $LiPF_6$ in DMC (Battery Grade, Sigma-Aldrich), Diethyl oxalate (98%, TCI Europe), Li acetylacetonate (98%, Sigma-Aldrich), Lithium ethylene mono-carbonate (LEMC) (GenoSynth GmbH), LiOH (anhydrous 98%, Alfa Aesar), Li trifluoroacetate (97% Alfa Aesar), Li_2O_2 (95%, Acros Organics), Li methoxide (98%, Sigma-Aldrich), Li_2CO_3 (99%, Sigma-Aldrich), LiF (99.98 trace metal basis, Sigma-Aldrich), $LiPF_6$ (98%, Alfa Aesar). The preparation was done in an argon glovebox (M. BRAUN, O_2 and H_2O kept <0.1 ppm) and the samples were brought to the experimental station in a sealed container. For the transfer into the vacuum chamber the time of air exposure was kept under 30 s. For LEMC as a particular air-sensitive sample, an Argon-filled glove bag (AtmosBag, Sigma-Aldrich) was used for the transfer and the experimental chamber was flushed with Argon priorly. The absorption spectra of the powder references were obtained through TEY measurements, measured as the drain current by an electrometer (Keithley 6514). Absorption spectra of reference compounds that are commercially available as liquids were recorded in transmission with my cell using the

bubble stabilized liquid thin-layer approach. For this, the cell was assembled with two uncoated SiN_x membrane windows inside a glove bag (AtmosBag, Sigma-Aldrich) that was flushed with Argon. Reference spectra sourced from literature where digitized using the software “GetData Graph Digitizer”.

IV.B.1.a X-ray Absorption Data Treatment

IV.B.1.a.1 Absorption Calculation and Contamination Correction

XAS at the oxygen K-edge demands the highest degree of diligence when it comes to oxygen contamination on beamline-optics upstream and on the photodiode. In this work, I calculated the absorption through (33). The calculation of the absorption is illustrated in Figure 56a-c based on a representative spectrum at the oxygen K-edge. While the drain current of the refocusing mirror is usually a good measurement for the incoming beam intensity, oxygen contaminations on the mirror, however, create a drain current signal that does not reflect the true incoming beam intensity and the mirror current is no longer proportional to the incoming photon flux. For this reason, the signal from the photodiode, I_D, is the best estimate of the true incoming beam intensity, I_0. As a bonus, this signal also contains the intrinsic gain of the photodiode and all contaminations on the photodiode, and, if used for the calculation of the absorption, it accounts for all these effects. However, it is only possible to measure the bare photodiode I_D^m and the sample I_S^m consecutively. In the following, D denotes the measurement of only the diode, while S the measurement with the cell/sample in the beam path. Individual, present fluctuations that are different from measurement to measurement (f_S and f_D) lead to a worse signal to noise ratio when I_D^m and I_S^m are used to calculate the absorption directly. As the main origin of these fluctuations, I identified vibrations of the grating or the refocusing mirror, uneven undulator movements or decaying beam currents in the top-up mode of BESSY II. I found these fluctuations influence the diode and mirror signal linearly and I assume $I_D^m = I_D\, f_D$, $I_S^m = I_S\, f_S$, $M_D^m = M\, a\, f_D$ and $M_S^m = M\, a\, f_S$, where m denotes the measured quantities, I_D and I_S are the actual diode signals, M is the actual intrinsic mirror current that is assumed to be the same for all measurements and a is a factor that accounts for the different influence of the fluctuations on the diode and mirror signal. Consequently, as shown in (33), I first calculate $\ln\left(\frac{I^m}{M^m}\right)$ for D and S, as shown in Figure 56b. Then, with $\ln\left(\frac{I_S^m}{M_S^m}\right) - \ln\left(\frac{I_D^m}{M_D^m}\right)$, I obtain the fluctuation free absorption $\mu = \ln\left(\frac{I_S}{I_D}\right) = \ln\left(\frac{I}{I_0}\right)$. Figure 56c demonstrates the reduced noise in $\ln\left(\frac{I_S^m}{M_S^m}\right) - \ln\left(\frac{I_D^m}{M_D^m}\right)$ over the direct $\ln\left(\frac{I_S^m}{I_D^m}\right)$ calculation. The D measurements were performed daily at the end of each beamtime shift and are the mean values of up to three consecutive measurements. The beamline parameters for D and S measurements are kept identical. Due to time constraints, there are missing D measurements for some days. In this

case, the measurements from the day before or after were used. In any case, the time difference is no longer than two days, and, based on my experience over many weeks of operation, I am confident the introduced deviations are negligible.

$$\ln\left(\frac{I_S^m}{M_S^m}\right) - \ln\left(\frac{I_D^m}{M_D^m}\right) = \ln\left(\frac{\frac{I_S^m}{M_S^m}}{\frac{I_D^m}{M_D^m}}\right) = \ln\left(\frac{\frac{I_S\, f_S}{M\, a\, f_S}}{\frac{I_D\, f_D}{M\, a\, f_D}}\right) = \ln\left(\frac{\frac{I_S}{M\, a}}{\frac{I_D}{M\, a}}\right) = \ln\left(\frac{I_S}{I_D}\right) = \ln\left(\frac{I}{I_0}\right) = \mu \quad (33)$$

The absorption calculation at the fluorine K-edge as well as the silicon L-edge was identical to the oxygen K-edge. However, due to the absence of noticeable contaminations, I relied on a single data set taken on the last day of each beamtime period for the diode only measurements D.

IV.B.1.a.2 Background and Normalization

At the oxygen K-edge, the applied removal of the background and the edge-step normalization procedure is illustrated in Figure 56d based on a representative spectrum at the oxygen K-edge. First two linear slope fits at the pre-edge (527 to 529.4 eV) and post-edge regions (556 to 558 eV) are calculated. Afterwards, an adaptive background is modelled where the pre-edge slope transitions into the post-edge slope between 530 and 550 eV. The transition region is described by a second-degree Bezier curve. Subtracting the adaptive background brings the pre- and post-edge region in parallel with the horizontal axis. Depending on the intended evaluation, the spectra can then be normalized to a mutual step height. Without this scaling, though, the step height keeps its initial value and remains an estimate for the atoms within the beam path.

The same adaptive background algorithm was applied to the fluorine K-edge, with the pre-edge region ranging from 685 eV to 682 eV, the post-edge region from 725 eV to 749 eV and the transition region between 700 eV to 720 eV.

IV.B.1.a.3 Quantification of the “Thickness Effect”

In analogy to Parratt *et al.* [189], I use the ratio between the intensity of the highest peak (PI) to the step height (SH) to quantify the degree of “washing out”. The determination of the SH and PI are illustrated in Figure 56d. The SH is determined from the difference between the post-ionization edge linear fit and the adaptive background at 540 eV. The PI is given by the difference between the absorption value of the highest peak to the adaptive background slope.

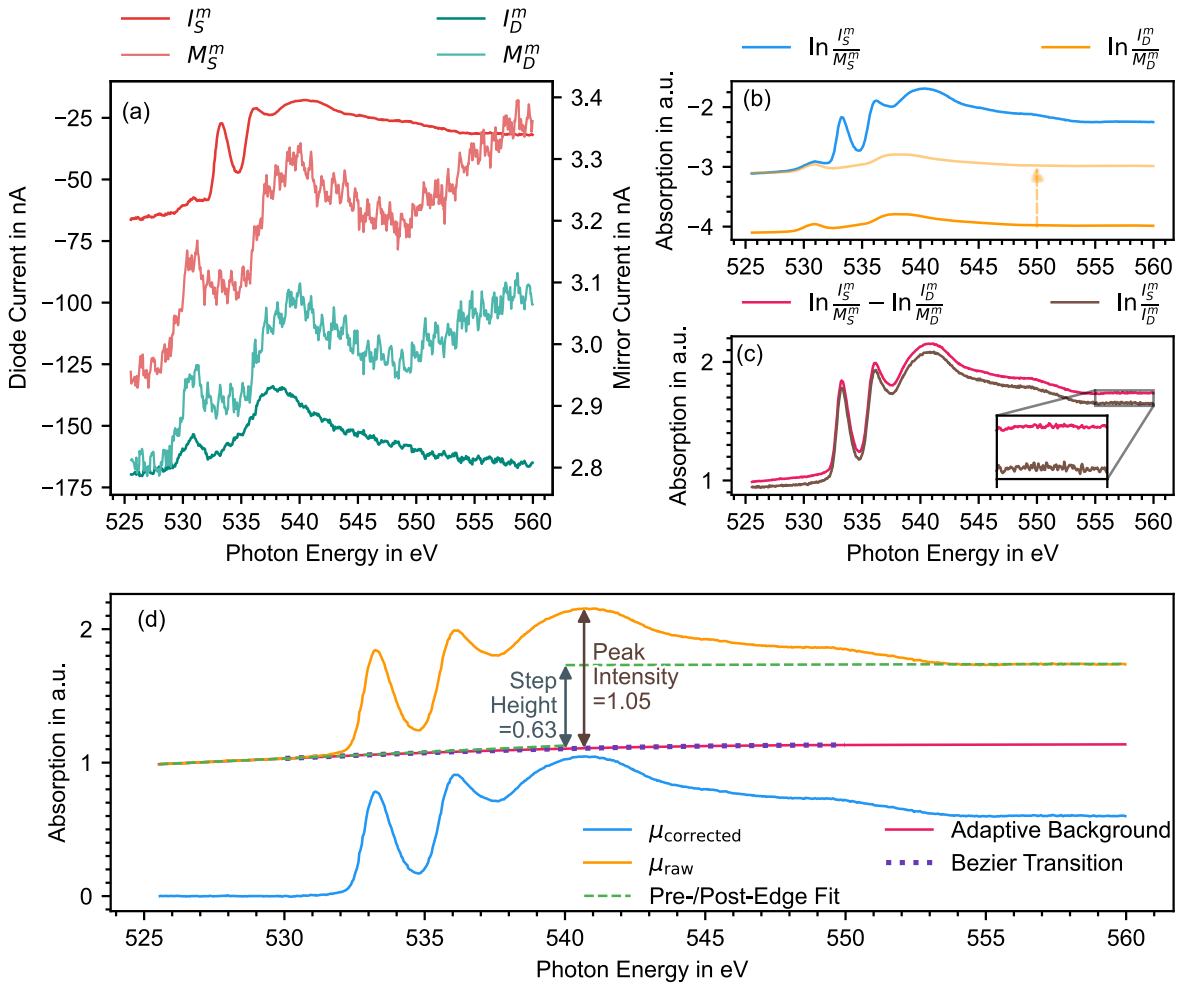

Figure 56 Summary of the absorption calculation based on a representative spectrum at the oxygen K-edge. (a) Measured diode current without sample I_D^m and corresponding measured mirror current M_D^m as well as measured diode current with sample I_S^m and corresponding measured mirror current M_S^m. (b) Calculated individual absorption of the measurement without sample $ln\left(\frac{I_D^m}{M_D^m}\right)$ and with sample $ln\left(\frac{I_S^m}{M_S^m}\right)$. (c) Comparison of the absorption calculated by subtracting the individual absorptions $ln\left(\frac{I_S^m}{M_S^m}\right) - ln\left(\frac{I_D^m}{M_D^m}\right)$ or by directly calculating the absorption based on the measured diode currents through $ln\left(\frac{I_S^m}{I_D^m}\right)$. (d) Summary of the background normalization and extraction of the step height and the peak intensity for the quantification of the "Thickness Effect" on a representative spectrum at the oxygen K-edge.

IV.B.1.a.4 Energy Calibration

At the oxygen K-edge the energy was calibrated using the 1s to $2\pi_u$ transition of CO_2 at 535.5 eV [186]. The CO_2 reference spectra were performed daily at the end of each beamtime shift by flushing the chamber with CO_2 gas up to a pressure of around 1.2 mbar and measuring the absorption directly with the diode as described before. For days when a reference measurement was not possible due to time constraints the energy was calibrated by aligning the $\ln\left(\frac{I_D^m}{M_D^m}\right)$ spectra accordingly.

For the energy calibration at the fluorine K-edge we relied on the energy calibration of the U49-2_PGM-1 [194] beamline of BESSY II. Our measurements of LiF at the fluorine K-edge

show the main feature at 692.36 eV, which is in sufficient agreement with literature values of 692.5 eV [284].

IV.B.1.b Thickness Estimation at the Oxygen K-edge

As described in (34), coming from the Beer-Lambert law, I correlate the edge step of the linear absorption coefficient μ to the edge step in the actual sample absorption values $\breve{\mu}$. The thickness d can be calculated through the ratio between the pre- and post-edge values of both quantities, as described in (34). For the estimation of the absorption coefficient I take the values of the EC:DMC electrolyte with an overall composition of $C_3H_5O_3$, and a density of 1.30 g cm^{-3} [40], [285]. The values are sourced from [221], [222] and shown in Figure 57a. I determine the edge step through a baseline of the pre-edge region by a linear fit, as shown in Figure 57a. Then, $\Delta\mu = \mu^{\mathrm{pre}} - \mu^{\mathrm{post}}$ is calculated as difference between the value at 585.7 eV and the baseline, as indicated by the arrow. From the individual XAS absorption spectra the edge-step of the $\breve{\mu}$ is calculated accordingly, as shown in Figure 57b and as it was described in chapter IV.B.1.a.2 and chapter IV.B.1.a.3 for a representative example.

$$
\begin{gathered}
I = I_0 e^{-\mu d} \\
\ln\left(\frac{I^{\mathrm{pre}}}{I_0^{\mathrm{pre}}}\right) + \mu^{\mathrm{pre}} d = \ln\left(\frac{I^{\mathrm{post}}}{I_0^{\mathrm{post}}}\right) + \mu^{\mathrm{post}} d \\
d = \frac{\ln\left(\frac{I^{\mathrm{post}}}{I_0^{\mathrm{post}}}\right) - \ln\left(\frac{I^{\mathrm{pre}}}{I_0^{\mathrm{pre}}}\right)}{\mu^{\mathrm{pre}} - \mu^{\mathrm{post}}} = \frac{\breve{\mu}^{\mathrm{post}} - \breve{\mu}^{\mathrm{pre}}}{\mu^{\mathrm{pre}} - \mu^{\mathrm{post}}} = \frac{\Delta\breve{\mu}}{\Delta\mu}
\end{gathered}
\tag{34}
$$

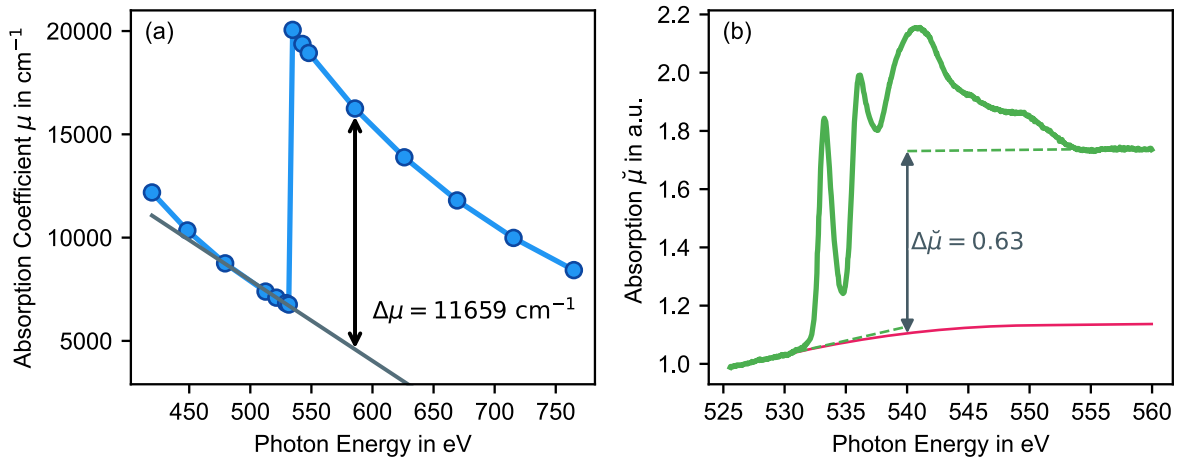

Figure 57 Graphical illustration of the thickness estimation. (a) Linear absorption coefficient for the EC:DMC electrolyte with an overall composition of $C_3H_5O_3$, and a density of 1.30 g cm^{-3} [40], [285]. Values of the linear absorption coefficient sourced from [221], [222]. The absorption edge jump of the absorption coefficient is determined based a linear fit of the pre-ionization edge-region at 585.7 eV, as indicated by the arrow. (b) Illustration of the determination of the absorption edge jump in a transmission XAS spectra of a representative sample.

IV.B.1.c Flux Estimations

To estimate the photon flux and dosages during my *in-situ* transmission sXAS measurements and bubble creation procedures, the intrinsic gain of the GaP photodiode (ifw optronics JEP5-365) at the oxygen and fluorine K-edge was determined. For this I correlated a reference measurement of the diode to the known beam intensities determined during beamline commissioning by the beamline scientists. The photon flux of the U49-2_PGM-1 [194] beamline at BESSY II is shown in Figure 58a,d for the oxygen and fluorine K-edge, respectively. The flux was normalized to the present ring current of 250 mA. My data of the diode and mirror current (drain current induced by the X-ray beam in the refocusing mirror as the last optics element upstream and proportional to the beam intensity) measured with the same beamline settings as the commissioning values but with a ring current of 298 mA are given in Figure 58b,e. By combining the data, I can calculate an intrinsic diode and mirror gain that correlates each current value to a photon flux, while taking the present ring current into account as well (see Figure 58c,f). I use these gain values to estimate the photon fluxes for each individual measurement, while assuming a linear relationship between the respective currents and photon fluxes throughout the whole intensity range.

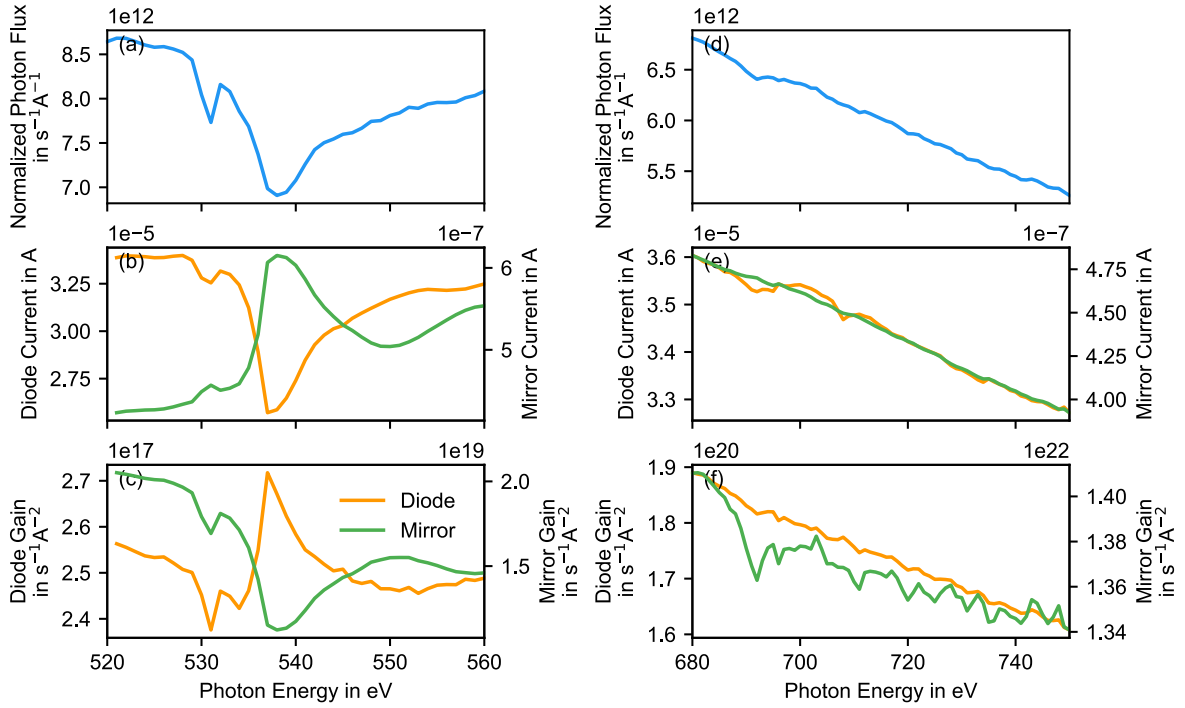

Figure 58: Reference diode and mirror current measurement with a known photon flux intensity to obtain an intrinsic gain for photon flux estimations throughout the experiment. (a) Photon flux of the U49-2_PGM-1 [194] beamline at BESSY II for a specific beamline setting as measured during beamline commission and provided by beamline scientists. Photon flux is normalized by the ring current of 250 mA. (b) Diode and mirror current at the oxygen K-edge (520 eV to 560 eV) with the beamline settings from (a) and a ring current of 298 mA. (c) Corresponding calculated intrinsic diode and mirror gain, again normalized by the ring current. (d-f) Analogous to (a-c) at the fluorine K-edge (680 eV to 750 eV).

IV.B.1.d Dosage and Beam Damage Considerations

To assess dosage and beam damage during transmission XAS measurements, I take the value calculated through the mirror current as the incoming beam flux and the value calculated through the diode current as the transmitted photon flux. Thus, the difference of these two values can be taken as a good estimation of the absorbed dosage. Figure 59a,b shows the incoming, transmitted and absorbed beam flux at the oxygen K-edge for two separate measurements, starting from 520 eV and 525 eV photon energy, respectively, with a scan speed of 0.1 eV s^{-1}. The integrated total photon dose is shown as well. At the oxygen K-edge the dose amounts to 1.5 µJ through $1.75 \cdot 10^{10}$ photons and 1.4 µJ through $1.56 \cdot 10^{10}$ photons for each measurement, respectively, taking the increasing photon energy into account. The same data is shown for one measurement at the fluorine K-edge in Figure 59e. There, I estimated the total photon dose to be around 4.4 µJ through $3.81 \cdot 10^{10}$ photons. These values are supposed to be taken as ballpark numbers, which are specific for the considered sample, based on its absorption spectrum. For different samples thicknesses and absorption, these values change accordingly.

Coffey *et al.* reported G-values (radiolysis events per 100 eV dose) for various different polymer films containing carbonyl functional groups ranging from 0.03 for poly(ethylene terephthalate) to 1.10 for poly(ethylene succinate) [224]. I want to take these values as the best and worst possible case for the stability of polymers against soft X-ray radiation. Further, with these G-values, I want to assess the beam damage up until and within the main region of interest from 530 eV to 534 eV as well as for one complete spectrum (520 to 560 eV) at the oxygen K-edge. Assuming a 1:1 fission event ($A \xrightarrow{\text{Radiolysis}} B + C$), I calculate the possible amount of substance created through beam damage for the first scan #1 in Figure 59a,c as a representative example. To put these numbers into perspective, I estimated the total amount of substance within the probing volume to be $2.7 \cdot 10^{-12}$ mol. In this approximation, I assume for the layer the properties of the electrolyte (EC:DMC, density 1.30 g cm^{-3}, molecular weight 89.07 g mol^{-1}). The volume was calculated for an 86 nm thick layer (estimated through the step height of 0.1 for scan #1 in Figure 59c, as described in chapter IV.B.1.b) and the X-ray beam spot dimensions (85 µm x 25 µm). With this, I can roughly calculate the mole fraction of radiolysis products within the probing volume and judge their spectral contribution. The calculated values are summarized in Table 4. I take the mole fractions of 1.27% and smaller for G-values up to 0.38 after scanning the main region of interest (until 534 eV) as unproblematic for the analysis presented in chapter IV.B.4. However, I pondered that for a G-value of 0.38 after a full measurement, and for very susceptible polymers (G-value of 1.1) already after the region of interest until 534 eV, the mole fraction of radiolysis products may already account for 4.43 % and 3.67 %, respectively. For this reason, I have decided for my

experimental procedure to pick a fresh sample spot for every XAS measurement. As sketched in Figure 60, even after avoiding the area of bubble creation, once again due to possible beam damage, the small beam spot size still allows for plenty of measurement area.

Table 4 Summary of the calculated values for the amount of substance expected through beam damage and the corresponding mole fraction in the probing volume for different assumed G-values.

G-value	Integration Limit in eV	Absorbed Dose in µJ	Amount of substance in mol	Mole fraction in %
poly(ethylene terephthalate) 0.03	530	0.29	$1.8 \cdot 10^{-15}$	0.07
	534	0.43	$2.7 \cdot 10^{-15}$	0.10
	560	1.50	$9.3 \cdot 10^{-15}$	0.35
poly(vinyl methyl ketone) 0.38	530	0.29	$2.3 \cdot 10^{-14}$	0.86
	534	0.43	$3.4 \cdot 10^{-14}$	1.27
	560	1.50	$1.2 \cdot 10^{-13}$	4.43
poly(ethylene succinate) 1.1	530	0.29	$6.6 \cdot 10^{-14}$	2.48
	534	0.43	$9.8 \cdot 10^{-14}$	3.67
	560	1.50	$3.4 \cdot 10^{-13}$	12.81

To back up my estimation experimentally, for some samples, I recorded two consecutive absorption spectra at the same sample position at the oxygen and fluorine K-edge to check if spectral changes reveal beam damage. As shown in Figure 59c,d, for consecutive scans I observe changing (decreasing or increasing) electrolyte contributions at the oxygen K-edge, which I correlate to a certain electrolyte/bubble movement under the X-ray influence (presumably heating). By calculating the difference between the two consecutive scans, the changes can clearly be attributed to the electrolyte contribution alone, as shown by the given electrolyte reference spectrum. Besides this, no new spectral contributions are observable as beam damage. In the same manner, in Figure 59f, two consecutive scans for three different sample positions (with varying convolutions of $LiPF_6$ and LiF, see chapter IV.B.4.b.2) demonstrate remarkable radiation stability at the fluorine K-edge under the low intensity X-ray. Based on this, I am confident that I observe no beam damage at both absorption edges with the low intensity X-ray when fresh sample spots are picked for every measurement.

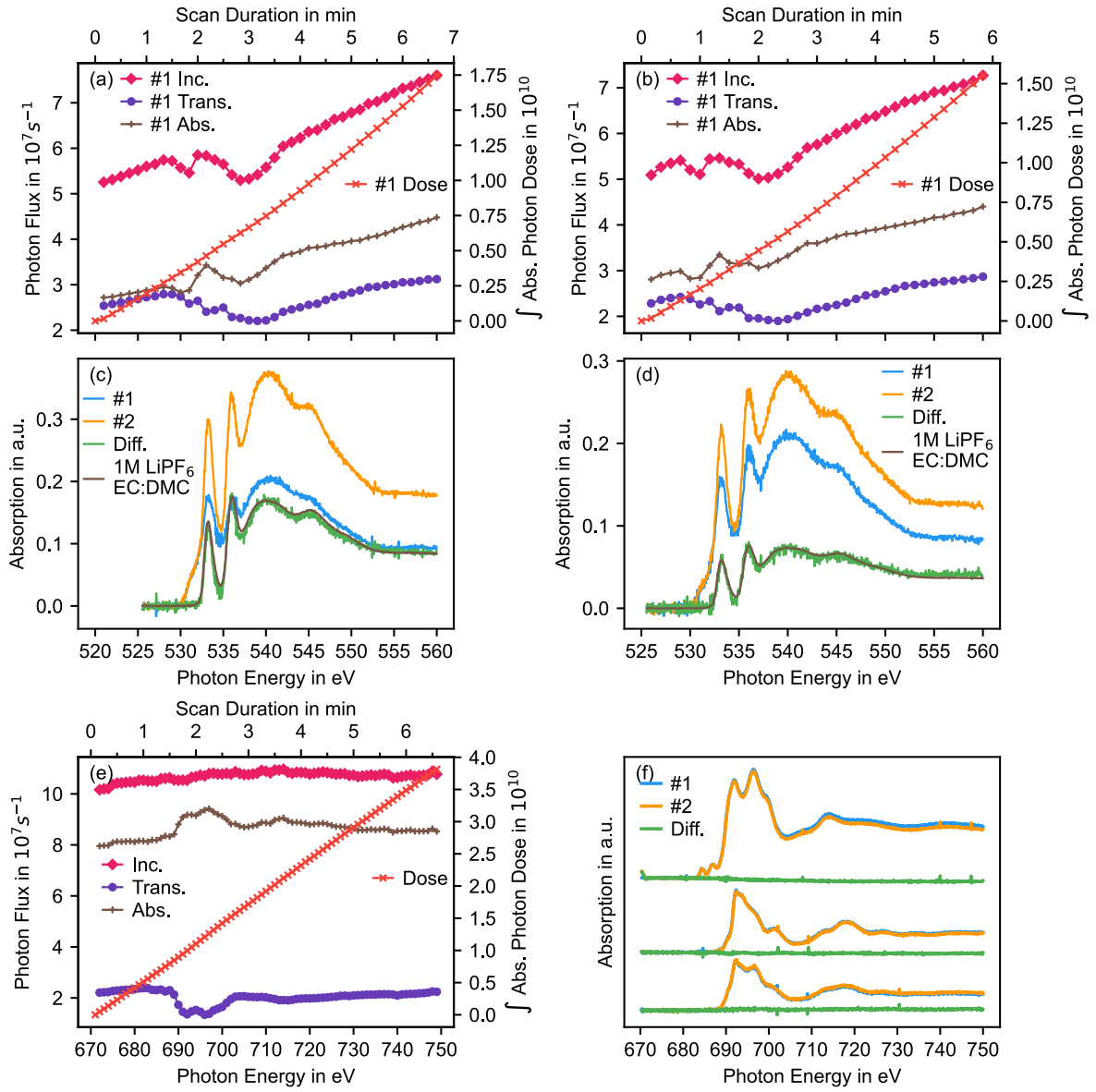

Figure 59 Summary of the beam damage evaluation at the oxygen and fluorine K-edge. ***(a)*** *Incoming, transmitted and absorbed photon flux from a XAS measurement at the oxygen K-edge starting at 520 eV, together with the accumulated total dose. The data correlates to the first iteration #1 from (c).* ***(b)*** *Incoming, transmitted and absorbed photon flux from a XAS measurement at the oxygen K-edge starting at 525 eV, together with the accumulated total dose. The data correlates to the first iteration #1 from (d).* ***(c, d)*** *Two consecutive oxygen K-edge XAS spectra at the same sample position from two different samples. For both samples differences can be correlated to an increased contribution of the electrolyte but no new spectral contribution through beam damage is observable.* ***(e)*** *Incoming, transmitted and absorbed photon flux from a XAS measurement at the fluorine K-edge, together with the accumulated total dose.* ***(f)*** *Two consecutive fluorine K-edge XAS spectra at the same sample position at the different positions which show different convolutions of $LiPF_6$ and LiF. The difference between the first and second iteration reveals no new spectral contribution through beam damage.*

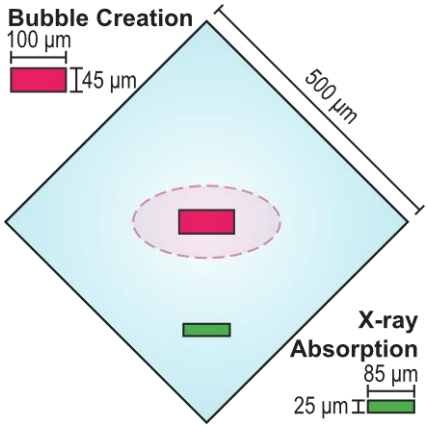

Figure 60 Sketch of the X-ray beam spot sizes used for the bubble creation and XAS measurements in relation to the sample size, namely the SiN_x membrane window. Due to the possibility of beam damage, the position of the bubble creation process is excluded from further XAS measurements, taking a certain safety radius into account.

IV.B.1.e *In-situ* X-ray Absorption Spectroscopy Sample Catalogue and Preparation

For the *in-situ* XAS investigation in this work, I present samples, that differ in their electrochemical treatment or the lack thereof. The different treatments were chosen to understand my measurement approach better and distinguish between the SEI formed by the electrochemistry itself and all possible by-products through the bubble formation/beam damage and ageing processes, together with all possible contaminations. I use the terms sample and cell interchangeably. All cells were prepared conventionally, as described in chapter III.D. The samples discussed in this work are summarized in Table 5, together with the corresponding electrochemical treatment, the cell configuration, the sample size, and the measurement time. The sample size refers to the number of cells from which each label's data was compiled. A statistical assessment of the aged, uncycled and cycled cells regarding the spectral shape in the pre-peak region of the oxygen K-edge, particularly important for the identification of the SEI, is given in Figure 66.

Table 5: Catalogue of in-situ samples/cells with corresponding electrochemical treatment, electrode cell configuration, sample size and the delay between measurement and cell assembly.

Label	El. chem. treatment	Cell configuration	Sample size	Delay
Aged	No	With electrodes	1	4 days under atm. cond.
Uncycled	No	With electrodes	1	No delay
Cycled	10 cycles, 1 ks potentiostatic holding time at 10 mV	With electrodes	3	No delay
1M $LiPF_6$ in DMC	No	No electrodes	1	No delay
1M $LiPF_6$ in EC:DMC	No	No electrodes	4	No delay

The amorphous silicon thin-films with 50 nm thickness were prepared using an RF-driven (13.56 MHz) capacitively coupled plasma enhanced chemical vapor deposition system located at the Energy Materials *In-Situ* Laboratory Berlin (EMIL). The base pressure was lower than $1x10^{-6}$ mbar. The electrode sizes are 6 inches in diameter. The deposition parameters were the following: substrate temperature of 180 °C, deposition pressure of 1.5 mbar, electrode spacing 650 mils, SiH_4 flow rate of 10 sccm, H_2 flow rate of 40 sccm, deposition power of 18 W, RF power density of 26.5 mW cm^{-2}, and a deposition time of 530 s. The actual sample thickness on the SiN_x membranes was determined by reference measurements of the same deposition parameters on flat silicon wafers using a Sentech SE850 DUV variable angle spectroscopic ellipsometer with Tauc-Lorentz model fitting.

IV.B.2 The Gas Bubble: Formation and Species Identification

IV.B.2.a Gas Bubble Formation Procedure

With the help of my simulation in chapter III.C.2, I have presented an ideal case for the formation of the bubble in my novel gas bubble-stabilized liquid thin-layer sXAS approach. The procedure is summarized in Figure 38, where the bubble is nucleated on demand through CO_2 after the electrolyte has been enriched with sufficient gas radiolysis products. Here, the bubble nucleation is triggered by increasing the beam intensity and, through this, by a higher electrolyte temperature and thus reduced CO_2 solubility. This way, the risk of premature bubble formation is reduced, making the process more reliable, while at the same time n_{Total} and $\mathrm{M}_{\mathrm{Trace}}$ as well as overall experimental time is minimized. However, the simulated procedure is an ideal case that requires all parameters, namely the beam position, the concentrations, and the temperature, to be known at any point in time. Unfortunately, the current implementation of my cell has no appropriate sensors, and these variables are not accessible in the actual experiment. Therefore, the ideal case procedure derived from my simulation cannot be fully adapted, yet. Nevertheless, the procedure I settled for in my experimental work still adopts its main ideas: enrich the electrolyte with a lower beam intensity first, and then trigger the bubble formation by increasing the beam intensity. The procedure is described in the following and the corresponding measurement data on which I rely to control the process is summarized in Figure 61 from five representative samples, S1 to S5.

First, to enrich the electrolyte with gaseous radiolysis products, I use a photon flux of $1 \cdot 10^{12}$ s^{-1} at 520 eV, as it does not risk any premature bubble formation according to my simulation. Then, after 50 to 90 s ($0.5 \cdot 10^{14}$ to $1.25 \cdot 10^{14}$ total photon dose), I gradually increase the photon flux by opening the undulator apertures until the bubble is formed. I observe the bubble formation as an almost instantaneous increase in the transmission diode current. Figure 61a shows representative applied beam intensity profiles, where the bubble formation is

highlighted by a circle. Due to limited measurement ranges of the Keithley electrometer and hence the overshooting thereof, the bubble formation dynamics cannot be followed along through the diode current. With the high intensity X-ray, the formation of the bubble correlates to a transmission diode current increase in the range from 10pA to 10 µA in less than a second, which cannot be covered by a single range. Furthermore, as soon as the diode current increases the beam shutter is closed to protect the SEI from the high-intensity X-ray. This monitoring was done manually and there is a chance that the SEI was exposed to the high-intensity X-ray for the length of an average human reaction time. To avoid any beam damage anomalies, the beam position for the bubble formation is recoded and excluded from the sXAS investigation, as illustrated in Figure 60.

Furthermore, it must be noted that the time window of 50 to 90 s was found experimentally through trial-and-error and might be highly individual to the specific system (sample, electrolyte, electrochemical procedure etc.). Besides this, the maximum beam intensity was limited to $7 \cdot 10^{12}$ s^{-1}, as I derived it from my simulation to be the safe limit for the electrolyte's thermal stability.

As shown in Figure 61a-c, there appears to be a high variation between samples in total radiation dosage until bubble formation, ranging from $0.5 \cdot 10^{14}$ photons (S4) up to $2.9 \cdot 10^{14}$ photons (S2 - Uncycled). I attribute these differences to the following three reasons. First, from the OM in Figure 54, I derive that gaseous product, presumably from the electrolyte decomposition during the electrochemical cycling procedure, are present a priori and exceed their solubility limit already. For higher a priori gas concentrations, less bubble gas needs to be created through radiolysis and in turn less radiation dose is required to finally induce the bubble. Unfortunately, due to the limited number of uncycled cells, a statistical evaluation of this claim cannot be given yet and further experiments are necessary. Nevertheless, the uncycled sample S2 in Figure 61a-c with the highest required dosage may be taken as a first hint. However, Veith *et al.* found the electrolyte ($LiPF_6$ in EC:DMC) to react with silicon's surface non-electrochemically driven, which may release gaseous products as well. Thus, even for uncycled samples a variance in the a priori gas concentration can be expected.

Second, in Figure 33, my simulation clearly demonstrates the influence of the beam position on the maximum electrolyte temperature. CO_2's solubility in the electrolyte decreases for higher temperatures (see Figure 36a) and the electrolyte temperature influences the degree of supersaturation and the nucleation behavior. Simply put, if the electrolyte is not heated as much, a higher concentration and thus more radiolysis is required to achieve the same degree of supersaturation. Thus, different beam positions could explain the observed differences in radiation dose until bubble formation. To investigate the influence of the beam position, I have

modelled the beam intensity profiles from Figure 61a in my simulation and calculated the corresponding CO_2's degree of supersaturation ζ_{CO_2}. The degree of supersaturation ζ_{CO_2} as function of the total photon dose of each beam intensity profile is shown in Figure 61c, where the upper limit of the colored area corresponds to the beam position right at the center $x = 0\,\mu m$ and the lower limit to the beam right next to the silicon frame at $x = 315\,\mu m$. The simulation was based on a $C_{\text{Radiolysis}}^{\text{Conversion}}$ of 5.7. The beam position clearly influences the degree of supersaturation, especially for the profiles with higher beam intensities up to $7 \cdot 10^{12}$ s^{-1}. Nevertheless, I argue the supersaturation at bubble formation of each profile do not overlap and a mutual degree of oversaturation is not apparent. Thus, the beam position appears unlikely to be the sole reason for the variance between samples in the radiation dosage until bubble formation.

Third, as implied by (31), heterogeneous nucleation is a statistical process which can take place for any degree of supersaturation $\zeta_i > 1$. Thus, the observed high variance between samples in the required dosage until bubble formation might be just part of this distribution. Unfortunately, with the limited number of samples the distribution itself cannot be revealed. In this case, however, samples like S4 in Figure 61 with $\zeta_{CO_2} < 1$ at bubble formation once again imply a certain a priori gas concentration, as mentioned in the first explanation.

Nevertheless, from my practical experience, aiming the beam right at the center of the probing chamber to create the bubble usually yields the best results regarding bubble stability. Unfortunately, in the course of this work I was not able to target it reliably due to the following reason. In the beginning of the sXAS experiment, to determine the position of the cell and properly aim at the probing chamber with the high intensity X-ray, I first scan with the beam along the cell and record the diode current from the transmitted X-ray. This is done with a photon flux of $1 \cdot 10^{11}$ s^{-1} at 520 eV photon energy. From scans like in Figure 61d,e, the outline and center of the SiN_x window can be inferred. The bright areas in the corners correlate to a higher transmission current since the bulging of the membranes under vacuum is less severe there. On the other hand, in the center of the window, where the membrane deflection and electrolyte thickness are most pronounced no diode signal is obtainable. In Figure 61c, this is shown for a sacrificial sample that was recorded with 20 narrow scan lines for 0.9 mm^2 scan area and a slow scan speed (30 µm s^{-1}) to establish the best possible resolution. For my actual *in-situ* samples, however, I argue such slow scans would already introduce too much beam damage, especially with the required high beam intensity. Hence, for these, I rely on fast scans (126 µm s^{-1}) with only 10 scan lines for 13 mm^2 scan area. Figure 61e shows the same sacrificial sample, but with the faster *in-situ* scan parameters. For easier comparison, the 4 pA diode current outline of the slower scan is superimposed as a white line. Although the window

outlines can still be guessed in the faster *in-situ* scans based on the two distinctive bright spots in the corner, it still leaves room for error in practice. This makes it unreliable to target the center of the probing chamber and leads to a certain variation in beam position between samples.

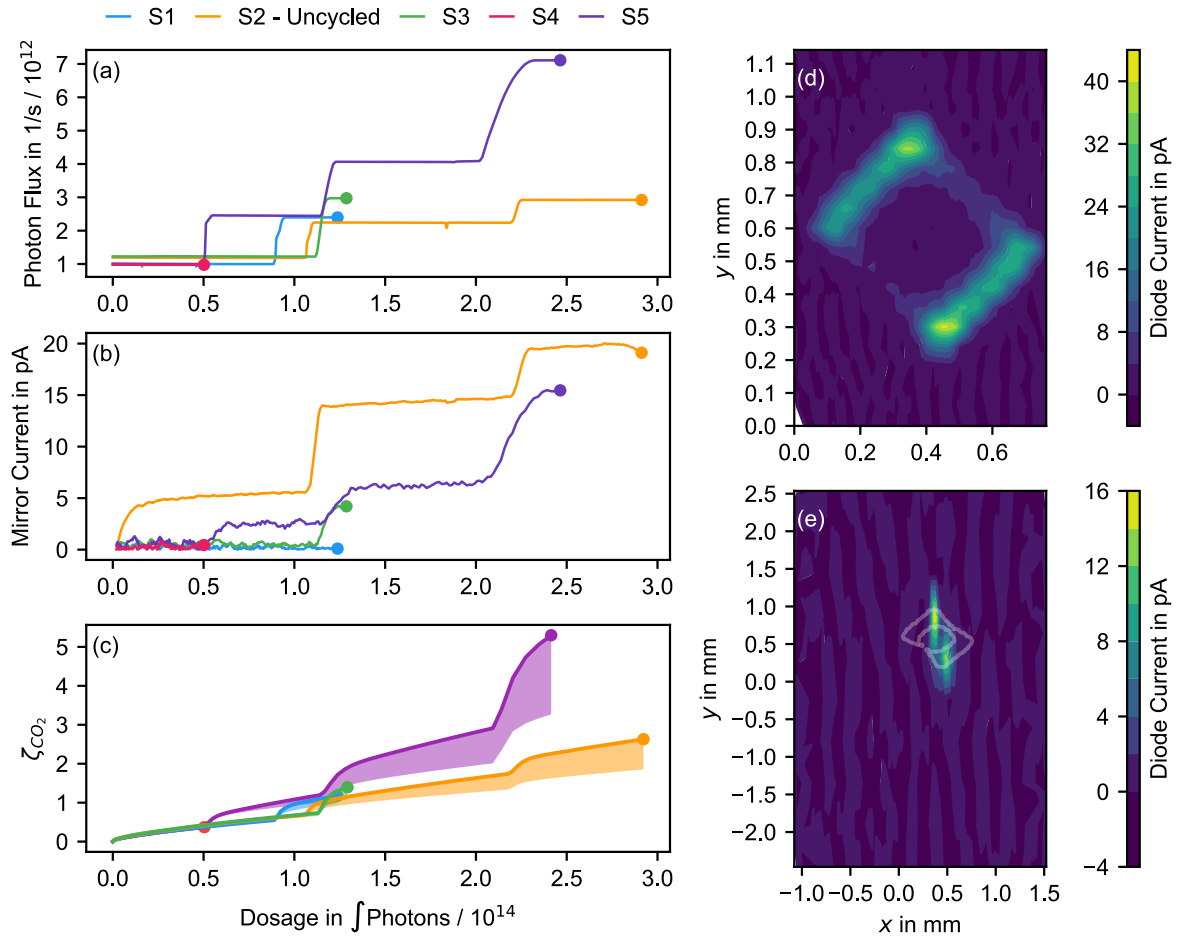

Figure 61 Summary of the experimental data that is used to control and characterize the bubble formation process from 5 representative cells with different beam intensity profiles S1 to S5. The photon flux is increased step wise until the bubble is formed. The circles mark the point in time where the bubble is formed explosively. Dosage was calculated by integration of the photon flux (estimated via mirror current) over time. (a) Beam intensity during the bubble formation as function of the total photon dose. (b) Transmission diode current during the bubble formation as function of the total photon dose. (c) Simulated degree of supersaturation of CO_2 as function of total photon dose for two different beam positions. Upper limit of the colored area corresponds to a centered beam at $x = 0\ \mu m$, the lower limit to an off-center beam close to the silicon frame at $x = 315\ \mu m$. Simulation assumed $C_{Radiolysis}^{Conversion}$ of 5.7. (d, e) Transmission diode current as function of beam position, scanned across the sample to determine proper beam position for bubble creation. (c) Spatial scan with high resolution setting: 20 scan lines for 0.9 mm² scan area and slow scanning speed (30 µm s⁻¹), resulting in high dosage and beam damage. (d) Spatial scan with low resolution setting: 10 scan lines for 13 mm² scan area and fast scanning speed (126 µm s⁻¹), resulting in low dosage and presumably negligible beam damage.

The differences in beam position can also be observed during bubble creation through the transmission intensity. Figure 61b shows the transmission diode currents measured during the bubble formation process of each cell. Except for S2, the transmission diode current is indistinguishable from the dark current for a photon flux of $1 \cdot 10^{12}$ s^{-1}. For samples S3 and S5 a diode current becomes detectible when the beam intensity is increased above $2 \cdot 10^{12}$ s^{-1},

which presumably corresponds to a beam position rather off-center with less membrane bulge and electrolyte thickness. On the other hand, a similar increase in beam intensity does not induce a transmission diode current for S1, arguably putting its beam position closer to the center with high membrane bulge and electrolyte thickness. Further, S2 appears to be the sample where the beam was positioned very close to the window's edges, making the transmission diode signal detectible even for a photon flux of $1 \cdot 10^{12}$ s^{-1}.

Besides this, when it comes to the beam position and the dosage required for bubble formation, the most obvious guess is that more photon flux is absorbed in the center than in the corners. However, the highest transmitted photon flux of S2 translates to a photon flux of only $1.5 \cdot 10^{6}$ s^{-1}. This indicates that the incoming beam flux ($7 \cdot 10^{12}$ s^{-1}) is still absorbed almost entirely, which is in good agreement with the theoretical calculation based on the Lambert-Beer law (34) in Figure 30 for my simulation.

IV.B.2.b Gas Species Identification

After the gas bubble has been created and a thin electrolyte thin-layer has been stabilized, the *in-situ* transmission sXAS investigation can be conducted. As explained in the beginning, this chapter's discussion of the sXAS analysis is structured in the order of the components the X-ray transmits: the gas bubble first, the liquid thin-layer, finally the SEI and at last the silicon anode. The goal here is to unravel the obtained transmission sXAS spectra into their individual components. In the following, I begin with the identification of the gas species inside the bubble.

Figure 62a shows oxygen K-edge spectra of an uncycled cell at different positions and time passed since the bubble creation (1) - (12). The spectra in Figure 62a are normalized to a common SH for easier visual comparison. The actual SH of each spectrum before normalization was extracted as shown in Figure 56d and the value is given alongside each spectrum. Throughout the following discussion I take the height of the ionization step as a measurement for the number of atoms in the beam path [178], [286]. Further, the transmission spectra obtained through my method can be considered a linear combination of each component in the beam's path. As depicted by the illustration in Figure 62b, for an uncycled cell this corresponds to the bubble gases and the electrolyte as well as the radiolysis trace products $\mathrm{M_{Trace}}$ inside it (see discussion in chapter III.C.2 with (32)). Considering the individual densities (gas vs. liquid), I assume that the biggest contribution to the overall SH stems from the electrolyte. Based on this, I correlate the SH to the thickness of the electrolyte liquid thin-layer, where high SH corresponds to a thick and a small SH to a thin layer.

I want to begin with the identification of the individual bubble gas species based on (1) first, and then discuss the bubble's evolution over time from (1) to (8). At the oxygen K-edge, I

identified CO_2 and CO as the main bubble gas species based on their spectral fingerprints from reference measurements. As it can be seen in (1), 3 minutes after the bubble creation and at a position with step height 0.12 where only little electrolyte is present, the spectrum is dominated by the core 1s to π* transition of CO at 534.2 eV [186], [287]. Additionally, CO_2 can be detected through its 1s to $2\pi_u$ transition at 535.5 eV and the 4s Rydberg transition at 539 eV. CO_2 and CO as the main bubble gas species is in good agreement with the expected radiolysis of EC:DMC. The molecular detachment of CO_2 and CO from (bio-) organic molecules under X-ray radiation is a known phenomenon and was termed as decarboxylation and decarbonylation by Zubavichus *et al.* [186], [288]. In particular, Coffey *et al.* found the carbonyl group (present in both EC and DMC) to be heavily susceptible to beam damage under soft X-ray radiation in a variety of different polymers [224]. Further, as demonstrated by Eberhardt *et al.*, the fragmentation of small organic molecules appears to be site specific, depending on the non-/resonant soft X-ray excitation energy [223]. The bubble formation is performed with a photon energy of 520 eV, and thus below any oxygen excitation or ionization energy. This might explain why no O_2 is observed in the gas bubble, as shown by the reference spectrum in Figure 62. However, the exact degradation process of EC:DMC through radiolysis appears to be highly specific and outside the scope of this work.

The next aspect I want to discuss here is the traceability of the gaseous species, or simply put, how easy their spectral contribution can be distinguished in a measured spectrum. Here, the comparison of (4), (9), and (5) yields a particular insight, because they are measured consecutively 16, 20 and 26 minutes after bubble creation, but at different sample positions with different SH of 0.08, 0.74, and 0.07, respectively. The three spectra clearly indicate that the amount of CO present in the timeframe from 16 to 26 min is not apparent/detectable at a position with SH of 0.75, because it is completely overshadowed by the spectral contribution of the electrolyte. This seems to be the case for all spectra with SH greater than 0.27, as (9) to (12) appear identical. Consequently, (9) to (12) resemble the spectrum of the EC:DMC electrolyte to the best possible degree. The spectrum of EC:DMC is discussed in more detail in the next chapter. This observation also has a decisive implication for the characterization of the SEI later. Due to the very small thickness of the SEI, this clearly demonstrates that the SEI layer is only distinguishable at sample positions with SH in the range of 0.10.

Furthermore, looking at spectra (1) to (8) in Figure 62, it is apparent that the system changes within the first hour after bubble creation. Right at the beginning, CO_2's spectral contribution significantly decreases within 4 minutes from (1) to (2). Looking at (1) to (8), the spectral contribution of CO decreases within one hour and the electrolyte spectrum becomes more and more visible. Here, the first explanation that comes to mind is the electrolyte flowing back and liquid thin-layer becoming thicker. However, the SH of all spectra (1) to (8) remains at or below

0.12, not indicating any change in liquid layer thickness. This becomes apparent when comparing (3) to (6). Both have the same SH of 10, but (6) exhibits a strongly reduced contribution of CO over (3). This behavior appears peculiar, and I am hesitant to give a definitive reason why the gas contribution disappears over time. However, I argue that the system has not reached its equilibrium state right after the bubble creation, where the temperature is still elevated and, looking back at Figure 41 to Figure 44, the concentration around the bubble has not reached its equilibrium value, yet. My simulation shows in Figure 36, the concentration reaches its equilibrium value only 30 minutes after the beam was turned off. Thus, I propose that the increased temperature and concentration right after bubble formation entail an increased partial pressure which slowly decreases as the system reaches its equilibrium over the course of an hour. The initially increased partial pressure in turn increases the bulging of the membranes according to (11) and (12). Consequently, the bubble volume decreases over time as the membranes deflate and move closer together while the liquid thin-layer thickness remains constant. This would explain why the gas contribution at the oxygen K-edge declines while the SH and electrolyte contribution remain constant. In this regard, the rapid vanishing of the CO_2 contribution can be linked to the strong temperature dependence of CO_2's solubility inside the electrolyte. As the electrolyte cools off, CO_2 quickly redissolves.

On top of that, although the exact radiolysis mechanism of EC:DMC lies outside the scope of this work, I still want to derive a rough estimate of the molar ratio between CO_2 and CO for my radiolysis simulation presented earlier. For this, I assume that the degassing kinetics for both species are equal. Then, the ratio between CO_2 and CO within the gas bubble right after its formation resembles their ratio within the electrolyte in first approximation. Here, spectrum (1) only 3 minutes after the bubble formation qualifies for further analysis. Like mentioned before, I take the height of the ionization step as a measurement for the number of atoms in the beam path. However, the liquid electrolyte overshadows the ionization edges of the gas species and their height is not directly accessible. Thus, to extract the SH of CO and CO_2, I perform a linear combination fit of their reference fingerprints together with the electrolyte EC:DMC to spectrum (1). The linear combination fit to (1) and the individual contributions from CO, CO_2 and the electrolyte are shown in Figure 62b. The induvial contributions of CO_2 and CO in the linear combination fit are about the same at their ionization potential (CO at 542.4 eV [186] and CO_2 at [289]). Consequently, distributing an equal number of oxygen atoms according to their individual stoichiometries yields a molar ratio between CO and CO_2 of 2:1, as I already assumed for my radiolysis simulation in (32).

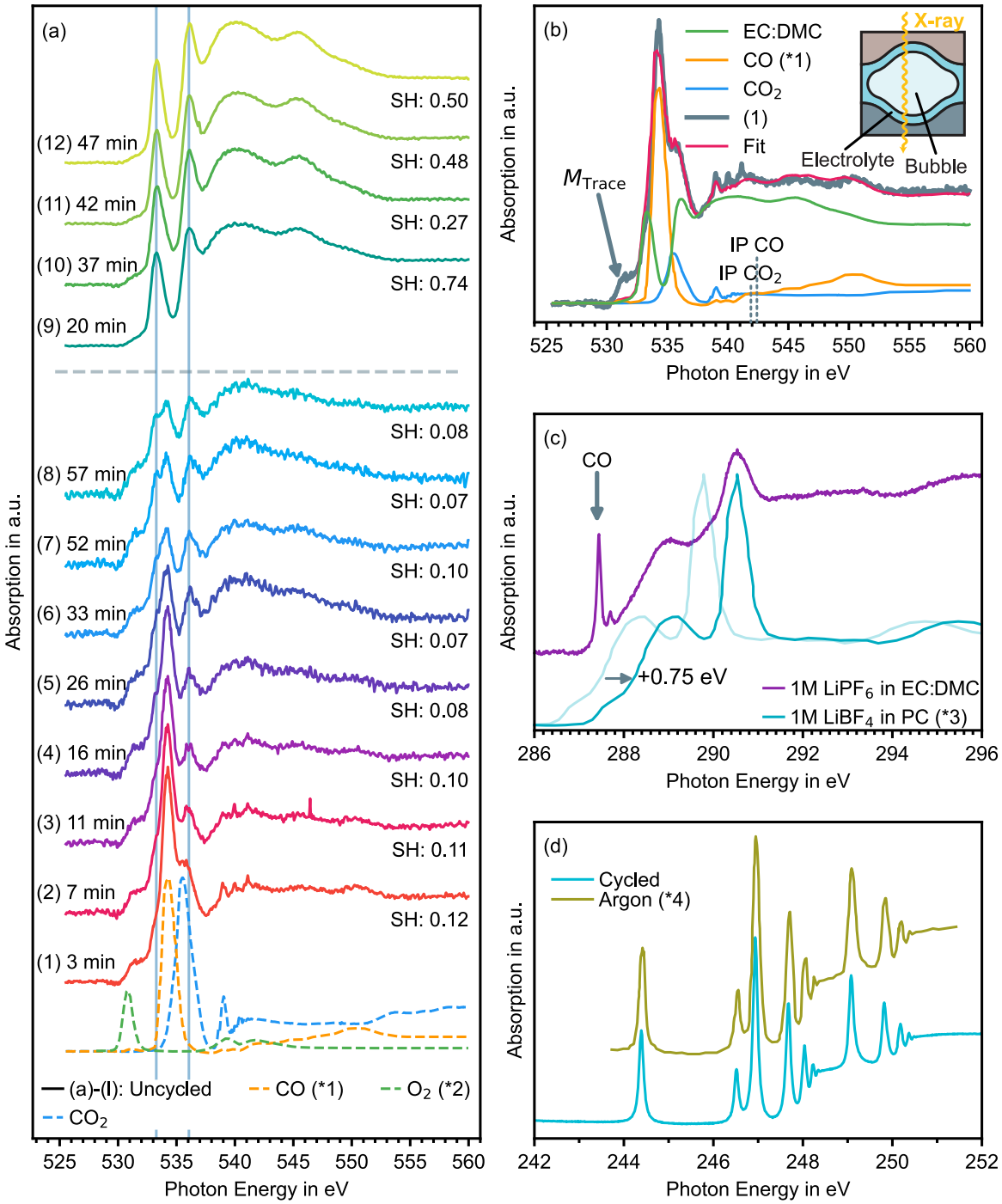

*Figure 62 Identification of the bubble gas species at the argon L-edge, oxygen K-edge and carbon K-edge. (a) Oxygen K-edge spectra from an uncycled cell at different sample positions with different SH and different amount of time passed after the bubble creation. Spectra are vertically stacked by an arbitrary amount to facilitate visual comparison. Spectra are grouped by their SH, above and below 0.12 and sorted by their amount of time passed since the bubble creation. CO_2, CO and O_2 reference spectra are shown, too. *1 from [186], [287], *2 from* [186], [290]. *(b) Linear combination fitting of CO_2, CO, and the electrolyte reference spectrum to (1) from (a). Ionization potentials for CO_2 and CO marked at 542.4 eV and 541.9 eV, respectively, according to [186], [289]. (c) Carbon K-edge spectra from 1M $LiPF_6$ in EC:DMC alongside a reference spectrum of 1M $LiBF_4$ in propylene carbonate from* [291]*, marked as (*3). The reference spectrum from* [291] *is shifted by 0.75 eV to ease comparison of the spectral shape to 1M $LiPF_6$ in EC:DMC. Original data is shown in a lighter color. (d) Comparison of the argon L-edge transmission sXAS spectrum from a cycled cell to an argon reference measurement from literature. *4 from* [292].

Besides this, I did not observe further gas species at the investigated silicon, carbon, and fluorine absorption edges. Although gaseous hydrocarbons are obvious candidates, obtaining reliable XAS data at the carbon K-edge was rather challenging due to carbon contaminations on the beamline optics upstream. However, as shown in Figure 62c, I could still verify the presence of CO through its core 1s to π* transition at 287.4 eV [287], [293], [294]. Adjacent to it, another sharp gas peak at 287.7 eV is visible. Based on the limited data and after thorough literature research, I propose that this peak may suggests the presence of gaseous iso- or neopentane [293], [295]. In their study, Coffey *et al.* observed both scission and crosslinking processes in the polymers under radiation. Thus, a possible crosslinking behavior could explain the proposed presence of gaseous hydrocarbon molecules like iso- or neopentane [224].

On top of that, I want to mention that I also identified argon through its very distinctive spectral fingerprint in the 2p excitation region (242 to 252 eV, argon L-edge) as a bubble gas species. The argon L-edge spectrum from a cycled cell is shown in Figure 62d. The transmission from the $2p_{3/2}$ and $2p_{1/2}$ core levels to the 4s valence band level together with the Rydberg series $2p_{x/2}$ to *n*d with *n* up to 7 are clearly visible and can be matched to an argon reference spectrum from literature [292]. The argon presumably stems from the glove box atmosphere, where the cell was assembled. It is priorly dissolved in the electrolyte and gets released due to the superheating and radiolysis of the electrolyte under the high intensity X-ray during the controlled bubble growth. Unfortunately, due to synchrotron time constraints, the data at the argon L-edge is limited and an estimation for the bubble's argon content cannot be given.

IV.B.3 The Liquid Thin-layer: Characterization of the Organic Model Battery Electrolyte System (ethylene carbonate, dimethyl carbonate, 1M $LiPF_6$) at the Oxygen K-edge

After the bubble is created, the electrolyte remains a thin-layer on top of the SEI. To be able to properly distinguish the SEI from the electrolyte, I will first present the transmission sXAS study of the neat electrolyte 1M $LiPF_6$ in EC:DMC. Here, I will also address the "Thickness Effect" as a significant intrinsic challenge for my novel gas bubble-stabilized transmission sXAS approach, which ultimately necessitates cautious interpretation of the obtain transmission absorption spectra. Further, I will demonstrate my novel approach's capability for the transmission XAS in the soft X-ray regime by comparing it to a liquid microjet measurement from literature of a comparable electrolyte, namely 1M $LiBF_4$ in PC.

The oxygen K-edge absorption spectra of 1M $LiPF_6$ in DMC and EC:DMC are summarized in Figure 63. The spectra in Figure 63 are normalized to a common SH for easier visual

comparison. The actual SH of each spectrum before normalization was extracted as shown in Figure 56d and the corresponding value is given in the legend of Figure 63a. For Figure 63b spectra with a similar SH are selected to allow for a better comparison of the spectral features. I will first describe the spectral features of EC:DMC at the oxygen K-edge and then discuss the SH as well as the "Thickness Effect" and its relevance for my novel approach. Further, the "1M $LiPF_6$" specification is omitted in the following discussion.

The EC:DMC absorption spectrum exhibits two sharp features at 533.27 eV and 536.06 eV photon energy and three broader peaks beyond the ionization edge at around 540 eV, 545.5 eV and 550 eV. To my knowledge, no XAS data on the EC:DMC system is available in the literature yet. However, the absorption spectra can be explained in analogy to the liquid microjet characterization by Smith *et al.* on a similar system, 1M $LiBF_4$ in PC, where the individual absorption peaks were correlated to energetic isosurfaces in a density functional theory simulation [291]. The oxygen K-edge absorption spectrum of 1M $LiBF_4$ in PC and neat PC from this study is shown in Figure 63a,b for comparison. Based on the work of Smith *et al.*, the sharp peak in the pre-edge region at 533.27 eV correlates with the core 1s to π* transition from the carbonyl oxygen atom. In the same way, the 1s to π* transition from the oxygen atom in the ring structure of EC and the chain structure of DMC is attributed to the sharp peak at 536.06 eV. In the post-ionization edge region, the broad features σ_1^*, σ_2^* and σ_3^* correlate to the core-1s-to-σ*-transitions. According to Smith *et al.*, in case of PC, the spectral intensity of these features cannot be allocated to a specific oxygen site. However, comparing the peak intensities of DMC to EC:DMC, it is apparent that the σ_2^* peak stems from the oxygen in the EC ring structure.

For the neat components the carbonyl 1s to π* transition is at 533.12 eV and 533.21 eV for DMC and EC, respectively. Upon adding salt, Smith *et al.* reported a shift of 0.07 eV of the carbonyl π* peak from neat PC to 1M $LiBF_4$. A similar shift of 0.1 eV for 1M $LiPF_6$ in EC:DMC was reported in an complementary X-ray Raman spectroscopy experiment [296]. Both reports attribute the shift to the Li^+-carbonyl interactions in solution. In this work, I observe a shift of 0.15 eV to higher photon energy from neat DMC at 533.12 eV to 533.27 eV for 1M $LiPF_6$ in DMC. For the carbonyl π* peak with 1M $LiPF_6$, there appears to be no difference between only DMC and the binary EC:DMC mixture. I attribute this to a rather strong Li^+-carbonyl interaction that overshadows any differences between the carbonyl group itself, that I otherwise observed in the neat sole components.

Furthermore, the ring/chain π* transitions of the neat individual components are at 536.12 eV and 536.21 eV for EC and DMC, respectively. Upon adding 1M $LiPF_6$ I observe a different behavior. For DMC, with the addition of 1M $LiPF_6$ the transition shifts to a 0.06 eV lower photon

energy of 536.15 eV. In contrast to the carbonyl π* transition, I observe a difference for the ring/chain π* transition between 1M $LiPF_6$ in only DMC and the binary EC:DMC solution. This suggests that the Li^+-chain/ring interaction is much weaker and intermolecular interactions between the two solvent components play an increasing role for the chain/ring π* orbitals. I assume these intermolecular interactions are also reflected in the overall shape of the chain/ring π* peak. It appears that the chain π* peak of the DMC is more asymmetrical with a pronounced shoulder to higher energies compared to the ring π* peak of the EC. This can be seen both for the neat DMC and the 1M $LiPF_6$ in DMC electrolyte. When adding EC the shoulder disappears in the 1M $LiPF_6$ in EC:DMC spectrum. This may suggest the chain π* orbitals become more confined through the intermolecular interaction with the EC.

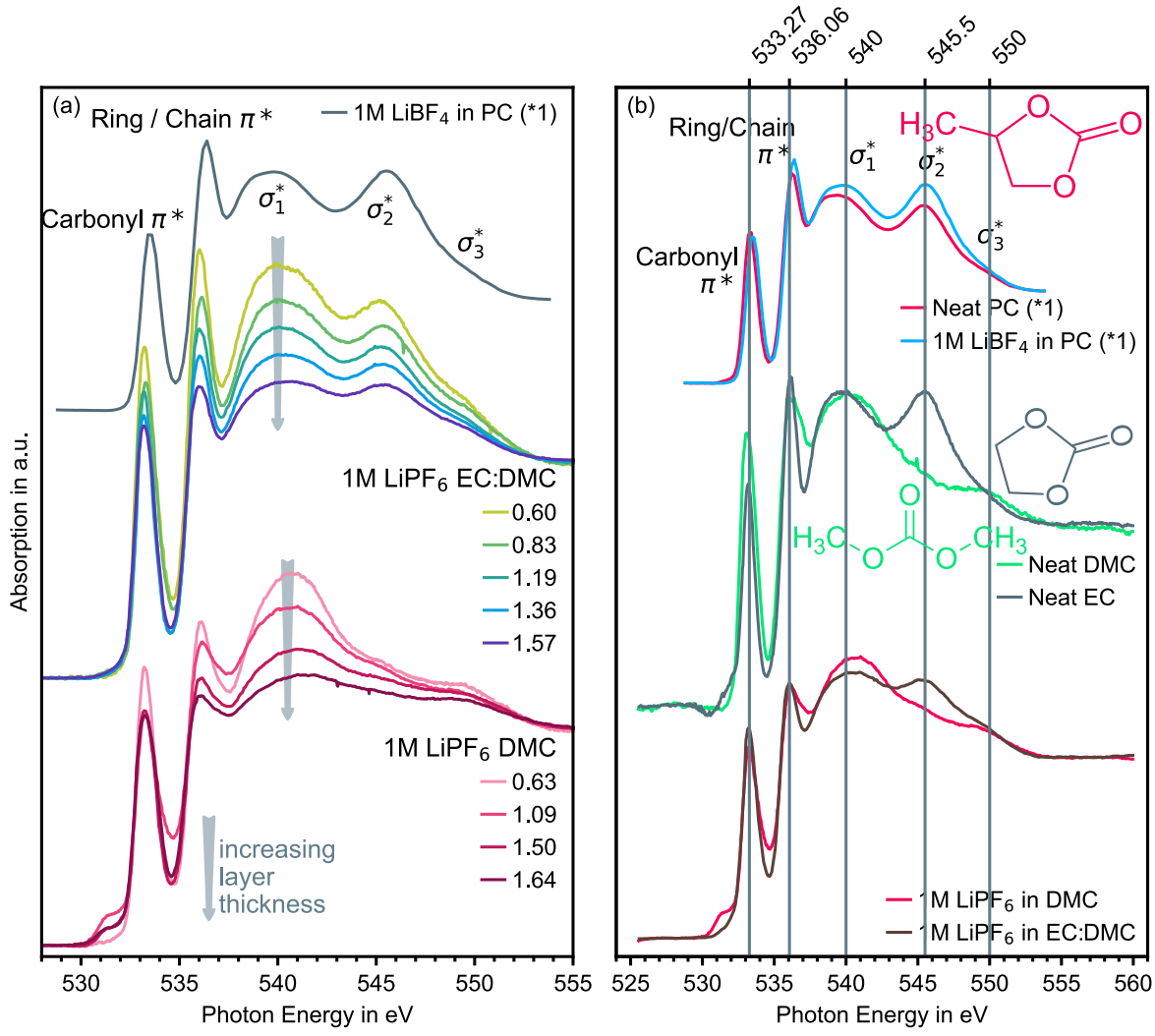

*Figure 63 Transmission sXAS spectra at the oxygen K-edge. (a) 1M $LiPF_6$ in DMC and EC:DMC together with 1M $LiBF_4$ in PC for comparison - Demonstration of the "Thickness Effect": 1M $LiPF_6$ in DMC and EC:DMC at different sample positions that exhibit a different Step Height (SH) prior to the normalization to a common SH. (b) Transmission sXAS spectra at the oxygen K-edge from 1M $LiPF_6$ in DMC and EC:DMC, neat EC, neat PC and 1M $LiBF_4$ in PC. *1 from* [291].

According to Smith *et al.*, in case of PC the spectral intensity of the σ^* features cannot be allocated to specific oxygen atom species. However, comparing the spectral shape of DMC vs. EC:DMC after the ionization step, it is apparent that the σ_2^* peak stems from the oxygen in the EC ring structure. To be even more precise, looking at the absorption spectra of the neat compounds, the σ_2^* spectral intensity clearly stems from the ring structure itself, and not from intermolecular interactions in the binary system. Additionally, comparing the neat components, the spectral intensity of σ_3^* can be allocated mainly to the DMC chain structure.

In summary, the discussed oxygen K-edge spectra of the neat EC:DMC electrolyte shows the capability of my novel gas bubble-stabilized liquid thin-layer approach. From a spectroscopy perspective, it clearly demonstrates that obtaining comparable results to a liquid microjet measurement is possible. Being based on SiN_x membrane windows, however, this approach offers the advantage to conduct *in-situ* transmission sXAS investigations on thin-film materials.

At last, to distinguish the SEI from the covering electrolyte layer later, I need to know how the electrolyte spectrum evolves with its thickness. Hence, I need to quantify the "Thickness Effect", which was discussed in detail in chapter II.B. In Figure 63a, a "washing out" of the ring/chain π* and the σ_1^* peak of DMC and EC:DMC is observable. A relative intensity decrease with increasing layer thickness is apparent as well. As the electrolyte-layer thickness is not accessible experimentally, I once again use the SH (before normalization) as measurement of how many atoms are in the beam's path [178], [286]. In Figure 64, I give a rough estimated thickness, based on an overall linear attenuation coefficient for EC:DMC with an overall composition of $C_3H_5O_3$ and a density of 1.30 g cm^{-3} [40], [285]. The estimation of the thickness is described in more detail in chapter IV.B.1.b and Figure 57. As proposed by Parratt *et al.*, I use the ratio between the intensity of the highest peak (PI) to the step height (SH) to quantify the degree of "washing out". The determination of the SH and PI are illustrated in Figure 56d. According to Parratt *et al.*, this ratio converges for thinner samples towards a value that resembles the true absorption for an infinite thin sample. For smaller SH the PI/SH ratio of DMC and EC:DMC appears to converge to a value of around 1.75 in Figure 64. The line given is a fit of (35) to the datapoints of EC:DMC, where $\mathcal{H}$ is the PI/SH ratio, ς is the SH, and A, B, C, and D are fit-parameters without physical meaning.

$$\mathcal{H} = A \exp\left(\frac{\varsigma - B}{C}\right) + D \qquad (35)$$

As we have noticed in the previous chapter when discussing the traceability of the gaseous bubble species in Figure 62, I expect the SEI layer to be only detectable beneath a very thin layer of electrolyte. Thus, for the SEI investigation, I intentionally picked areas where the SEI appears to be covered only by a thin layer of electrolyte based on the overall transmission signal for my *in-situ* samples. With the SEI itself expected to be only a few nanometers thick,

these measurements conclusively have an SH below 0.25, as shown in Figure 64. At the same time, these samples exhibit PI/SH ratios overall ranging from 2 to 3. However, we would not expect such high values from the electrolyte itself, even when taking the “Thickness Effect” into account and extrapolating it to an infinitely thin layer. Consequently, from Figure 64 one can already deduce the presence of SEI species by comparing the cycled cells to the uncycled ones and the electrolyte. In the next chapter I will compare the individual XAS spectra at the oxygen K-edge of cycled cells and isolate the SEI spectrum by adept subtraction.

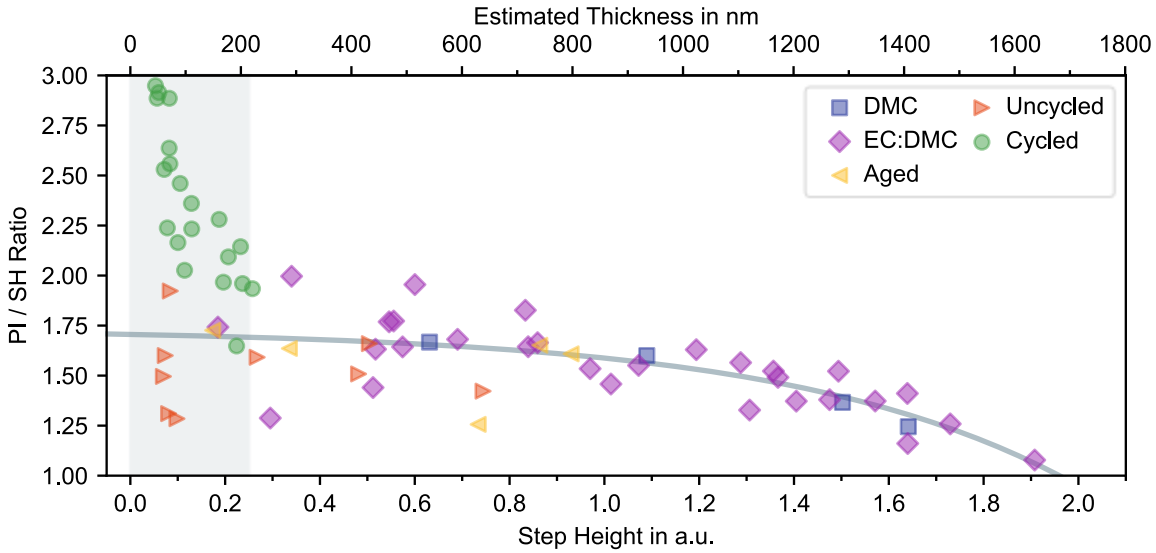

Figure 64 Quantification of the “Thickness Effect”: Correlation between the PI/SH ratio and the SH for 1M $LiPF_6$ in DMC and EC:DMC and aged, uncycled and cycled samples. A total thickness is estimated through the SH and given as secondary axis. The line is a fit of the data from DMC and EC:DMC to (34) and shown as a visual aid without physical reasoning of the fitting parameters.

IV.B.4 The Solid Electrolyte Interphase on the Silicon Thin-film Anodes

IV.B.4.a Extraction of the Solid Electrolyte Interphase Spectrum

To isolate the SEI spectrum, I take the absorption values as measured without any normalization. This way, I can treat the obtained spectra as a linear combination of all individual chemical species within the beam path. Then, an adept comparison of the spectra allows me to distinguish the individual contributions. Figure 65a shows absorption spectra at the oxygen K-edge from a cycled sample at six different positions (P1 to P6) that exhibit different step heights. Between P1 and P6 the overall spectral shape varies drastically, except for a small shoulder at 531 eV. This shoulder indicates the presence of a uniform SEI layer that is present throughout the cycled samples and absent on the uncycled one. Simultaneously, I attribute the change in the SH to the varying amounts of the electrolyte on top of the SEI. It must be noted that the uniformity refers to the SEI layer being present with comparable thickness at every sample position. The SEI layer in itself might be inhomogeneous as I will discuss later in more detail.

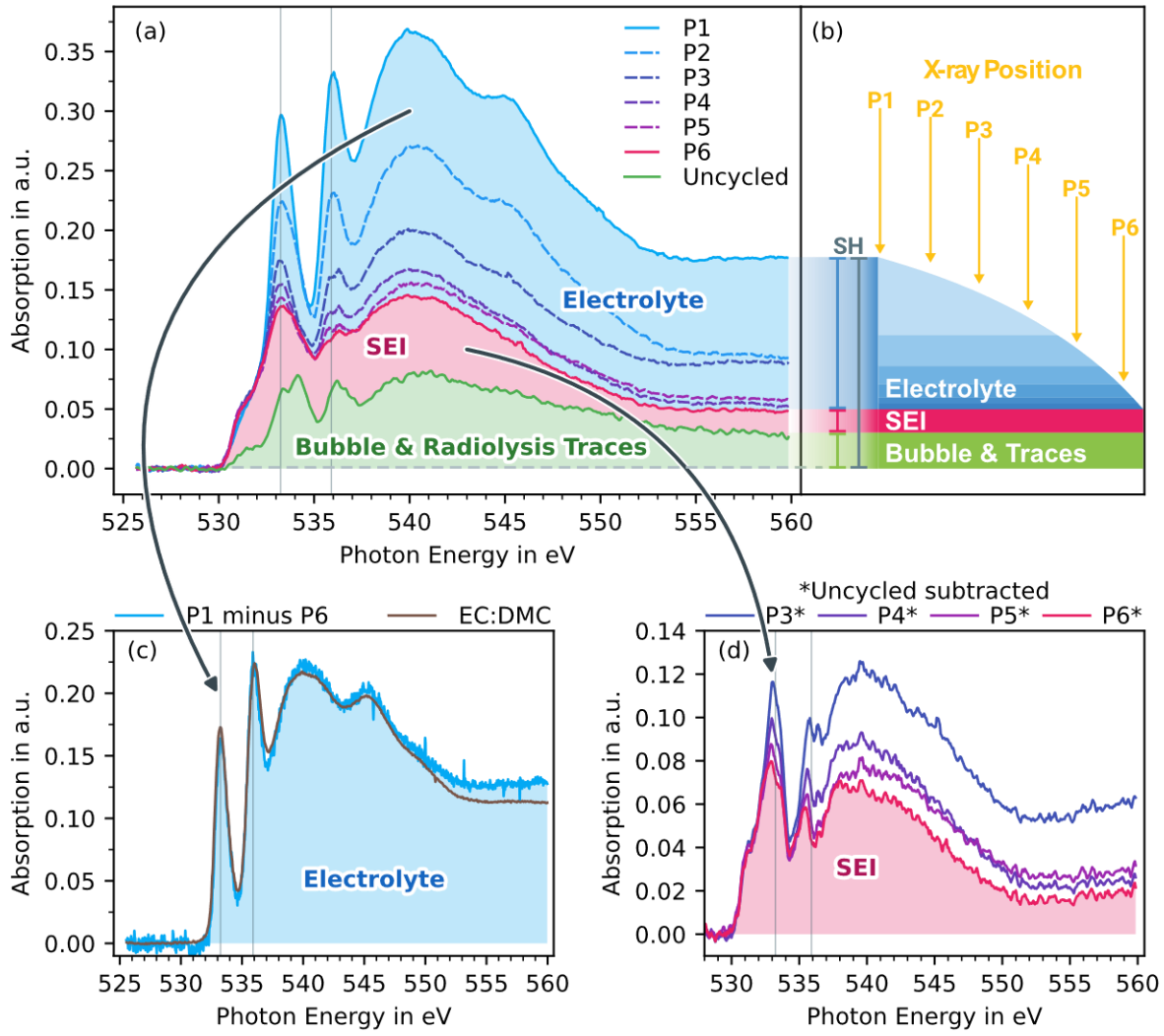

Figure 65 Extraction of the SEI spectrum from the overshadowing electrolyte spectrum and subtraction of the bubble and radiolysis traces. (a) Oxygen K-edge transmission sXAS spectra of cycled cells at six different sample positions P1 to P6 alongside one spectrum of an uncycled cell. The blue background represents the contribution of the overlying electrolyte, red for the SEI, and green represents the bubble and radiolysis traces. (b) Illustration of the individual spectral contributions from (a) in a layer scheme: the bubble and radiolysis traces form the background of the spectrum, the SEI has a constant contribution throughout the whole sample (P1 to P6) as indicated by the constant shoulder at 531 eV and depending on the sample position the electrolyte has varying thickness where the spectral contribution decreasing accordingly from P1 to P6. (c) Isolation of the electrolyte spectrum that sits on top of the SEI by subtracting P6 from P1. For comparison a spectrum of 1M $LiPF_6$ in EC:DMC with a SH of 0.60 is scaled to 19% and shown alongside the isolated electrolyte spectrum. (d) Isolation of the SEI spectrum by subtracting the uncycled spectrum from P3 to P6.

Consequently, for P1 with the highest SH, the thick electrolyte layer overshadows the SEI entirely, and the overall spectral shape appears to match the electrolyte. In contrast, at positions P2 to P6 with a more minor SH, less electrolyte is present, and the spectral shape of the SEI is revealed more and more. This interpretation is illustrated in Figure 65b, where the different positions P1 to P6 refer to locations with different electrolyte layer thicknesses. This idea can be confirmed by subtracting P6 from P1. The corresponding difference spectrum is shown in Figure 65c and matches an electrolyte spectrum of 1M $LiPF_6$ in EC:DMC. The measured electrolyte reference spectrum has an SH of 0.6 and was multiplied by a factor of

0.19. The extracted electrolyte spectrum P1 minus P6 has an SH of roughly 0.13, which correlates to an estimated electrolyte thickness of about 112 nm (see Figure 65c). The matching spectra with SH 0.6 and 0.13 back up my assumption that the “Thickness Effect” becomes negligible for smaller SH and that the electrolyte spectrum with SH 0.6 already resembles the true spectral shape at a reasonable degree.

So far, I only distinguished the electrolyte contributions in my spectral data, but one can refine the fingerprints of the SEI even further. As discussed before, the gas bubble contains gaseous oxygen species and after the creation of the bubble non-gaseous radiolysis products remain dissolved as trace products $\mathrm{M_{Trace}}$ within the electrolyte thin-layer. As illustrated in Figure 65b (“Bubble & Traces”), I take both contributions (gas species and residual radiolysis traces) as an underlying background and obtain this data experimentally from an uncycled sample. Consequently, differences between the uncycled and cycled spectra can directly be correlated to the electrochemically formed SEI. The corresponding difference spectra are shown in Figure 65d. From my experimental data it is straightforward that P6 is the spectrum with the smallest electrolyte contribution and hence with the most dominant SEI signal. In the following I refer to the corresponding difference spectrum P6* from Figure 65d as the SEI spectrum and analyze it in more detail in the next chapter.

Nevertheless, before discussing the SEI spectrum in more detail in the next chapter, I still want to double down on the process of unraveling each obtained transmission sXAS spectrum. As illustrated in Figure 65b, every transmission spectrum is a linear combination of the following contributions I^i: the electrolyte (including all trace hydrolysis products $\mathrm{M_{Trace}}$), the bubble gas species, and finally the SEI itself. The individual combination in each spectrum is intrinsically unknown. Thus, for the subtraction approach, when the individual contributions I^i in each spectrum, I_1^i and I_2^i, are intrinsically unknown, so is the difference $\Delta I^i_{\mathrm{isolation}} = \left|I_2^i - I_1^i\right|$. Consequently, when interpreting an SEI spectrum which was isolated through subtraction, every $\Delta I^i_{\mathrm{isolation}}$ still must be considered, as I consider a coincidental $\Delta I^i_{\mathrm{isolation}} = 0$ to be highly unlikely. But, as I argue in the following, when dealt with properly, this is not an intrinsic drawback of my approach. With distinct spectra for each contribution I^i, the linear combination thereof is mathematically unambiguous. Subtracting spectra from each other does not disrupt the unambiguousness nor does it introduce any errors. I want to point out that spectrum P1 in Figure 65a contains all contributions I^i. Albeit particularly challenging, one could unravel P1 into its distinctive contributions, even when the electrolyte spectrum heavily overshadows all SEI contributions. Thus, the main purpose of the subtraction is to peel off most distracting contributions to finally arrive at a spectrum, which predominantly reveals SEI species and allows the easy distinction of individual species. To me, with the current data available, using

the uncycled spectrum is the best way to do so. Having said that, I expect the extracted SEI spectrum to still contain the electrolyte and bubble signal to a minor degree, which must be accounted for in the following discussion of the next chapter.

Besides this, I want to mention at this point that I consider any beam damage of the SEI itself during bubble creation by the high intensity X-ray highly unlikely. The silicon anode and the SEI are located on the back facing SiN_x window and both are shielded by the full thickness of the electrolyte (72 µm). Figure 30 demonstrates the efficiency of this shielding by showing how quickly the photon density decays entirely within 10 µm of the electrolyte. As a further precaution, as illustrated in Figure 60, I exclude the beam position of the bubble creation from any further XAS measurements, to rule out any beam damage artifacts. As for potential beam damage of the SEI during XAS itself, based on the extremely low beam intensity, I estimated the expected mole fractions of potential radiolysis products to be uncritical, especially if a fresh sample spot is picked for every measurement. This was backed up experimentally by consecutive measurements (at the oxygen and fluorine K-edge) at the same sample spot, which did not reveal any apparent beam damage. A detailed assessment of the SEI's beam damage during XAS was discussed in chapter IV.B.1.d with Figure 59 and Table 4.

Furthermore, I also want to emphasize that the shoulder at 531 eV cannot be correlated to the radiolysis trace components $\mathrm{M_{Trace}}$. In that case, one would expect a correlation between the shoulder height and the SH, as it resembles the thickness of the electrolyte and with a thicker electrolyte layer more $\mathrm{M_{Trace}}$ remain in the beam path. However, this is not the case, as the shoulder at 531 eV does not change with the SH, as clearly visible in Figure 65. Thus, I assume $\mathrm{M_{Trace}}$ is sufficiently accounted for by the subtraction of the uncycled sample, as described before.

Finally, Figure 66 shows the pre-shoulder region of the electrolyte carbonyl π* peak at 531 eV in more detail. For a more statistical approach, it summarizes my data for the aged, uncycled and cycled cells by giving the minimum, maximum (boundaries of the filled area) and mean values (solid line) of all considered spectra. Except for the aged cell where I could not obtain a measurement with a step height smaller than 0.33, only measurements with a step height smaller than 0.3 were considered. The number of considered spectra for each sample is given in the legend in Figure 66. When looking at the step heights of the uncycled and cycled cells, I could not identify a correlation between the intensity of the shoulder and the step height. Nevertheless, the spectral shape and the intensity varies slightly between points of measurement and sample as shown in Figure 66. This indicates either an inhomogeneous nature of the electrolyte or that the bubble creation process may disturb the supposedly fragile SEI to a varying degree between samples. However, all cycled cells spectra show a

pronounced shoulder compared to the aged and uncycled one, again indicating that the shoulder correlates to an electrochemically produced SEI layer.

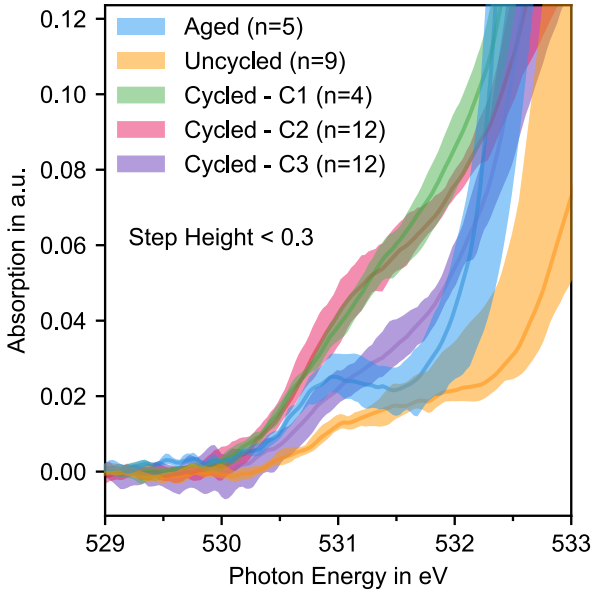

Figure 66 Agglomerated transmission sXAS spectra of n measurements from the aged, uncycled and 3 cycled cells in the SEI pre shoulder energy region from 529 eV to 533 eV. Boundaries of the filled area are the minimum and maximum value; the solid line is the mean value. Except for the aged cell, only spectra with a step height below 0.3 were considered.

The smallest step height I recorded for the aged cell was 0.33, which makes the comparison to other samples difficult. However, in Figure 66, the onset of the large electrolyte carbonyl π* peak of the aged cell can be taken as a reference of how good the shoulder at 531 eV can still be distinguished even for thicker electrolyte layers. Furthermore, the spectrum of the aged cell shows a minor peak at around 530.8 eV, that increases with bigger step heights. I take this peak as oxygen gas that is dissolved in the electrolyte and hence becomes more pronounced with a thicker electrolyte layer. Because this peak is not present in the uncycled cell, I assume the dissolved oxygen stems from either an ageing reaction that takes place without electrochemical procedures or leaks from the surrounding environment into the cell over the 4-day ageing period. Since I did not notice any signs of leakage inside the vacuum chamber during the XAS measurements, I assume the former. However, I sometimes witnessed similar pre-peaks for few samples and therefore cannot rule out any oxygen contaminations completely based on the limited data and the oxygen K-edge alone. But, as we will see at the fluorine K-edge, the aged cell also exhibits a presumably hydrogen fluoride peak, which clearly indicates ageing reactions as well.

IV.B.4.b Identification of the Solid Electrolyte Interphase Species through Reference Compounds

IV.B.4.b.1 Solid Electrolyte Interphase Species at the Oxygen K-edge: Qualitative Analysis and Linear Combination Fitting of Reference Fingerprints

In the previous chapter I have unraveled the obtained transmission sXAS spectra of cycled samples and isolated an SEI spectrum through adept comparisons at the oxygen K-edge. In the following two chapters I want to continue the analysis and identify the individual, oxygen-containing chemical SEI species that make up the SEI spectrum. Once again, I treat the SEI spectrum as a linear combination of all its chemical species. First, I pursue a qualitative approach and identify possible SEI species by comparing the SEI spectrum with fingerprint spectra of several potential candidates. Afterwards, I attempt a quantitative analysis with a linear combination fitting approach.

IV.B.4.b.1.1 Qualitative Identification of the Solid Electrolyte Interphase Species through Reference Fingerprinting

To identify possible SEI species I compare the SEI spectrum with the absorption spectra of several potential candidates. For this I have compiled a collection of oxygen K-edge reference spectra in Figure 67, where the SEI spectrum is shown as the white on grey background in each plot. I selected candidates based on two criteria: first, species with spectral contributions that could be correlated to the SEI spectrum and second, species commonly mentioned in literature as possible SEI components and I think are un-/likely be part of the SEI in my work. My evaluation of how well a reference fingerprint matches the SEI spectrum is summarized in Table 6 and the individual assessment of each reference is discussed in more detail in the following.

As marked in Figure 67a, the SEI spectrum itself shows six distinct features to which the references are matched: (I) the rather asymmetric main peak at 533.0 eV with a broader shoulder at 531.4 eV (II) and a sharper shoulder at 533.5 eV (III); another pronounced peak at 535.6 eV (V); the main pre-edge valley (IV) at 534.5 eV; and one broad, single hump (VI) above the ionization edge at round 540 eV.

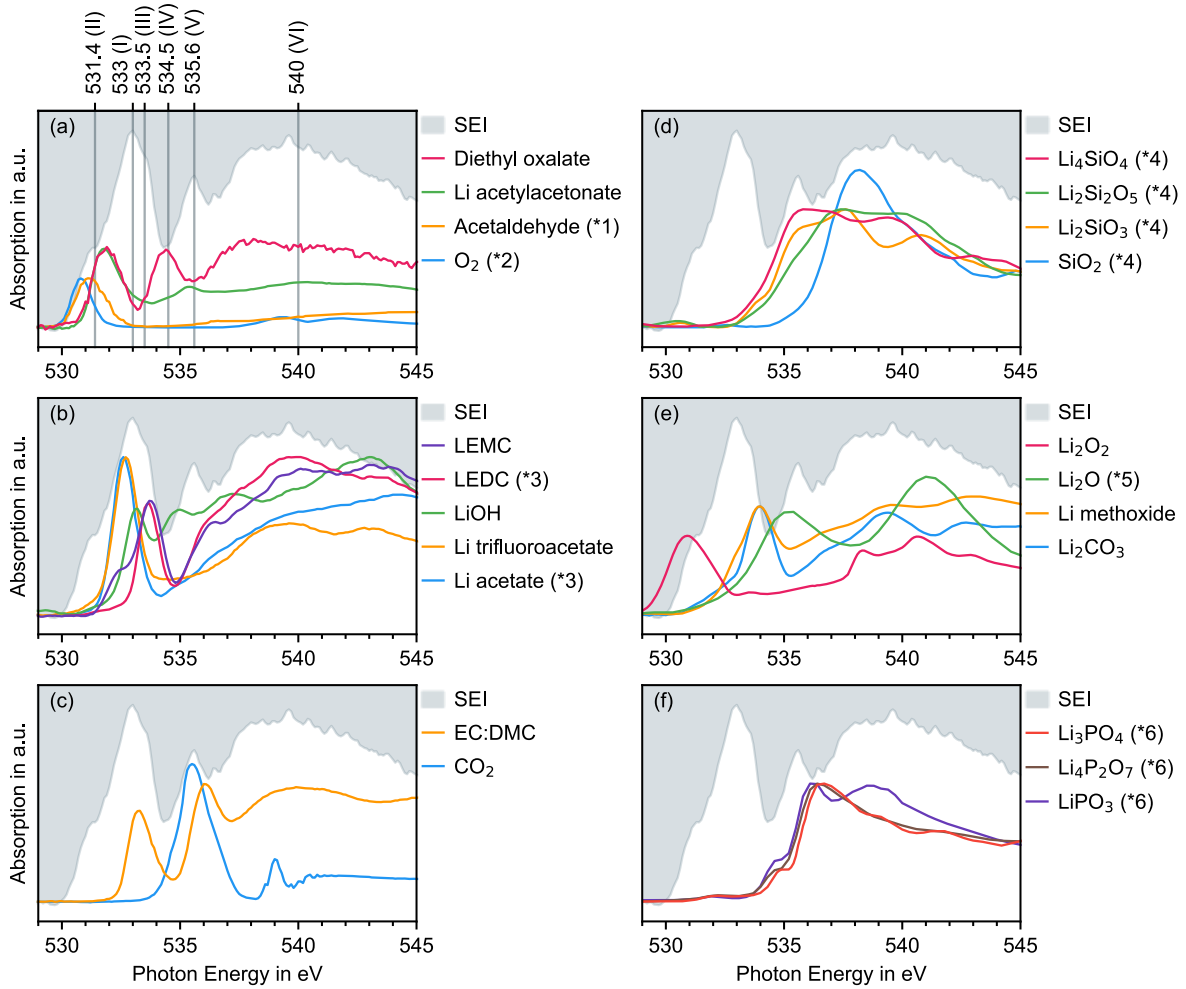

Figure 67 Comparison of the SEI spectrum (P6 from Figure 65d) to a variety of possible SEI reference species at the oxygen K-edge. The SEI spectrum is shown as the white on grey background throughout (a-f). The reference species are grouped by their possible correlation to the individual peaks (I) to (VI) as indicated in (a) or by the class of substance.* ***(a)*** *Pre-shoulder (II): O_2 (*2 from [186]), Diethyl oxalate, Li acetylacetonate and Acetaldehyde (*1 from [297]).* ***(b)*** *Main peak (I) and (III): LEMC, LEDC, LiOH, Li trifluoroacetate, Li acetate (3* from [163]).* ***(c)*** *Second main peak (V): 1M $LiPF_6$ in EC:DMC and CO_2.* ***(d)*** *Lithium silicates: Li_4SiO_4, $Li_2Si_2O_5$, Li_2SiO_3, Li_2SiO_3 and SiO_2 (*4 from [298]).* ***(e)*** *Li_2O_2, Li_2O (*5 from [299], [300]), Li methoxide and Li_2CO_3.* ***(f)*** *Lithium phosphates: Li_3PO_4, $Li_4P_2O_7$ and $LiPO_3$ (*6 from [301]).*

Based on the general trends of the carbonyl core 1s to π* transition established by Urquhart *et al.* [180], I identified aldehyde functional groups as possible candidates that correspond to the broader pre-shoulder (II) at 531.4 eV. As one of the simplest molecules with an aldehyde group, acetaldehyde is shown in Figure 67a as a representative. The presence of liquid aldehyde species in the *Solid Electrolyte Interphase* may appear peculiar at first. However, a possible explanation may be given by the SEI model recently proposed by He *et al.* [165], which I discussed earlier in chapter I.C.5 and is summarized in Figure 15. In their EDX tomography and cryogenic scanning TEM study on silicon nanowires, they observed a progressive growth of the SEI towards the center of the nanowire, leading to a strongly interwoven, “plum-pudding”-like morphology of silicon and SEI. This structural change is mediated by the proceeding formation and interconnection of pores, which form percolation

channels for the electrolyte to permeate and be trapped in. Due to the X-ray micro spot (85 µm x 25 µm), spatially resolving the proposed “plum-pudding”-like morphology at the nanoscale is not possible, yet. Nevertheless, the model of He *et al.* may give a first explanation for the presence of liquid aldehyde species within the SEI’s morphology. This would indicate, that the engulfed electrolyte may not only consist of the neat components EC:DMC, but also of aldehyde species as possible reduction products thereof.

Table 6: Summary of the qualitative SEI species evaluation regarding their matching spectral fingerprint. L is likely, P is possible, and U is unlikely.

Name	Peak	Prob.	Name	Peak	Prob.	Name	Peak	Prob.
Li acetate	(I)	L	Li trifluoroacetate	(I)	L	LiOH	(I)	L
Acetaldehyde	(II)	L	Li acetylacetonate	(II)	L	LEDC	(III)	L
LEMC	(III)	L	CO_2	(V)	L	EC:DMC	(V)	L
O_2	(II)	P	Diethyl oxalate	(II)	P	SiO_2	(VI)	P
Li_2SiO_3	-	U	$Li_2Si_2O_5$	-	U	Li_4SiO_4	-	U
$LiPO_3$	-	U	Li_3PO_4	-	U	$Li_4P_2O_7$	-	U
Li_2CO_3	-	U	Li methoxide	-	U			
Li_2O	-	U	Li_2O_2	-	U			

It must be noted that O_2 gas has a sharp peak at 530.8 eV, too. Looking at the spectrum of the uncycled sample in Figure 65a and Figure 62a, the bubble itself appears to have a minor, but similar contribution, which could be correlated to a small O_2 content inside the bubble. Consequently, the isolated SEI spectrum might still contain a contribution of the bubble O_2, which was not fully accounted for by the subtraction of the uncycled sample ($\Delta I_{\mathrm{isolation}}^{\mathrm{O_2}} > 0$ as discussed above). However, I thoroughly compared all cycled and uncycled XAS spectra in this region of interest (as shown in Figure 67) and I am confident that the residual O_2 gas contribution in the isolated SEI spectrum, if present at all, is only minor. Thus, the pre-shoulder (II) at 531.4 eV mainly stems from acetaldehyde species as discussed earlier. This is backed up by the slightly more fitting peak position of acetaldehyde over O_2 gas in Figure 67a as well.

Furthermore, in their work on the SEI on copper electrodes Zhuo *et al.* suggested the presence of oxalate species in their XAS data [163]. Based on this, I also identified diethyl oxalate (Figure 67a) as a possible contribution to (II). By screening several organic lithium compounds, I found that Li acetylacetonate like diethyl oxalate shows a peak at 531.6 eV but lacks the second peak at 534.3 eV. Considering that the second peak of diethyl oxalate directly coincides with the valley (IV) in the SEI spectrum, Li acetylacetonate seems a more likely match.

For the main peak (I) at 533.0 eV, I could not identify a species that contributes to this peak single-handedly. On top of that, the asymmetric shape and the sharp shoulder (III) suggest that this peak is a convolution of peaks from several species. Based on the overall peak position, I identified lithium acetates, namely acetate and trifluoroacetate, and lithium hydroxide as possible involved species (see Figure 67b). While the overall spectral shapes of lithium acetate and lithium trifluoroacetate are in good agreement, the main peak is shifted by 0.1 eV from 532.6 eV to 532.7 eV for the acetate and trifluoroacetate, respectively. It is unclear if the shift is caused by the fluorination or stems from a discrepancy in energy calibration between our measurement and the values reported in the literature. However, besides the energy shift, the additional smaller peaks after the ionization edge for the trifluoroacetate indicate the former.

Lithium ethylene di-carbonate (LEDC) was commonly accepted as the main single-electron-pathway reduction product of EC and was assumed to be the main organic constituent of the SEI in EC-containing electrolytes [35]–[38]. However, there is still open debate if LEDC was mistaken for lithium ethylene mono-carbonate (LEMC) [39]. My own measurement of LEMC and one of LEDC sourced from literature is shown in Figure 67b. It is very likely that either or both species contribute to the sharp side shoulder (III), but a distinction is hardly possible with the limited data. As with the acetates, the overall spectral shape of LEDC and LEMC is identical, but the main peak is also shifted by 0.1 eV from 533.6 eV to 533.7 eV for LEDC and LEMC, respectively. I note that the spectral contribution at 532.5 eV in my own measurement of LEMC might be due to contamination of lithium acetate. Future measurements will determine if a discrimination between LEDC and LEMC based on their oxygen K-edge XAS spectra is experimentally possible. In any case, the spectral shape of LEMC, LEDC and the acetate species all fit the broader hump (VI) in the post-edge region of the SEI spectrum notably well.

It appears that the contributing of CO_2 and EC:DMC was not fully accounted for by subtracting the uncycled sample, which resembles $\Delta I_{\mathrm{isolation}}^{\mathrm{CO_2}} > 0$ and $\Delta I_{\mathrm{isolation}}^{\mathrm{EC:DMC}} > 0$. Thus, both species need to be considered when interpreting the SEI spectrum and I attribute the other pronounced peak (V) at 535.5 eV to the CO_2 1s to $2\pi_u$ transition and to the chain/ring π* peak of EC:DMC, as shown in Figure 67c. Consequently, I assume the carbonyl π* peak of EC:DMC contributes to (I) and (III) as well.

For native oxide terminated silicon anodes it is reasonable to assume SiO_2 and lithium silicates ($Li_xSi_yO_z$) are part of the forming SEI. Based on *in-situ* synchrotron X-ray reflectivity and *ex-situ* X-ray photoelectron spectroscopy with first principles calculations, Cao *et al.* proposed a comprehensive picture of an inorganic SEI [152]. In their model, SiO_2 is transformed into an

inorganic SEI layer made from Li_xSiO_y, Li_xSi and Li_2O, which in turn is covered by an organic SEI layer. Due to detection limitations and sample preparation constraints, they left the organic SEI layer somehow undefined. Cao *et al.* [152] specified the thickness of the inorganic SEI layer to be only 4 nm. Thus, the thin layer of lithium silicates may be overshadowed by the post-ionization edge spectral contribution of the organic layer and may be difficult to distinguish. Looking at Figure 67d, I consider the lithium silicates (Li_4SiO_4, $Li_2Si_2O_5$, Li_2SiO_3) to be not apparent in the measured SEI spectrum, but I cannot fully rule out their presence in the SEI. Nevertheless, SiO_2 may still be present and contribute to the broader hump (VI) at around 538 eV.

Nevertheless, based on Figure 67e, I think the presence of Li_2O and Li_2O_2 is improbable. The missing pronounced peak can rule out the existence of Li_2O_2 at 531 eV and the distinct features past the ionization edge at 539 eV and 541 eV. For Li_2O, I would expect the second peak at around 541 eV to be more present in the SEI spectrum's post ionization region and disturb the relatively smooth (VI) hump. As it was summarized by Heiskanen *et al.* [34], Li_2O is not a direct reduction product of the electrolyte but rather created over time upon the SEI's ageing. Thus, large quantities of Li_2O are not expected in the freshly prepared SEI investigated here.

The research on the SEI on graphite sparked many debates and one of the most debated examples is Li_2CO_3 as the main constituent of the SEI [19], [33]. While Li_2CO_3 was found in most studies, there is no common agreement whether it is indeed a SEI component or just an artefact through environmental exposure [55]–[57]. As it can be seen in Figure 67e, the main peak of Li_2CO_3 at 534.1 eV closely coincides with the main valley (IV), and thus it is unlikely that it contributes to the sharp side shoulder (III). While some small contribution of Li_2CO_3 could be overshadowed as a minor component in the pre-edge region, I would expect its distinctive features in the post-edge region at 539.2 eV and 542.8 eV to appear more apparent. In many XAS studies in literature, these post-edge features were the most evident and a distinct fingerprint of Li_2CO_3, while in many cases even overshadowing all other components [302]–[305]. Based on this, I find the presence of Li_2CO_3 in the SEI on the silicon thin-film anodes investigated in this work to be unlikely, but I cannot rule out the presence in minor quantity. I note that Li methoxide has a strikingly similar spectral shape compared to Li_2CO_3 (see Figure 67e), whereby it could have easily been mistaken in literature before, especially in particularly noisy TEY and TFY XAS data.

Li *et al.* proposed that lithium phosphates $Li_xP_yO_z$ might be SEI constituents [305]. I show the absorption spectra of Li_3PO_4, $Li_4P_2O_7$, and $LiPO_3$ in Figure 67f. The detection of the phosphates suffers from the identical drawbacks as the silicates, where organic species can

easily overshadow their spectral contribution. While phosphates are not clearly present in my SEI spectra, I cannot rule out their presence in minor quantities either.

IV.B.4.b.1.2 Quantitative Identification of the Solid Electrolyte Interphases Species through Linear Combination Fitting

As of this writing, quantitative analysis in the form of a linear combination fitting of the reference species poses a major challenge to my novel gas bubble-stabilized liquid thin-layer sXAS approach and highlights one of its intrinsic drawbacks. Due to the “Thickness Effect” the overall spectral shape and, to some degree, the peak positions of every component need to be considered as a function of its SH. However, the transmission measurement only yields the linear combination of all species within the beam path while the individual SHs remain intrinsically unknown. To fully deconstruct the spectrum, the spectral shape-to-SH-correlation of every component is necessary. The spectra of the reference compounds were either measured by me through TEY or taken from literature. In most cases, only one fingerprint is available without any information on the spectral shape-to-SH-correlation. Although aware of this limitation, I still want to present a linear combination fitting to illustrate how the main peak of the SEI spectrum can be composed of several reference SEI species. I constrained the fit to the pre-ionization edge peaks, which are least affected by the “Thickness Effect”. Nevertheless, I want to emphasize that the linear combination fit presented in the following resembles a certain overinterpretation of the currently available data. Thus, my intention here is to demonstrate how linear combination fitting can be used to further unravel the obtained SEI spectra once the necessary data regarding the spectral shape-to-SH-correlation of a sufficient number of reference compounds is available.

The linear combination fitting was conducted according to the method of Kim *et al.* [286]. For the fitting procedure I followed the established combinatorial fitting approach of the ATHENA, ARTEMIS, HEPHAESTUS software package from Ravel *et al.* [306], but developed my own implementation of it which was specifically tailored to my data pipeline. The least-squares optimization of the linear combination was solved with the “Trust Region Reflective” algorithm by Branch *et al.* [307], as implemented in the scientific computing package SciPy 1.0 [308]. The combinatorial approach fits all possible combinations of a certain number of references $n = 1, 2, 3, 4, \ldots$ and evaluates the fit quality based on the reduced chi-squared value. I evaluated fits up to $n = 14$ and to introduce a penalty for numerical overfitting, I set a lower limit for each spectral contribution of 10%, based on the highest peak in the pre-ionization edge energy region. The considered SEI species were: O_2, Li_2O, Li_3PO_4, Li acetylacetonate, LiOH, diethyl oxalate, acetaldehyde, lithium ethylene di-carbonate (LEDC), lithium ethylene mono-carbonate (LEMC), Li_2CO_3, Li methoxide, CO_2, 1M $LiPF_6$ in EC:DMC and Li acetate. The corresponding absorption spectra are all shown in Figure 67.

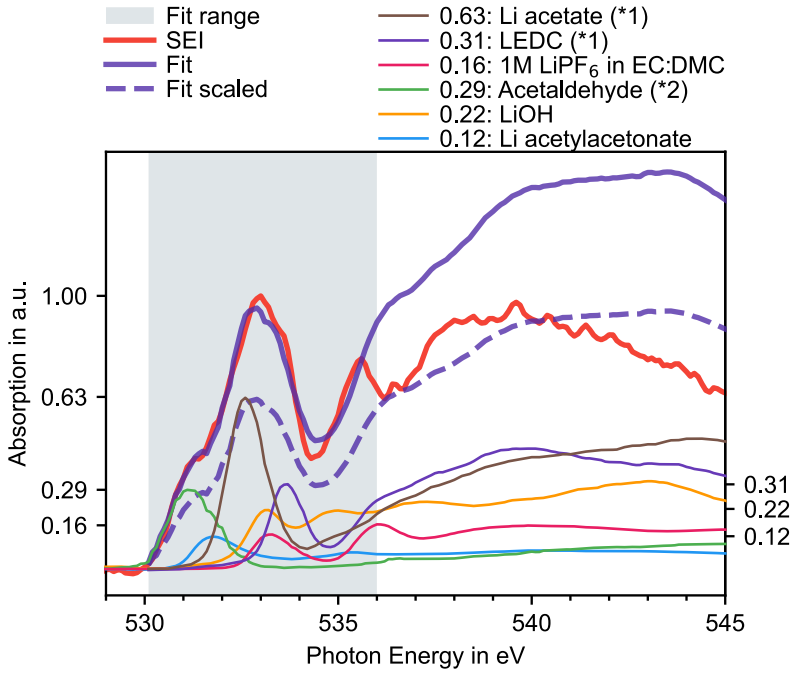

Figure 68: Linear combination fit of reference SEI species (Li acetylacetonate, LiOH, Acetaldehyde, 1M $LiPF_6$ in EC:DMC, LEDC and Li acetate) to the SEI spectrum P6 from Figure 65d in the fit range from 531.1 eV to 536 eV. 1* from [163], *2 from [297]. Additional scaled fit to allow easier visual comparison of the post-edge region outside of the fit range.*

Figure 68 shows the linear combination fit of several SEI reference species to the SEI spectrum between 531.1 eV and 536 eV photon energy. The fitting algorithm identified Li acetylacetonate, LiOH, acetaldehyde, LEDC, and Li acetate as the main SEI components. It also includes a minor amount of $LiPF_6$ in EC:DMC, which confirms my assumption that a small contribution of electrolyte still remains within the SEI spectrum ($\Delta I_{\text{isolation}}^{\text{EC:DMC}} > 0$). The individual components are drawn in Figure 68 with their corresponding spectral contribution and the respective numerical values are given in the legend. The numerical values correspond to the fraction of the highest spectral contribution in the fit range. Due to the unknown extend of the "Thickness Effect" of each induvial reference spectrum and the lack of calibration curves, an actual compositional content value cannot be deduced. The fit appears to correctly resolve the main SEI spectrum peak (I) with its broader shoulder (II), and the sharp side shoulder (III), as well as the main valley (IV). Due to increasing "Thickness Effect"-distortions for higher, post ionization edge energies, it cannot resolve the second pronounced peak (V). Further, I assume the fitting algorithm did not select CO_2 due to the relatively large full width at half maximum of the 1s to $2\pi_u$ transition in the reference spectrum. However, scaling the fit also indicates that the linear combination resolves the broad hump (VI) behind the ionization edge notably well, although this region was not included in the fit range.

IV.B.4.b.2 Qualitative Identification of the Solid Electrolyte Interphase Species at the Fluorine K-edge

I interpret the XAS data at the fluorine K-edge in analogy to the oxygen K-edge in Figure 65. Figure 69a shows the fluorine K-edge at three different sample positions, P1 to P3, from a cycled sample. The smaller the SH the more the spectral shape of the SEI is revealed. One can isolate the spectrum of the electrolyte by subtracting P3 from P1, which is shown in Figure 69b, and is in excellent agreement with the electrolyte spectrum of 1M $LiPF_6$ in EC:DMC. At the fluorene K-edge the electrolyte spectrum correlates to the 1M $LiPF_6$ salt dissolved in EC:DMC and a reference TEY XAS spectrum of $LiPF_6$ powder is given in Figure 69b accordingly.

In Figure 69a, P1 shows two main peaks at 691.7 eV (I) and 696.4 eV (II) photon energy with a peak ratio of 1.02, and a side peak at 699.9 eV (III), as well as a broader peak between 713.2 and 718.1 eV. From P1 to P3, the first main peak (I) shifts slightly to higher energies and the spectral contribution of the second main peak (II) decreases while the side peak (III) shifts to higher energies as well. Figure 69c shows the fluorine K-edge of cycled samples at 5 different positions with the main peak (I) normalized to one to emphasize the changes. P1 to P5 have increasing pre-normalization SH values, where P1 reveals the SEI the most. I identify LiF as the main SEI species by comparing the overall spectral shapes at the fluorine K-edge. A TEY XAS reference spectrum of LiF powder is given in Figure 69b and Figure 69c for comparison. Additionally, P1 to P3 in Figure 69b shows an additional side shoulder at slightly higher energies than the main LiF peak. I propose that this peak could hint at trifluoroacetic acid (TFAA) species in the SEI, as shown by the reference spectrum in Figure 69c. I suggest that this may be correlated to the Li acetate species I presumably identified at the oxygen K-edge before (compare Figure 67b). The lithium acetate may be fluorinated and therefore shows up as TFAA species at the fluorine K-edge.

The isolated electrolyte spectrum (P1 minus P3) and the reference 1M $LiPF_6$ in EC:DMC electrolyte spectrum in Figure 69b both show a peak ratio of 0.97 between the main peaks (I) and (II). Hence, I consider any discrepancy in this ratio as an indication for underlying SEI species. This can be seen for P1 where its peak ratio of 1.02 can be correlated to the underlying spectral contribution of the LiF. Due to synchrotron time constrains, I was unable to obtain fluorene K-edge spectra from uncycled samples to check and compare for any spectral fingerprints of beam damage. However, because both the isolated electrolyte spectrum, P1 minus P3, and 1M $LiPF_6$ in EC:DMC show a peak ratio of 0.97, I assume the beam damage caused by the bubble formation is minimal, and the LiF indeed correlates to the SEI formed through the electrochemical cycling. I consider the $LiPF_6$ TEY reference

measurement shown in Figure 69b to be contaminated with LiF as well, due to its I-to-II peak ratio of 1.02. I still include it to show the overall spectral fingerprint of $LiPF_6$.

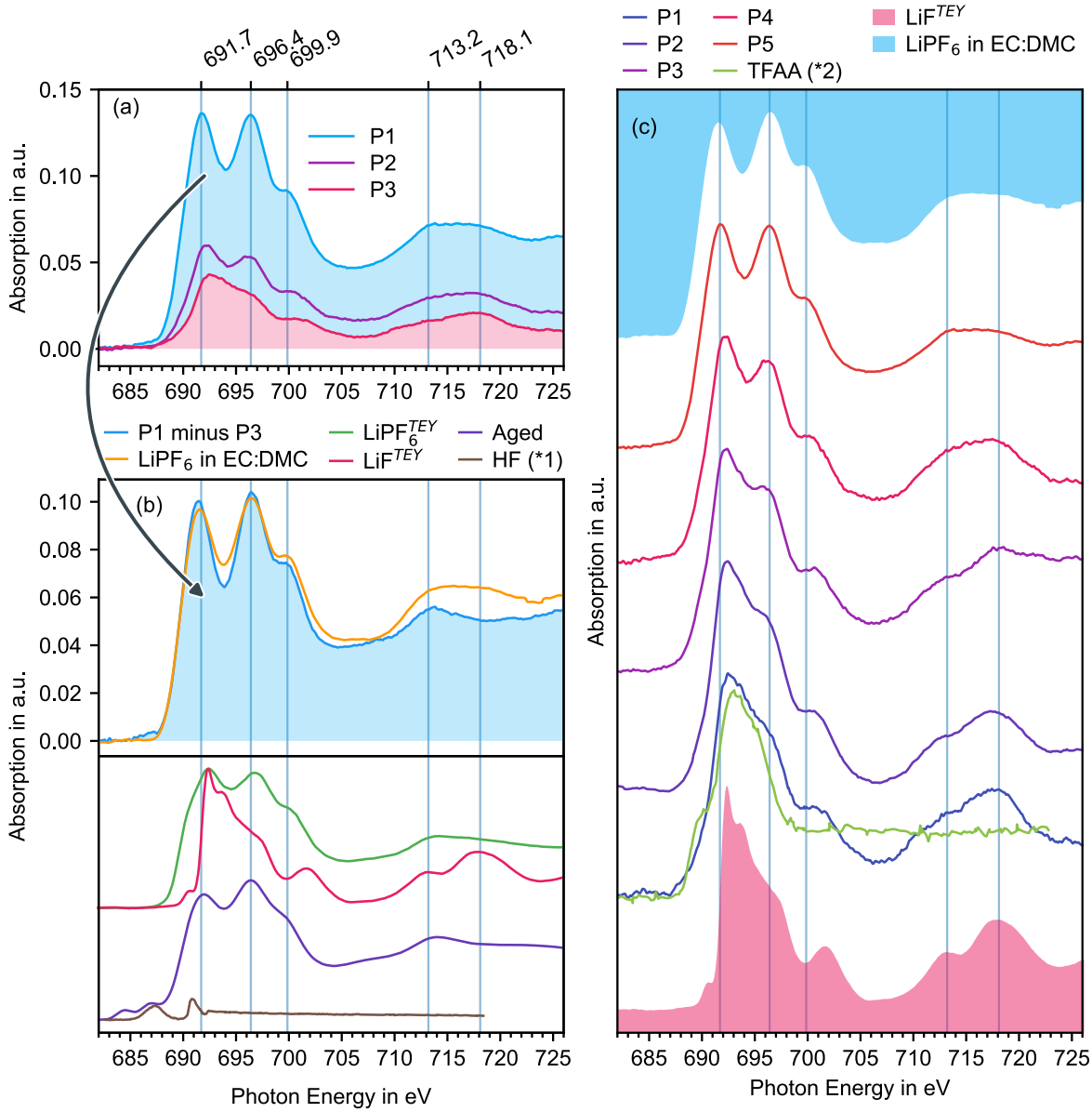

*Figure 69: Isolation and identification of the SEI species at the fluorine K-edge. (a) Fluorine K-edge transmission sXAS spectra of a cycled sample at 3 different sample positions P1 to P3. Contribution of the electrolyte salt $LiPF_6$ is shaded in blue and the contribution of the SEI is shaded in red. (b) Extraction of the electrolyte salt $LiPF_6$ spectrum that sits on top of the SEI by subtracting P3 from P1. Reference spectra of 1M $LiPF_6$ in EC:DMC, $LiPF_6$ powder (TEY) and LiF powder (TEY) are shown for comparison. Additionally, fluorine K-edge transmission sXAS spectrum of an aged cell (mean value of 4 spectra) together with a reference spectrum of HF (*1 from [309]). Spectra are stacked vertically by an arbitrary value. (c) Fluorine K-edge transmission sXAS spectra of cycled samples at 5 different positions P1 to P5. The spectra are normalized to the individual highest absorption value and stacked vertically by an arbitrary value. Reference measurements of 1M $LiPF_6$ in EC:DMC, LiF powder (TEY) and trifluoroacetic acid (TFAA) are shown for comparison (*2 from [310]).*

Similarly, the aged sample in Figure 69b exhibits an I-to-II peak ratio of 0.95, hinting at fluorine species that develop as ageing products without any electrochemical procedure. This also becomes apparent from the additional pronounced peaks at 684.5 eV and 686.9 eV. I correlate the second peak at 686.9 eV to the presence of hydrogen fluoride (HF) (compare

the reference spectrum in Figure 69b). The evolution of HF is a known phenomenon in lithium-ion battery technology and is often connected to water and moisture contamination of the electrolyte or cell. I take the absence of any HF signal in non-aged samples as confirmation that water and moisture contamination is not an issue for the 12-hour time frame of the *in-situ* measurements.

IV.B.5 The Silicon Thin-film Anodes: Monitoring the Anodes' Degree of Lithiation at the Silicon L-edge

The de-/lithiation of the silicon thin-film anodes can be observed at the silicon L-edge. Figure 70 shows silicon L-edge XAS spectra of the aged and cycled anodes together with a pristine sample obtained from an empty cell without electrolyte, i.e., under *ex-situ* conditions. The overall spectral shape of the samples at the silicon L-edge is dominated by the broad absorption hump of the SiN_x windows at around 105 eV photon energy. For comparison, a reference spectrum from silicon nitride Si_3N_4 is shown in Figure 70, as well. Silicon exhibits additional spectral features between 99 eV and 102 eV. In this energy region, the spectrum of the pristine amorphous silicon thin-film anode resembles a reference spectrum of amorphous silicon (a-Si) from the literature [311]. However, the two main peaks of a-Si at 100.4 eV and 101.0 eV appear to be much better resolved in transmission compared to the usual TEY measurements common in literature. I attribute this to the surface sensitivity of the TEY measurement that picks up the interfering signal of the native SiO_2 layer as apparent from the SiO_2 reference spectrum in Figure 70a.

Consequently, the overall spectral shape of the samples can be interpreted as a linear combination of the 50 nm thick sample itself with two SiN_x windows, 50 nm in thickness each. The aged sample shows the same spectral shape as the pristine *ex-situ* sample, demonstrating that the *ex-situ* measurement can be reproduced with the *in-situ* bubble approach and shows that the silicon thin-film itself does not undergo any ageing process, e.g., oxidation to SiO_2. I assume for the aged sample that the bubble formation did not sufficiently remove the excess electrolyte. The resulting thicker electrolyte layer shows up as an artificial erroneous absorption signal in the energy range from 106 eV to 112 eV and correlates to the oxygen K-edge in the fifth diffraction order from 530 eV to 560 eV. The corresponding energy scale of the fifth diffraction order is given in Figure 70a accordingly.

I notice from the cycled samples that the lithiation broadens the two main peaks of the a-Si (100.4 eV and 101.0 eV), slightly shifts them to lower energies, and that a broad side shoulder at around 99.6 eV emerges. I further assume the bubble formation freezes the degree of lithiation in time, because the bubble formation pushes away most electrolyte. The bubble was

created at 0.53 V during the delithiation sweep and at 0.44 V during the lithiation sweep for the two samples shown in Figure 70. Based on *operando* UV/Vis investigation in chapter IV.A.2.a, I correlate the different spectral shapes to a-Si* and a-Li_xSi, respectively. Thus, I attribute the differences to an increased degree of lithiation. Here, the gas bubble-stabilized liquid thin-layer approach for transmission XAS presented in this work appears suitable to establish a more fine-grained correlation with future experiments. Ultimately, the goal would be to correlate the degree of lithiation to the SEI composition.

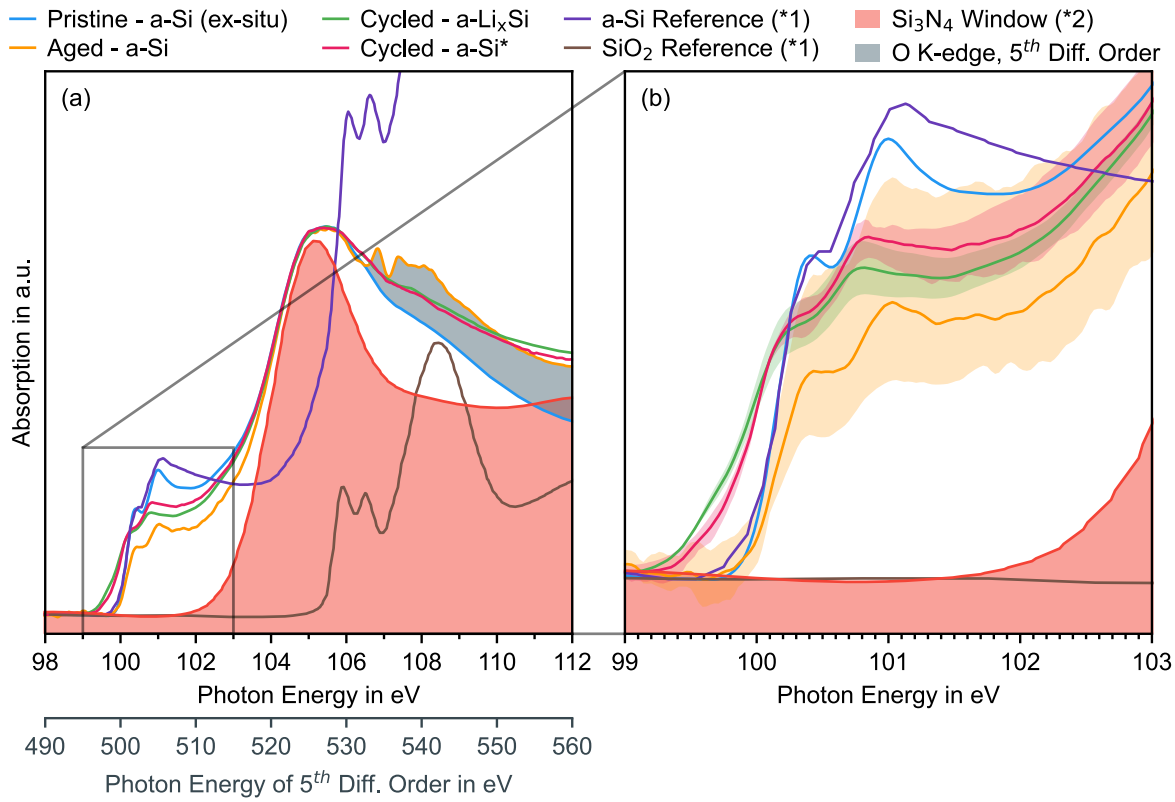

Figure 70: Silicon L-edge transmission sXAS spectra of a pristine silicon thin-film anode under ex-situ conditions, aged and cycled samples in the energy range from 98 eV to 112 eV. The boundaries of the filled areas (b) are the minimum and maximum values and the solid line is the mean value from several individual spectra for the pristine sample, aged, cycled - Li_xSi and cycled - a-Si, respectively. Reference spectra of amorphous silicon (a-Si), SiO_2, and Si_3N_4 are shown alongside for comparison (*1 from [311], *2 from [312]). Due to the nature of undulator radiation and the plane grating monochromator of the U49-2_PGM-1 [194] beamline, the radiation in the energy region of the silicon L-edge also contains contributions of higher energy photons. The monochromator setting for the silicon L-edge energy range coincides with the fifth diffraction order for higher energetic photons from the oxygen K-edge between 490 eV and 560 eV. The photon energy scale is given accordingly. The respective absorption that stems from the supposedly overlap of the silicon L-edge and the oxygen K-edge is marked in grey.*

Overall, the spectral shape of the *in-situ* samples at the Silicon L-edge can entirely be explained by the lithiation of a-Si and the underlying spectral contribution of the SiN_x windows. No additional peaks of further silicon-containing SEI species can be observed. Thus, although lithium silicates and phosphates were proposed in the literature, I could not verify their presence in the SEI investigated in this work at the silicon L-edge.

IV.B.6 Conclusion of the *In-situ* X-ray Absorption Spectroscopy Investigation on Silicon Anodes' Solid Electrolyte Interphase

As summarized in Table 6, based on spectral sXAS fingerprints at the oxygen K-edge, I identified acetates (based on Li acetate and Li trifluoroacetate), Li ethylene carbonates (based on LEMC and LEDC), acetonates (based on Li acetylacetonate), and LiOH as the solid species which are most likely to be present in the SEI on the silicon anodes investigated in this work. At the fluorine K-edge, I identified LiF to be the main fluorine-containing species in the SEI. Besides this, I suspect that the acetate species may be fluorinated and hence can be correlated to the observed trifluoroacetic acid fingerprint. Furthermore, even though reported in the literature, from my oxygen K-edge and silicon L-edge spectra I could not find clear evidence of lithium silicates or lithium phosphates.

LEMC or LEDC (the ongoing dispute aside [39]) are accepted to be the main reduction products of EC-containing electrolytes and together with LiF were found in many SEIs on both graphite and silicon [33], [34], [313], [38], [39], [56], [149], [150], [155], [172], [305]. Thus, the results clearly demonstrate the feasibility of my novel approach to investigate the SEI on silicon anodes though transmission sXAS. However, I found acetate species to be more likely to make up the biggest SEI contribution over LEMC or LEDC. As Schroder *et al.* demonstrated for crystalline silicon anodes, the electrochemical preparation heavily influences the SEI's composition [57]. Based on this, with the current data, it is too early to evaluate whether the increased acetate content is of general nature and was revealed through my *in-situ* measurements or is specific to my approach with the chosen electrochemical treatment. Thus, it is necessitated to establish a connection between the electrochemical preparation and the SEI's composition with future measurements.

In this regard, CO and CO_2 can be considered electrolyte additives themselves [314]–[316]. To name two convincing examples, Krause *et al.* [314] and Hopkins [315] *et al.* both reported improved cycling performance based on higher coulombic efficiency, when the electrolyte (1M $LiPF_6$ 3:7 EC:EMC) was enriched with CO_2 through the addition of dry ice (Krause *et al.*) and the dosing with a gas-tight syringe (Hopkins *et al.*). In both studies, the achieved performance through CO_2 and the observed SEI composition and structure was comparable to results from studies with FEC or VC additives. While the CO_2 was present throughout the electrochemical cycling in both studies, CO and CO_2 inside the gas bubble and inside the electrolyte thin-layer in my approach may influence the SEI composition afterwards. Krause *et al.* suggested Li_2CO_3 as one of the most likely reaction products. While the presence of Li_2CO_3 is not apparent in the sXAS analysis, with the current state of the experiment and data at hand, I cannot fully rule out the influence of the bubble's gas species on the observed SEI composition. However,

both CO and CO_2 are expected as side-products from the SEI formation in any case. As visible in Figure 54c-g, gas (presumably CO and CO_2) is already present (at its solubility limit) after the electrochemical treatment alone, even before the bubble formation. Thus, I argue the presence of the bubble does not change the SEI's environment in a fundamental way and the obtained results of the sXAS investigation remain valid.

I still want to mention that I also found evidence for the presence of liquid aldehyde species at the oxygen K-edge. While liquid species in the *Solid Electrolyte Interphase* admittedly sound peculiar at first, a possible early explanation for their presence may be given by the SEI model recently proposed by He *et al.* [165]. Based on their TEM and EDX tomography work on silicon nanowires, He *et al.* describe the silicon and its SEI as a "plum-pudding"-like structure in which's interconnected pores the liquid electrolyte can permeate and be trapped in. Based on the similar dimensions (60-90 nm wire diameter vs. 50 nm film thickness) I think their model is applicable to this work. Here, my complementary spectroscopic findings could indicate, that the entrapped electrolyte (localized through the EDX mapping of oxygen in the work of He *et al.*) may not only consist of the neat components EC:DMC, but also of aldehyde species as possible reduction products thereof. He *et al.* suggested that the observed capacity loss partly stems from increased impedance within the porous structure. Changing solvent composition, e.g., increasing aldehyde content, may explain the observed increase in impedance. This indicates the necessity to find ways, like electrolyte additives, to improve not only the SEI itself, but alleviate detrimental changes in the solvent chemistry as well.

However, due to the limited resolution given by the X-ray micro spot size, the "plum-pudding"-like morphology at the nanoscale could not be spatially resolved in this work and further investigation is needed. For this I imagine the future adaption of my cell/approach to scanning transmission X-ray microscopes at the BESSY II facility, which would allow nanoscale resolution.

V Summary and Outlook for the *In-situ* X-ray Absorption Spectroscopy on Silicon Anodes' Solid Electrolyte Interface with a Gas Bubble-Stabilized Liquid Thin-Layer

In this work, I introduced a new approach for transmission XAS on liquids and thin-film battery electrode materials in the soft X-ray regime under *in-situ* conditions. My unique method puts a novel twist on conventional SiN_x window-based liquid cells for transmission sXAS. The electrochemical cell I designed for this approach consists of two silicon nitride membranes with an electrolyte channel in-between. The silicon thin-film anodes under investigation are deposited via plasma enhanced chemical vapor deposition onto the back-facing silicon nitride window. The anodes are then electrochemically cycled in a two-electrode setup with a metallic lithium counter electrode, where the SEI forms on top of the then lithiated Li_xSi_y anodes. Afterwards, a bubble is formed by a high intensity X-ray beam in a controlled manner to push away the excess electrolyte. What is left in the beam path is a thin-layer of electrolyte that covers the SEI and the anode, keeping both under *in-situ* conditions. Finally, the SEI is investigated *in-situ* through transmission sXAS with a low X-ray intensity to avoid any beam damage.

The reliability and success of this approach relies heavily on the controlled formation of a stable bubble through the high intensity X-ray. Thus, I have explored the bubble formation through an extensive FEM simulation using the commercial COMSOL Multiphysics® software package. The first part of my simulation models the emerging temperature and concentration distributions of the radiolysis products within the electrolyte under the high intensity X-ray beam. Based on my simulation, I identified the beam intensity and the beam position as the main experimental control variables and showed that moving the beam to the corner of the square-shaped SiN_x membrane windows reduces the electrolyte's maximum temperature by up to 55%.

Furthermore, I take the bubble formation to be governed by the interplay between elevated temperature, rising radiolysis gas species concentrations, and finally them exceeding their temperature-dependent solubility limits. The experimental sXAS investigation observed CO and CO_2 as main bubble gas species from the radiolysis of the model electrolyte 1M $LiPF_6$ in EC:DMC. Given its temperature-dependent high solubility but much lower nucleation supersaturation limit, I identified CO_2 as the bubble nucleation agent, while CO drives the bubble growth, due to its much lower solubility. My simulation showed that CO_2 can be brought into a state of supersaturation by increasing the electrolyte's temperature. Thus, the bubble nucleation can be triggered on demand by rapidly heating the electrolyte through a sudden

increase in X-ray beam intensity. Thus, after sufficient CO for a desired bubble size has been formed, triggering the bubble nucleation allows the reliable formation of a bubble and precise control of its size. Additionally, it minimizes the amount of non-gaseous radiolysis trace products. These traces remain in the electrolyte thin-layer and their concentration must be kept to a minimum for easy interpretation of the obtained XAS spectra.

However, the electrolyte's temperature and the gas concentrations are not accessible in the current implementation of my electrochemical cell. Thus, the proposed procedure cannot be fully adapted, as it relies on both quantities when to ideally trigger the bubble formation. Nevertheless, I still adopted its main idea in my experimental work: enriching the electrolyte with a lower beam intensity first, and then triggering the bubble formation by stepwise increasing the beam intensity. As I have demonstrated in this work, this preliminary and rudimentary approach is sufficient to deliver a proof-of-concept for the transmission sXAS. However, to allow more precise control, gaining access to the electrolyte's temperature and dissolved gas concentrations is the next step for the further development of my novel approach. Thus, the challenge to overcome is how to experimentally probe the small volume between the two SiN_x membrane windows. Recently, in 2022, Tsutsui *et al.* reported their findings on the ionic heat dissipation in solid-state pores through SiN_x membranes [317]. For their study, they fabricated gold/platinum nanowire thermocouples on top of SiN_x membranes in the vicinity of the pores through a series of electron beam lithography and metal deposition processes. Their integrated nanowire thermocouple showed remarkable sensitivity between 300 and 450 K. I propose that the beam-facing SiN_x membrane window inside my cell could be equipped with an array of similar nanowire thermocouples. These thermocouples could yield valuable readings of the electrolyte's temperature under the high intensity X-ray beam.

Accessing the gas concentrations, however, appears to be more intricate and I suggest adapting the cell to Differential Electrochemical Mass Spectroscopy (DEMS) [318], [319] is the most promising way forward. In conventional DEMS, the gas species produced at an electrode surface are extracted through porous Teflon membranes. While their surface tension prevents most electrolytes from penetrating the pores (tens of nanometers), the dissolved gas species readily evaporate through them into the surrounding vacuum, where they are picked up and analyzed by a mass spectrometer. Thus, I propose a separate experiment where the back-facing SiN_x membrane window is replaced with a Teflon membrane through which the gaseous radiolysis products are extracted and analyzed through mass spectroscopy. This setup resembles the geometry of the actual *in-situ* sXAS experiment to the best degree and allows probing the gas concentrations directly inside the probing chamber. The DEMS investigation will yield decisive insight into the nature of radiolysis species and the individual amounts of substance. The values for the photon-radiolysis conversion coefficient $C_{\text{Radiolysis}}^{\text{Conversion}}$ obtained

through this experiment will verify and highly increase the quality of the radiolysis simulation presented in this work.

On top of that, in the second part of my simulation, I used the concentration distributions obtained in the first part to model the bubble growth through CFD. The CFD simulation of the bubble growth unveiled 3 decisive growth stages: a rapid initial growth in both dimensions until touching the upper and lower membrane windows in less than a second, followed by a horizontal growth of the bubble to 90% of its size within about a minute and finally a sluggish growth to its final size over the course of several minutes. The simulated bubble growth also demonstrated that, due to the concave shape of the probing chamber, the bubble always ends up sitting symmetrically at the center. This makes the method fail-safe in case the beam position and nucleation location cannot be controlled precisely. Furthermore, the SEI is not expected to adhere strongly to the anode's surface and the bubble growth may influence the SEI's morphology. Here, my simulation showed that the concentration distribution influences not only the bubble's final size but its growth speed as well. The two improvements suggested above enable access to the temperature and provide refined concentration distributions. In the future, this can allow the fine-tuning of the bubble growth and help to preserve the SEI's morphology to the best possible degree.

When it comes to future adaptions, I want to give an outlook into future capabilities of my novel gas bubble-stabilized liquid thin-layer transmission sXAS approach. The liquid thin-layer between the bubble and the electrode surface remains in contact with the surrounding electrolyte. One could imagine performing the electrochemical procedures even after the bubble creation, where only very little volume of electrolyte is necessary. Thus, for some applications like investigations of surface catalytic reactions with small mass turnover, this approach still appears to be viable for *operando* experiments where the transmission sXAS is conducted simultaneously with the electrochemical experiment. Besides this, Eberhardt *et al.* unveiled that the fragmentation of small organic molecules appears to be site specific, depending on the non-/resonant soft X-ray excitation energy [223]. Thus, the tunable energy of synchrotron radiation could allow to target the radiolysis at a specific molecule / atomic bond. Based on this, I want to propose the idea of an experiment where the gas bubble is created through the targeted degradation of a specific sacrificial agent without damaging the sample molecules of interest.

Furthermore, in a thorough electrochemical characterization, the silicon thin-film anodes investigated in this work showed all distinct features of the de-/lithiation of a-Si, when cycled inside my sXAS cell. On top of that, to complement the electrochemical characterization, I adapted my cell to *operando* UV/Vis and *operando* OM. By combining the electrochemical

characterization with the *operando* UV/Vis investigation, I demonstrated that the degree of lithiation of the silicon thin-film anodes can be monitored through the absorption at 450 nm. From the observed continuous change in the UV/Vis absorption throughout each cycle, I deduced that, after the initial cycle, the silicon thin-films remain in the amorphous regime and the cycling takes place between a-Si* and a-Li_xSi. Besides this, the *operando* OM revealed a reversible wrinkling of the membrane/silicon bilayer upon de-/lithiation, indicating a swing between tensile and compressive stress within each cycle. On top of that, the OM investigation showed that, after the initial cycle, the lithiation appears to be homogeneous throughout the whole SiN_x window and a homogeneous SEI formation is expected for the *in-situ* sXAS. Both UV/Vis and OM verified that the anodes remain crack-free for the cycle count of the *in-situ* XAS investigation.

At the BESSY II synchrotron facility in Berlin, I applied my novel gas bubble-stabilized liquid-thin layer *in-situ* transmission sXAS approach to investigate the SEI composition on silicon thin-film anodes for LIBs. The silicon anodes were cycled ten times between 10 mV and 800 mV vs. Li/Li^+ in the model electrolyte 1M $LiPF_6$ in EC:DMC. Through a qualitative analysis of spectral fingerprints at the oxygen K-edge, I identified acetates, Li ethylene carbonates (LEMC or LEDC), acetonates, and LiOH as the main solid species in the silicon anodes' SEI investigated in this work. At the fluorine K-edge, LiF was revealed as the main fluorine-containing species in the SEI. Furthermore, the acetate species observed at the oxygen K-edge may be fluorinated and hence can be correlated to the observed trifluoroacetic acid fingerprint. Furthermore, even though reported in the literature, from my oxygen K-edge and silicon L-edge spectra I could not find clear evidence of lithium silicates or lithium phosphates. Additionally, I found evidence for the presence of liquid aldehyde species at the oxygen K-edge, which indicates possible liquid inclusions within a presumably porous SEI morphology. I correlated the liquid inclusions to the porous "plum-pudding"-like SEI structure recently proposed by He *et al.* [165]. However, due to the limited resolution given by the X-ray micro spot size of the U49-2_PGM-1 beamline, where I conducted most of my experimental work, the proposed "plum-pudding"-like morphology at the nanoscale could not be spatially resolved in this work, yet. Thus, I imagine the adaption of my cell/approach to scanning transmission X-ray microscopes at the BESSY II facility to obtain nanoscale resolution in the future.

Li ethylene carbonates are accepted to be the main reduction products of EC-containing electrolytes and together with LiF were found in most SEIs on both graphite and silicon anodes. Based on this, the results obtained in this work clearly demonstrated the feasibility of my novel approach to investigate the SEI on silicon anodes though transmission sXAS under *in-situ* conditions.

To further back up my qualitative evaluation, I presented a preliminary quantitative analysis based on a linear combination fitting of reference spectra to the isolated SEI spectrum. While the achieved linear combination fit already resolved the pre-edge region notably well, the post-ionization region is still distorted by the “Thickness Effect”. Because the “Thickness Effect” is unavoidable in transmission XAS, to fully deconstruct the SEI spectrum through linear combination fitting, the spectral shape-to-thickness-correlation of every component is necessary. For the future improvement of my approach and a reliable deconstruction of the SEI’s spectrum via linear combination fitting, a library that contains reference spectra with said spectral shape-to-thickness-correlation is necessary.

Nevertheless, the qualitative analysis demonstrated that the novel approach presented in this work gives direct access to the SEI composition. With this, the next steps are clear. It is commonly accepted that the electrochemical preparation, e.g., the charging treatment in the first few cycles, heavily influences the SEI’s composition. With future experiments, my novel approach could help to establish a connection between the charging treatment, the SEI’s composition and the cycle stability. With a proper charging treatment, this could help to optimize the SEI for the silicon anodes’ large volume swings upon de-/lithiation.

Moreover, I highlighted the importance of electrolyte additives in the first chapter of this work. To gain traction in the LiBs landscape, silicon must be a viable drop-in solution that works with current electrolytes. Therefore, when it comes to the optimization of the electrolyte, additives that improve the SEI’s properties and make it viable for silicon anodes are the only feasible option for the near future. Because exploring the working principle of each additive turned out to be at least as difficult as the initial SEI problem itself, most endeavors of finding proper additives can be considered plain trial-and-error approaches so far. These trial-and-error approaches are slow, and often are associated with steep upfront costs and a high risk of lost returns. This makes electrolyte additives the most kept trade secrets in the industry. To support these trial-and-error approaches, my approach allows rapid, more efficient screening of new battery electrolyte formulations in future experiments. Furthermore, by promising a correlation between electrolyte formulation, SEI composition and SEI/anode performance, my approach may yield a mechanistic understanding of the additive’s role in the SEI formation. This may facilitate a more goal-oriented coarse of action and overall accelerates development times. With this prospect, I consider the novel method presented in this work an appropriate tool to successfully engineer a stable, efficient SEI on a future silicon-anode based LIB.

VI Literature

[1] D. Linden and T. B. Reddy, “Handbook of Batteries,” John Wiley & Sons, Inc.

[2] M. Gao *et al.*, “Lithium metal batteries for high energy density: Fundamental electrochemistry and challenges,” *J. Energy Chem.*, vol. 59, pp. 666–687, 2021, doi: 10.1016/j.jechem.2020.11.034.

[3] D. Fouchard and J. B. Taylor, “The molicel® rechargeable lithium system: Multicell aspects,” *J. Power Sources*, vol. 21, no. 3–4, pp. 195–205, Oct. 1987, doi: 10.1016/0378-7753(87)80054-X.

[4] F. C. Laman and K. Brandt, “Effect of discharge current on cycle life of a rechargeable lithium battery,” *J. Power Sources*, vol. 24, no. 3, pp. 195–206, Oct. 1988, doi: 10.1016/0378-7753(88)80115-0.

[5] M. Li, J. Lu, Z. Chen, and K. Amine, “30 Years of Lithium-Ion Batteries,” *Adv. Mater.*, vol. 30, no. 33, p. 1800561, Aug. 2018, doi: 10.1002/adma.201800561.

[6] NobelPrize.org. Nobel Prize Outreach, “John B. Goodenough – Nobel Lecture.” https://www.nobelprize.org/prizes/chemistry/2019/goodenough/lecture/ (accessed Feb. 01, 2022).

[7] M. S. Whittingham, “Electrointercalation in transition-metal disulphides,” *J. Chem. Soc. Chem. Commun.*, no. 9, p. 328, 1974, doi: 10.1039/c39740000328.

[8] M. S. WHITTINGHAM, “Electrical Energy Storage and Intercalation Chemistry,” *Science (80-.).*, vol. 192, no. 4244, pp. 1126–1127, Jun. 1976, doi: 10.1126/science.192.4244.1126.

[9] M. S. Whittingham and F. R. Gamble, “The lithium intercalates of the transition metal dichalcogenides,” *Mater. Res. Bull.*, vol. 10, no. 5, pp. 363–371, 1975, doi: 10.1016/0025-5408(75)90006-9.

[10] M. S. Whittingham, “Lithium batteries and cathode materials,” *Chem. Rev.*, vol. 104, no. 10, pp. 4271–4301, 2004, doi: 10.1021/cr020731c.

[11] K. Mizushima, P. C. Jones, P. J. Wiseman, and J. B. Goodenough, “LixCoO2 (0<x<-1): A new cathode material for batteries of high energy density,” *Mater. Res. Bull.*, vol. 15, no. 6, pp. 783–789, Jun. 1980, doi: 10.1016/0025-5408(80)90012-4.

[12] A. N. Dey, “Electrochemical Alloying of Lithium in Organic Electrolytes,” *J. Electrochem. Soc.*, vol. 118, no. 10, p. 1547, 1971, doi: 10.1149/1.2407783.

[13] D. Fauteux and R. Koksbang, “Rechargeable lithium battery anodes: alternatives to metallic lithium,” *J. Appl. Electrochem.*, vol. 23, no. 1, pp. 1–10, Jan. 1993, doi: 10.1007/BF00241568.

[14] J. O. Besenhard, “The electrochemical preparation and properties of ionic alkali metal-and NR4-graphite intercalation compounds in organic electrolytes,” *Carbon N. Y.*, vol. 14, no. 2, pp. 111–115, 1976, doi: 10.1016/0008-6223(76)90119-6.

[15] J. O. Besenhard and H. P. Fritz, “Cathodic reduction of graphite in organic solutions of alkali and NR4+ salts,” *J. Electroanal. Chem. Interfacial Electrochem.*, vol. 53, no. 2, pp. 329–333, Jun. 1974, doi: 10.1016/S0022-0728(74)80146-4.

[16] G. Eichinger, “Cathodic decomposition reactions of propylene carbonate,” *J. Electroanal. Chem. Interfacial Electrochem.*, vol. 74, no. 2, pp. 183–193, Dec. 1976, doi: 10.1016/S0022-0728(76)80234-3.

[17] A. N. Dey and B. P. Sullivan, “The Electrochemical Decomposition of Propylene Carbonate on Graphite,” *J. Electrochem. Soc.*, vol. 117, no. 2, p. 222, 1970, doi: 10.1149/1.2407470.

[18] E. Peled, “The Electrochemical Behavior of Alkali and Alkaline Earth Metals in Nonaqueous Battery Systems—The Solid Electrolyte Interphase Model,” *J. Electrochem. Soc.*, vol. 126, no. 12, pp. 2047–2051, Dec. 1979, doi: 10.1149/1.2128859.

[19] K. Xu, “Electrolytes and Interphases in Li-Ion Batteries and Beyond,” *Chem. Rev.*, vol. 114, no. 23, pp. 11503–11618, Dec. 2014, doi: 10.1021/cr500003w.

[20] A. Yoshino, “Secondary battery, US patent 4668595A,” 1987.

[21] Y. Nishi, “Lithium ion secondary batteries; Past 10 years and the future,” *J. Power Sources*, vol. 100, no. 1–2, pp. 101–106, 2001, doi: 10.1016/S0378-7753(01)00887-4.

[22] J. B. Goodenough and K. S. Park, “The Li-ion rechargeable battery: A perspective,” *J. Am. Chem. Soc.*, vol. 135, no. 4, pp. 1167–1176, 2013, doi: 10.1021/ja3091438.

[23] W. Liu *et al.*, “Nickel-Rich Layered Lithium Transition-Metal Oxide for High-Energy Lithium-Ion Batteries,” *Angew. Chemie Int. Ed.*, vol. 54, no. 15, pp. 4440–4457, Apr. 2015, doi: 10.1002/anie.201409262.

[24] N. Lebedeva, F. Di Persio, and L. Boon-Brett, “Lithium ion battery value chain and related opportunities for Europe,” 2016. [Online]. Available: https://ec.europa.eu/jrc/sites/jrcsh/files/jrc105010_161214_li-ion_battery_value_chain_jrc105010.pdf.

[25] T. Ohzuku, A. Ueda, and M. Nagayama, “Electrochemistry and Structural Chemistry of LiNiO2 (R3m) for 4 Volt Secondary Lithium Cells,” *J. Electrochem. Soc.*, vol. 140, no. 7, pp. 1862–1870, Jul. 1993, doi: 10.1149/1.2220730.

[26] M. G. S. R. Thomas, W. I. F. David, J. B. Goodenough, and P. Groves, “Synthesis and structural characterization of the normal spinel Li[Ni2]O4,” *Mater. Res. Bull.*, vol. 20, no. 10, pp. 1137–1146, Oct. 1985, doi: 10.1016/0025-5408(85)90087-X.

[27] H. Li, M. Cormier, N. Zhang, J. Inglis, J. Li, and J. R. Dahn, “Is Cobalt Needed in Ni-Rich Positive Electrode Materials for Lithium Ion Batteries?,” *J. Electrochem. Soc.*, vol. 166, no. 4, pp. A429–A439, 2019, doi: 10.1149/2.1381902jes.

[28] J. B. Goodenough and Y. Kim, “Challenges for Rechargeable Li Batteries †,” *Chem. Mater.*, vol. 22, no. 3, pp. 587–603, Feb. 2010, doi: 10.1021/cm901452z.

[29] K. Hayashi, Y. Nemoto, S. I. Tobishima, and J. I. Yamaki, “Mixed solvent electrolyte for high voltage lithium metal secondary cells,” *Electrochim. Acta*, vol. 44, no. 14, pp. 2337–2344, 1999, doi: 10.1016/S0013-4686(98)00374-0.

[30] M. Egashira, H. Takahashi, S. Okada, and J. I. Yamaki, “Measurement of the electrochemical oxidation of organic electrolytes used in lithium batteries by microelectrode,” *J. Power Sources*, vol. 92, no. 1–2, pp. 267–271, 2001, doi: 10.1016/S0378-7753(00)00553-X.

[31] X. Zhang, R. Kostecki, T. J. Richardson, J. K. Pugh, and P. N. Ross, “Electrochemical and Infrared Studies of the Reduction of Organic Carbonates,” *J. Electrochem. Soc.*, vol. 148, no. 12, p. A1341, 2001, doi: 10.1149/1.1415547.

[32] J. Asenbauer, T. Eisenmann, M. Kuenzel, A. Kazzazi, Z. Chen, and D. Bresser, “The success story of graphite as a lithium-ion anode material – fundamentals, remaining challenges, and recent developments including silicon (oxide) composites,” *Sustain. Energy Fuels*, vol. 4, no. 11, pp. 5387–5416, 2020, doi: 10.1039/D0SE00175A.

[33] P. Verma, P. Maire, and P. Novák, “A review of the features and analyses of the solid electrolyte interphase in Li-ion batteries,” *Electrochim. Acta*, vol. 55, no. 22, pp. 6332–6341, Sep. 2010, doi: 10.1016/j.electacta.2010.05.072.

[34] S. K. Heiskanen, J. Kim, and B. L. Lucht, “Generation and Evolution of the Solid Electrolyte Interphase of Lithium-Ion Batteries,” *Joule*, vol. 3, no. 10, pp. 2322–2333, 2019, doi: 10.1016/j.joule.2019.08.018.

[35] D. Aurbach, Y. Gofer, M. Ben-Zion, and P. Aped, “The behaviour of lithium electrodes in propylene and ethylene carbonate: Te major factors that influence Li cycling efficiency,” *J. Electroanal. Chem.*, vol. 339, no. 1–2, pp. 451–471, 1992, doi: 10.1016/0022-0728(92)80467-I.

[36] D. Aurbach, Y. Ein-Eli, O. Chusid (Youngman), Y. Carmeli, M. Babai, and H. Yamin, “The Correlation Between the Surface Chemistry and the Performance of Li-Carbon Intercalation Anodes for Rechargeable ‘Rocking-Chair’ Type Batteries,” *J. Electrochem. Soc.*, vol. 141, no. 3, pp. 603–611, 1994, doi: 10.1149/1.2054777.

[37] K. Xu *et al.*, “Syntheses and characterization of lithium alkyl mono- and bicarbonates as components of surface films in Li-ion batteries,” *J. Phys. Chem. B*, vol. 110, no. 15, pp. 7708–7719, 2006, doi: 10.1021/jp0601522.

[38] G. V. Zhuang, K. Xu, H. Yang, T. R. Jow, and P. N. Ross, “Lithium Ethylene Dicarbonate Identified as the Primary Product of Chemical and Electrochemical Reduction of EC in 1.2 M LiPF 6 /EC:EMC Electrolyte,” *J. Phys. Chem. B*, vol. 109, no. 37, pp. 17567–17573, Sep. 2005, doi: 10.1021/jp052474w.

[39] L. Wang *et al.*, “Identifying the components of the solid–electrolyte interphase in Li-ion batteries,” *Nat. Chem.*, vol. 11, no. 9, pp. 789–796, Sep. 2019, doi: 10.1038/s41557-019-0304-z.

[40] M. S. Ding, K. Xu, and T. R. Jow, “Liquid-Solid Phase Diagrams of Binary Carbonates for Lithium Batteries,” *J. Electrochem. Soc.*, vol. 147, no. 5, p. 1688, 2000, doi: 10.1149/1.1393419.

[41] T. Liu *et al.*, “In situ quantification of interphasial chemistry in Li-ion battery,” *Nat. Nanotechnol.*, vol. 14, no. 1, pp. 50–56, 2019, doi: 10.1038/s41565-018-0284-y.

[42] B. Strehle, S. Solchenbach, M. Metzger, K. U. Schwenke, and H. A. Gasteiger, “ The Effect of CO 2 on Alkyl Carbonate Trans-Esterification during Formation of Graphite Electrodes in Li-Ion Batteries ,” *J. Electrochem. Soc.*, vol. 164, no. 12, pp. A2513–A2526, 2017, doi: 10.1149/2.1001712jes.

[43] M. Nie, D. P. Abraham, Y. Chen, A. Bose, and B. L. Lucht, “Silicon solid electrolyte interphase (SEI) of lithium ion battery characterized by microscopy and spectroscopy,” *J. Phys. Chem. C*, vol. 117, no. 26, pp. 13403–13412, 2013, doi: 10.1021/jp404155y.

[44] D. M. Seo, D. Chalasani, B. S. Parimalam, R. Kadam, M. Nie, and B. L. Lucht, “Reduction reactions of carbonate solvents for lithium ion batteries,” *ECS Electrochem. Lett.*, vol. 3, no. 9, pp. 91–94, 2014, doi: 10.1149/2.0021409eel.

[45] K. Xu, Y. Lam, S. S. Zhang, T. R. Jow, and T. B. Curtis, “Solvation sheath of Li+ in nonaqueous electrolytes and its implication of graphite/electrolyte interface chemistry,” *J. Phys. Chem. C*, vol. 111, no. 20, pp. 7411–7421, 2007, doi: 10.1021/jp068691u.

[46] A. Von Wald Cresce, O. Borodin, and K. Xu, “Correlating Li+ solvation sheath structure with interphasial chemistry on graphite,” *J. Phys. Chem. C*, vol. 116, no. 50, pp. 26111–26117, 2012, doi: 10.1021/jp303610t.

[47] K. Xu and A. von Wald Cresce, “Li + -solvation/desolvation dictates interphasial processes on graphitic anode in Li ion cells,” *J. Mater. Res.*, vol. 27, no. 18, pp. 2327–2341, Sep. 2012, doi: 10.1557/jmr.2012.104.

[48] K. Xu, “‘Charge-Transfer’ Process at Graphite/Electrolyte Interface and the Solvation Sheath Structure of Li[sup +] in Nonaqueous Electrolytes,” *J. Electrochem. Soc.*, vol. 154, no. 3, p. A162, 2007, doi: 10.1149/1.2409866.

[49] J. O. Besenhard, M. Winter, J. Yang, and W. Biberacher, “Filming mechanism of lithium-carbon anodes in organic and inorganic electrolytes,” *J. Power Sources*, vol. 54, no. 2, pp. 228–231, 1995, doi: 10.1016/0378-7753(94)02073-C.

[50] M. R. Wagner, J. H. Albering, K. C. Moeller, J. O. Besenhard, and M. Winter, “XRD evidence for the electrochemical formation of Li+(PC) yCn- in PC-based electrolytes,” *Electrochem. commun.*, vol. 7, no. 9, pp. 947–952, 2005, doi: 10.1016/j.elecom.2005.06.009.

[51] L. Xing *et al.*, “Deciphering the Ethylene Carbonate-Propylene Carbonate Mystery in Li-Ion Batteries,” *Acc. Chem. Res.*, vol. 51, no. 2, pp. 282–289, 2018, doi: 10.1021/acs.accounts.7b00474.

[52] M. Nie, D. Chalasani, D. P. Abraham, Y. Chen, A. Bose, and B. L. Lucht, “Lithium ion battery graphite solid electrolyte interphase revealed by microscopy and spectroscopy,” *J. Phys. Chem. C*, vol. 117, no. 3, pp. 1257–1267, 2013, doi: 10.1021/jp3118055.

[53] B. S. Parimalam, A. D. MacIntosh, R. Kadam, and B. L. Lucht, “Decomposition Reactions of Anode Solid Electrolyte Interphase (SEI) Components with LiPF6,” *J. Phys. Chem. C*, vol. 121, no. 41, pp. 22733–22738, 2017, doi: 10.1021/acs.jpcc.7b08433.

[54] T. Yoon, M. S. Milien, B. S. Parimalam, and B. L. Lucht, “Thermal Decomposition of the Solid Electrolyte Interphase (SEI) on Silicon Electrodes for Lithium Ion Batteries,” *Chem. Mater.*, vol. 29, no. 7, pp. 3237–3245, 2017, doi: 10.1021/acs.chemmater.7b00454.

[55] S. S. Harilal, J. P. Allain, A. Hassanein, M. R. Hendricks, and M. Nieto-Perez, “Reactivity of lithium exposed graphite surface,” *Appl. Surf. Sci.*, vol. 255, no. 20, pp. 8539–8543, 2009, doi: 10.1016/j.apsusc.2009.06.009.

[56] K. Edström, M. Herstedt, and D. P. Abraham, “A new look at the solid electrolyte interphase on graphite anodes in Li-ion batteries,” *J. Power Sources*, vol. 153, no. 2, pp. 380–384, 2006, doi: 10.1016/j.jpowsour.2005.05.062.

[57] K. W. Schroder, H. Celio, L. J. Webb, and K. J. Stevenson, “Examining Solid Electrolyte Interphase Formation on Crystalline Silicon Electrodes: Influence of Electrochemical Preparation and Ambient Exposure Conditions,” *J. Phys. Chem. C*, vol. 116, no. 37, pp. 19737–19747, Sep. 2012, doi: 10.1021/jp307372m.

[58] C. Pillot, “Lithium-Ion Battery Raw Material Supply and Demand 2016 – 2025,” 2017.

[59] J. Kalhoff, G. G. Eshetu, D. Bresser, and S. Passerini, “Safer electrolytes for lithium-ion batteries: State of the art and perspectives,” *ChemSusChem*, vol. 8, no. 13, pp. 2154–2175,

2015, doi: 10.1002/cssc.201500284.

[60] S. S. Zhang, “A review on electrolyte additives for lithium-ion batteries,” *J. Power Sources*, vol. 162, no. 2, pp. 1379–1394, Nov. 2006, doi: 10.1016/j.jpowsour.2006.07.074.

[61] Z. Liu *et al.*, “Synthesis of Copper Nanowires via a Complex-Surfactant-Assisted Hydrothermal Reduction Process,” *J. Phys. Chem. B*, vol. 107, no. 46, pp. 12658–12661, Nov. 2003, doi: 10.1021/jp036023s.

[62] W. Zhao *et al.*, “Recent advances in the research of functional electrolyte additives for lithium-ion batteries,” *Curr. Opin. Electrochem.*, vol. 6, no. 1, pp. 84–91, 2017, doi: 10.1016/j.coelec.2017.10.012.

[63] D. Y. Wang, N. N. Sinha, R. Petibon, J. C. Burns, and J. R. Dahn, “A systematic study of well-known electrolyte additives in LiCoO 2/graphite pouch cells,” *J. Power Sources*, vol. 251, pp. 311–318, 2014, doi: 10.1016/j.jpowsour.2013.11.064.

[64] B. Zhang *et al.*, “Role of 1,3-propane sultone and vinylene carbonate in solid electrolyte interface formation and gas generation,” *J. Phys. Chem. C*, vol. 119, no. 21, pp. 11337–11348, 2015, doi: 10.1021/acs.jpcc.5b00072.

[65] A. L. Michan *et al.*, “Fluoroethylene carbonate and vinylene carbonate reduction: Understanding lithium-ion battery electrolyte additives and solid electrolyte interphase formation,” *Chem. Mater.*, vol. 28, no. 22, pp. 8149–8159, 2016, doi: 10.1021/acs.chemmater.6b02282.

[66] L. El Ouatani *et al.*, “The Effect of Vinylene Carbonate Additive on Surface Film Formation on Both Electrodes in Li-Ion Batteries,” *J. Electrochem. Soc.*, vol. 156, no. 2, p. A103, 2009, doi: 10.1149/1.3029674.

[67] M. Nie *et al.*, “Effect of Vinylene Carbonate and Fluoroethylene Carbonate on SEI Formation on Graphitic Anodes in Li-Ion Batteries,” *J. Electrochem. Soc.*, vol. 162, no. 13, pp. A7008–A7014, 2015, doi: 10.1149/2.0021513jes.

[68] X. Wang, H. Naito, Y. Sone, G. Segami, and S. Kuwajima, “New Additives to Improve the First-Cycle Charge–Discharge Performance of a Graphite Anode for Lithium-Ion Cells,” *J. Electrochem. Soc.*, vol. 152, no. 10, p. A1996, 2005, doi: 10.1149/1.2030127.

[69] D. Xiong, J. C. Burns, A. J. Smith, N. Sinha, and J. R. Dahn, “A High Precision Study of the Effect of Vinylene Carbonate (VC) Additive in Li/Graphite Cells,” *J. Electrochem. Soc.*, vol. 158, no. 12, p. A1431, 2011, doi: 10.1149/2.100112jes.

[70] N. N. Sinha, J. C. Burns, and J. R. Dahn, “Storage Studies on Li/Graphite Cells and the Impact of So-Called SEI-Forming Electrolyte Additives,” *J. Electrochem. Soc.*, vol. 160, no. 4, pp. A709–A714, 2013, doi: 10.1149/2.008306jes.

[71] C. Wang, H. Nakamura, H. Komatsu, M. Yoshio, and H. Yoshitake, “Electrochemical behaviour of a graphite electrode in propylene carbonate and 1,3-benzodioxol-2-one based electrolyte system,” *J. Power Sources*, vol. 74, no. 1, pp. 142–145, 1998, doi: 10.1016/S0378-7753(98)00017-2.

[72] X. Sun, H. S. Lee, X. Q. Yang, and J. McBreen, “Using a boron-based anion receptor additive to improve the thermal stability of LiPF6-based electrolyte for lithium batteries,” *Electrochem. Solid-State Lett.*, vol. 5, no. 11, 2002, doi: 10.1149/1.1510321.

[73] X. Sun, H. S. Lee, X. Q. Yang, and J. McBreen, “The compatibility of a boron-based anion receptor with the carbon anode in lithium-ion batteries,” *Electrochem. Solid-State Lett.*, vol. 6, no. 2, pp. 10–14, 2003, doi: 10.1149/1.1536475.

[74] M. Herstedt, M. Stjerndahl, T. Gustafsson, and K. Edström, “Anion receptor for enhanced thermal stability of the graphite anode interface in a Li-ion battery,” *Electrochem. commun.*, vol. 5, no. 6, pp. 467–472, 2003, doi: 10.1016/S1388-2481(03)00106-1.

[75] Z. Chen and K. Amine, “Tris(pentafluorophenyl) Borane as an Additive to Improve the Power Capabilities of Lithium-Ion Batteries,” *J. Electrochem. Soc.*, vol. 153, no. 6, p. A1221, 2006, doi: 10.1149/1.2194633.

[76] H. S. Lee, X. Q. Yang, J. McBreen, Y. Okamoto, and L. S. Choi, “A new family of anion receptors and their effect on ion pair dissociation and conductivity of lithium salts in non-aqueous solutions,” *Electrochim. Acta*, vol. 40, no. 13–14, pp. 2353–2356, 1995, doi: 10.1016/0013-4686(95)00192-H.

[77] X. Sun, H. S. Lee, X. Q. Yang, and J. McBreen, “Comparative Studies of the Electrochemical and Thermal Stability of Two Types of Composite Lithium Battery Electrolytes Using Boron-

Based Anion Receptors," *J. Electrochem. Soc.*, vol. 146, no. 10, pp. 3655–3659, 1999, doi: 10.1149/1.1392529.

[78] S. Komaba, T. Itabashi, M. Watanabe, H. Groult, and N. Kumagai, "Electrochemistry of Graphite in Li and Na Salt Codissolving Electrolyte for Rechargeable Batteries," *J. Electrochem. Soc.*, vol. 154, no. 4, p. A322, 2007, doi: 10.1149/1.2472552.

[79] C. J. Wen and R. A. Huggins, "Chemical diffusion in intermediate phases in the lithium-silicon system," *J. Solid State Chem.*, vol. 37, no. 3, pp. 271–278, May 1981, doi: 10.1016/0022-4596(81)90487-4.

[80] R. A. Sharma and R. N. Seefurth, "Thermodynamic Properties of the Lithium-Silicon System," *J. Electrochem. Soc.*, vol. 123, no. 12, pp. 1763–1768, Dec. 1976, doi: 10.1149/1.2132692.

[81] H. Okamoto, "The Li-Si (Lithium-Silicon) system," *Bull. Alloy Phase Diagrams*, vol. 11, no. 3, pp. 306–312, Jun. 1990, doi: 10.1007/BF03029305.

[82] A. M. Wilson and J. R. Dahn, "Lithium Insertion in Carbons Containing Nanodispersed Silicon," *J. Electrochem. Soc.*, vol. 142, no. 2, pp. 326–332, Feb. 1995, doi: 10.1149/1.2043994.

[83] P. Limthongkul, Y.-I. Jang, N. J. Dudney, and Y.-M. Chiang, "Electrochemically-driven solid-state amorphization in lithium-silicon alloys and implications for lithium storage," *Acta Mater.*, vol. 51, no. 4, pp. 1103–1113, Feb. 2003, doi: 10.1016/S1359-6454(02)00514-1.

[84] M. N. Obrovac and L. Christensen, "Structural Changes in Silicon Anodes during Lithium Insertion/Extraction," *Electrochem. Solid-State Lett.*, vol. 7, no. 5, p. A93, 2004, doi: 10.1149/1.1652421.

[85] J. Li and J. R. Dahn, "An In Situ X-Ray Diffraction Study of the Reaction of Li with Crystalline Si," *J. Electrochem. Soc.*, vol. 154, no. 3, p. A156, 2007, doi: 10.1149/1.2409862.

[86] M. Kim, Z. Yang, and I. Bloom, "Review—The Lithiation/Delithiation Behavior of Si-Based Electrodes: A Connection between Electrochemistry and Mechanics," *J. Electrochem. Soc.*, vol. 168, no. 1, p. 010523, Jan. 2021, doi: 10.1149/1945-7111/abd56f.

[87] M. T. McDowell, S. W. Lee, W. D. Nix, and Y. Cui, "25th Anniversary Article: Understanding the Lithiation of Silicon and Other Alloying Anodes for Lithium- Ion Batteries," *Adv. Mater.*, vol. 25, no. 36, pp. 4966–4985, Sep. 2013, doi: 10.1002/adma.201301795.

[88] M. N. Obrovac and V. L. Chevrier, "Alloy Negative Electrodes for Li-Ion Batteries," *Chem. Rev.*, vol. 114, no. 23, pp. 11444–11502, Dec. 2014, doi: 10.1021/cr500207g.

[89] B. Key, M. Morcrette, J.-M. Tarascon, and C. P. Grey, "Pair Distribution Function Analysis and Solid State NMR Studies of Silicon Electrodes for Lithium Ion Batteries: Understanding the (De)lithiation Mechanisms," *J. Am. Chem. Soc.*, vol. 133, no. 3, pp. 503–512, Jan. 2011, doi: 10.1021/ja108085d.

[90] X. H. Liu *et al.*, "In situ atomic-scale imaging of electrochemical lithiation in silicon," *Nat. Nanotechnol.*, vol. 7, no. 11, pp. 749–756, Nov. 2012, doi: 10.1038/nnano.2012.170.

[91] B. Key, R. Bhattacharyya, M. Morcrette, V. Seznéc, J.-M. Tarascon, and C. P. Grey, "Real-Time NMR Investigations of Structural Changes in Silicon Electrodes for Lithium-Ion Batteries," *J. Am. Chem. Soc.*, vol. 131, no. 26, pp. 9239–9249, Jul. 2009, doi: 10.1021/ja8086278.

[92] V. L. Chevrier and J. R. Dahn, "First Principles Model of Amorphous Silicon Lithiation," *J. Electrochem. Soc.*, vol. 156, no. 6, p. A454, 2009, doi: 10.1149/1.3111037.

[93] M. K. Y. Chan, C. Wolverton, and J. P. Greeley, "First Principles Simulations of the Electrochemical Lithiation and Delithiation of Faceted Crystalline Silicon," *J. Am. Chem. Soc.*, vol. 134, no. 35, pp. 14362–14374, Sep. 2012, doi: 10.1021/ja301766z.

[94] M. Gu *et al.*, "Electronic Origin for the Phase Transition from Amorphous Li x Si to Crystalline Li 15 Si 4," *ACS Nano*, vol. 7, no. 7, pp. 6303–6309, Jul. 2013, doi: 10.1021/nn402349j.

[95] M. N. Obrovac and L. J. Krause, "Reversible Cycling of Crystalline Silicon Powder," *J. Electrochem. Soc.*, vol. 154, no. 2, p. A103, 2007, doi: 10.1149/1.2402112.

[96] M. N. Obrovac, L. Christensen, D. B. Le, and J. R. Dahn, "Alloy Design for Lithium-Ion Battery Anodes," *J. Electrochem. Soc.*, vol. 154, no. 9, p. A849, 2007, doi: 10.1149/1.2752985.

[97] V. L. Chevrier and J. R. Dahn, "First Principles Studies of Disordered Lithiated Silicon," *J. Electrochem. Soc.*, vol. 157, no. 4, p. A392, 2010, doi: 10.1149/1.3294772.

[98] J. Li, A. Smith, R. J. Sanderson, T. D. Hatchard, R. A. Dunlap, and J. R. Dahn, "In Situ [sup 119]Sn Mössbauer Effect Study of the Reaction of Lithium with Si Using a Sn Probe," *J. Electrochem. Soc.*, vol. 156, no. 4, p. A283, 2009, doi: 10.1149/1.3073879.

[99] J. W. Wang *et al.*, “Two-Phase Electrochemical Lithiation in Amorphous Silicon,” *Nano Lett.*, vol. 13, no. 2, pp. 709–715, Feb. 2013, doi: 10.1021/nl304379k.

[100] M. T. McDowell *et al.*, “In Situ TEM of Two-Phase Lithiation of Amorphous Silicon Nanospheres,” *Nano Lett.*, vol. 13, no. 2, pp. 758–764, Feb. 2013, doi: 10.1021/nl3044508.

[101] V. Baranchugov, E. Markevich, E. Pollak, G. Salitra, and D. Aurbach, “Amorphous silicon thin films as a high capacity anodes for Li-ion batteries in ionic liquid electrolytes,” *Electrochem. commun.*, vol. 9, no. 4, pp. 796–800, Apr. 2007, doi: 10.1016/j.elecom.2006.11.014.

[102] P. Meister, H. Jia, J. Li, R. Kloepsch, M. Winter, and T. Placke, “Best Practice: Performance and Cost Evaluation of Lithium Ion Battery Active Materials with Special Emphasis on Energy Efficiency,” *Chem. Mater.*, vol. 28, no. 20, pp. 7203–7217, Oct. 2016, doi: 10.1021/acs.chemmater.6b02895.

[103] A. Mukanova, A. Jetybayeva, S.-T. Myung, S.-S. Kim, and Z. Bakenov, “A mini-review on the development of Si-based thin film anodes for Li-ion batteries,” *Mater. Today Energy*, vol. 9, pp. 49–66, Sep. 2018, doi: 10.1016/j.mtener.2018.05.004.

[104] X. Zuo, J. Zhu, P. Müller-Buschbaum, and Y.-J. Cheng, “Silicon based lithium-ion battery anodes: A chronicle perspective review,” *Nano Energy*, vol. 31, no. November 2016, pp. 113–143, Jan. 2017, doi: 10.1016/j.nanoen.2016.11.013.

[105] K. Rhodes, N. Dudney, E. Lara-Curzio, and C. Daniel, “Understanding the Degradation of Silicon Electrodes for Lithium-Ion Batteries Using Acoustic Emission,” *J. Electrochem. Soc.*, vol. 157, no. 12, p. A1354, 2010, doi: 10.1149/1.3489374.

[106] A. Tranchot, A. Etiemble, P. X. Thivel, H. Idrissi, and L. Roué, “In-situ acoustic emission study of Si-based electrodes for Li-ion batteries,” *J. Power Sources*, vol. 279, pp. 259–266, 2015, doi: 10.1016/j.jpowsour.2014.12.126.

[107] J. Christensen and J. Newman, “Stress generation and fracture in lithium insertion materials,” *J. Solid State Electrochem.*, vol. 10, no. 5, pp. 293–319, May 2006, doi: 10.1007/s10008-006-0095-1.

[108] M. J. Chon, V. A. Sethuraman, A. McCormick, V. Srinivasan, and P. R. Guduru, “Real-time measurement of stress and damage evolution during initial lithiation of crystalline silicon,” *Phys. Rev. Lett.*, vol. 107, no. 4, pp. 1–4, 2011, doi: 10.1103/PhysRevLett.107.045503.

[109] X. H. Liu, L. Zhong, S. Huang, S. X. Mao, T. Zhu, and J. Y. Huang, “Size-Dependent Fracture of Silicon,” *ACS Nano*, vol. 6, no. 2, pp. 1522–1531, 2012.

[110] K. Zhao *et al.*, “Concurrent Reaction and Plasticity during Initial Lithiation of Crystalline Silicon in Lithium-Ion Batteries,” *J. Electrochem. Soc.*, vol. 159, no. 3, pp. A238–A243, Jan. 2012, doi: 10.1149/2.020203jes.

[111] R. Deshpande, Y.-T. Cheng, M. W. Verbrugge, and A. Timmons, “Diffusion Induced Stresses and Strain Energy in a Phase-Transforming Spherical Electrode Particle,” *J. Electrochem. Soc.*, vol. 158, no. 6, p. A718, 2011, doi: 10.1149/1.3565183.

[112] M. Salah, P. Murphy, C. Hall, C. Francis, R. Kerr, and M. Fabretto, “Pure silicon thin-film anodes for lithium-ion batteries: A review,” *J. Power Sources*, vol. 414, no. November 2018, pp. 48–67, Feb. 2019, doi: 10.1016/j.jpowsour.2018.12.068.

[113] H.-C. Shin, J. A. Corno, J. L. Gole, and M. Liu, “Porous silicon negative electrodes for rechargeable lithium batteries,” *J. Power Sources*, vol. 139, no. 1–2, pp. 314–320, Jan. 2005, doi: 10.1016/j.jpowsour.2004.06.073.

[114] A. Casimir, H. Zhang, O. Ogoke, J. C. Amine, J. Lu, and G. Wu, “Silicon-based anodes for lithium-ion batteries: Effectiveness of materials synthesis and electrode preparation,” *Nano Energy*, vol. 27, pp. 359–376, Sep. 2016, doi: 10.1016/j.nanoen.2016.07.023.

[115] J. P. Maranchi, A. F. Hepp, and P. N. Kumta, “High Capacity, Reversible Silicon Thin-Film Anodes for Lithium-Ion Batteries,” *Electrochem. Solid-State Lett.*, vol. 6, no. 9, p. A198, 2003, doi: 10.1149/1.1596918.

[116] S. Bourderau, T. Brousse, and D. M. Schleich, “Amorphous silicon as a possible anode material for Li-ion batteries,” *J. Power Sources*, vol. 81–82, pp. 233–236, 1999, doi: 10.1016/S0378-7753(99)00194-9.

[117] J. Graetz, C. C. Ahn, R. Yazami, and B. Fultz, “Highly Reversible Lithium Storage in Nanostructured Silicon,” *Electrochem. Solid-State Lett.*, vol. 6, no. 9, p. A194, 2003, doi: 10.1149/1.1596917.

[118] J. R. Szczech and S. Jin, “Nanostructured silicon for high capacity lithium battery anodes,” *Energy Environ. Sci.*, vol. 4, no. 1, pp. 56–72, 2011, doi: 10.1039/C0EE00281J.

[119] X. Su *et al.*, “Silicon-Based Nanomaterials for Lithium-Ion Batteries: A Review,” *Adv. Energy Mater.*, vol. 4, no. 1, p. 1300882, Jan. 2014, doi: 10.1002/aenm.201300882.

[120] M. Salah *et al.*, “Doped and reactive silicon thin film anodes for lithium ion batteries: A review,” *J. Power Sources*, vol. 506, no. June, p. 230194, Sep. 2021, doi: 10.1016/j.jpowsour.2021.230194.

[121] T. Takamura, S. Ohara, M. Uehara, J. Suzuki, and K. Sekine, “A vacuum deposited Si film having a Li extraction capacity over 2000 mAh/g with a long cycle life,” *J. Power Sources*, vol. 129, no. 1, pp. 96–100, Apr. 2004, doi: 10.1016/j.jpowsour.2003.11.014.

[122] S. Ohara, J. Suzuki, K. Sekine, and T. Takamura, “A thin film silicon anode for Li-ion batteries having a very large specific capacity and long cycle life,” *J. Power Sources*, vol. 136, no. 2, pp. 303–306, Oct. 2004, doi: 10.1016/j.jpowsour.2004.03.014.

[123] S. Ohara, J. Suzuki, K. Sekine, and T. Takamura, “Li insertion/extraction reaction at a Si film evaporated on a Ni foil,” *J. Power Sources*, vol. 119–121, pp. 591–596, Jun. 2003, doi: 10.1016/S0378-7753(03)00301-X.

[124] J. Li, A. K. Dozier, Y. Li, F. Yang, and Y.-T. Cheng, “Crack Pattern Formation in Thin Film Lithium-Ion Battery Electrodes,” *J. Electrochem. Soc.*, vol. 158, no. 6, p. A689, 2011, doi: 10.1149/1.3574027.

[125] T. Takamura, M. Uehara, J. Suzuki, K. Sekine, and K. Tamura, “High capacity and long cycle life silicon anode for Li-ion battery,” *J. Power Sources*, vol. 158, no. 2, pp. 1401–1404, Aug. 2006, doi: 10.1016/j.jpowsour.2005.10.081.

[126] M. Wang and Z. Geng, “Facile synthesis of multilayer-like Si thin film as high-performance anode materials for lithium-ion batteries,” *Appl. Phys. A*, vol. 122, no. 5, p. 528, May 2016, doi: 10.1007/s00339-016-0068-x.

[127] M. T. Demirkan, L. Trahey, and T. Karabacak, “Cycling performance of density modulated multilayer silicon thin film anodes in Li-ion batteries,” *J. Power Sources*, vol. 273, pp. 52–61, Jan. 2015, doi: 10.1016/j.jpowsour.2014.09.027.

[128] G. Zhao, Y. Meng, N. Zhang, and K. Sun, “Electrodeposited Si film with excellent stability and high rate performance for lithium-ion battery anodes,” *Mater. Lett.*, vol. 76, pp. 55–58, Jun. 2012, doi: 10.1016/j.matlet.2012.02.064.

[129] F. Dogan, L. D. Sanjeewa, S.-J. Hwu, and J. T. Vaughey, “Electrodeposited copper foams as substrates for thin film silicon electrodes,” *Solid State Ionics*, vol. 288, pp. 204–206, May 2016, doi: 10.1016/j.ssi.2016.02.001.

[130] R. Lin, S. Zhang, Z. Du, H. Fang, Y. Ren, and X. Wu, “Copper nanowires based current collector for light-weight and flexible composite silicon anode with high stability and specific capacity,” *RSC Adv.*, vol. 5, no. 106, pp. 87090–87097, 2015, doi: 10.1039/C5RA13568K.

[131] X. H. Huang, J. B. Wu, Y. Q. Cao, P. Zhang, Y. Lin, and R. Q. Guo, “Cobalt nanosheet arrays supported silicon film as anode materials for lithium ion batteries,” *Electrochim. Acta*, vol. 203, pp. 213–220, Jun. 2016, doi: 10.1016/j.electacta.2016.04.041.

[132] M. K. Datta *et al.*, “Amorphous silicon–carbon based nano-scale thin film anode materials for lithium ion batteries,” *Electrochim. Acta*, vol. 56, no. 13, pp. 4717–4723, May 2011, doi: 10.1016/j.electacta.2011.01.124.

[133] A. Ulvestad, H. F. Andersen, J. P. Mæhlen, Ø. Prytz, and M. Kirkengen, “Long-term Cyclability of Substoichiometric Silicon Nitride Thin Film Anodes for Li-ion Batteries,” *Sci. Rep.*, vol. 7, no. 1, p. 13315, Dec. 2017, doi: 10.1038/s41598-017-13699-0.

[134] S.-W. Song and S.-W. Baek, “Silane-Derived SEI Stabilization on Thin-Film Electrodes of Nanocrystalline Si for Lithium Batteries,” *Electrochem. Solid-State Lett.*, vol. 12, no. 2, p. A23, 2009, doi: 10.1149/1.3028216.

[135] R. Epur, M. Ramanathan, F. R. Beck, A. Manivannan, and P. N. Kumta, “Electrodeposition of amorphous silicon anode for lithium ion batteries,” *Mater. Sci. Eng. B*, vol. 177, no. 14, pp. 1157–1162, Aug. 2012, doi: 10.1016/j.mseb.2012.04.027.

[136] B. Gattu *et al.*, “Pulsed Current Electrodeposition of Silicon Thin Films Anodes for Lithium Ion Battery Applications,” *Inorganics*, vol. 5, no. 2, p. 27, Apr. 2017, doi: 10.3390/inorganics5020027.

[137] J. Shin, T. H. Kim, Y. Lee, and E. A. Cho, “Key functional groups defining the formation of Si anode solid-electrolyte interphase towards high energy density Li-ion batteries,” *Energy Storage Mater.*, vol. 25, no. July, pp. 764–781, 2020, doi: 10.1016/j.ensm.2019.09.009.

[138] G. G. Eshetu and E. Figgemeier, “Confronting the Challenges of Next-Generation Silicon Anode-Based Lithium-Ion Batteries: Role of Designer Electrolyte Additives and Polymeric Binders,” *ChemSusChem*, vol. 12, no. 12, pp. 2515–2539, Jun. 2019, doi: 10.1002/cssc.201900209.

[139] B. Philippe *et al.*, “Nanosilicon Electrodes for Lithium-Ion Batteries: Interfacial Mechanisms Studied by Hard and Soft X-ray Photoelectron Spectroscopy,” *Chem. Mater.*, vol. 24, no. 6, pp. 1107–1115, Mar. 2012, doi: 10.1021/cm2034195.

[140] B. Philippe, R. Dedryvère, M. Gorgoi, H. Rensmo, D. Gonbeau, and K. Edström, “Role of the LiPF 6 Salt for the Long-Term Stability of Silicon Electrodes in Li-Ion Batteries – A Photoelectron Spectroscopy Study,” *Chem. Mater.*, vol. 25, no. 3, pp. 394–404, Feb. 2013, doi: 10.1021/cm303399v.

[141] C. K. Chan, R. Ruffo, S. S. Hong, and Y. Cui, “Surface chemistry and morphology of the solid electrolyte interphase on silicon nanowire lithium-ion battery anodes,” *J. Power Sources*, vol. 189, no. 2, pp. 1132–1140, Apr. 2009, doi: 10.1016/j.jpowsour.2009.01.007.

[142] E. Radvanyi, E. De Vito, W. Porcher, and S. Jouanneau Si Larbi, “An XPS/AES comparative study of the surface behaviour of nano-silicon anodes for Li-ion batteries,” *J. Anal. At. Spectrom.*, vol. 29, no. 6, pp. 1120–1131, 2014, doi: 10.1039/C3JA50362C.

[143] Y.-C. Yen, S.-C. Chao, H.-C. Wu, and N.-L. Wu, “Study on Solid-Electrolyte-Interphase of Si and C-Coated Si Electrodes in Lithium Cells,” *J. Electrochem. Soc.*, vol. 156, no. 2, p. A95, 2009, doi: 10.1149/1.3032230.

[144] U. S. Vogl *et al.*, “The Mechanism of SEI Formation on a Single Crystal Si(100) Electrode,” *J. Electrochem. Soc.*, vol. 162, no. 4, pp. A603–A607, Jan. 2015, doi: 10.1149/2.0391504jes.

[145] C. C. Nguyen and B. L. Lucht, “Comparative Study of Fluoroethylene Carbonate and Vinylene Carbonate for Silicon Anodes in Lithium Ion Batteries,” *J. Electrochem. Soc.*, vol. 161, no. 12, pp. A1933–A1938, Sep. 2014, doi: 10.1149/2.0731412jes.

[146] V. Etacheri *et al.*, “Effect of Fluoroethylene Carbonate (FEC) on the Performance and Surface Chemistry of Si-Nanowire Li-Ion Battery Anodes,” *Langmuir*, vol. 28, no. 1, pp. 965–976, Jan. 2012, doi: 10.1021/la203712s.

[147] K. Schroder *et al.*, “The Effect of Fluoroethylene Carbonate as an Additive on the Solid Electrolyte Interphase on Silicon Lithium-Ion Electrodes,” *Chem. Mater.*, vol. 27, no. 16, pp. 5531–5542, Aug. 2015, doi: 10.1021/acs.chemmater.5b01627.

[148] K. W. Schroder, A. G. Dylla, S. J. Harris, L. J. Webb, and K. J. Stevenson, “Role of surface oxides in the formation of solid-electrolyte interphases at silicon electrodes for lithium-ion batteries,” *ACS Appl. Mater. Interfaces*, vol. 6, no. 23, pp. 21510–21524, 2014, doi: 10.1021/am506517j.

[149] I. Hasa *et al.*, “Electrochemical Reactivity and Passivation of Silicon Thin-Film Electrodes in Organic Carbonate Electrolytes,” *ACS Appl. Mater. Interfaces*, vol. 12, no. 36, pp. 40879–40890, Sep. 2020, doi: 10.1021/acsami.0c09384.

[150] J. Yang, N. Solomatin, A. Kraytsberg, and Y. Ein-Eli, “In-Situ Spectro-electrochemical Insight Revealing Distinctive Silicon Anode Solid Electrolyte Interphase Formation in a Lithium-ion Battery,” *ChemistrySelect*, vol. 1, no. 3, pp. 572–576, Mar. 2016, doi: 10.1002/slct.201600119.

[151] F. Shi, P. N. Ross, G. A. Somorjai, and K. Komvopoulos, “The Chemistry of Electrolyte Reduction on Silicon Electrodes Revealed by in Situ ATR-FTIR Spectroscopy,” *J. Phys. Chem. C*, vol. 121, no. 27, pp. 14476–14483, 2017, doi: 10.1021/acs.jpcc.7b04132.

[152] C. Cao *et al.*, “Solid Electrolyte Interphase on Native Oxide-Terminated Silicon Anodes for Li-Ion Batteries,” *Joule*, vol. 3, no. 3, pp. 762–781, 2019, doi: 10.1016/j.joule.2018.12.013.

[153] C. Cao, H. Steinrück, B. Shyam, and M. F. Toney, “The Atomic Scale Electrochemical Lithiation and Delithiation Process of Silicon,” *Adv. Mater. Interfaces*, vol. 4, no. 22, p. 1700771, Nov. 2017, doi: 10.1002/admi.201700771.

[154] G. M. Veith, M. Doucet, R. L. Sacci, B. Vacaliuc, J. K. Baldwin, and J. F. Browning, “Determination of the Solid Electrolyte Interphase Structure Grown on a Silicon Electrode Using a Fluoroethylene Carbonate Additive,” *Sci. Rep.*, vol. 7, no. 1, p. 6326, Dec. 2017, doi: 10.1038/s41598-017-06555-8.

[155] G. M. Veith *et al.*, “Direct Determination of Solid-Electrolyte Interphase Thickness and Composition as a Function of State of Charge on a Silicon Anode,” *J. Phys. Chem. C*, vol. 119, no. 35, pp. 20339–20349, Sep. 2015, doi: 10.1021/acs.jpcc.5b06817.

[156] G. M. Veith, L. Baggetto, R. L. Sacci, R. R. Unocic, W. E. Tenhaeff, and J. F. Browning, “Direct measurement of the chemical reactivity of silicon electrodes with LiPF6-based battery electrolytes,” *Chem. Commun.*, vol. 50, no. 23, p. 3081, 2014, doi: 10.1039/c3cc49269a.

[157] A. L. Michan, M. Leskes, and C. P. Grey, “Voltage Dependent Solid Electrolyte Interphase Formation in Silicon Electrodes: Monitoring the Formation of Organic Decomposition Products,” *Chem. Mater.*, vol. 28, no. 1, pp. 385–398, 2016, doi: 10.1021/acs.chemmater.5b04408.

[158] Y. Jin *et al.*, “Identifying the Structural Basis for the Increased Stability of the Solid Electrolyte Interphase Formed on Silicon with the Additive Fluoroethylene Carbonate,” *J. Am. Chem. Soc.*, vol. 139, no. 42, pp. 14992–15004, Oct. 2017, doi: 10.1021/jacs.7b06834.

[159] J. Kim, O. B. Chae, and B. L. Lucht, “Perspective—Structure and Stability of the Solid Electrolyte Interphase on Silicon Anodes of Lithium-ion Batteries,” *J. Electrochem. Soc.*, vol. 168, no. 3, p. 030521, Mar. 2021, doi: 10.1149/1945-7111/abe984.

[160] K. Leung, F. Soto, K. Hankins, P. B. Balbuena, and K. L. Harrison, “Stability of Solid Electrolyte Interphase Components on Lithium Metal and Reactive Anode Material Surfaces,” *J. Phys. Chem. C*, vol. 120, no. 12, pp. 6302–6313, Mar. 2016, doi: 10.1021/acs.jpcc.5b11719.

[161] H. Wu *et al.*, “Stable cycling of double-walled silicon nanotube battery anodes through solid-electrolyte interphase control,” *Nat. Nanotechnol.*, vol. 7, no. 5, pp. 310–315, 2012, doi: 10.1038/nnano.2012.35.

[162] F. Ozanam and M. Rosso, “Silicon as anode material for Li-ion batteries,” *Mater. Sci. Eng. B*, vol. 213, pp. 2–11, Nov. 2016, doi: 10.1016/j.mseb.2016.04.016.

[163] Z. Zhuo *et al.*, “Breathing and oscillating growth of solid-electrolyte-interphase upon electrochemical cycling,” *Chem. Commun.*, vol. 54, no. 7, pp. 814–817, 2018, doi: 10.1039/C7CC07082A.

[164] W. Huang *et al.*, “Dynamic Structure and Chemistry of the Silicon Solid-Electrolyte Interphase Visualized by Cryogenic Electron Microscopy,” *Matter*, vol. 1, no. 5, pp. 1232–1245, Nov. 2019, doi: 10.1016/j.matt.2019.09.020.

[165] Y. He *et al.*, “Progressive growth of the solid–electrolyte interphase towards the Si anode interior causes capacity fading,” *Nat. Nanotechnol.*, Jul. 2021, doi: 10.1038/s41565-021-00947-8.

[166] S. Zhang, M. He, C. C. Su, and Z. Zhang, “Advanced electrolyte/additive for lithium-ion batteries with silicon anode,” *Curr. Opin. Chem. Eng.*, vol. 13, pp. 24–35, 2016, doi: 10.1016/j.coche.2016.08.003.

[167] M. Sina *et al.*, “Direct Visualization of the Solid Electrolyte Interphase and Its Effects on Silicon Electrochemical Performance,” *Adv. Mater. Interfaces*, vol. 3, no. 20, p. 1600438, Oct. 2016, doi: 10.1002/admi.201600438.

[168] J. Tan, J. Matz, P. Dong, J. Shen, and M. Ye, “A Growing Appreciation for the Role of LiF in the Solid Electrolyte Interphase,” *Adv. Energy Mater.*, vol. 11, no. 16, p. 2100046, Apr. 2021, doi: 10.1002/aenm.202100046.

[169] N.-S. Choi, K. H. Yew, K. Y. Lee, M. Sung, H. Kim, and S.-S. Kim, “Effect of fluoroethylene carbonate additive on interfacial properties of silicon thin-film electrode,” *J. Power Sources*, vol. 161, no. 2, pp. 1254–1259, Oct. 2006, doi: 10.1016/j.jpowsour.2006.05.049.

[170] S. Dalavi, P. Guduru, and B. L. Lucht, “Performance Enhancing Electrolyte Additives for Lithium Ion Batteries with Silicon Anodes,” *J. Electrochem. Soc.*, vol. 159, no. 5, pp. A642–A646, Jan. 2012, doi: 10.1149/2.076205jes.

[171] H. Nakai, T. Kubota, A. Kita, and A. Kawashima, “Investigation of the Solid Electrolyte Interphase Formed by Fluoroethylene Carbonate on Si Electrodes,” *J. Electrochem. Soc.*, vol. 158, no. 7, p. A798, 2011, doi: 10.1149/1.3589300.

[172] B. T. Young, D. R. Heskett, C. C. Nguyen, M. Nie, J. C. Woicik, and B. L. Lucht, “Hard X-ray Photoelectron Spectroscopy (HAXPES) Investigation of the Silicon Solid Electrolyte Interphase (SEI) in Lithium-Ion Batteries,” *ACS Appl. Mater. Interfaces*, vol. 7, no. 36, pp. 20004–20011, Sep. 2015, doi: 10.1021/acsami.5b04845.

[173] C. C. Nguyen and S.-W. Song, “Interfacial structural stabilization on amorphous silicon anode for improved cycling performance in lithium-ion batteries,” *Electrochim. Acta*, vol. 55, no. 8, pp.

3026–3033, Mar. 2010, doi: 10.1016/j.electacta.2009.12.067.

[174] Y.-G. Ryu *et al.*, “Electrochemical Behaviors of Silicon Electrode in Lithium Salt Solution Containing Alkoxy Silane Additives,” *J. Electrochem. Soc.*, vol. 155, no. 8, p. A583, 2008, doi: 10.1149/1.2940310.

[175] F. Aupperle *et al.*, “The Role of Electrolyte Additives on the Interfacial Chemistry and Thermal Reactivity of Si-Anode-Based Li-Ion Battery,” *ACS Appl. Energy Mater.*, vol. 2, no. 9, pp. 6513–6527, Sep. 2019, doi: 10.1021/acsaem.9b01094.

[176] S. S. Zhang, “Aromatic isocyanate as a new type of electrolyte additive for the improved performance of Li-ion batteries,” *J. Power Sources*, vol. 163, no. 1 SPEC. ISS., pp. 567–572, 2006, doi: 10.1016/j.jpowsour.2006.09.046.

[177] G. Bunker, *Introduction to XAFS*. Cambridge: Cambridge University Press, 2010.

[178] J. Stöhr, *NEXAFS Spectroscopy*, vol. 25, no. 9. Berlin, Heidelberg: Springer Berlin Heidelberg, 1992.

[179] A. Nefedov and C. Wöll, “Advanced Applications of NEXAFS Spectroscopy for Functionalized Surfaces,” in *Springer Series in Surface Sciences*, vol. 51, no. 1, 2013, pp. 277–303.

[180] S. G. Urquhart and H. Ade, “Trends in the Carbonyl Core (C 1S, O 1S) → π* C=O Transition in the Near-Edge X-ray Absorption Fine Structure Spectra of Organic Molecules,” *J. Phys. Chem. B*, vol. 106, no. 34, pp. 8531–8538, Aug. 2002, doi: 10.1021/jp0255379.

[181] D. Attwood, *Soft X-Rays and Extreme Ultraviolet Radiation*, vol. 7, no. 6. Cambridge University Press, 1999.

[182] B. L. Henke, E. M. Gullikson, and J. C. Davis, “X-Ray Interactions: Photoabsorption, Scattering, Transmission, and Reflection at E = 50-30,000 eV, Z = 1-92,” *At. Data Nucl. Data Tables*, vol. 54, no. 2, pp. 181–342, Jul. 1993, doi: 10.1006/adnd.1993.1013.

[183] J. W. Smith and R. J. Saykally, “Soft X-ray Absorption Spectroscopy of Liquids and Solutions,” *Chem. Rev.*, vol. 117, no. 23, pp. 13909–13934, Dec. 2017, doi: 10.1021/acs.chemrev.7b00213.

[184] M. O. Krause, “Atomic radiative and radiationless yields for K and L shells,” *J. Phys. Chem. Ref. Data*, vol. 8, no. 2, pp. 307–327, Apr. 1979, doi: 10.1063/1.555594.

[185] F. M. F. de Groot, M. A. Arrio, P. Sainctavit, C. Cartier, and C. T. Chen, “Fluorescence yield detection: Why it does not measure the X-ray absorption cross section,” *Solid State Commun.*, vol. 92, no. 12, pp. 991–995, Dec. 1994, doi: 10.1016/0038-1098(94)90027-2.

[186] F. Frati, M. O. J. Y. Hunault, and F. M. F. de Groot, “Oxygen K-edge X-ray Absorption Spectra,” *Chem. Rev.*, vol. 120, no. 9, pp. 4056–4110, May 2020, doi: 10.1021/acs.chemrev.9b00439.

[187] J. Jaklevic, J. A. Kirby, M. P. Klein, A. S. Robertson, G. S. Brown, and P. Eisenberger, “Fluorescence detection of exafs: Sensitivity enhancement for dilute species and thin films,” *Solid State Commun.*, vol. 23, no. 9, pp. 679–682, 1977, doi: 10.1016/0038-1098(77)90548-8.

[188] D. Schön *et al.*, “Introducing Ionic-Current Detection for X-ray Absorption Spectroscopy in Liquid Cells,” *J. Phys. Chem. Lett.*, vol. 8, no. 9, pp. 2087–2092, May 2017, doi: 10.1021/acs.jpclett.7b00646.

[189] L. G. Parratt, C. F. Hempstead, and E. L. Jossem, “‘Thickness Effect’ in Absorption Spectra near Absorption Edges,” *Phys. Rev.*, vol. 105, no. 4, pp. 1228–1232, Feb. 1957, doi: 10.1103/PhysRev.105.1228.

[190] G. S. Henderson, F. M. F. De Groot, and B. J. A. Moulton, “X-ray absorption near-edge structure (XANES) spectroscopy,” *Rev. Mineral. Geochemistry*, vol. 78, no. February, pp. 75–138, 2014, doi: 10.2138/rmg.2014.78.3.

[191] S. L. M. Schreoeder, G. D. Moggridge, E. Chabala, R. M. Ormerod, T. Rayment, and R. M. Lambert, “Possibilities and limitations of a new experimental technique,” *Faraday Discuss.*, vol. 105, no. 0, pp. 317–336, 1996.

[192] D. M. Pease, “Thickness Effect in X-Ray Absorption Edges of Metals and Alloys.,” *Appl. Spectrosc.*, vol. 30, no. 4, pp. 405–410, 1976, doi: 10.1366/000370276774457056.

[193] E. A. Stern and K. Kim, “Thickness effect on the extended-x-ray-absorption-fine-structure amplitude,” *Phys. Rev. B*, vol. 23, no. 8, pp. 3781–3787, 1981, doi: 10.1103/PhysRevB.23.3781.

[194] T. Kachel, “The plane grating monochromator beamline U49-2 PGM-1 at BESSY II,” *J. large-scale Res. Facil. JLSRF*, vol. 2, pp. 2–5, 2016, doi: 10.17815/jlsrf-2-75.

[195] J. Schwinger, “On the Classical Radiation of Accelerated Electrons,” *Phys. Rev.*, vol. 75, no. 12,

pp. 1912–1925, Jun. 1949, doi: 10.1103/PhysRev.75.1912.

[196] Helmholtz-Zentrum Berlin, “U49-2.” https://www.helmholtz-berlin.de/pubbin/igama_output?modus=einzel&gid=1834&typoid=75136 (accessed Feb. 01, 2022).

[197] Helmholtz-Zentrum Berlin, “U49-2_PGM-1.” https://www.helmholtz-berlin.de/pubbin/igama_output?modus=einzel&gid=1655&typoid=75136 (accessed Feb. 01, 2022).

[198] Helmholtz-Zentrum Berlin, “UE56-2.” https://helmholtz-berlin.de/pubbin/igama_output?modus=einzel&gid=1838&typoid=50734 (accessed Feb. 01, 2022).

[199] Helmholtz-Zentrum Berlin, “UE56-2_PGM-2.” https://www.helmholtz-berlin.de/pubbin/igama_output?modus=einzel&gid=1633&typoid= (accessed Feb. 01, 2022).

[200] M. Fondell *et al.*, “Time-resolved soft X-ray absorption spectroscopy in transmission mode on liquids at MHz repetition rates,” *Struct. Dyn.*, vol. 4, no. 5, 2017, doi: 10.1063/1.4993755.

[201] M. Ekimova, W. Quevedo, M. Faube, P. Wernet, and E. T. J. Nibbering, “A liquid flatjet system for solution phase soft-x-ray spectroscopy,” *Struct. Dyn.*, vol. 2, no. 5, 2015, doi: 10.1063/1.4928715.

[202] J. W. Smith and R. J. Saykally, “Soft X-ray Absorption Spectroscopy of Liquids and Solutions,” *Chem. Rev.*, vol. 117, no. 23, pp. 13909–13934, 2017, doi: 10.1021/acs.chemrev.7b00213.

[203] J. R. Dwyer and M. Harb, “Through a Window, Brightly: A Review of Selected Nanofabricated Thin-Film Platforms for Spectroscopy, Imaging, and Detection,” *Appl. Spectrosc.*, vol. 71, no. 9, pp. 2051–2075, Sep. 2017, doi: 10.1177/0003702817715496.

[204] M. Nagasaka, T. Hatsui, T. Horigome, Y. Hamamura, and N. Kosugi, “Development of a liquid flow cell to measure soft X-ray absorption in transmission mode: A test for liquid water,” *J. Electron Spectros. Relat. Phenomena*, vol. 177, no. 2–3, pp. 130–134, 2010, doi: 10.1016/j.elspec.2009.11.001.

[205] Norcada Inc., “Image SiNx window.” https://www.norcada.com/wp-content/uploads/2012/05/TEM_small.jpg.

[206] S. Schreck, G. Gavrila, C. Weniger, and P. Wernet, “A sample holder for soft x-ray absorption spectroscopy of liquids in transmission mode,” *Rev. Sci. Instrum.*, vol. 82, no. 10, p. 103101, Oct. 2011, doi: 10.1063/1.3644192.

[207] C. Schwanke, L. Xi, and K. M. Lange, “A soft XAS transmission cell for operando studies,” *J. Synchrotron Radiat.*, vol. 23, no. 6, pp. 1390–1394, Nov. 2016, doi: 10.1107/S1600577516014697.

[208] G. Zhu, Y. Jiang, W. Huang, H. Zhang, F. Lin, and C. Jin, “Atomic resolution liquid-cell transmission electron microscopy investigations of the dynamics of nanoparticles in ultrathin liquids,” *Chem. Commun.*, vol. 49, no. 93, p. 10944, 2013, doi: 10.1039/c3cc46667a.

[209] J. M. Grogan, N. M. Schneider, F. M. Ross, and H. H. Bau, “Bubble and Pattern Formation in Liquid Induced by an Electron Beam,” *Nano Lett.*, vol. 14, no. 1, pp. 359–364, Jan. 2014, doi: 10.1021/nl404169a.

[210] J. M. Grogan, N. M. Schneider, F. M. Ross, and H. H. Bau, “The nanoaquarium: A new paradigm in electron microscopy,” *J. Indian Inst. Sci.*, vol. 92, no. 2, pp. 295–308, 2012.

[211] J. M. Grogan and H. H. Bau, “The nanoaquarium: A platform for in situ transmission electron microscopy in liquid media,” *J. Microelectromechanical Syst.*, vol. 19, no. 4, pp. 885–894, 2010, doi: 10.1109/JMEMS.2010.2051321.

[212] Y. Wang, X. Chen, H. Cao, C. Deng, X. Cao, and P. Wang, “A structural study of escherichia coli cells using an in situ liquid chamber TEM technology,” *J. Anal. Methods Chem.*, vol. 2015, 2015, doi: 10.1155/2015/829302.

[213] COMSOL AB, “COMSOL Multiphysics®.” Stockholm, Sweden, 2018, [Online]. Available: www.comsol.com.

[214] M. G. Allen, M. Mehregany, R. T. Howe, and S. D. Senturia, “Microfabricated structures for the in situ measurement of residual stress, Young’s modulus, and ultimate strain of thin films,” *Appl. Phys. Lett.*, vol. 51, no. 4, pp. 241–243, 1987, doi: 10.1063/1.98460.

[215] W. H. Chuang, T. Luger, R. K. Fettig, and R. Ghodssi, “Mechanical property characterization of LPCVD silicon nitride thin films at cryogenic temperatures,” *J. Microelectromechanical Syst.*, vol.

13, no. 5, pp. 870–879, 2004, doi: 10.1109/JMEMS.2004.836815.

[216] A. Khan, J. Philip, and P. Hess, “Young’s modulus of silicon nitride used in scanning force microscope cantilevers,” *J. Appl. Phys.*, vol. 95, no. 4, pp. 1667–1672, 2004, doi: 10.1063/1.1638886.

[217] D. Maier-Schneider, J. Maibach, and E. Obermeier, “A new analytical solution for the load-deflection of square membranes,” *J. Microelectromechanical Syst.*, vol. 4, no. 4, pp. 238–241, 1995, doi: 10.1109/84.475551.

[218] M. Kawaji and P. M. Y. Chung, “Adiabatic gas-liquid flow in microchannels,” *Microscale Thermophys. Eng.*, vol. 8, no. 3, pp. 239–257, 2004, doi: 10.1080/10893950490477518.

[219] R. Bird, *Transport phenomena*. New York: J. Wiley, 2002.

[220] R. Jafari and T. Okutucu-Özyurt, “Phase-Field Modeling of Vapor Bubble Growth in a Microchannel,” *J. Comput. Multiph. Flows*, vol. 7, no. 3, pp. 143–158, Sep. 2015, doi: 10.1260/1757-482X.7.3.143.

[221] C. T. Chantler, “Theoretical Form Factor, Attenuation, and Scattering Tabulation for Z =1–92 from E =1–10 eV to E =0.4–1.0 MeV,” *J. Phys. Chem. Ref. Data*, vol. 24, no. 1, pp. 71–643, Jan. 1995, doi: 10.1063/1.555974.

[222] C.T. Chantler *et al.*, “X-Ray Form Factor, Attenuation, and Scattering Tables,” 2019. http://physics.nist.gov/ffast.

[223] W. Eberhardt *et al.*, “Site-Specific Fragmentation of Small Molecules Following Soft-X-Ray Excitation,” *Phys. Rev. Lett.*, vol. 50, no. 14, pp. 1038–1041, Apr. 1983, doi: 10.1103/PhysRevLett.50.1038.

[224] T. Coffey, S. . Urquhart, and H. Ade, “Characterization of the effects of soft X-ray irradiation on polymers,” *J. Electron Spectros. Relat. Phenomena*, vol. 122, no. 1, pp. 65–78, Jan. 2002, doi: 10.1016/S0368-2048(01)00342-5.

[225] H. Wallander and J. Wallentin, “Simulated sample heating from a nanofocused X-ray beam,” *J. Synchrotron Radiat.*, vol. 24, no. 5, pp. 925–933, Sep. 2017, doi: 10.1107/S1600577517008712.

[226] S. Zumdahl, *Chemistry*. Boston, MA: Cengage, 2017.

[227] E. D. Snijder, M. J. M. Riele, G. F. Versteeg, and W. P. M. Van Swaaij, “Diffusion Coefficients of CO, COS,” pp. 37–39, 1996.

[228] V. Pokorný, V. Štejfa, M. Fulem, C. Červinka, and K. Růžička, “Vapor Pressures and Thermophysical Properties of Dimethyl Carbonate, Diethyl Carbonate, and Dipropyl Carbonate,” *J. Chem. Eng. Data*, vol. 62, no. 10, pp. 3206–3215, Oct. 2017, doi: 10.1021/acs.jced.7b00295.

[229] A. Kazakov, C. Muzny, R. Chirico, V. Diky, and M. Frenkel, “Web Thermo Tables – an On-Line Version of the TRC Thermodynamic Tables,” no. 113, 2008.

[230] K. Kroenlein *et al.*, “NIST/TRC Web Thermo Tables (WTT) NIST Standard Reference Subscription Database 2 - Lite Edition Version 2.” NIST/TRC Web Thermo Tables (WTT) - Lite Edition, 2011.

[231] Sigma-Aldrich, “Safety Data Sheet Lithium hexafluorophosphate solution,” 2020. https://www.sigmaaldrich.com/catalog/product/ALDRICH/746711?lang=en&region=GB.

[232] S.-I. Lee, U.-H. Jung, Y.-S. Kim, M.-H. Kim, D.-J. Ahn, and H.-S. Chun, “A study of electrochemical kinetics of lithium ion in organic electrolytes,” *Korean J. Chem. Eng.*, vol. 19, no. 4, pp. 638–644, Jul. 2002, doi: 10.1007/BF02699310.

[233] P. D. Desai, “Thermodynamic Properties of Iron and Silicon,” *J. Phys. Chem. Ref. Data*, vol. 15, no. 3, pp. 967–983, Jul. 1986, doi: 10.1063/1.555761.

[234] C. Y. Ho, R. W. Powell, and P. E. Liley, “Thermal Conductivity of the Elements,” *J. Phys. Chem. Ref. Data*, vol. 1, no. 2, pp. 279–421, Apr. 1972, doi: 10.1063/1.3253100.

[235] C. A. Swenson, “Recommended Values for the Thermal Expansivity of Silicon from 0 to 1000 K,” *J. Phys. Chem. Ref. Data*, vol. 12, no. 2, pp. 179–182, Apr. 1983, doi: 10.1063/1.555681.

[236] M. S. Ding, K. Xu, S. Zhang, and T. R. Jow, “Liquid/Solid Phase Diagrams of Binary Carbonates for Lithium Batteries Part II,” *J. Electrochem. Soc.*, vol. 148, no. 4, p. A299, 2001, doi: 10.1149/1.1353568.

[237] Q. WANG, J. SUN, and C. CHEN, “Thermal stability of LiPF6/EC + DMC + EMC electrolyte for lithium ion batteries,” *Rare Met.*, vol. 25, no. 6, pp. 94–99, Oct. 2006, doi: 10.1016/S1001-0521(07)60052-7.

[238] B. Ravdel, K. . Abraham, R. Gitzendanner, J. DiCarlo, B. Lucht, and C. Campion, “Thermal stability of lithium-ion battery electrolytes,” *J. Power Sources*, vol. 119–121, pp. 805–810, Jun. 2003, doi: 10.1016/S0378-7753(03)00257-X.

[239] H. Yang, G. V. Zhuang, and P. N. Ross, “Thermal stability of LiPF6 salt and Li-ion battery electrolytes containing LiPF6,” *J. Power Sources*, vol. 161, no. 1, pp. 573–579, Oct. 2006, doi: 10.1016/j.jpowsour.2006.03.058.

[240] G. G. Botte, R. E. White, and Z. Zhang, “Thermal stability of LiPF6-EC:EMC electrolyte for lithium ion batteries,” *J. Power Sources*, vol. 97–98, pp. 570–575, 2001, doi: 10.1016/S0378-7753(01)00746-7.

[241] P. S. Epstein and M. S. Plesset, “On the stability of gas bubbles in liquid-gas solutions,” *J. Chem. Phys.*, vol. 18, no. 11, pp. 1505–1509, 1950, doi: 10.1063/1.1747520.

[242] F. F. Abraham and A. C. Zettlemoyer, “Homogeneous Nucleation Theory,” *Phys. Today*, vol. 27, no. 12, pp. 52–53, Dec. 1974, doi: 10.1063/1.3129038.

[243] P. G. Bowers, K. Bar-Eli, and R. M. Noyes, “Unstable supersaturated solutions of gases in liquids and nucleation theory,” *J. Chem. Soc. Faraday Trans.*, vol. 92, no. 16, p. 2843, 1996, doi: 10.1039/ft9969202843.

[244] X. Y. Liu, “Heterogeneous nucleation or homogeneous nucleation?,” *J. Chem. Phys.*, vol. 112, no. 22, pp. 9949–9955, Jun. 2000, doi: 10.1063/1.481644.

[245] M. Anouti, Y. R. Dougassa, C. Tessier, L. El Ouatani, and J. Jacquemin, “Low pressure carbon dioxide solubility in pure electrolyte solvents for lithium-ion batteries as a function of temperature. Measurement and prediction,” *J. Chem. Thermodyn.*, vol. 50, pp. 71–79, 2012, doi: 10.1016/j.jct.2012.01.027.

[246] Y. R. Dougassa, J. Jacquemin, L. El Ouatani, C. Tessier, and M. Anouti, “Viscosity and carbon dioxide solubility for LiPF6, LiTFSI, and LiFAP in alkyl carbonates: Lithium salt nature and concentration effect,” *J. Phys. Chem. B*, vol. 118, no. 14, pp. 3973–3980, 2014, doi: 10.1021/jp500063c.

[247] M. S. Shaharun, H. Mukhtar, and B. K. Dutta, “Solubility of carbon monoxide and hydrogen in propylene carbonate and thermomorphic multicomponent hydroformylation solvent,” *Chem. Eng. Sci.*, vol. 63, no. 11, pp. 3024–3035, 2008, doi: 10.1016/j.ces.2008.02.035.

[248] S. D. Lubetkin, “Why Is It Much Easier To Nucleate Gas Bubbles than Theory Predicts?,” *Langmuir*, vol. 19, no. 7, pp. 2575–2587, Apr. 2003, doi: 10.1021/la0266381.

[249] C. Sauter, R. Zahn, and V. Wood, “Understanding Electrolyte Infilling of Lithium Ion Batteries,” *J. Electrochem. Soc.*, vol. 167, no. 10, p. 100546, Jan. 2020, doi: 10.1149/1945-7111/ab9bfd.

[250] J. Seo *et al.*, “Electrolyte-resistant epoxy for bonding batteries based on sandwich structures,” *J. Appl. Polym. Sci.*, vol. 135, no. 15, pp. 1–9, 2018, doi: 10.1002/app.46059.

[251] R. Raccichini, M. Amores, and G. Hinds, “Critical review of the use of reference electrodes in li-ion batteries: A diagnostic perspective,” *Batteries*, vol. 5, no. 1, pp. 1–24, 2019, doi: 10.3390/batteries5010012.

[252] P. T. Torma *et al.*, “Performance and Properties of Ultra-Thin Silicon Nitride X-ray Windows,” *IEEE Trans. Nucl. Sci.*, vol. 61, no. 1, pp. 695–699, Feb. 2014, doi: 10.1109/TNS.2014.2298434.

[253] P. T. Torma *et al.*, “Ultra-Thin Silicon Nitride X-Ray Windows,” *IEEE Trans. Nucl. Sci.*, vol. 60, no. 2, pp. 1311–1314, Apr. 2013, doi: 10.1109/TNS.2013.2243754.

[254] A. S. da Silva Sobrinho, M. Latrèche, G. Czeremuszkin, J. E. Klemberg-Sapieha, and M. R. Wertheimer, “Transparent barrier coatings on polyethylene terephthalate by single- and dual-frequency plasma-enhanced chemical vapor deposition,” *J. Vac. Sci. Technol. A Vacuum, Surfaces, Film.*, vol. 16, no. 6, pp. 3190–3198, 1998, doi: 10.1116/1.581519.

[255] C. R. Harris *et al.*, “Array programming with NumPy,” *Nature*, vol. 585, no. 7825, pp. 357–362, 2020, doi: 10.1038/s41586-020-2649-2.

[256] W. McKinney, “Data Structures for Statistical Computing in Python,” 2010, pp. 56–61, doi: 10.25080/Majora-92bf1922-00a.

[257] Riverbank Computing, “PyQt5 Framework.” [Online]. Available: https://www.riverbankcomputing.com/static/Docs/PyQt5/.

[258] Qt Group, “Qt Framework.” [Online]. Available: https://doc.qt.io/.

[259] “PyQtGraph.” [Online]. Available: https://pyqtgraph.readthedocs.io/en/latest/.

[260] “PySerial.” [Online]. Available: https://pyserial.readthedocs.io/en/latest/pyserial.html.

[261] “PyVISA Library.” [Online]. Available: https://pyvisa.readthedocs.io/en/latest/index.html.

[262] The University of Chicago, “PyEpics.” [Online]. Available: https://pyepics.github.io/pyepics/.

[263] H. Xia, S. Tang, and L. Lu, “Properties of amorphous Si thin film anodes prepared by pulsed laser deposition,” *Mater. Res. Bull.*, vol. 42, no. 7, pp. 1301–1309, Jul. 2007, doi: 10.1016/j.materresbull.2006.10.007.

[264] Y. Y. Tang *et al.*, “Cobalt nanomountain array supported silicon film anode for high-performance lithium ion batteries,” *Electrochim. Acta*, vol. 88, pp. 664–670, Jan. 2013, doi: 10.1016/j.electacta.2012.10.119.

[265] A. Reyes Jiménez *et al.*, “A Step toward High-Energy Silicon-Based Thin Film Lithium Ion Batteries,” *ACS Nano*, vol. 11, no. 5, pp. 4731–4744, May 2017, doi: 10.1021/acsnano.7b00922.

[266] T. L. Kulova, A. M. Skundin, Y. V. Pleskov, E. I. Terukov, and O. I. Kon’kov, “Lithium insertion into amorphous silicon thin-film electrodes,” *J. Electroanal. Chem.*, vol. 600, no. 1, pp. 217–225, 2007, doi: 10.1016/j.jelechem.2006.07.002.

[267] T. Ikonen, T. Nissinen, E. Pohjalainen, O. Sorsa, T. Kallio, and V. P. Lehto, “Electrochemically anodized porous silicon: Towards simple and affordable anode material for Li-ion batteries,” *Sci. Rep.*, vol. 7, no. 1, pp. 1–8, 2017, doi: 10.1038/s41598-017-08285-3.

[268] A. Ronneburg *et al.*, “Morphological evolution of a single crystal silicon battery electrode during lithiation and delithiation: An operando phase-contrast imaging study,” *Energy Storage Mater.*, vol. 32, no. July, pp. 377–385, 2020, doi: 10.1016/j.ensm.2020.06.007.

[269] M. Ruttert, V. Siozios, M. Winter, and T. Placke, “Synthesis and Comparative Investigation of Silicon Transition Metal Silicide Composite Anodes for Lithium Ion Batteries,” *Zeitschrift für Anorg. und Allg. Chemie*, vol. 645, no. 3, pp. 248–256, Feb. 2019, doi: 10.1002/zaac.201800436.

[270] J. Wu *et al.*, “Multilayered silicon embedded porous carbon/graphene hybrid film as a high performance anode,” *Carbon N. Y.*, vol. 84, no. 1, pp. 434–443, 2015, doi: 10.1016/j.carbon.2014.12.036.

[271] H. Jia *et al.*, “Facile Synthesis and Lithium Storage Properties of a Porous NiSi 2 /Si/Carbon Composite Anode Material for Lithium-Ion Batteries,” *ACS Appl. Mater. Interfaces*, vol. 7, no. 3, pp. 1508–1515, Jan. 2015, doi: 10.1021/am506486w.

[272] Y. Horowitz, H. L. Han, P. N. Ross, and G. A. Somorjai, “In Situ Potentiodynamic Analysis of the Electrolyte/Silicon Electrodes Interface Reactions - A Sum Frequency Generation Vibrational Spectroscopy Study,” *J. Am. Chem. Soc.*, vol. 138, no. 3, pp. 726–729, 2016, doi: 10.1021/jacs.5b10333.

[273] M. Zhao, H. D. Dewald, F. R. Lemke, and R. J. Staniewicz, “Electrochemical Stability of Graphite-Coated Copper in Lithium-Ion Battery Electrolytes,” *J. Electrochem. Soc.*, vol. 147, no. 11, p. 3983, 2000, doi: 10.1149/1.1394007.

[274] C. Pereira-Nabais *et al.*, “Interphase chemistry of Si electrodes used as anodes in Li-ion batteries,” *Appl. Surf. Sci.*, vol. 266, pp. 5–16, Feb. 2013, doi: 10.1016/j.apsusc.2012.10.165.

[275] L.-F. Cui, R. Ruffo, C. K. Chan, H. Peng, and Y. Cui, “Crystalline-Amorphous Core−Shell Silicon Nanowires for High Capacity and High Current Battery Electrodes,” *Nano Lett.*, vol. 9, no. 1, pp. 491–495, Jan. 2009, doi: 10.1021/nl8036323.

[276] B. Laïk, D. Ung, A. Caillard, C. S. Cojocaru, D. Pribat, and J. P. Pereira-Ramos, “An electrochemical and structural investigation of silicon nanowires as negative electrode for Li-ion batteries,” *J. Solid State Electrochem.*, vol. 14, no. 10, pp. 1835–1839, 2010, doi: 10.1007/s10008-010-1045-5.

[277] E. Pollak, G. Salitra, V. Baranchugov, and D. Aurbach, “In Situ Conductivity, Impedance Spectroscopy, and Ex Situ Raman Spectra of Amorphous Silicon during the Insertion/Extraction of Lithium,” *J. Phys. Chem. C*, vol. 111, no. 30, pp. 11437–11444, Aug. 2007, doi: 10.1021/jp0729563.

[278] V. A. Sethuraman, M. J. Chon, M. Shimshak, V. Srinivasan, and P. R. Guduru, “In situ measurements of stress evolution in silicon thin films during electrochemical lithiation and delithiation,” *J. Power Sources*, vol. 195, no. 15, pp. 5062–5066, Aug. 2010, doi: 10.1016/j.jpowsour.2010.02.013.

[279] V. A. Sethuraman, V. Srinivasan, A. F. Bower, and P. R. Guduru, “In Situ Measurements of

Stress-Potential Coupling in Lithiated Silicon," *J. Electrochem. Soc.*, vol. 157, no. 11, p. A1253, 2010, doi: 10.1149/1.3489378.

[280] R. Seidel, M. N. Pohl, H. Ali, B. Winter, and E. F. Aziz, "Advances in liquid phase soft-x-ray photoemission spectroscopy: A new experimental setup at BESSY II," *Rev. Sci. Instrum.*, vol. 88, no. 7, 2017, doi: 10.1063/1.4990797.

[281] E. F. Aziz, J. Xiao, R. Golnak, and M. Tesch, "LiXEdrom: High Energy Resolution RIXS Station dedicated to Liquid Investigation at BESSY II," *J. large-scale Res. Facil. JLSRF*, vol. 2, pp. 1–4, 2016, doi: 10.17815/jlsrf-2-85.

[282] A. Balzer, M. Witt, E. Suljoti, and E. Schierle, "Status of the Continuous Mode Scan for Undulator Beamlines at BESSY II," *Proc. 15th Int. Conf. Accel. Large Exp. Phys. Control Syst.*, vol. JACOW, 201, pp. 1091–1095, 2015, [Online]. Available: http://icalepcs2015.vrws.de/papers/thha3o02.pdf.

[283] R. Follath, J. S. Schmidt, M. Weigand, and K. Fauth, "The x-ray microscopy beamline UE46-PGM2 at BESSY," *AIP Conf. Proc.*, vol. 1234, no. 1, pp. 323–326, 2010, doi: 10.1063/1.3463201.

[284] Y. Joly, C. Cavallari, S. A. Guda, and C. J. Sahle, "Full-Potential Simulation of X-ray Raman Scattering Spectroscopy," *J. Chem. Theory Comput.*, vol. 13, no. 5, pp. 2172–2177, 2017, doi: 10.1021/acs.jctc.7b00203.

[285] S. Han, "A salient effect of density on the dynamics of nonaqueous electrolytes," *Sci. Rep.*, vol. 7, no. April, pp. 1–9, 2017, doi: 10.1038/srep46718.

[286] K. Kim, P. Zhu, N. Li, X. Ma, and Y. Chen, "Characterization of oxygen containing functional groups on carbon materials with oxygen K-edge X-ray absorption near edge structure spectroscopy," *Carbon N. Y.*, vol. 49, no. 5, pp. 1745–1751, Apr. 2011, doi: 10.1016/j.carbon.2010.12.060.

[287] A. P. Hitchcock and C. E. Brion, "K-shell excitation spectra of CO, N2 and O2," *J. Electron Spectros. Relat. Phenomena*, vol. 18, no. 1, pp. 1–21, 1980, doi: 10.1016/0368-2048(80)80001-6.

[288] Y. Zubavichus *et al.*, "Soft X-ray-induced decomposition of amino acids: An XPS, mass spectrometry, and NEXAFS study," *Radiat. Res.*, vol. 161, no. 3, pp. 346–358, 2004, doi: 10.1667/RR3114.1.

[289] B. X. Yang, J. Kirz, and T. K. Sham, "Oxygen K-edge absorption spectra of O2, CO and CO2," *Phys. Lett. A*, vol. 110, no. 6, pp. 301–304, Aug. 1985, doi: 10.1016/0375-9601(85)90777-7.

[290] B. M. McLaughlin, C. P. Ballance, K. P. Bowen, D. J. Gardenghi, and W. C. Stolte, "HIGH PRECISION K-SHELL PHOTOABSORPTION CROSS SECTIONS FOR ATOMIC OXYGEN: EXPERIMENT AND THEORY," *Astrophys. J.*, vol. 771, no. 1, p. L8, Jun. 2013, doi: 10.1088/2041-8205/771/1/L8.

[291] J. W. Smith *et al.*, "X-Ray absorption spectroscopy of LiBF 4 in propylene carbonate: A model lithium ion battery electrolyte," *Phys. Chem. Chem. Phys.*, vol. 16, no. 43, pp. 23568–23575, 2014, doi: 10.1039/c4cp03240c.

[292] T. Gejo *et al.*, "Angle-resolved photoion spectroscopy of NO2 and SO2," *Chem. Phys.*, vol. 289, no. 1, pp. 15–29, Apr. 2003, doi: 10.1016/S0301-0104(02)00724-3.

[293] S. C. B. Myneni, "Soft X-ray Spectroscopy and Spectromicroscopy Studies of Organic Molecules in the Environment," *Rev. Mineral. Geochemistry*, vol. 49, no. 1, pp. 485–579, Jan. 2002, doi: 10.2138/gsrmg.49.1.485.

[294] A. Knop-Gericke, M. Hävecker, T. Schedel-Niedrig, and R. Schlögl, "High-pressure low-energy XAS: A new tool for probing reacting surfaces of heterogeneous catalysts," *Top. Catal.*, vol. 10, no. 3–4, pp. 187–198, 2000, doi: 10.1023/A:1019101109313.

[295] A. P. Hitchcock and I. Ishii, "Carbon K-shell excitation spectra of linear and branched alkanes," *J. Electron Spectros. Relat. Phenomena*, vol. 42, no. 1, pp. 11–26, 1987, doi: 10.1016/0368-2048(87)85002-8.

[296] D. Ketenoglu *et al.*, "X-ray Raman spectroscopy of lithium-ion battery electrolyte solutions in a flow cell," *J. Synchrotron Radiat.*, vol. 25, no. 2, pp. 537–542, 2018, doi: 10.1107/S1600577518001662.

[297] A. P. Hitchcock and C. E. Brion, "Inner-shell excitation of formaldehyde, acetaldehyde and acetone studied by electron impact," *J. Electron Spectros. Relat. Phenomena*, vol. 19, no. 2, pp.

231–250, 1980, doi: 10.1016/0368-2048(80)87006-X.

[298] E. de Clermont Gallerande *et al.*, “Quantification of non-bridging oxygens in silicates using X-ray Raman scattering,” *J. Non. Cryst. Solids*, vol. 528, pp. 1–27, 2020, doi: 10.1016/j.jnoncrysol.2019.119715.

[299] M. J. Zachman, Z. Tu, S. Choudhury, L. A. Archer, and L. F. Kourkoutis, “Cryo-STEM mapping of solid–liquid interfaces and dendrites in lithium-metal batteries,” *Nature*, vol. 560, no. 7718, pp. 345–349, 2018, doi: 10.1038/s41586-018-0397-3.

[300] R. Qiao, Y.-D. Chuang, S. Yan, and W. Yang, “Soft X-Ray Irradiation Effects of Li2O2, Li2CO3 and Li2O Revealed by Absorption Spectroscopy,” *PLoS One*, vol. 7, no. 11, p. e49182, Nov. 2012, doi: 10.1371/journal.pone.0049182.

[301] S. Yang *et al.*, “Soft X-ray XANES studies of various phases related to LiFePO4 based cathode materials,” *Energy Environ. Sci.*, vol. 5, no. 5, pp. 7007–7016, 2012, doi: 10.1039/c2ee03445j.

[302] S. J. Rezvani *et al.*, “SEI Dynamics in Metal Oxide Conversion Electrodes of Li-Ion Batteries,” *J. Phys. Chem. C*, vol. 121, no. 47, pp. 26379–26388, Nov. 2017, doi: 10.1021/acs.jpcc.7b08259.

[303] R. Qiao *et al.*, “Distinct Solid-Electrolyte-Interphases on Sn (100) and (001) Electrodes Studied by Soft X-Ray Spectroscopy,” *Adv. Mater. Interfaces*, vol. 1, no. 3, pp. 1–6, 2014, doi: 10.1002/admi.201300115.

[304] S. J. Rezvani *et al.*, “Is the Solid Electrolyte Interphase an Extra-Charge Reservoir in Li-Ion Batteries?,” *ACS Appl. Mater. Interfaces*, vol. 9, no. 5, pp. 4570–4576, 2017, doi: 10.1021/acsami.6b12408.

[305] Q. Li *et al.*, “Identification of the Solid Electrolyte Interface on the Si/C Composite Anode with FEC as the Additive,” *ACS Appl. Mater. Interfaces*, vol. 11, no. 15, pp. 14066–14075, 2019, doi: 10.1021/acsami.8b22221.

[306] B. Ravel and M. Newville, “ATHENA, ARTEMIS, HEPHAESTUS: Data analysis for X-ray absorption spectroscopy using IFEFFIT,” *J. Synchrotron Radiat.*, vol. 12, no. 4, pp. 537–541, 2005, doi: 10.1107/S0909049505012719.

[307] M. A. Branch, T. F. Coleman, and Y. Li, “A Subspace, Interior, and Conjugate Gradient Method for Large-Scale Bound-Constrained Minimization Problems,” *SIAM J. Sci. Comput.*, vol. 21, no. 1, pp. 1–23, Jan. 1999, doi: 10.1137/S1064827595289108.

[308] P. Virtanen *et al.*, “SciPy 1.0: fundamental algorithms for scientific computing in Python,” *Nat. Methods*, vol. 17, no. 3, pp. 261–272, Mar. 2020, doi: 10.1038/s41592-019-0686-2.

[309] A. P. Hitchcock and C. E. Brion, “K-shell excitation of HF and F2 studied by electron energy-loss spectroscopy,” *J. Phys. B At. Mol. Phys.*, vol. 14, no. 22, pp. 4399–4413, 1981, doi: 10.1088/0022-3700/14/22/022.

[310] M. B. Robin, I. Ishii, R. McLaren, and A. P. Hitchcock, “Fluorination effects on the inner-shell spectra of unsaturated molecules,” *J. Electron Spectros. Relat. Phenomena*, vol. 47, no. C, pp. 53–92, 1988, doi: 10.1016/0368-2048(88)85005-9.

[311] S. Y. Turishchev *et al.*, “Surface deep profile synchrotron studies of mechanically modified top-down silicon nanowires array using ultrasoft X-ray absorption near edge structure spectroscopy,” *Sci. Rep.*, vol. 9, no. 1, pp. 1–7, 2019, doi: 10.1038/s41598-019-44555-y.

[312] P. E. Batson, K. L. Kavanagh, C. Y. Wong, and J. M. Woodall, “Local bonding and electronic structure obtained from electron energy loss scattering,” *Ultramicroscopy*, vol. 22, no. 1–4, pp. 89–101, 1987, doi: 10.1016/0304-3991(87)90053-2.

[313] S. J. An, J. Li, C. Daniel, D. Mohanty, S. Nagpure, and D. L. Wood, “The state of understanding of the lithium-ion-battery graphite solid electrolyte interphase (SEI) and its relationship to formation cycling,” *Carbon N. Y.*, vol. 105, pp. 52–76, Aug. 2016, doi: 10.1016/j.carbon.2016.04.008.

[314] L. J. Krause, V. L. Chevrier, L. D. Jensen, and T. Brandt, “The Effect of Carbon Dioxide on the Cycle Life and Electrolyte Stability of Li-Ion Full Cells Containing Silicon Alloy,” *J. Electrochem. Soc.*, vol. 164, no. 12, pp. A2527–A2533, Aug. 2017, doi: 10.1149/2.1121712jes.

[315] E. J. Hopkins *et al.*, “Examining CO 2 as an Additive for Solid Electrolyte Interphase Formation on Silicon Anodes,” *J. Electrochem. Soc.*, vol. 168, no. 3, p. 030534, Mar. 2021, doi: 10.1149/1945-7111/abec66.

[316] C. N. Krishnan, R. H. Hauge, and J. L. Margrave, “Studies of carbon monoxide activation with atomic lithium: IR spectra of LiCO, LiOC, LiC2O2 and Li2C2O2 in cryogenic matrices,” *J. Mol.*

Struct., vol. 157, no. 1–3, pp. 187–196, Mar. 1987, doi: 10.1016/0022-2860(87)87092-8.

[317] M. Tsutsui, A. Arima, K. Yokota, Y. Baba, and T. Kawai, “Ionic heat dissipation in solid-state pores,” *Sci. Adv.*, vol. 8, no. 6, pp. 1–9, Feb. 2022, doi: 10.1126/sciadv.abl7002.

[318] A. A. Abd-El-Latif *et al.*, “Insights into electrochemical reactions by differential electrochemical mass spectrometry,” *TrAC Trends Anal. Chem.*, vol. 70, pp. 4–13, Jul. 2015, doi: 10.1016/j.trac.2015.01.015.

[319] B. Rowden and N. Garcia-Araez, “A review of gas evolution in lithium ion batteries,” *Energy Reports*, vol. 6, pp. 10–18, May 2020, doi: 10.1016/j.egyr.2020.02.022.

[320] T. Inc., “MWWHF2 Fiber-Coupled LEDs Thorlabs Inc.” https://www.thorlabs.com/images/popupImages/MWWHF2_data.xlsx.

[321] M. Schellenberger, R. Golnak, W. G. Quevedo Garzon, S. Risse, and R. Seidel, “Accessing the solid electrolyte interphase on silicon anodes for lithium-ion batteries in-situ through transmission soft X-ray absorption spectroscopy,” *Mater. Today Adv.*, vol. 14, p. 100215, Jun. 2022, doi: 10.1016/j.mtadv.2022.100215.

[322] G. Csiszár, M. Schellenberger, and G. Schmitz, “Synthesis and thermal reaction of stainless steel nanowires,” *Nanoscale*, vol. 12, no. 2, pp. 731–745, 2020, doi: 10.1039/C9NR06946A.

[323] L. Xi *et al.*, “Structural Monitoring of NiB i Modified BiVO 4 Photoanodes Using in Situ Soft and Hard X-ray Absorption Spectroscopies,” *ACS Appl. Energy Mater.*, vol. 2, no. 6, pp. 4126–4134, Jun. 2019, doi: 10.1021/acsaem.9b00304.

[324] L. Xi, M. Schellenberger, R. F. Präg, R. Golnak, G. Schuck, and K. M. Lange, “Ionic Current Mn K -Edge X-ray Absorption Spectra Obtained in a Flow Cell,” *J. Phys. Chem. C*, vol. 122, no. 27, pp. 15588–15594, Jul. 2018, doi: 10.1021/acs.jpcc.8b04693.

VII Appendix

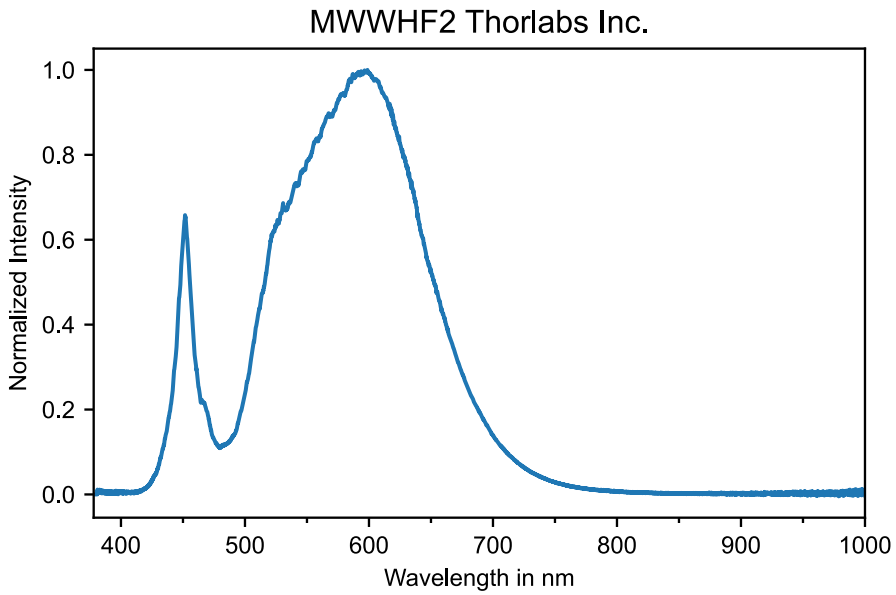

Appendix 1 Emission spectrum of the "MWWHF2 Fiber-Coupled LED 4000 K" from Thorlabs Inc. [320]

Publications

Accessing the solid electrolyte interphase on silicon anodes for lithium-ion batteries in-situ through transmission soft X-ray absorption spectroscopy

M. Schellenberger, R. Golnak, W. G. Quevedo Garzon, S. Risse, and R. Seidel
Mater. Today Adv., vol. 14, 2022, ref [321]

Synthesis and thermal reaction of stainless steel nanowires

G. Csiszár, **M. Schellenberger**, and G. Schmitz
Nanoscale, vol. 12, 2020, ref [322]

Structural Monitoring of NiB_i Modified $BiVO_4$ Photoanodes Using in Situ Soft and Hard X-ray Absorption Spectroscopies

L. Xi, **M. Schellenberger**, R. F. Präg, D. Gao, D. Drevon, P. Plate, P. Bagdanoff, R. van de Krol, and K. M. Lange
ACS Appl. Energy Mater., vol. 2, 2019, ref [323]

Ionic Current Mn K -Edge X-ray Absorption Spectra Obtained in a Flow Cell

L. Xi, **M. Schellenberger**, R. F. Präg, R. Golnak, G. Schuck, and K. M. Lange
J. Phys. Chem. C, vol. 122, 2018, ref [324]

Acknowledgments

I am extremely grateful to Dr. Robert Seidel for adopting me as a stray dog after my old working group disbanded and giving me the opportunity to still finish my PhD three years later, for putting all that trust in me, for all the sweets and chocolate, for turning a blind eye on my grumpy and rude self when long nightshifts turned sour, for inciting hope when experiments failed one too many times, for showing me The Land of the Not So Free Anymore, and of course, all scientific guidance throughout the years. You always went out of your way to support me in every possible way. I truly appreciate it.

I would like to thank all members of my dissertation committee, especially Prof. Simone Raoux and Prof. John Hemminger, who reviewed this thesis.

I would like to thank Dr. Sebastian Risse for introducing me to the topic of silicon anodes and for the insightful input as well as the scientific guidance throughout the years.

I would like to thank Dr. Ronny Golnak for entrusting me with his precious LiXEdrom. When I was left to my own, non-existing devices, you went out of your way to teach me what there was to know: from properly closing a KF flange to operating a beamline or sealing a cell with way too much glue. I truly appreciate your guidance and all knowledge you shared with me.

I would like to thank Herrmann Thiel from BESSY's sample environment for saving my ass way too many times. My clumsy hands should never touch power tools and you always helped me out. I could count on you for getting things done quickly, on Friday evenings and Monday mornings. Your last-minute fixes saved more of my beamtimes than I'd like to admit. I truly appreciate it.

I would like to thank Karsten Harbauer and Dr. Engin Özkol for the preparation of my samples. You tolerated my hectic beamtime schedules, always helped me out on short notice and, through your amazing work, blessed me with stellar reproducibility. I truly appreciate it.

I would like to thank Dr. Fatwa Firdaus Abdi and the Helmholtz Energy Materials Foundry for providing me access to the COMSOL Multiphysics® software package.

I would like to thank the precious members of my group, Dr. Wilson Quevedo, Garlef Wartner, Dennis Hein, and Hanna Trzesniowski, for the many fruitful discussions, numerous advice, shared desperation and laid-back atmosphere around the office and beamlines. I truly appreciate it and wish you all the best.

I would like to thank my parents for supporting me and blessing me with the privilege to pursue an academic career.

Finally, I would like to thank my friends who helped me push, when push came to shove.